universität wien

DISSERTATION

Titel der Dissertation

A universal matter-wave interferometer with optical gratings

Verfasser

Mag. Philipp Haslinger

angestrebter akademischer Grad

Doktor der Naturwissenschaften (Dr.rer.nat.)

Wien, 2013

Studienkennzahl lt. Studienblatt:	A 091 411
Dissertationsgebiet lt. Studienblatt:	Physik
Betreuerin / Betreuer:	Univ.-Prof. Dr. Markus Arndt

Contents

Table of contents

ZUSAMMENFASSUNG

Die Quantenmechanik wurde ursprünglich entwickelt um mikroskopische Vorgänge genauer und besser beschreiben zu können. Doch bald stießen WissenschaftlerInnen auf weitreichende und zum Teil mit hergebrachten Vorstellungen unvereinbare Vorhersagen, wie den Welle-Teilchen Dualismus von Materie [1,2] oder die quantenmechanische Verschränkung von Teilchen [3,4]. In keinem einzigen Experiment konnte jedoch die Quantenmechanik falsifiziert werden. Heute ist sie die am meisten getestete Theorie der Physik. Es stellt sich jedoch die Frage nach möglichen Grenzen des Gültigkeitsbereiches der Quantenmechanik. Wie makroskopisch, komplex und massiv dürfen Quantensysteme sein? Wie weit voneinander und für welche Zeit kann man Wellenfunktionen kohärent trennen? Welche Dekohärenz-Mechanismen gibt es, die unsere Welt so klassisch erscheinen lassen?

Während meiner Dissertation setzte ich mich theoretisch als auch experimentell mit Materiewellen-Interferometrie von Atomen bis Molekülen und molekularen Clustern auseinander.

Während meines Forschungsaufenthalts in der Gruppe von Prof. Holger Müller an der University of California, Berkeley, konnten wir die dazumal größte Raum-Zeit Aufspaltung von atomaren Wellenfunktionen zeigen [5]. Dabei wurden die Materiewellen von Cäsiumatomen bis zu 8.8 mm und für 500 ms kohärent getrennt und anschließend wieder vereinigt. Entscheidend für diese große räumliche und zeitliche Separation der Materiewellen war die Kompensation der Erdrotation, die durch die Corioliskraft ein kohärentes Zusammenfügen der Materiewellen verhindert.

Das zentrale Thema meiner Dissertation an der Universität Wien war der Aufbau eines rein optischen ionisierenden Talbot-Lau Materiewellen-Interferometer (OTIMA) [6,7], das komplexe Teilchen an nur einigen Nanosekunden langen Lichtgittern beugt. Dadurch kann man erreichen, Teilchen unabhängig von ihrer Geschwindigkeit zu interferieren. Dieser Effekt wurde schon für bestimmte Atome

beobachtet [8] und wurde nun zum ersten Mal auch für komplexe Teilchen bis zu 2300 amu durch das OTIMA-Interferometer gezeigt. Diese fundamentale Art der zeitlichen Interferenz ist nur noch abhängig von der Masse der Teilchen. Ein Interferenzmuster kann jetzt nicht nur im Raum, sondern auch in der Massenverteilung von Teilchen gemessen werden. Die gepulsten Lichtgitter erzeugen aus einer unkollimierten Molekülwolke ein Interferenzmuster, das eine Periode von 78.5 nm besitzt und dadurch sehr empfindlich auf äußere Einflüsse ist. Diese hohe Empfindlichkeit zusammen mit der Geschwindigkeitsunabhängigkeit kann in zukünftigen Deflektometrie-Experimenten genutzt werden, kleinste auf Teilchen wirkende Kräfte sehr präzise zu messen.

ABSTRACT

Quantum mechanics was initially developed to describe microscopic processes but scientists quickly came to far-reaching predictions, such as the wave-particle dualism of matter [1,2] or the entanglement of particles [3,4], which often contradict our classical intuition. However, not even a single experiment could falsify any theoretical prediction of quantum mechanics. Today it is the most tested theory in physics. The question of the range and limits of its validity arises. To which extend can systems be macroscopic, complex and massive while retaining their quantum features? Is there a spatial and temporal restriction to the separation of wave functions? Which decoherence mechanisms force systems at macroscopic scales to appear classical?

During my thesis I focused theoretically as well as experimentally on matter-wave interferometry with atoms, molecules and molecular clusters.

During my 3 month exchange stay in the group of Prof. Müller at the University of California at Berkeley we have carried out an experiment to show the largest space-time area interferometer at that time [9]. Here, matter waves of caesium atoms have been coherently split and recombined up to 8.8 mm and for 500 ms. Key to run this experiment was to compensate for earth´s rotation. Without this compensation the Coriolis force would have prevented the split matter-waves from a precise recombination.

The main subject of my thesis at the University of Vienna was the experimental realization of the (first) all *O*ptical *T*ime-domain *I*onizing *Ma*tter-wave (OTIMA) interferometer [6,7]. It consists of three pulsed nanosecond standing light waves which act on the particles with a well-defined timing sequence. Interference in the time-domain is independent of the particles' velocities and of their de Broglie wavelengths. This has been demonstrated earlier for atoms by addressing laser light to certain atomic levels [8]. In contrast to that, the OTIMA interferometer uses optical ionization gratings [10] which allow us to coherently manipulate many atoms, molecules and nanoparticles, since photo ionization is mostly independent of

the specific internal level structure of the nanoparticle. As a result we can interfere different particles simultaneously. Quantum interference in the OTIMA setup is not only visible in the spatial interference pattern but also in the mass selective transmission, which is a feature of the time-domain. This has been proven for Anthracene clusters up to 2300 amu [6]. The interference pattern has a period of 78.5 nm and is therefore highly sensitive to external forces. This feature as well as the accurate timing of the OTIMA offer an enormous advantage for future deflectometry experiments.

1 Interferometry: Introduction to the concept of time-domain

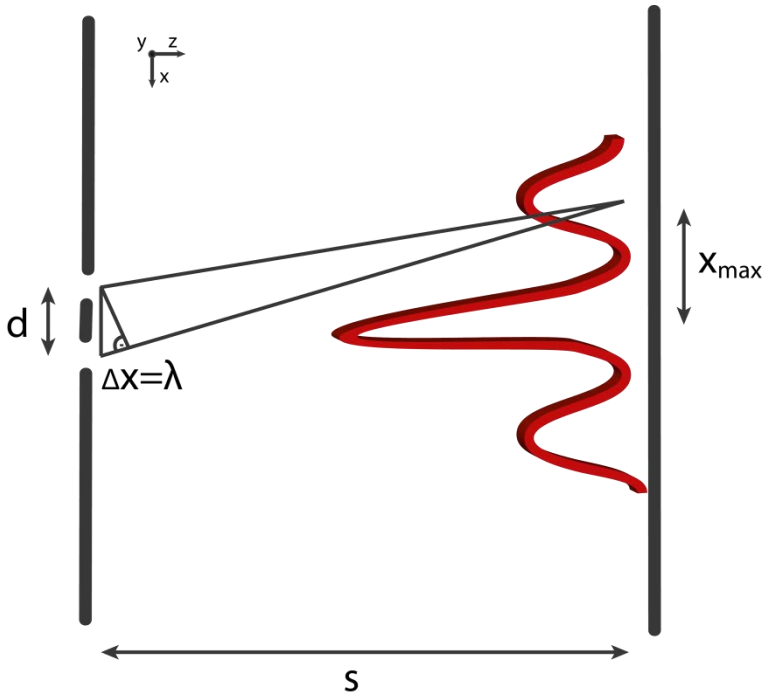

Figure 1-1 Sketch of a far field interferometer

A normal "double slit experiment" consists of two slits separated by the distance *d* and a device that detects the particles after a distance *s*. The particles/waves approach the double slit (see Figure 1-1) from the left with nearly parallel trajectories (collimated by slits). Such double slit experiments have been performed with light [11] electrons, atoms, small and large molecules [12–15] to demonstrate their wave properties. The vertical position of the interference maximum is given by

$$x_{max} = n\lambda\frac{s}{d} \qquad \text{(E 1-1)}$$

where n is the interference order and λ the wavelength. Good wavelength selection is necessary to observe a high contrast interference pattern. Photons from a thermal source, a light bulb for instance, can be optically filtered in order to achieve a "monochromatic" beam. This is more challenging for thermal particles. The de Broglie wavelength [1] is given by

$$\lambda_{dB} = \frac{h}{mv}$$

h denotes the Plank´s constant, m the mass and v the velocity of the particle. To restrict the spectrum of different de Broglie wavelengths in a thermal beam, the velocity and/or the mass distribution must be narrowed. Mass distributions are much easier to control, for example by using chemical preselected molecules/atoms and/or post mass selection in time-of-flight or quadrupole mass-spectrometer [16,17]. The velocity of a certain thermal particle is random and follows the Maxwell-Boltzmann distribution. In order to detect just a narrow band of velocities, the beam can be chopped or pulsed. However, this restriction of velocities is not crucial. Changing equation (E 1-1) slightly to

$$x_{max} = \frac{h}{mv}\frac{s}{d} = \frac{ht}{md}$$

eliminates the velocity dependence. The position x_{max} depends on $t = \frac{s}{v}$, a time, defined by the slit separation d and the mass m. This is the time the matter-wave needs to become diffracted by a distance x_{max}. After the same time all particles with the same mass produce the same interference, regardless of their velocities. To make it more intuitive, a momentum kick can be extracted from this formula

$$p_d = \frac{h}{d}$$

which only depends on the grating constant d. This grating kick is equal for all particles irrespective of their velocities or masses.

Let us now assume an experiment with a pulsed source placed in front of the double slit, which produces plane matter-waves. A particle pulse containing different velocities is emitted and passes through the two slits. After some time an interference pattern forms in space (x-z plane), see Figure 1-2. This interference pattern spreads out along the z-axis (beam-direction) corresponding to the various velocities of the molecules, but it is totally non-dispersive in the x-axis (parallel to the grating). If the particles were detected on a screen with a fixed position, the interference contrast would be reduced because of the different transit times between the double slit and the screen. This smearing can be avoided by a time-domain detection scheme using a pulsed standing light wave of the same period as the appearing interference fringes. The standing light wave can be produced by a pulsed laser beam that is retro-reflected on a mirror. The wavelength of the laser photons has to be chosen in order to efficiently ionize the particles in the antinodes of the standing light wave. The laser grating acts like a spatially filtering mask and it is applied at a time when x_{max} is of the size of the grating constant d_λ of the laser grating, over a wide area in the z-y plane. In other words, a pulsed standing light wave with a grating constant d_λ is used to scan over an interference pattern with the period d_λ. The remaining particles are afterwards detected and plotted as a function of the vertical position of the scanning laser grating. In order to guarantee that all detected particles have interacted with the diffraction grating at the same starting time, the material diffraction grating has to be replaced by a pulsed laser grating of period d_λ.

An important property of the particle beam is spatial coherence. It can be created by sending the massive particles through a transmission grating. When we translate the van Cittert-Zernike theorem [18] into the time-domain it tells us that a molecular beam, as provided by a transmission grating, coherently illuminates after a fixed time a diffraction grating with the same grating constants.

Thus, the combination of three light gratings (one to produce a coherent beam, one to diffract the matter waves and one to detect the interference pattern) forms an interferometer in the time-domain. The spatial realization of this three grating near-field interferometer is known as Talbot-Lau interferometer [19,20].

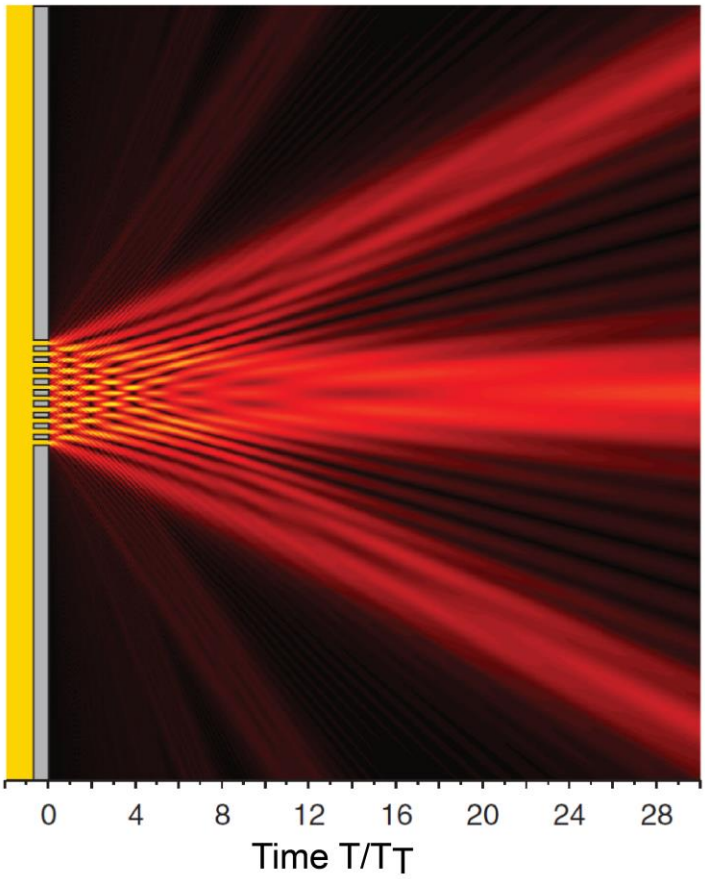

Figure 1-2 Simulation of the transition from the near-field to the far-field: A grating is illuminated from the left by a spatially coherent wave of particles with a certain mass. Regions of bright colors indicate high intensity. After the time T_T the particles show an interference pattern similar to the grating structure. This is repeated several times T/T_T=1, 2, 3, ... At larger distances the principal far-field diffraction orders are built up. Figure from[21], modified.

1.1 Talbot-Lau interferometry in space and time

In this chapter I would like to connect the concept of the Talbot-Lau interferometer, which works in the near-field regime, with the idea of time-domain interferometry [8]. I will start with a short description of the Talbot-Lau interferometer (TLI) with three material gratings [19,20]. Then I will replace the second material grating with a laser grating and introduce the Kapitza-Dirac-Talbot-Lau interferometer (KDTLI)[22]. Finally, I will focus on the all optical implementation of a TLI, an *O*ptical *T*ime-domain *I*onizing *MA*tter (OTIMA) interferometer [6,7,10]. This interferometer works in a pulsed way and is suitable to interfere matter in the time-domain. But first I would like to establish a quantity which measures the intensity of the interference contrast.

1.1.1 Interference Contrast – Visibility

To compare the quality of the interference patterns, one can define the quantity visibility *V*. The visibility is a function of the maximal S_{max} and minimal S_{min} signal intensities of an interference pattern[18].

$$V := \frac{S_{max} - S_{min}}{S_{max} + S_{min}} \quad \in \quad [0,1]$$

Figure 1-3 shows the expected near-field interference pattern behind a grating, which is illuminated by a plane wave. A carpet of different periodicities builds up as a function of the distance from the grating. These entire patterns can be decomposed at each position in a Fourier spectrum and written in a basis of sinusoidal functions. The interference fringes in a TLI are resolved by scanning the third grating with a grating period *d* over these patterns. The transmitted signal, a function of the position *x,* is given in first order approximation by:

$$S(x) = S_0 + 2S_1 sin(n\frac{2\pi x}{d})$$

Where d denotes the grating constant and $n = \left(\frac{L}{L_T} mod 1\right)^{-1}$ defines the periodicity of the interference pattern. This leads to a visibility given by the amplitude and the offset of a sine function.

$$V_{exp} = \frac{2S_1}{S_0} \qquad \text{(E 1-2)}$$

Instead of scanning the interference pattern over several periods, it is in various experiments sufficient to measure just at two positions in order to extract the amplitude (if knowledge about the frequency can be assumed). In experiments where the absolute knowledge of the visibility is not necessary, or only relative changes in the visibility are measured, it is appropriate to accumulate the transmitted particles at one x-point near the interference maximum S_{qua} of the formed interference pattern and without interference S_{cla} (for example with misaligned gratings).

In this case we will make use of a more general quantity, the normalized signal difference

$$\Delta S_N = \frac{(S_{qua} - S_{cla})}{S_{cla}} \qquad \text{(E 1-3)}$$

1.1.2 Talbot-Lau in space

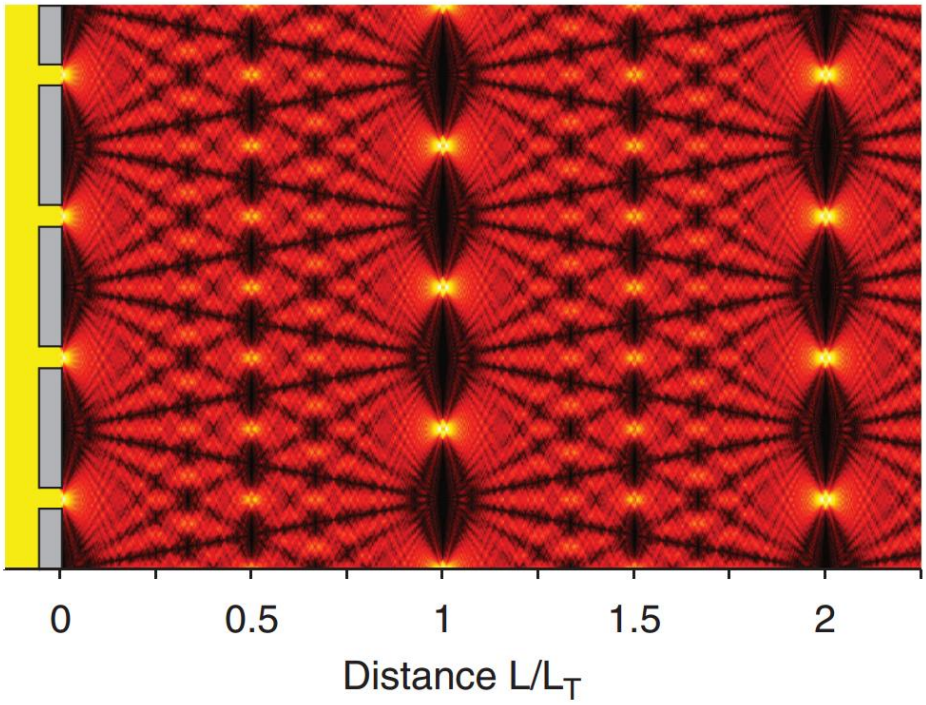

Figure 1-3 The Talbot carpet illustrates the near field interference pattern of a grating illuminated from the left with a monochromatic plane wave. Various interference fringes emerge with periods of multiple integer of the grating constant *d*. After a distance L_T, an interference pattern is formed with the same period as the grating *d*. Regions of bright colors indicate high intensities. Figure from [21].

In 1836 William Henry Fox Talbot discovered that intensity variations of parallel monochromatic light behind an illuminated grating reproduce the grating structure after certain distance [23]. This so called Talbot distance L_T depends on the grating constant *d* and the wavelength of the incoming light λ.

$$L_T = \frac{nd^2}{\lambda}$$

The lateral periodicity of this effect is denoted by *n*. If *n* is an even integer, the observed interference pattern reproduces exactly the grating. For odd integers, the

pattern is laterally shifted by a half grating period. For non-integers but rational multiples, the fringes show higher spatial periods as the original grating (see Figure 1-3).

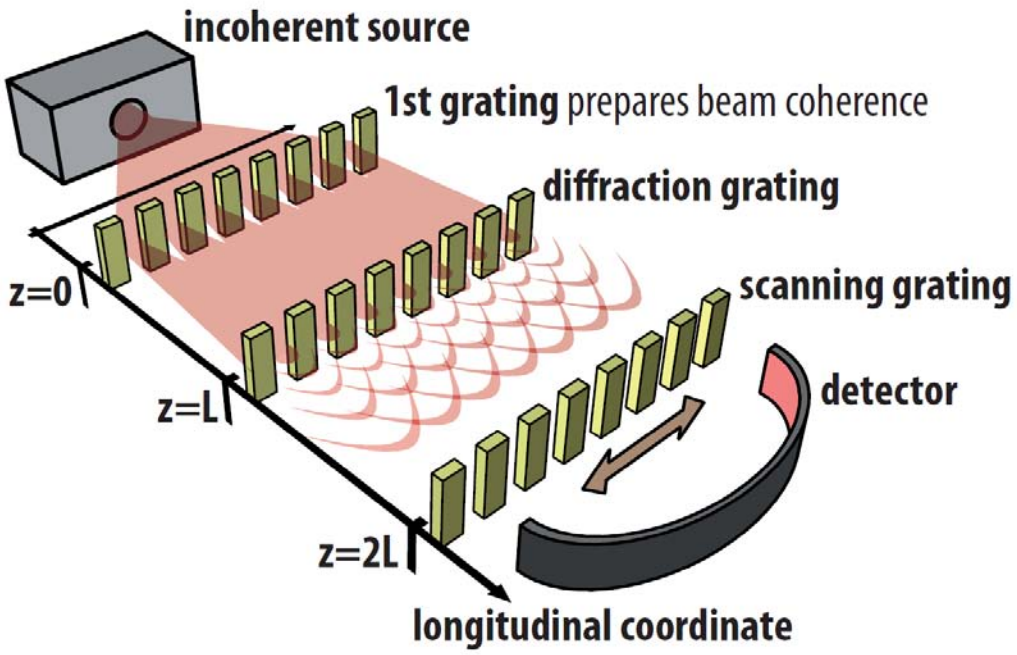

Figure 1-4 A Talbot-Lau-interferometer (TLI) consists of 3 gratings with the same grating constant. The distance between the gratings has to be equal in order to fulfill the Talbot [23] and the Lau [24] condition. The first grating prepares coherence from an incoherent beam at the position of the second grating, which is used to diffract the particles-waves. The appearing interference pattern is scanned by shifting the third grating. The remaining particles are detected and counted as a function of the position of the third grating. Figure from [25].

In order to use the Talbot-effect a source of monochromatic plane waves is needed [26]. Laser like sources have been built for atoms [27–30], but for complex molecules it is necessary to use point sources with collimated and velocity selected beams, as discussed in 3.1.

An efficient way to produce sufficient coherence is provided by the Lau-effect [24]. It is an experimental implementation of the Van Cittert-Zernike theorem, which states that the coherence function at a certain distance (the Talbot-length L_T) behind

an incoherently illuminated aperture has the same shape as the interference pattern under coherent illumination of the same aperture [18]. The aperture given by a grating with the period *d* has the needed shape to produce (after a distance $L_{T)}$ the required coherence function for the diffraction grating. A TLI is formed [19,20,31] by combining the Talbot- and the Lau-effect, see Figure 1-4.

The Lau-effect provides the coherence and the Talbot effect delivers an interference pattern. In order to detect the interference pattern of periodicity *d,* a third grating with the same period can be used. It acts as a transmission mask and is scanned over the matter density pattern. When the transmitted signal is detected as a function of the position of the third grating, it represents a measure of molecular interference. The main advantage of the Talbot-Lau concept compared to far-field diffraction is the compatibility with laterally incoherent particle beams. This allows one to renounce on collimation slits and to work with thousands of coherence preparation slits in parallel - which results in an enormous signal enhancement over the single slit collimator. In addition, this scheme offers a favorable length scaling behavior with the wavelength: The required grating period decreases with the square root of λ_{dB} in the near-field whereas it scales linearly in the far-field regime.

1.1.3 Van der Waals interaction and optical phase grating

The TL interferometer would be a perfect instrument to prove the quantum wave properties of heavy particles if it were not for the van der Waals interaction [32], which attracts the particles towards the grating walls. It is caused by dipole fluctuations of the polarizable particles in interaction with their induced image charges in the grating walls. It scales with [33]

$$V \approx -\frac{C_3}{r^3}, \rightarrow V \approx -\frac{C_4}{r^4}$$

The first equation holds close the grating wall (van der Waals regime), while the reduced potential on the right-hand side is valid for large distances to the wall

(Casimir Polder regime). The typical transition between short and long distances is of the order of the wavelength of the strongest dipole transition in the polarizable particle, in practice several dozen nanometers. r denotes the distance between the particle and the grating wall and $C_4 = 3\hbar c\alpha/8\pi$ is a constant that only depends on the particles's polarizability for the case of a perfectly conducing metal surface.

The constant C_3 depends on the total frequency spectrum of both the polarizability and the gratings dielectric constant [34]. In order to study interference of heavier particles, the particle velocity should be slow enough to ensure compatibility of the de Broglie wavelength with the experimental settings. However, the deflection caused by the van der Waals force grows quadratically with the interaction time at the grating [35,36]. This results in a smearing out of the interference pattern and it effectively reduces the grating's open fraction. The acceleration towards the gratings walls will lead to absorption of particles within a certain distance from the walls.

Let´s consider for example [33] a Au_{5000} cluster with a mass of about 10^6amu in a distance of 50 nm from a 100 nm long grating wall. At a velocity of 1 m/s, which is required for the interference of a 10^6 amu particle in a tabletop experiment, the cluster is absorbed after ~100 ns. This illustration shows the technical limitation for material diffraction gratings. Although grating structures fabricated with ultra-thin membranes like atomically thin grapheme [37] or meta-material [38] may overcome this restriction, even the thinnest grating membranes will still influence particles while approaching and escaping the grating structure by a van der Waals dispersive interaction.

A way to get rid of this problem is given by gratings made out of standing light waves, which act as phase gratings to diffract the particles (see 2.3). The periodically modulated electrical field of a standing light wave interacts with the optical polarizability of the particles. Far-field diffraction experiments [35] with standing light waves as well as the experimental implementation of a TL-interferometer with a diffraction grating made of a standing light wave (Kapitza - Dirac Talbot – Lau interferometer (KDTLI)) have been successfully shown [22,39]. The KDTLI holds the current record of the heaviest diffracted particles [40]. Quantum interference has been demonstrated for tailor-made organic molecules with

about 430 atoms [41] and a mass of 6910 amu most recently even more than 800 atoms and masses beyond 10100 amu [42].
Nevertheless the van der Waals interaction still plays a role in this experiment since the first and the third grating have to act as absorptive mechanical masks and are therefore material gratings. In addition, velocity selection is needed to form molecular beam with a moderate monochromaticity of better than $\delta v/v \leq 20\%$. All these restrictions are circumvented by implementing a Talbot-Lau interferometer by three ionizing pulsed standing light waves in the time-domain.

1.1.4 Talbot-Lau interferometry in the time-domain

Now we´ll have a closer look at the formula of the Talbot length. That's the distance a particle with a certain λ_{dB} needs to fulfill both Talbot [23] and Lau [24] conditions.

$$L_T = n\frac{d^2}{\lambda_{dB}} \qquad \text{(E 1-4)}$$

is the length which is needed to diffract the particles by the grating period d or a n-fold multiple of it. The de Broglie wavelength is given by $\lambda_{dB} = h/mv$ and we focus on the case where $n = 1$.

$$L_T = \frac{d^2 mv}{h}$$

Dividing this Talbot length by the velocity of the particle, we get an expression with the dimension of time.

$$T_T = \frac{L_T}{v} = \frac{d^2 m}{h} \qquad \text{(E 1-5)}$$

T_T is the time that particles of mass m need to become diffracted by one grating period d. The interference pattern is now elongated in the z- axes (flight direction) corresponding to the different particles velocities and to their different Talbot-Lau lengths L_T. Nevertheless, the Talbot-time T_T depends on the mass of the particles. The momentum kick

$$p_d = \frac{h}{d}$$

is imparted on all particles during the interaction with the grating. It is the key for interference in the space-time-domain and leads us to the central statement of pure de Broglie (i.e. center of mass) matter-wave interferometry where the interaction time of the particle and the grating are externally set.

After the same time all particles with the same mass produce the same interference, regardless of their velocities.

To implement this idea of Talbot-Lau interferometry in the time-domain, it is necessary to find diffraction structures which can be applied on particles with high temporal precision [31,43]. Ideal candidates for this diffraction structures are gratings made of standing light waves [10,13,22,44–49]. Compared to material gratings, light gratings are advantageous since they avoid deflection due to Van der Waals forces.

2 A universal matter wave interferometer in the time-domain with optical gratings

Figure 2-1 gives an overview of the experimental implementation of time-domain interferometry for complex molecules. The setup consists of a source with a fast pulsed valve (V) which emits neutral particles (see 3.1) as well as delimiters to restrict height (H) and width (W) of the particle beam. A 2-inch mirror provides the boundary condition for the standing light waves. The three laser pulses emitted from three F2-excimer lasers ($\lambda = 157nm$) at $t_1 = 0$, $t_2 = T$ and $t_3 = 2T$ are back-reflected and form three standing light waves (see 2.3) with a period of $\lambda/2$. The first laser beam is used to prepare the needed spatial coherence, the second one coherently rephases the matter-waves and the third grating acts like an absorptive filter which resolves the appearing interference pattern in space (see 2.4). The remaining neutral particles are ionized by a pulsed laser beam (L) and they are detected in a time-of-flight mass-spectrometer TOF-MS (see 3.2). A fast photodiode records the timing and energy (relative to each other) of the three laser pulses. A computer program analyses these pulses and corrects the temporal settings and laser powers, if necessary (see 3.5). In order to reduce decoherence by collisions with the residual gas, high vacuum conditions have to be ensured. Therefore the source chamber, with a pressure of up to $p_1 > 10^{-5}$ mbar, has to be separated from the main interference chamber with $p_2 < 10^{-8}$ mbar by a differential pumping stage.

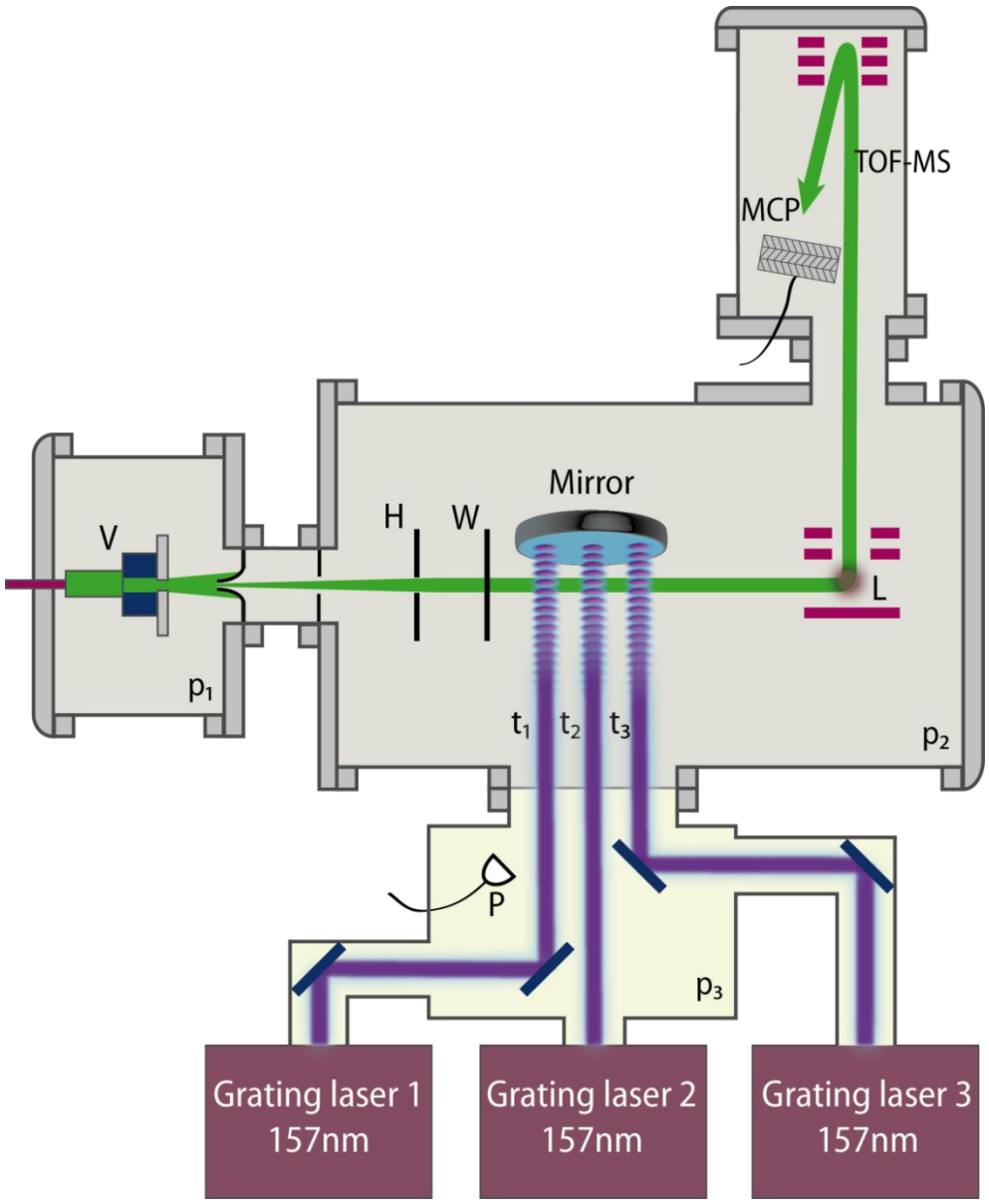

Figure 2-1 Experimental overview of the OTIMA interferometer. From left to right: The setup consists of a pulsed source (V), the Even-Lavie valve (see 3.1.2). The source and the main interferometer chamber are separated by a differential pumping stage to ensure suitable vacuum conditions for interferometry. The particle beam is restricted with variable slits in height (H) and width (W). As soon as the particles pass below the 2-inch mirror the retro-reflected laser pulses at $t_1 = 0$, $t_2 = T$ and $t_3 = 2T$ form three ionizing standing light waves. The first beam is needed to prepare a certain spatial coherence, the second one is the main diffraction element and the last grating acts like a spatial filter which resolves the appearing matter-wave interference pattern, which forms as a spatial density pattern at a well-defined resonance time. The transmitted neutral particles are afterwards ionized by the detection laser (L) and mass analyzed in a TOF-MS (see 3.2). A fast photodiode (P) is used to record the laser pulse timing which changes slightly over time due to thermal drifts. Picture adapted from [6].

2.1 Advantages of light gratings

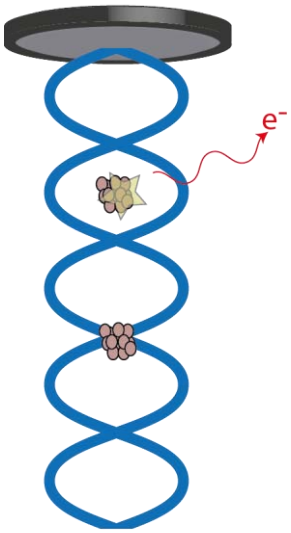

Figure 2-2 Ionizing standing light wave

Gratings, made of standing light waves [50], are ideal diffraction elements for matter wave interferometry in the time domain. The timing between the pulses can be adjusted with better than nanosecond precision. The interaction time and strength can be controlled over pulse energy and pulse length. Commercial laser systems provide coherent laser pulses with high pulse energy at UV or even VUV[1] (157 nm) wavelengths. Standing light waves with periods down to 78.5 nm reduce the time which is needed to interfere the particles and they provide an absorptive grating structure via ionization in the antinodes (Figure 2-2). The Talbot-time is given by the equation (E 1-5). A grating constant of $d = 78.5\ nm$ leads to

$$T_T = 15.4\ \mathrm{ns/amu}$$

That is the time per atomic mass unit (amu) which is at least needed to diffract the particles by a distance of *d*.

The first molecular Talbot-Lau experiments [20] were performed with gold gratings of a period of 1 µm, which corresponds to $T_T = 2.5\ \mu\mathrm{s/amu}$. Nowadays far-field interference patterns are routinely observed [12] using mechanical grating periods of 100 nm. One of the drawbacks of tiny material grating periods is that they suffer from being easily clogged by particles. Furthermore, particles interact in a dispersive way with the grating walls due to the van der Waals interaction. With light gratings we overcome these limitations.

[1] F2-Excimer laser 157nm

2.2 Theoretical description

The main elements of the OTIMA-interferometer are the three standing light waves. The laser beams are retro-reflected from a single 2-inch mirror which defines a common boundary condition for the standing light waves.
The electrical field of a running light wave is given by

$$\vec{E}\,(x,y,z,t) = Re\{\vec{\varepsilon}E_0(x,y,z)e^{i\omega t}\}$$

Here $\vec{\varepsilon}$ denotes the polarization vector and $E_0(x,y,z)$ is the spatially varying electrical field amplitude given in a Gauss-shape (ω_y, ω_z) by

$$E_0(x,y,z) = E_{0max}\sin(k_x x)e^{\left(-2\frac{y^2}{\omega_y^2}-2\frac{z^2}{\omega_z^2}\right)}$$

where we choose x to be the grating axis. The intensity of a standing light wave is given by

$$I(x,y,z) = \frac{1}{2}c\varepsilon_0\left|\vec{E}(x,y,z)\right|^2 = \frac{8\,\mathcal{P}}{\pi\omega_y\omega_z}cos^2\left(\frac{\pi x}{d}\right)e^{\left(-2\frac{y^2}{\omega_y^2}-2\frac{z^2}{\omega_z^2}\right)}$$

where $\mathcal{P}$ denotes the power of the laser beam.

The **particles interact with** the standing **light** field mainly in three ways:

On the one hand, they **absorb photons** and on the other hand they interact with the fast oscillating E-field via their optical polarizability and thus **accumulate a phase**. When the size of the particle becomes comparable with the wavelength, Rayleigh or even Mie **scattering** [51] also become relevant.

2.2.1 Absorption of a photon

Assuming that all absorption events are independent of each other, the probability of having k photons absorbed by a specific particle if, on average, a particle absorbs q photons, is described by Poissonian statistics,

$$P_q(k) = \frac{q^k}{k!} e^{-q}$$

The expectation value q is both the mean and the variance of this distribution and k denotes the number of the expected events. The average number of absorbed photons per particle is given by

$$n_0 = \sigma_A(\lambda) \frac{\mathcal{P} \cdot \tau}{h\nu\, A}$$

where $\sigma_A(\lambda)$ *is* the absolute absorption cross section for a certain wavelength λ , which we assume to be constant regardless of the number of absorbed photons. $\mathcal{P}$ denotes the power, A the area of the laser beam ($\omega_y \omega_z$), τ the laser pulse length and $h\nu$ the energy of a single photon.

The probability to absorb at least one photon for a fixed mean absorbed photon number n_0 is set by the Poissonian probability of the complementary event,

$$p(n > 0) = 1 - P_{n_0}(0) = \quad 1 - e^{-n_0}$$

For a given laser energy $\mathcal{P} \cdot t$, different particles see different grating structures/opening fractions due to their individual $\sigma_A(\lambda)$. Exactly in the nodes, the probability to absorb photons is zero. However, in the antinodes the particles feel the highest alternating electrical field which corresponds to the maximal density of photons. If one photon is sufficient to ionize or somehow mark the particle[2], then the transmission function *t(x)* through the standing light wave has the shape Figure 2-3).

[2] Particles can be pumped into a dark state [47] or

$$t(x) = e^{-n_0 sin^2(\frac{\pi x}{g})} \qquad \in \ [0,1]$$

To calculate the transmission through such a standing light wave, *t(x)* has to be integrated over 2π.

$$trans = \frac{1}{2\pi}\int_0^{2\pi} e^{-n_0 sin^2(\frac{\pi x}{d})} dx$$

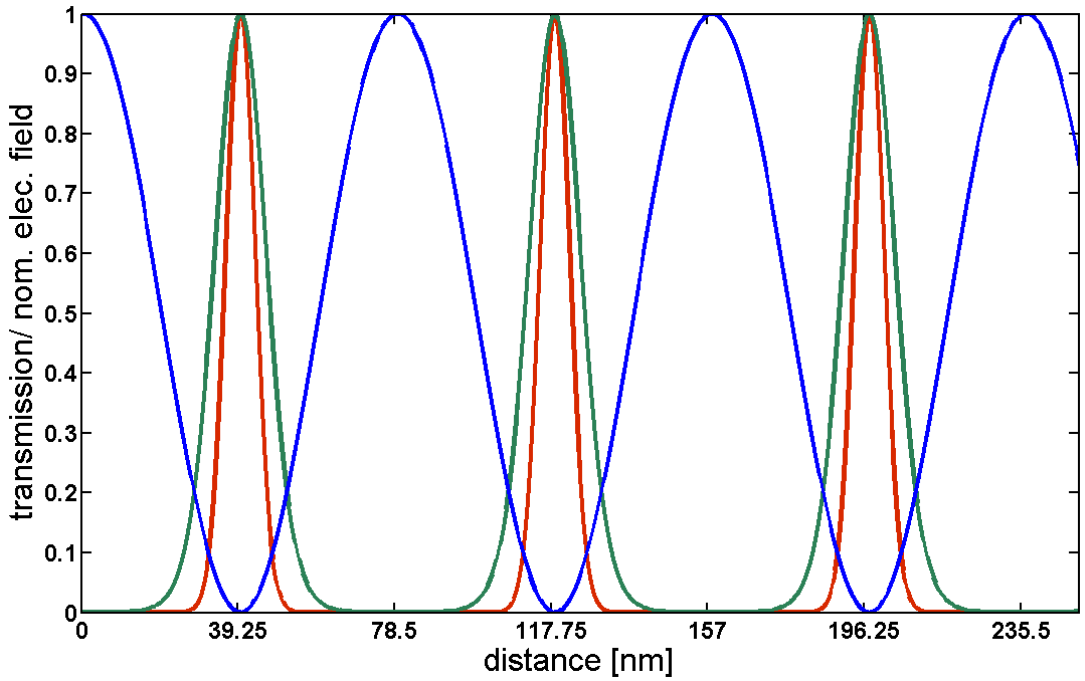

Figure 2-3 Normalized electric field of a standing light wave with a period of 78.5 nm (blue). The grating structure differs for particles of different absorption cross section or different laser intensities. Particles are counted as transmitted if they do not absorb any photon. The transmission function is plotted for the case that in the anti-nodes of the standing light wave the average number of absorbed photons amounts to n_0=8 (green) or n_0=24 (red). Increasing the cross section or intensity is tantamount to reducing the effective slit width of this tunable transmission grating.

---

be marked by depletion of an added molecule see 4.2.1

2.2.2 E-field particle interaction

Neutral particles interact with an alternating electric field via the optical polarizability and develop an induced dipole moment. Here, the oscillation frequency *f* is given by the VUV wavelength λ, 157 nm and the speed of light c.

$$f = \frac{c}{\lambda} = 1.9 \cdot 10^{15} Hz$$

The way the charge distribution of the particle behaves depends on the particles´ properties. If the electron density can follow the excitation frequency with a phase shift in a range of $-\pi/2 < \varphi < \pi/2$, the particle is accelerated to higher E-fields (high field seeker). This is the typical case for large particles. Particles with a slower electrical response, a phase shift of $\pi/2 < \varphi < 3\pi/2$, are deflected towards lower electrical fields (low field seeker). Particles with phase shifts of $\varphi = \frac{\pi}{2}$ or $\varphi = \frac{3\pi}{2}$ show no deflection [52].

The deflection grows linear with the laser intensity $I(x, y, z)$ at the particles position. The proportional factor is called optical polarizability α_λ and we can write an effective potential [53]

$$V(x, y, z) = \frac{-2\pi\alpha_\lambda I(x, y, z)}{c}$$

Particles accumulate a phase $\phi(x, \tau)$ in the presence of a potential. The phase is given by

$$\phi(x, \tau) = -V(x)\tau/\hbar$$

This phase can also be independent of the generated force (see Aharonov-Bohm effect [54–56]). The accumulated phase in the center of a Gaussian laser beam profile standing light wave is given by

$$\phi(x) = \frac{16\mathcal{P}\,\tau\,\alpha_{\lambda L}}{\hbar c \omega_y \omega_z}\cos^2\left(\frac{\pi x}{d}\right) =: V_0\cos^2\left(\frac{\pi x}{d}\right),$$

where ω_y and ω_z are the length and the width of the Gaussian beam profile and $\mathcal{P}\cdot\tau$ denotes the energy of the laser pulse.

2.2.3 Photon scattering

The effect of Rayleigh or Mie scattering becomes only important for particles whose sizes is comparable to the photon wavelength and it can therefore be neglected in the following [7]. A gold cluster of 10^9 amu for example has a diameter of 55 nm and Rayleigh scattering will only cause a visibility reduction of about 20% [7]. A particle of this mass, however, corresponds to a Talbot time of 15 seconds (assuming a 78.5 nm grating period) which exceeds the capability of Earth-based table top experiments by several orders of magnitude.

2.3 Particle light interaction

Accordingly the interaction of matter with light in the OTIMA interferometer is given by two mechanisms, the absorption of photons and the phase accumulation (E-field particle interaction). The overall particle standing light wave interaction can be written as a complex transmission function [7]:

$$t(x) = exp\left(\left(\frac{-n_0}{2} + iV_0\right)\cdot\ sin^2\left(\frac{\pi x}{d}\right)\right)$$

For the first and the third grating the complex phase part can be neglected because the initial momentum distribution of the particles is broader than the ‘grating kick’

$\Delta k = 2h/d$. The first grating just acts as an absorptive grating in order to prepare spatial coherence for the rephasing second grating (see 1.1.2). At the second grating the absorptive as well as the phase part of the standing light wave contribute to the interaction. The third grating is used to resolve the interference fringes by scanning over the emergent particle density distribution and the phase can again be ignored. The mean number of absorbed photons $n_0^{(1,2,3)}$ in the antinodes of each standing light wave (1, 2, 3) determines the contrast and is thus essential for the characterization of all gratings.

An exact theoretical description of the quantum propagation through an ionizing time-domain Talbot-Lau interferometer is given in 'Concept of an ionizing time-domain matter-wave interferometer'[7] as well as in other papers [57] and theses[58,59]. Here, I will summarize and comment the results!

The expected interference fringes will form periodic structures which can be resolved by scanning the third grating. The visibility (see 1.1.1) of this structure depends strongly on three particle properties: $\boldsymbol{\sigma_A}$ **the absolute absorption cross-section**, $\boldsymbol{\alpha_\lambda}$ **the polarizability** both at the grating wavelength of 157 nm and its **mass m**.

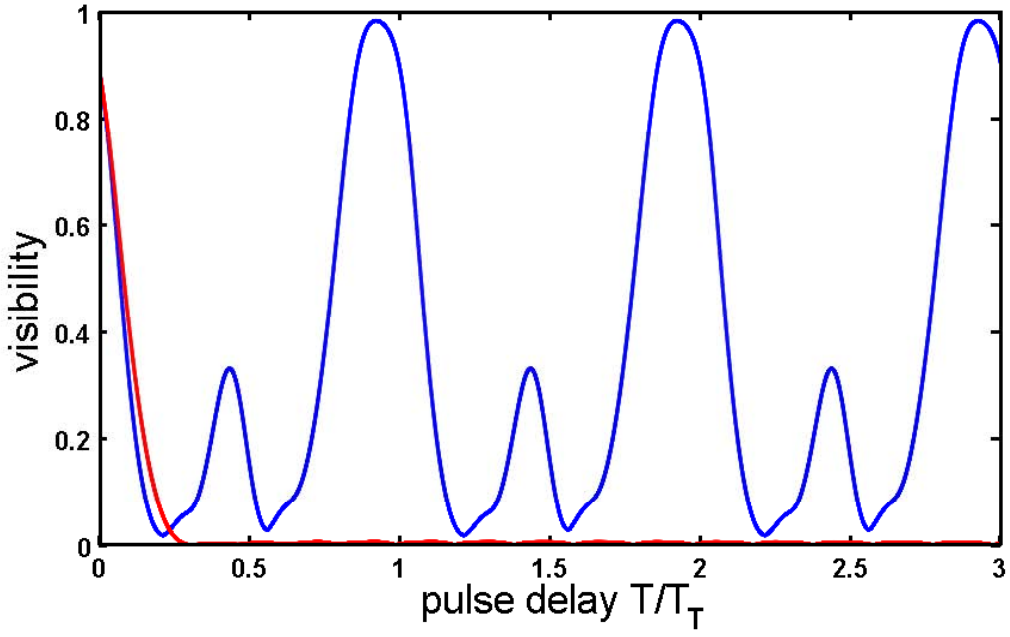

Figure 2-4 Simulation of the quantum visibility as a function of the pulse delay T/T_T for n_0=10 photons at all gratings and β=1 (blue). The corresponding classical contrast is plotted in red**.**

The transmission function of each grating is independent of the particles mass. However all three gratings together - pulsed with the right timing - show a strong mass dependent transmission as a function of the position of the third light grating. The transmission function is also significantly influenced by the ratio of σ_A and $\alpha_{\lambda L}$

$$\beta := \frac{\lambda_L \sigma_A}{8\pi^2 \alpha_{\lambda L}} = \frac{n_0}{2V_0} \qquad \text{(E 2-1)}$$

This ratio is dimensionless. $|\beta| < 1$ indicates the importance of the optical polarizability compared to the absorption cross section. $|\beta| \gg 1$ will lead to interference fringes where the effect of the optical polarizability can be neglected (see Figure 2-5). A positive β indicates a high field seeking state of the particles at 157 nm. Low field seeking states have a negative β.

2.4 How to record interference pattern?

There are several ways to record the interference patterns and to prove the quantum nature of matter with time-domain Talbot-Lau interferometry:

- A) The quantum phase is imprinted in **the mass dependent transmission** through the interferometer as a function of the pulse separation time. Each mass shows highest interference contrast around integer multiples of the Talbot-Lau time $T_T = \frac{md^2}{h}$. (Figure 2-5)

- B) The mass dependent transmission for a fixed pulse timing corresponds to the appearance of a **sinusoidal interference pattern in space**. This interference pattern can be resolved by scanning the third laser grating transversally over this structure. (Figure 2-3)

- C) The visibility of the interference pattern is **strongly influenced by the intensity of the second laser grating**. In the vicinity of the Talbot-time different β show a unique visibility function depending on the mean number of photons $n_0^{(2)}$ that are absorbed in G2. (Figure 2-6)

In the experimental section you will find an experimental verification for all points A), B), C) which are demonstrations of the quantum mechanical behaviour of massive and complex particles. On the other hand they offer us new ways to:

A) **measure and filter the mass of neutral particles** by searching for their Talbot times when they form β-independent interference patterns.
B) **measure deflections of the interference pattern** due to the particle interaction with external potentials (E-field, B-field,… see 4.14.1)
C) **measure the β – parameter** of particles and from that in combination with transmission curves the particle's optical polarizability and cross section.

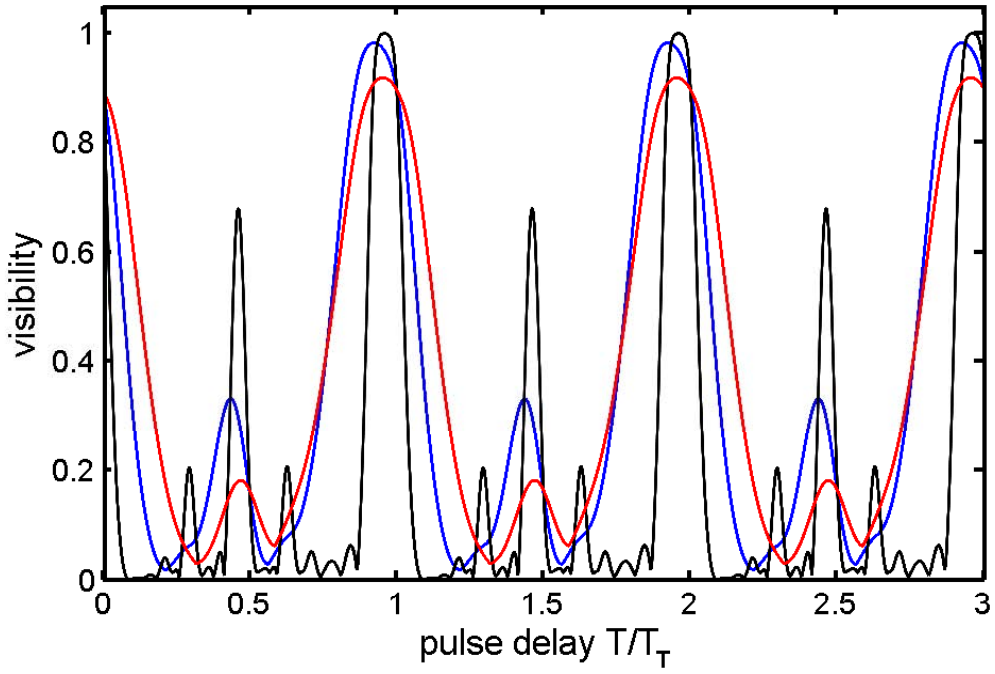

Figure 2-5 Simulated visibility as a function of the pulse delay T/T_T for different β. n_0=10 for all three gratings. β =0.3 (black), β =1 (blue), β =3 (red). Exactly at the T=1, the Talbot-time, the expected visibility is independent of β. The periodicity of the interference fringes scales with $n = \left(\frac{L}{L_T} mod 1\right)^{-1}$ (see also Figure 1-3).

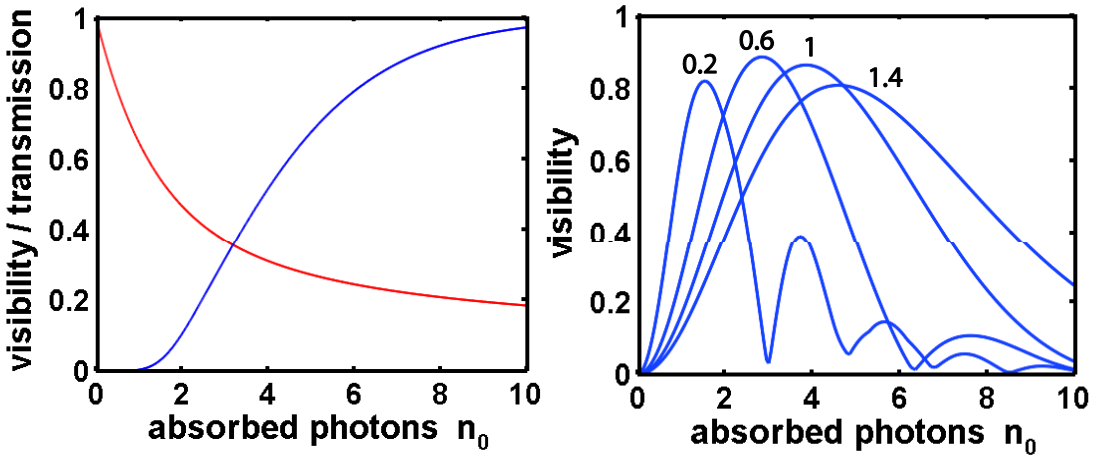

Figure 2-6 (left) Simulated visibility at the β independent Talbot-Lau time versus mean number of absorbed photons in the antinode $n_0^{(1,2,3)}$(blue). All three gratings are assumed to be identical. The red line indicates the simulated transmission as a function of n_0 for one grating. (right) Simulated visibility at ¾ of the Talbot-time. The first and the third grating are fixed at $n_0^{(1,3)}$=10 photons. The middle grating varies the power. Four blue plots are shown (from left to right) β=0.2, β=0.6 β=1, β=1.4 .

How to record interference pattern?

3 Experimental realization

In order to build an optical time-domain ionization matter-wave interferometer it is necessary to use particle sources and detection schemes which fit the pulsed character of the interferometer. The lasers have to emit photons of sufficient energy to allow single photon ionization. The light has to be sufficiently monochromatic to create a distinctive standing light wave and the laser pulses have to be sufficiently short and accurately timed that the interferometer can be operated in the time-domain. However, the wavelength should be in a range where high quality optics is still available. The quality and reliability of optics decreases for shorter wavelengths. Furthermore, we had to develop a fast data acquisition routine and find new experimental schemes to proof the quantum nature of matter in a time-domain experiment.

3.1 Sources

A beam of cold neutral molecules and molecular clusters is favourable for our interferometry experiments. The particles have to be cold enough in order not to emit photons during the time they spend in the interferometer which would lead to decoherence (see 4.2). Charged particles interact strongly with any electromagnetic field which introduces dispersive effects. In this section I will therefore focus on neutral molecular beams, their particle density, mass distribution, velocity and internal temperature. Pulsed sources may provide a higher particle density than most continuous sources and they are particularly favourable for the intrinsically pulsed scheme of the OTIMA interferometer.

Thermal sources such as sublimation ovens [60] produce a thermal beam of vaporized molecules. They can be seeded with rare gases which allows for internally cold supersonic beams [60]. The velocity of the molecules is close to that of the seed gas. Such sources are often combined with a pulsed valve [61] and offer a molecular

beam [62] which is sufficiently cold to initiate a clustering process. Magnetron sputter sources [63] sputter atoms from a target into a cold buffer gas atmosphere where they thermalize, condensate and form clusters. Laser desorption [60] of molecules with short laser pulses heats the particles rapidly and supplies very intense beams of hot molecular particles and atoms. They can also be seeded and cooled with added rare gases [64]. Long laser pulses heat the particles slowly and evaporate them therefore with a colder thermal velocity.

3.1.1 Magnetron sputter source

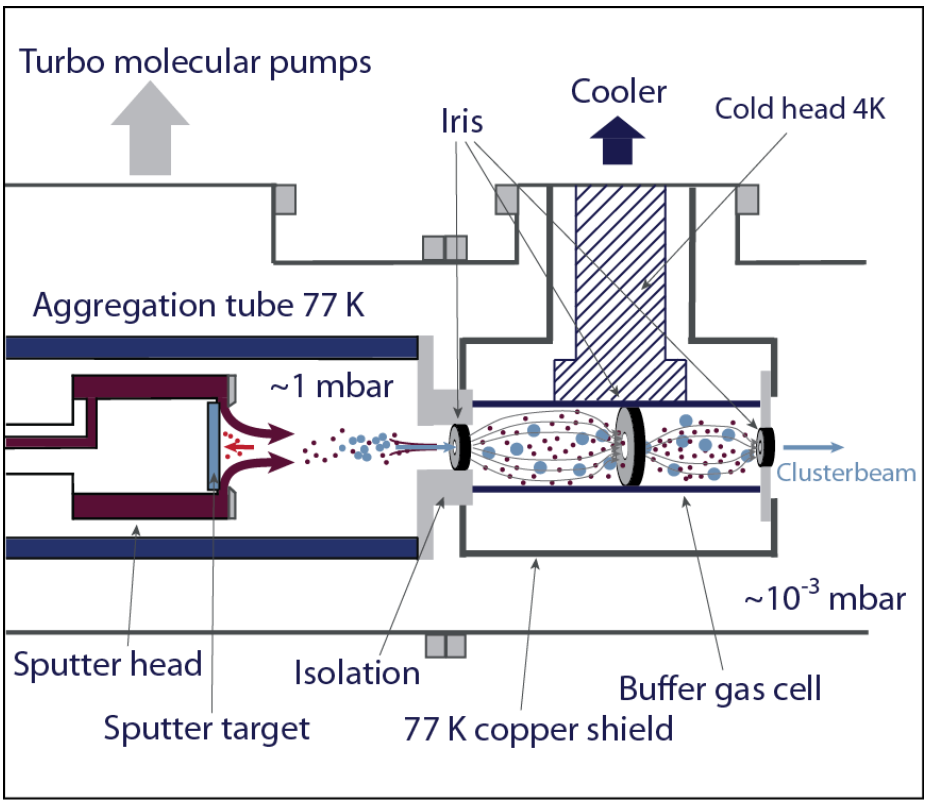

Figure 3-1 Schematic view of a magnetron sputter source and the added buffer gas cell. The buffer gas cell can reach temperatures down to 4 K and is divided into 2 sections by three adjustable irises in order to optimize velocity and cluster distribution. Figure form [58], modified.

Our magnetron sputter source was provided by the group of Bernd von Issendorff at the Albert-Ludwigs University in Freiburg. It consists of a sputter head, a liquid nitrogen cooled aggregation tube and gas feed-throughs. An electrical field applied on the sputter head accelerates charged particles towards a metal/semiconductor target and sputters mainly atoms, but also dimers and trimmers [65], which are partly charged and therefore enhance the sputter process. The particles thermalize with the liquid nitrogen cooled buffer gas (He, Ne, Ar) and start to condensate. The buffer gas pressure is usually set to 1 mbar by a tunable opening (iris) from where it expands to 10^{-3} mbar vacuum. The pressure is a very important parameter for the clustering process and can be controlled by two flow controllers at the inlets for the

buffer gas. Also the time in the aggregation tube influences the particle condensation process. This time can be controlled with the distance between the sputter head and the iris and the iris opening (see Figure 3-1).

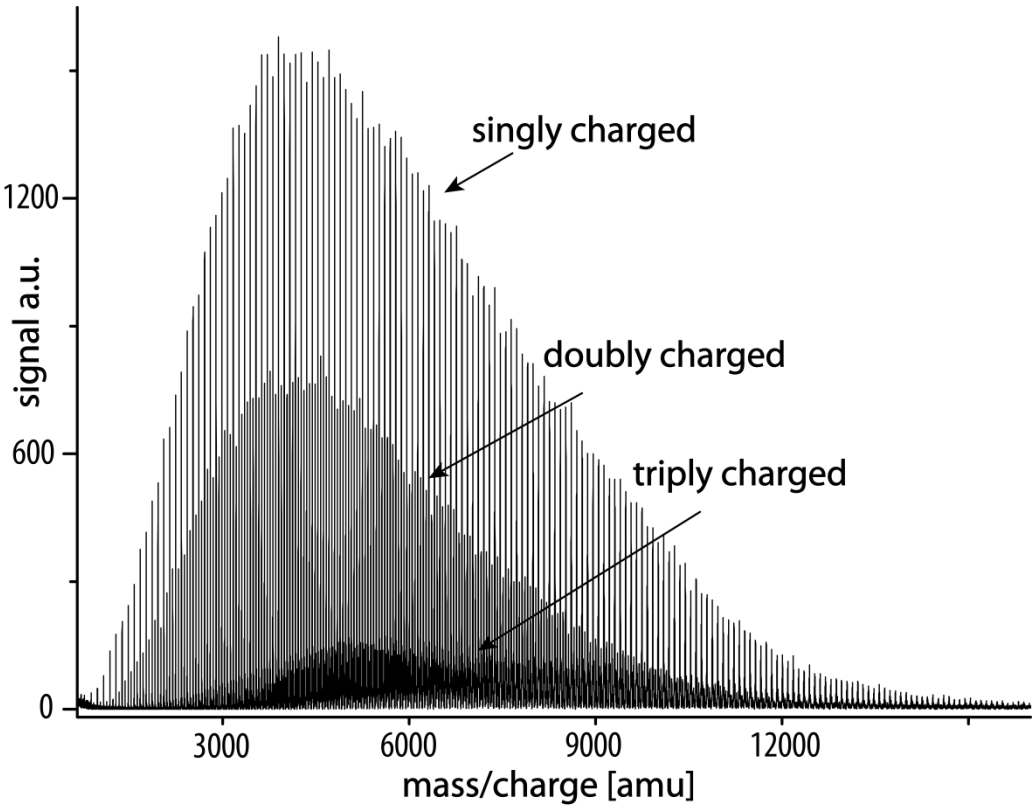

Figure 3-2 Mass spectrum of photo-ionized (157 nm) Niobium clusters. Three different classes of charged clusters have been detected. The main distribution corresponds to the singly charged clusters (highest signal); doubly charged particles form up to the middle distribution. Particles which have lost three electrons contribute also to the signal.

The magnetron sputter source provides a molecular beam travelling at 300-400 m/s with a mass distribution as shown in Figure 3-2.

In order to tune the source to slower molecular velocities we added a buffer gas cell which was cooled by a pulse-tube cooler[3]. This buffer gas cell further slows the

[3] SHI Cryocooler MODEL SRP-082B-F70H (low vibration version)

Cooling Capacity:

1st stage: 40W at 45K

cluster beam via thermalisation down to 4 K. We use three irises placed at the end of the aggregation tube, in the middle and at the end of the buffer gas cell to optimize the beam parameters. This permits to separate the sputter process from the cooling stage, which requires different buffer gas conditions. The operation pressure in the aggregation tube as well as in the buffer gas cell is in the range of 0.1-10 mbar. At this pressure, the buffer gas builds up streamlines and also turbulences and can be well guided by optimizing all irises to each other. At temperatures below the boiling point of the buffer gas all the gas molecules reaching the cell surface condensate and stick on it. That changes the aerodynamic totally.

Table 3-1 Most probably velocity of buffer gases at their boiling points.

Buffergas	**Mass [amu]**	**Boiling point [K]**	**v_{max} [m/s]**
Helium	4	4.2	133
Neon	20	27	151
Argon	40	87	192
Xenon	131	165	145

The magnetron sputter source provides a continuous flow of particles which has to be chopped in order to suit the OTIMA interferometer. The OTIMA interferometer runs with a maximal repetition rate of 200 Hz, which is limited by the repetition rate of the grating lasers as well as by the limited data acquisition and real time processing of 200 Mb/s of time of flight (TOF) mass spectra. Assuming an average particle velocity of 300 m/s and a used beam width of 2 mm (ionisation area **2** x 1 x 0.3 mm³ delimited by slits, in the TOF) per experimental run (200 Hz), just 0.13% of the particle beam is actually used.

2nd stage: 1.0W at 4.2K

3.1.2 The Even-Lavie –Valve

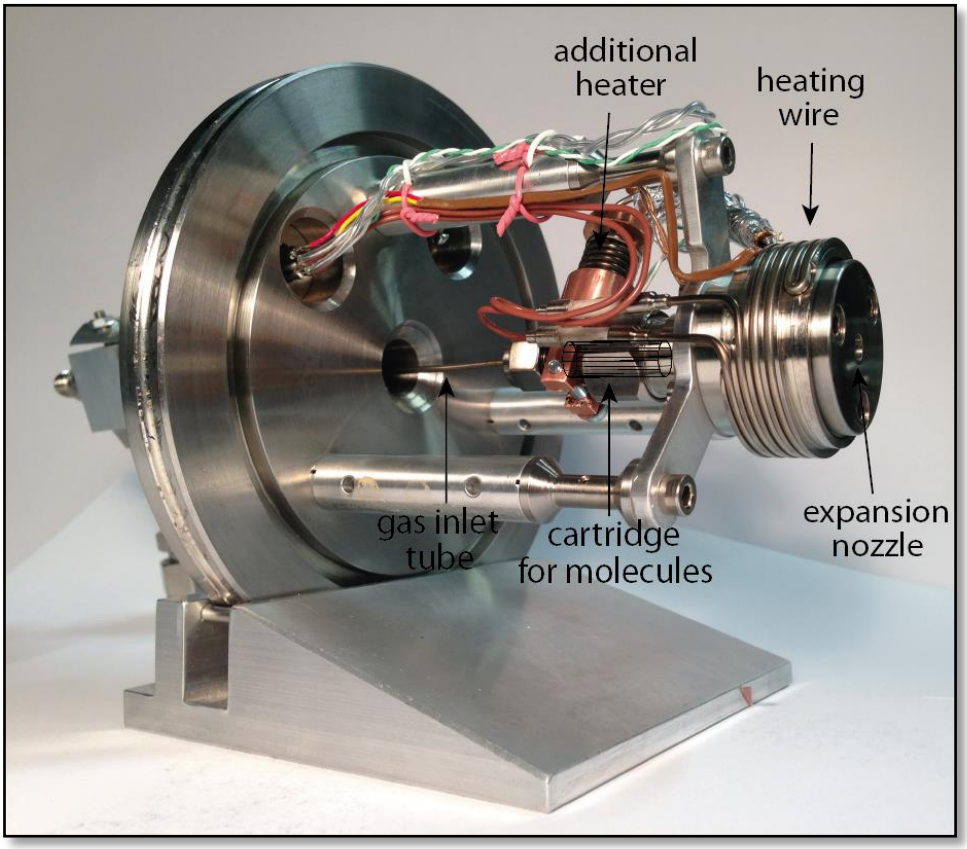

Figure 3-3 Picture of the assembled Even – Lavie – valve. The temperature at the cartridge for the molecules is controlled with a self-made additional heater.

Supersonic molecular beam methods have been widely used in atomic and molecular physics. This technique allows to produce an intense and cold beam of particles with well-defined kinetic energy. Internal particle temperatures down to 0.8 - 1.6 mK have been observed by proving the existence of the weakly bound van der Waals cluster $^4He_2$ in a matter-wave diffraction experiment [66].

Our commercially available pulsed supersonic source, the Even-Lavie-valve [61,62], consists of a small oven chamber connected to a pulsed valve with a 150 µm nozzle. The whole source setup can be heated up to 550 K. The oven chamber is connected to a gas inlet. Different kinds of gases can be added to the evaporating molecules. These gases are normally rare gases like He, Ne or Ar and can be varied in pressure from 1-100 bar. Depending on the pressure of the molecule/carrier gas

mixture, the particles undergo an adiabatic cooling process by the expansion. This technique also works for complex and large molecules like Anthracene or Aniline. Internal temperatures below 1 K have been measured [56]. If the partial pressure of molecules during the expansion process is sufficiently high, the cold particles start to condensate and form Van der Waals clusters. Also Van der Waals cluster of molecules with gas atoms have been observed (see Figure 3-4). As a rule of thumb: for clustering, the internal temperature of each cluster has to be lower than the boiling point of each component. These mixed clusters can be used to extend the single photon ionization grating to a depletion grating. If absorption of a single photon doesn´t lead to ionization then it can heat the cluster to a degree that weakly bound molecules or atoms evaporate. Such technics have been used in depletion spectroscopy and will be explained in (4.2.1).

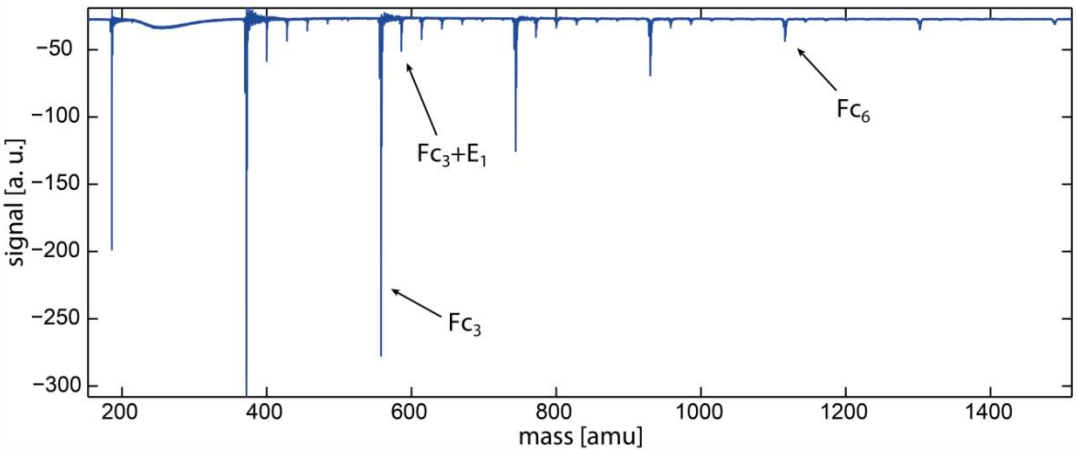

Figure 3-4 Mass spectrum of Ferrocene **Fc** ($C_{10}H_{10}Fe$) clusters with attached Ethene **E** (C_2H_4) molecules. The internal temperature of every cluster has to be lower than the boiling point of each component!

A drawback of this source is the high velocity of the emitted particles which is determined by the carrier gas and its temperature and pressure. The velocity of the particles is a very important parameter for interferometry because it sets an upper limit on the passage time through the interferometer which limits the maximal Talbot-Lau time T_T.

The mean velocity of gases which have a constant- pressure molar heat capacity C_p, which is independent of temperature, is given by [67]

$$v_{max} = \sqrt{\frac{2C_pT_0}{m}}$$

Every ideal monoatomic inert gas has a heat capacity of $C_p = \frac{5}{2}R$. This leads to theoretical mean velocities as listed in Table 3-2. Note that the speed of the inert gas under these ideal assumptions is independent of the backing pressure. Under real conditions we only measure the velocity of the co-expanded molecules such as Anthracene Ac (because it can be easily photo ionized by 157 nm radiation). The experimentally measured mean velocities of 960 m/s for Neon and 640 m/s for Argon at 500 K are lower but quite close to the ideal predicted case. This discrepancy is known in literature as "velocity slip" [67,68]. During the expansion process heavy particles with slower super-sonic velocities are repetitively bombarded by the lighter inert gas atoms and asymptotically accelerated to the inert gas velocity. In case the starting pressure is too low, they will never undergo enough collisions to reach the terminal velocity of the buffer gas.

Table 3-2 Estimated velocities for different inert gases after supersonic expansion under ideal gas conditions (see text)

Buffer gas	**Mass [amu]**	**v_{max} @ 500 K [m/s]**
Helium	4	2280
Neon	20	1020
Argon	40	720
Xenon	131	400

3.1.3 Laser desorption – Thermal laser evaporation

Laser desorption is a well-established technique to evaporate thermally unstable particles as well as refractory alloys and metals. Most commonly are Nd:YAG lasers with pulse lengths of less than 10 ns and wavelengths between near IR and soft UV that are focused to an area of some 10 µm² in order to achieve rapid heating and evaporation [16,64,69].

The temperatures in the focus point can exceed the boiling point of the material by far, but only for a very short time, which also allows desorption of particles which dissociate before they evaporate in an oven.

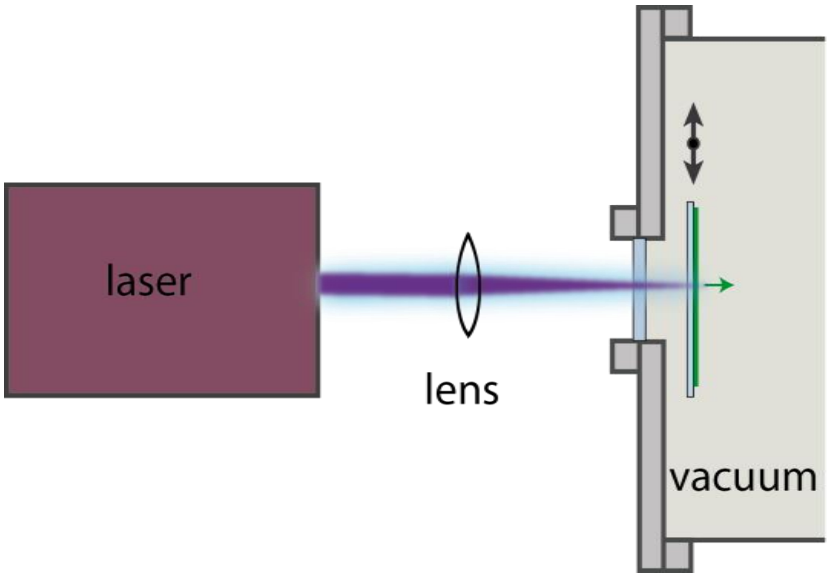

Figure 3-5 Thermal laser evaporation source. A laser beam heats molecules (green) to evaporate them from a moveable glass plate.

A slightly different approach is to focus a continuous laser beam directly on a molecule coated vacuum viewport [12] as shown in Figure 3-5. In this scheme, molecules are heated slowly until they evaporate. This evaporation method is also quite soft because the heated molecules spend just a very short time in a thermally excited state until the molecule-molecule binding is cracked and the particles start to evaporate. The evaporation temperature is lower than in the case of nanosecond pulsed laser desorption, because the molecules are slowly heated and leave the heating laser beam as soon as they have absorbed enough photons.

Both methods evaporate thermally unstable particles into the gas phase. Thermal laser evaporation is expected to generate beams of slower velocity while nanosecond evaporation may possible even address more thermo-labile particles.

In the experiment we will focus a cw-laser diode on a molecule-coated vacuum viewport which can be vertically and horizontally translated to transport new molecules into the laser beam. The laser can be switched on and off within microseconds to chop the beam.
From a single shot onto an area of 4000 µm² one gets $10^{25}/(4\pi)$ molecules/sr/m² [70]. Another advantage of this source is that only a very small part of the "source" is heated, this improves the vacuum conditions during the evaporation process and reduces the need of additional differential pumping stages. In other words, the source can be mounted close to the interferometer. The resulting compact setup is of great advantage since the signal loss of a pulsed source scales like $1/r^3$, where r denotes the distance from the source to the detection.

3.2 Detection - Time of flight mass-spectrometer

A time of flight mass-spectrometer (TOF-MS) works in a pulsed way and is able to distinguish particles of different masses over a wide range in a single measurement. This is important for the OTIMA interferometer because the interference pattern is also imprinted on the transmitted mass spectrum (see Figure 3-12).
After VUV ionization of the interfered neutral particles the TOF-MS accelerates all ions with the same electrical field into a drift tube. Particles with a different mass-to-charge ratio arrive at different times on a multi-channel plate[4] (MCP). The incident ions release electrical pluses which are digitized and post processed with a computer.

[4] Three layer multi-channel plate (MCP) with 40 mm active diameter

The TOF-MS at the OTIMA interferometer is a *Kaesdorf RFT50* (reflectron type). The high post-acceleration of up to 20 kV and a three layer MCP stack ensures optimized detection of massive particles up to 100.000 amu with a time resolution $t/\Delta t$ of some 1000.

3.3 Laser system and beam line for VUV radiation at 157nm

The OTIMA interferometer is built up with 3 F_2-Excimer lasers[5]. Each laser emits 7-8 ns long pulses with a maximal repetition rate of 250 Hz. The maximum pulse energy is 4.5 mJ. Sansonetti et al. [71] report an emission spectrum with two major lines at a wavelength of 157.63094(10) nm (79%) and 157.52433(10) nm (19%) as well as some spontaneous emission lines in the red wavelength range measured with a standard F_2-Excimer laser. A photon at 157.6 nm carries an energy of 7.89 eV. The beam profile is a flat top with ≈ 2 x 9 mm, illustrated in Figure 3-6.

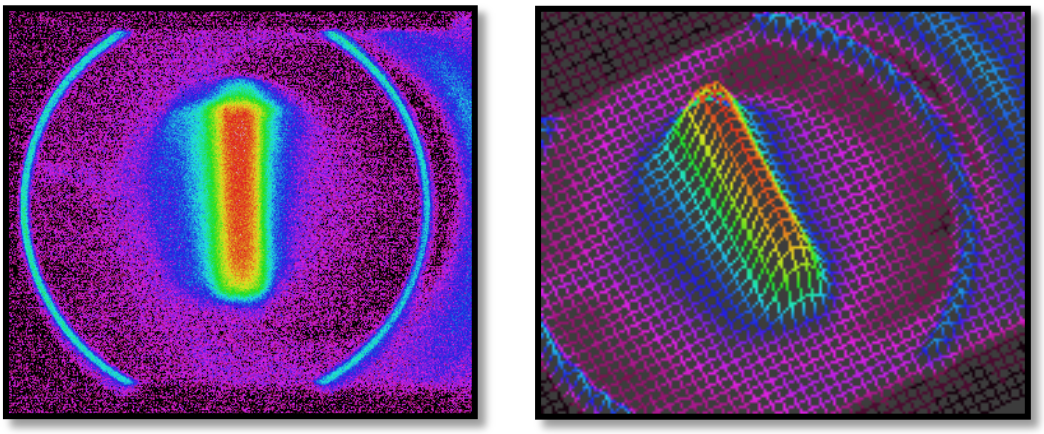

Figure 3-6 The flat top beam profile of the EX50 laser has a width of 2 x 9 mm; measured with a fluorescence plate and a CCD camera. Figure taken from [58].

[5] EX50 Gam Laser Inc.

Radiation of $\lambda = 157\,\text{nm}$ has a penetration depth of about 40 µm in normal atmospheric air (oxygen is the main absorber [72]). As a consequence, the whole optical beam line must be kept at a partial pressure of less than 10^{-3} mbar of oxygen in order to avoid significant absorption of the lasers light. In addition, it is also strongly absorbed by hydrocarbon-based contaminants which form laser-induced debris on the optics even under vacuum conditions [73]. This film can be seen with the bare eye as a brownish layer, with the shape of the laser beam profile. Hydrocarbon based substances are often used as grease for mirror mounts. It is also known that this laser-induced deposited film can be removed with traces of oxygen or water added to a highly-pure purge gas like nitrogen [74]. In our setup we take great care of the used mirror mount grease components and remove as much ooze as possible. The whole optical setup is placed in a clean vacuum chamber. The optical beam line is pumped down to 10^{-6} mbar during the time when we are not operating the laser system. For the utilisation period of the laser system pure nitrogen (99.9999%) constantly flows as a purging gas to all optical components. The pressure in the vacuum chamber increases to around 1 mbar. This procedure ensures a reliable optical system without laser-induced deposited films.

The intrinsic jitter of our Excimer-lasers is about 4-5 ns. However, a slow long time drift of about 100 ns is added to this jitter in both directions. The pulse-to-pulse stability under perfect conditions is better than 2 %. These conditions are only fulfilled if the laser has recently been refilled and operates at the highest excitation voltage. Typically, a pulse-to-pulse stability of about < 5 % is observed.
For high visibility interference it is very important to ensure that the delays between the laser grating pulses are equal, see Figure 3-7. To overcome the jitter and power stability issues we place a photodiode in the beam line. The photodiode[6] is mounted to detect the diffuse light which is reflected from the interferometer mirror. This ensures that the measured pulse times correspond to the interaction times with the matter-waves. Due to the different optical light paths of the lasers, the pulse emission time is not equal to the time when the light grating is formed.

[6] GaP photodiode G1962 (Hamamatsu)

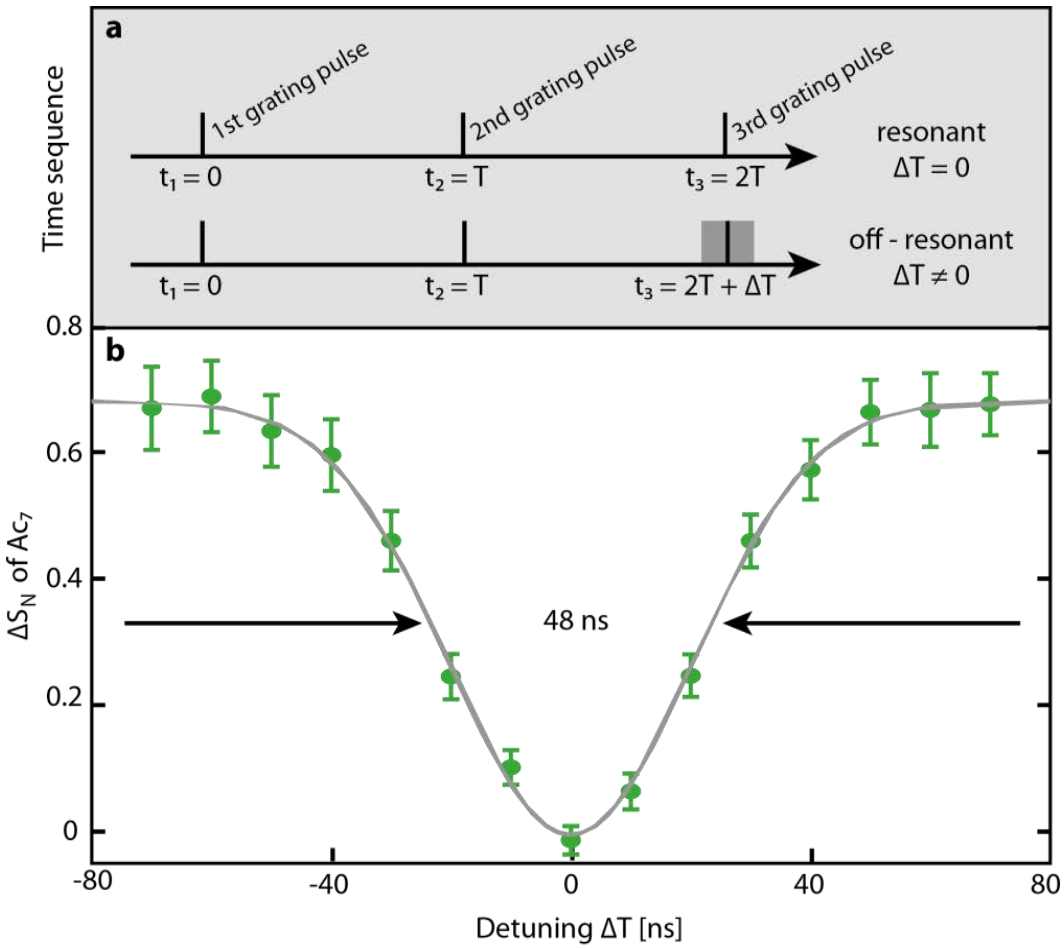

Figure 3-7 Interferometric resonance. a) The contrast of the Talbot-Lau interference pattern strongly depends on the equality of the time delays between the three laser gratings. b) Shows the difference between the interference pattern recorded at the resonant condition and the interference pattern with a delay of ΔT (off-resonant). Recorded is the normalized signal difference ΔS_N (E 1-3) of the Anthracene 7 cluster (Ac_7) at a pulse separation time T = 18.9 µs as a function of ΔT. The interference pattern lasts 48 ns (full-width at half-maximum). Figure from [6].

The timing is even sensitive to the length of the laser pulses. Initially we measure all delays with respect to the rising flanks. Since we shifted the starting points of the delays to the end of the first laser pulse, to the middle of the second pulse and to the starting flank of the last pulse, the interference contrast was improved by 5 %. The temporal change amounts to 5 ns, but it is actually also physically motivated. The

starting point of the free propagation of the matter-wave is given by the end of the interaction with the first laser grating and stops by applying the third grating.
To improve the timing stability, we record each laser pulse and each measured mass spectrum is stored in its correct time delay class. If the averaged timing is wrong by more than 1 ns, the computer corrects the delays automatically in the software controlled pulse generator.

3.4 Mirror at 157 nm

The central element in the OTIMA interferometer-setup is a 2-inch mirror. The reflective mirror surface provides the boundary condition for all three standing light waves. All light gratings extend in all three dimensions. They are perfectly aligned to each other if one can overlap their grating structures just by translations. That is provided if all gratings have the same period and the node/antinode planes are parallel to each other. The grating period of each standing light wave is given by half the laser wavelength and scales with $cos(\alpha)$, the angle between incoming and reflected laser beam [31].
The main advantage of the one mirror setup is given by the parallelism of all standing light waves. This design is also insensitive to vibrations and drifts of the whole mirror which occur at a timescale longer than the time between the first and the last laser pulse (see 1.1.4). This translations and rotations influence the position of all three grating structures and correlating to the intercept theorem no shift of the appearing interference pattern is caused.
The vertical displacement Δs_{ges} of the interference pattern relative to the third grating can be expressed by

$$\Delta s_{ges} = \Delta s_1 - 2\Delta s_2 + \Delta s_3 \qquad \text{(E 3-1)}$$

$\Delta s_{1,2,3}$ indicate the displacements of each grating. The displacement of the first and the last grating scales with the position of the interference fringes, while the position of the second grating shifts the interference pattern twice as much due to the

intercept theorem. Vibrations with a high frequency will shift the interference fringes depending on their relative amplitude at the times of the applied light gratings corresponding to (E 3-1). These displacements will change $\Delta s_{1,2,3}$ in a random way and lead to an averaging of differently shifted interference patterns. To avoid this, we have built an optical Michelson interferometer that was mounted underneath the interferometer mirror on a commercial low vibration stage[7] to read out the vibration amplitudes at each grating time and to correlate the Δs_{ges} to a constructive interference pattern (see Figure 3-8). A similar idea is used in atom interferometry: if two atomic interference patterns are recorded at the same time and correlated to each other, the resulting correlation is insensitive to vibration [75].

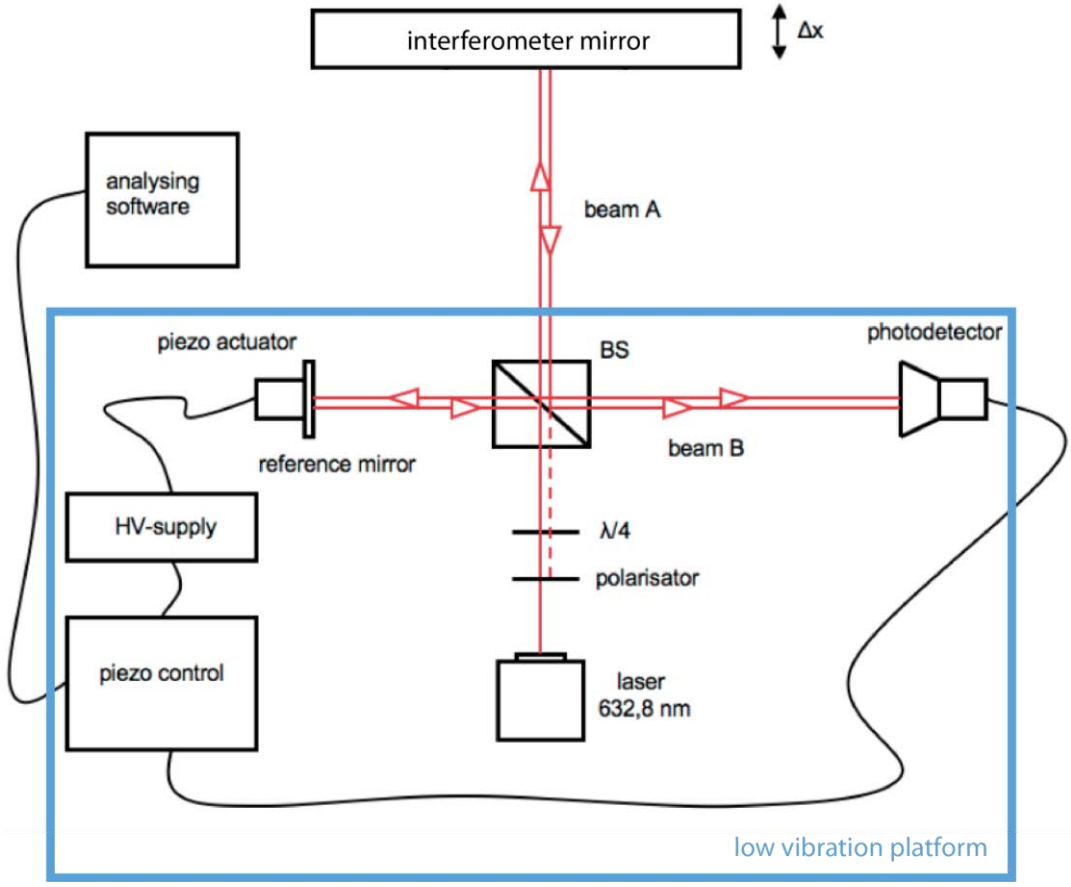

Figure 3-8 Setup to record the vibrations of the interference mirror. The position of interference mirror is recorded in respect to a low vibration stage at the time of every light grating. Therefore each molecular interference pattern can be corrected with the vibration induced phase shift. Figure from [76], modified.

[7] Minus K

The OTIMA interferometer mirror was fabricated and coated by Jenoptik AG. The coating has a reflectivity of 96% at normal incident, which is a high standard for 157 nm radiation [74]. The flatness of the mirror was measured by the Physikalisch-Technische Bundesanstalt Germany, see Figure 3-9.

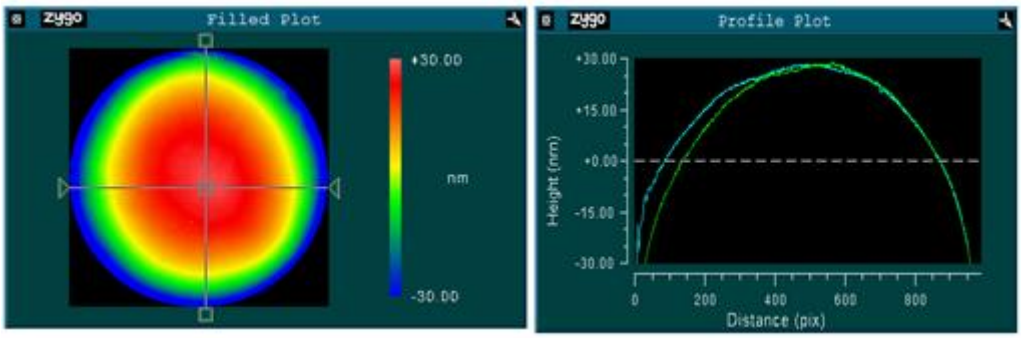

Figure 3-9 Topographic map of the mirror surface. This data was measured by comparing the phase of 632 nm laser light reflected by the interference mirror and a reference surface. Measured by PTB Germany.

The convex shape of the mirror influences the interference pattern in a negative way. The node/antinode planes of each grating are not parallel and enclose an angle to each other. Let us assume a laser grating width of 5 mm along the particle beam direction. The grating at the left part of the mirror is tilted with an angle of 0.2 µrad to the "flat" middle grating. That corresponds to a translation of the grating of 10 nm over its length (see Figure 3-9, convex shape). An angle of 1.6 µrad amounts to a displacement of one grating period over the laser beam width (5 mm). Integrating the signal corresponding to Δs_{ges} (see (E 3-1)) over this width leads to a complete disappearance of the interference fringes. However, a 10 nm shift leads - in a worst case approximation - to a visibility reduction of about 13%. Assuming a mirror shape like in Figure 3-9, also the right part of the mirror, where the third grating is located, is tilted and also reduces the expected visibility.

In order to reduce this effect we select a small fraction in the vertical direction with the TOF ionization laser of the interfered beam. This reduces the effective used grating diameter of each laser.

3.5 Measurement routine - Data acquisition

Once the interferometer is aligned, the experimental data acquisition is fully automatically controlled by a computer program (MOPS). This program has been developed in our group and fulfils all the real-time processing requirements to run the OTIMA interferometer. For the time delay management the program controls two pulse generators[8]. These delay/pulse generators handle the timing for the pulsed source (see The Even-Lavie –Valve3.1.2), for the detection unit (see 3.2) including the detection ionization laser and for the three grating lasers. Due to the high sensitivity of the interference contrast on the grating laser delays, all grating laser pulses are recorded by a single photodiode. The use of a single photodiode ensures that no delays caused by differently long response times of the diodes or propagation delays in the wiring lead to wrong laser pulse timings. The photodiode as well as the TOF mass-spectrometer are connected to a fast 10-Bit digitizer card[9] with a maximum resolution of 2 GS/s. All digitized signals are transferred in real time (up to 200Mb/s) to the MOPS-program. Here the photodiode signals are automatically analysed to get the actual pulse timings and heights. Depending on the energy of the grating laser (height of the signals) and the temporal delays, the program saves the corresponding mass spectra in different folders. These folders can be post-processed for later analysis. Each laser is regulated with an individual feedback loop stabilizing the laser power besides the pulse delay.

The experiment normally runs with a repetition rate of 100 Hz. After each run we record the remaining neutral particles by ionizing them with a 157 nm laser and detecting them in a TOF mass-spectrometer.

[8] BNC Model 575 Pulse/Delay generator

[9] Agilent technologies Acqiris CC103

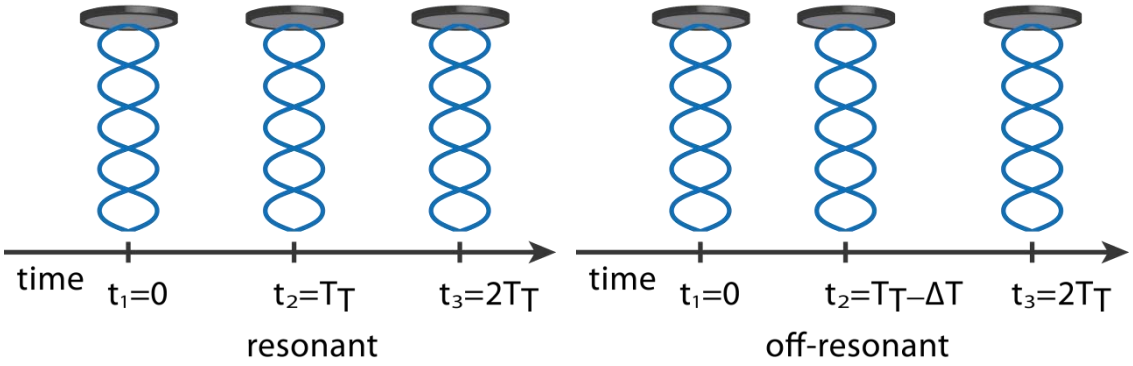

Figure 3-10 Experimental data are taken for two different light grating timings. In the resonant mode an interference pattern is built up at $t_3=2T_T$. In the off-resonant mode the second light grating is shifted by ΔT and no interference pattern is built up at $t_3=2T_T$.

To observe quantum enhanced/reduced transmission of certain mass (see 2.4) we have to run the experiment twice but with slightly modified laser pulse delays. One time the pulse delays between the three laser gratings are equal (R) and at the next run the pulse timing of the second laser is changed by 100 ns (O), which causes a mismatch of the delays by 200 ns. In Figure 3-7 one can see that the interference pattern just remains for 48 ns (FWHM). With the 100 ns pulse delay asymmetry, the Talbot-Lau condition breaks and no interference pattern is observed. Normally, we repeat the experiment for about 10 minutes. This corresponds to 60 000 recorded mass spectra which have to be analysed and averaged. To evaluate the interference contrast we assume that in the off-resonate mode (O) the transmission of the particles is equal to the average of a sinusoidal interference pattern, which correlates to the offset of equation (E 1-2) for the visibility.

In the resonate mode (R) we find the quantum enhanced/reduced transmission of mass classes depending on the phase between the interference pattern and the third laser grating (see Figure 3-11).

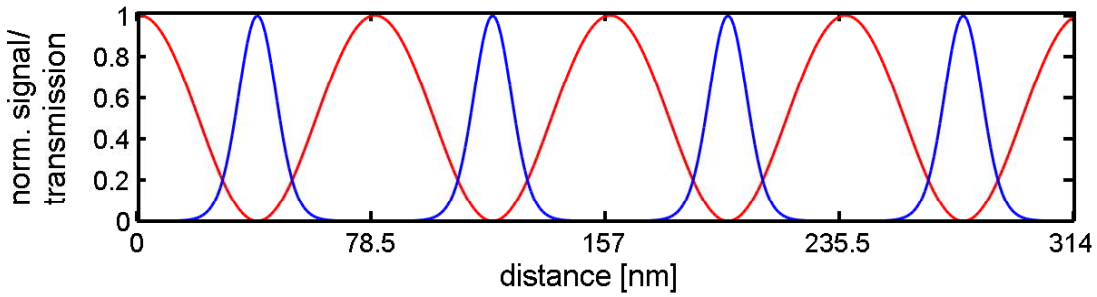

Figure 3-11 The evaluated interference contrast depends on the relative position of the appearing interference pattern (red) to the position of the transmission function of the third laser grating (blue). In the illustrated sketch we will evaluate the highest negative contrast (lowest transmission). Translating the last laser grating by $78.5/2$ nm leads to highest transmission and a contrast of 1.

The mass dependent transmission of the interferometer is experimentally seen in Figure 3-12 and Figure 3-13. The figures show the different mass spectra of Anthracene clusters recorded in the resonant/off-resonant way of interacting with the three light gratings at a pulse separation time of 25.9 µs and 18.9 µs. The different pulse timings are caused by the different velocities of Anthracene clusters seeded in the source with Argon or Neon (see The Even-Lavie –Valve3.1.2). A pulse delay of 25.9 µs corresponds to the first order Talbot-time of a mass of 1730 amu as well as to the second order Talbot-time of a mass of 865 amu. At around these masses, the highest transmission is expected. All data have been recorded at fixed pulse energy of the laser gratings. However, the Ac clusters show an increase of the absorption cross-sections for heavier clusters. This leads to different transmissions through the gratings and therefore to lower visibility for small clusters with a lower cross-section.

The theoretically predicted contrast (violet) has been calculated assuming that the β-parameter (see 2.3) stays constant for all clusters. Literature values only exist for the single Anthracene molecule [77,78]. This assumption can be motivated; both properties, absorption cross section and polarizability, show in general a dependence on the number of contributing electrons. The relative cross-sections were evaluated for each individual clusters by measuring the transmission probability through a

single standing light grating with an assumed single photon ionization yield of 100%. The polarizability is then chosen such that the β-parameter stays constant.

The interference contrast ΔS_N is extracted for each mass by its signal S_R accumulated in the resonant mode and the signal S_O in the off-resonant mode.

$$\Delta S_N = \frac{S_R - S_O}{S_O}$$

In all measurements we optimize the relative phase of the third grating to the interference pattern in order to observe high contrast. This is done by using the topography of the mirror and the formula (E 3-1):

$$\Delta s_{ges} = \Delta s_1 - 2\Delta s_2 + \Delta s_3$$

Δs_{ges} is the resulting shift of the interference pattern. In order to find topographies of highest contrast on the mirror corresponding to Δs_{ges} (see 0), the delay between source and first laser grating or the Talbot-time itself is slightly changed.

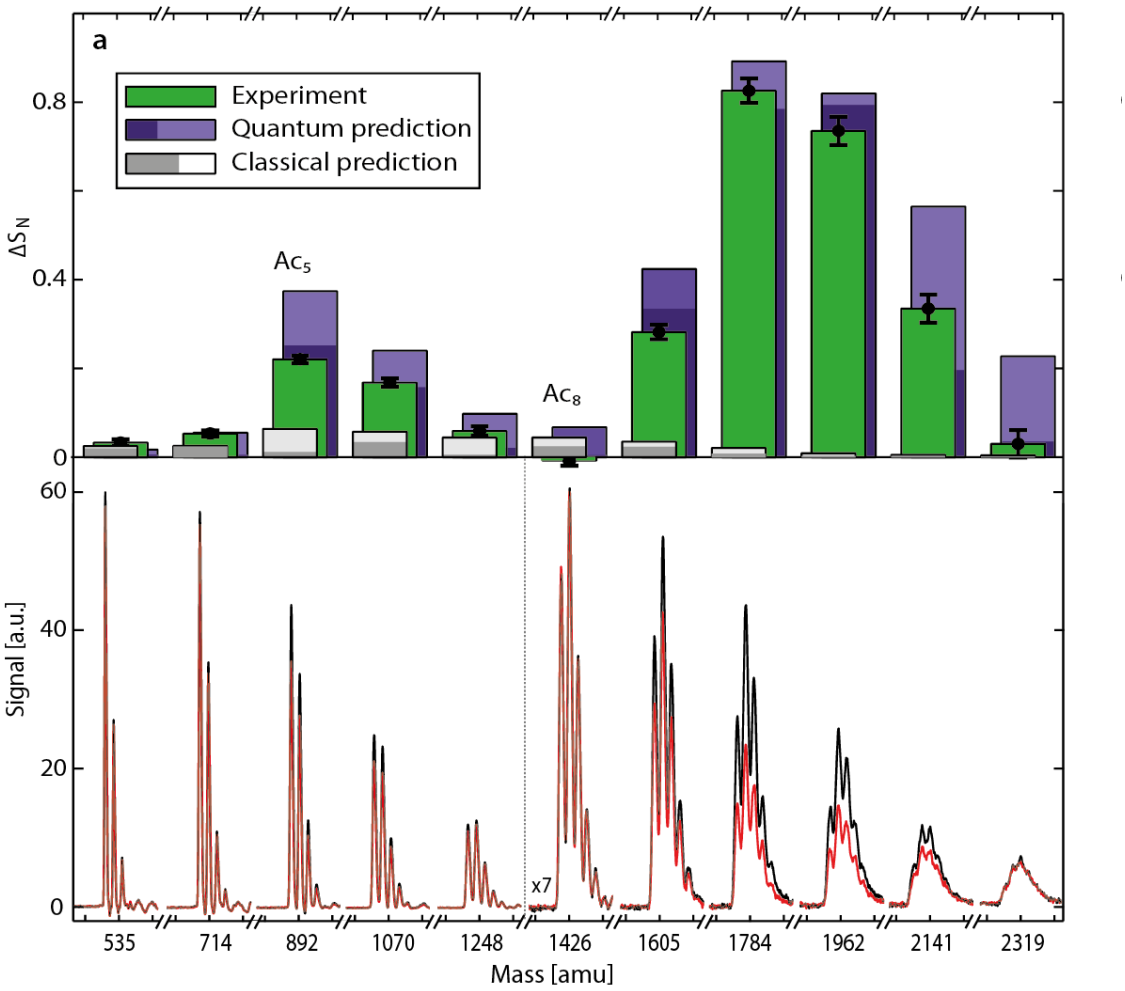

Figure 3-12 The experimental data confirm the quantum enhanced transmission of Anthracene (Ac) clusters through the OTIMA interferometer. The lower panels show the mass spectra recorded in the resonant (black line) and the off-resonant mode ($\Delta T = 200\,ns$, red line) of Ac clusters seeded in an argon jet with a pulse separation time of 25.9 µs.. In the upper panels the corresponding interference contrasts for each cluster ΔS_N are indicated in green. The dark violet/grey bars indicate the theoretical quantum/classical predictions. The light violet/grey areas in these bars point out a theoretical $\pm 30\%$ variation of the optical polarizability σ_{157} of the clusters. For statistical error see 3.6. Figure from [6].

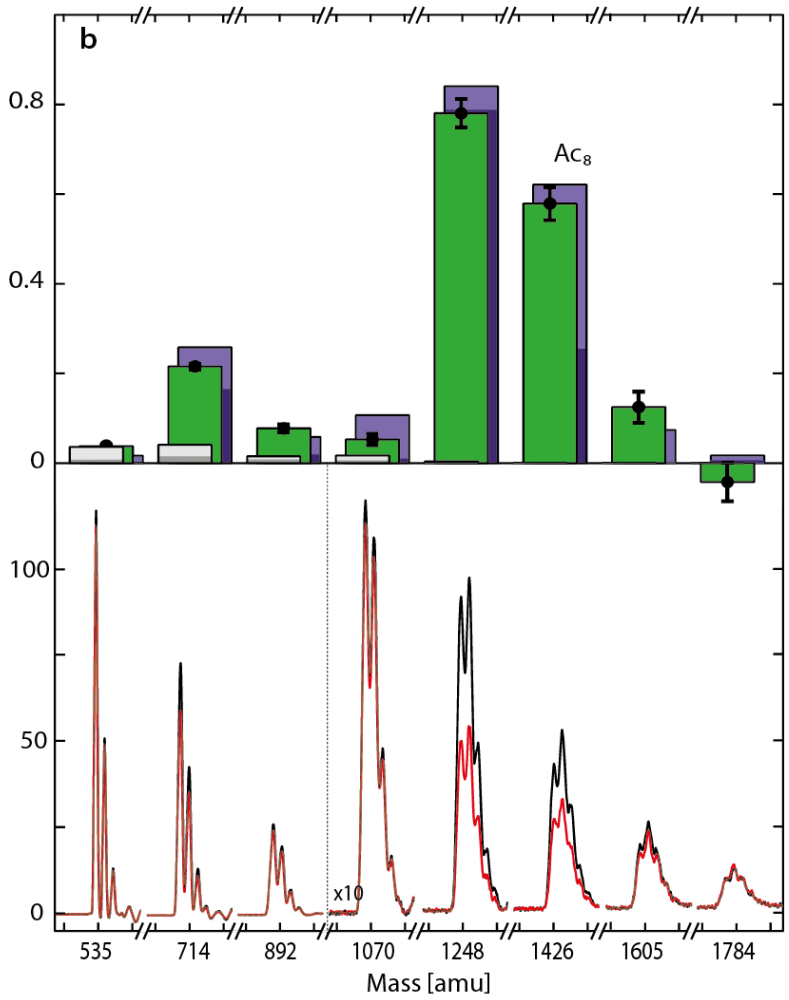

Figure 3-13 Experimental data confirms the quantum enhanced transmission of Anthracene (Ac) clusters through the OTIMA interferometer (see Figure 3-12). The data are recorded at a pulse separation time of 18.9 µs (seeded in Neon) which corresponds to the Talbot-time of the mass 1260 amu and the second order Talbot time of 630 amu. Around these masses highest transmission is expected. Figure from [6].

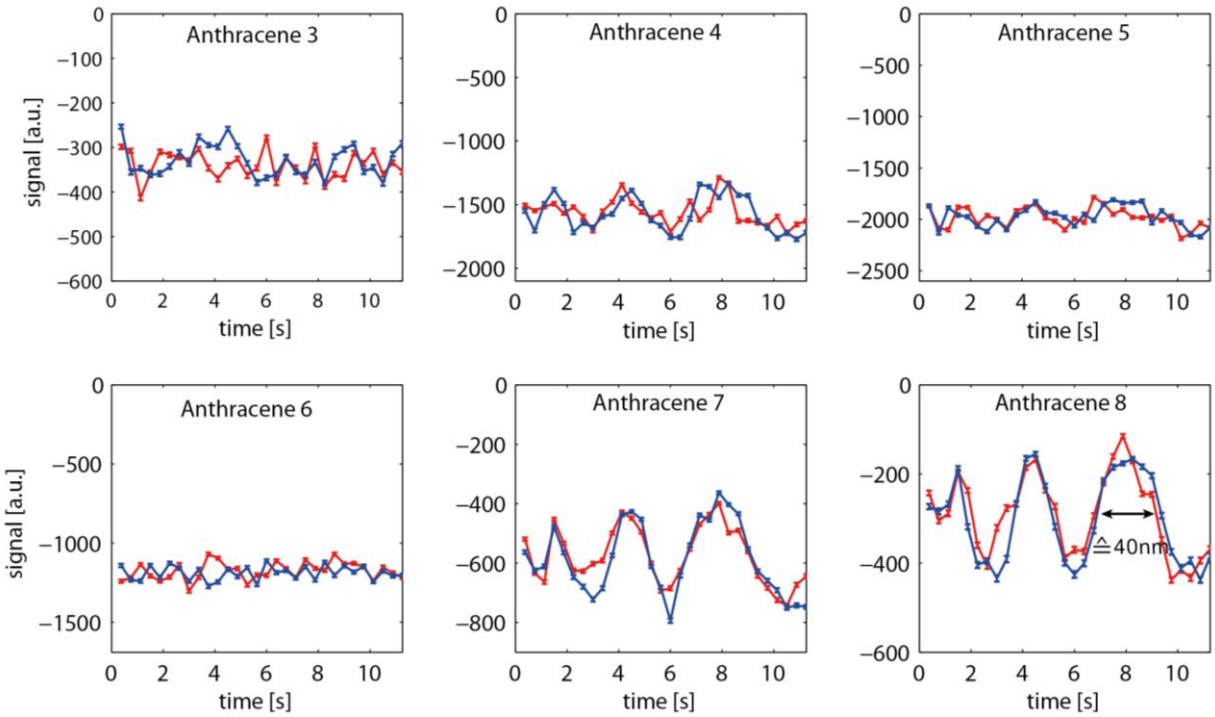

Figure 3-14 A continuous laser is used to heat a certain area of the interferometer mirror (see Figure 8-3). This leads to a thermal expansion of the mirror surface and translates the second light grating. The signal is averaged at the indicated times for 0.37 seconds, after the heating laser (1.4 W) is turned on (red) and switched off (blue). In the beginning of the heating/cooling cycle, the thermalisation and therefore the expansion of the mirror are faster.

Another way to scan the last grating across the interference pattern can be realized by actively transforming the topology of the mirror. Relying on the formula (E 3-1) for Δs_{ges} a translation of the second grating shifts the interference pattern twice as much as the first or the third. In our case we use heat to shift the mirror surface at the second laser grating (see Figure 3-14 and Figure 8-3). We coated the middle area of the mirror´s backside with graphite. A continuous diode laser beam 0 – 1.8 W (445 nm)[10] with a size of 10 x 7 mm shines onto this coated area, which absorbs the laser light and warms up. The 8 mm thick interferometer mirror is made of Calcium fluoride which has a thermal expansion coefficient of around $20 \cdot 10^{-6}/°C$. Between

[10] WarnLaser: 2w Blue Laser Luna™ Series

0 and 1.8 W an interference scan over more than 2.5 periods ($\triangleq 100\,nm$) is possible. After varying the laser power, a certain time is needed to reach a thermal equilibrium until the mirror surface stays constant.

3.6 Error consideration - Statistical error

Each measured value is subject to a measurement error. This error consists of a systematic and a random error. The **systematic error** always shows the same value if the experiment is repeated in the same way. The **random error** is changing for each repetition of the experiment. Only the random error can be considered in a statistical way. One of the main error contributions in the OTIMA interferometer is the low signal especially at large clusters numbers. The cluster formation of huge clusters is already reduced at the source by the fact that the clusters are built up due to condensation from the monomer. Massive clusters have big absorption cross sections and therefore tend to "see" very small grating opening fractions, which reduce the transmission through the interferometer. To observe quantum interference over a wide mass range, the laser power has to be optimized for the absorption cross section of the smallest particles (see Figure 2-6). Also the detection efficiency at the TOF mass-spectrometer given by the MCP[11] decreases with increasing mass [79]. To estimate the error at low count rates it is important to know the real number of detected particles at each mass.

The peak height of the detected particles depends strongly on the TOF mass-spectrometer settings (acceleration voltages), on the mass and on the composition of the clusters [79] and is difficult to convert into corresponding particle numbers.

To discriminate each peak from the background noise, we record a noise height distribution (see Figure 3-15) and calculate its standard deviation. Assuming a Gaussian distribution, at a discriminator level of 3σ it is ensured that 99.73 % of the detected peaks are real ion peaks.

[11] Multi-channel plate (MCP) scales with the impact velocity of the ions and not with the kinetic energy.

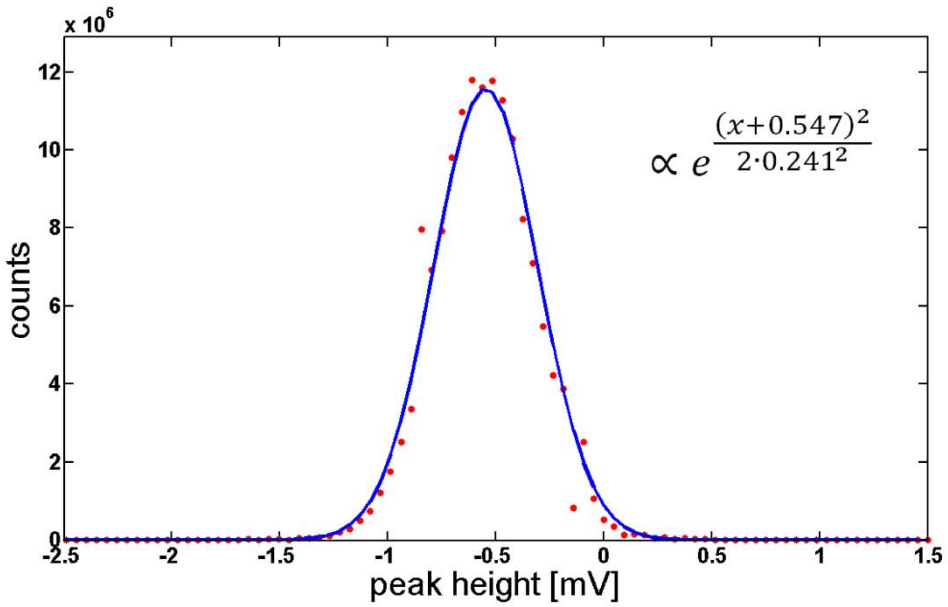

Figure 3-15 Height distribution of the background noise and at the Anthracene 10 cluster (red). A Gaussian distribution is fitted in blue. $\sigma = 0.241$

The lowest number of particles S_{min}, after N repeated experiments that could have contributed to the signal at a certain mass region, is given by simply counting the peaks at each recorded mass spectrum. Every peak has the value of a single ion. But that's normally not the case, also two and more ions can reach the detector at the same time and contribute to the same peak. A more accurate estimate of the particle number is given by a statistical estimate. In the OTIMA interferometer each interference pattern consists of individual particles. Let's assume that the detection of these particles, follows a Poisson distribution $P(k)$.

$$P(k) = \frac{q^k}{k!} e^{-q}$$

The expectation value q is the mean value as well as the variance and k denotes the number of expected events. Then the probability to observe "no count" $P(0)$ is given by

$$P(0) = \frac{N - S_{min}}{N}$$

Which is the number of repetitions with no peaks divided by the total number of repetitions N. It follows

$$q = -\ln(P(0))$$

This gives a better estimate of the mean number particles Nq as well as of the standard deviation $\sqrt{Nq}$, than achieved by counting just the peaks S_{min}.

4 A tool for quantum enhanced measurements

To interfere particles one has to reduce the interaction of the particles with the environment to a minimum. Even smallest deflections, for example caused by collisions with the background gas [80], absorption/emission of photons [81] or deflection by magnetic/electric fields, shift the interfering particle and can lead to a reduction of the fringe visibility. The high sensitivity of matter-wave interferometry can be used to measure deflections caused by interaction potentials [82], even if no force is applied as described with the Aharonov–Bohm effect [55,56]. One has to distinguish between dephasing and decoherence [83]. Coherent interactions (dephasing) don´t transport the "which way information" to the environment. The interfering particle is not entangled with another object and the interference pattern can be reconstructed with the knowledge of the interacted potentials (E-field, B-field, gravitation, vibrations,…). In contrast to that, decoherent interactions are caused for example by collisions with background particles or absorption and emission of blackbody radiation. In this case the information of the particles position is transferred.

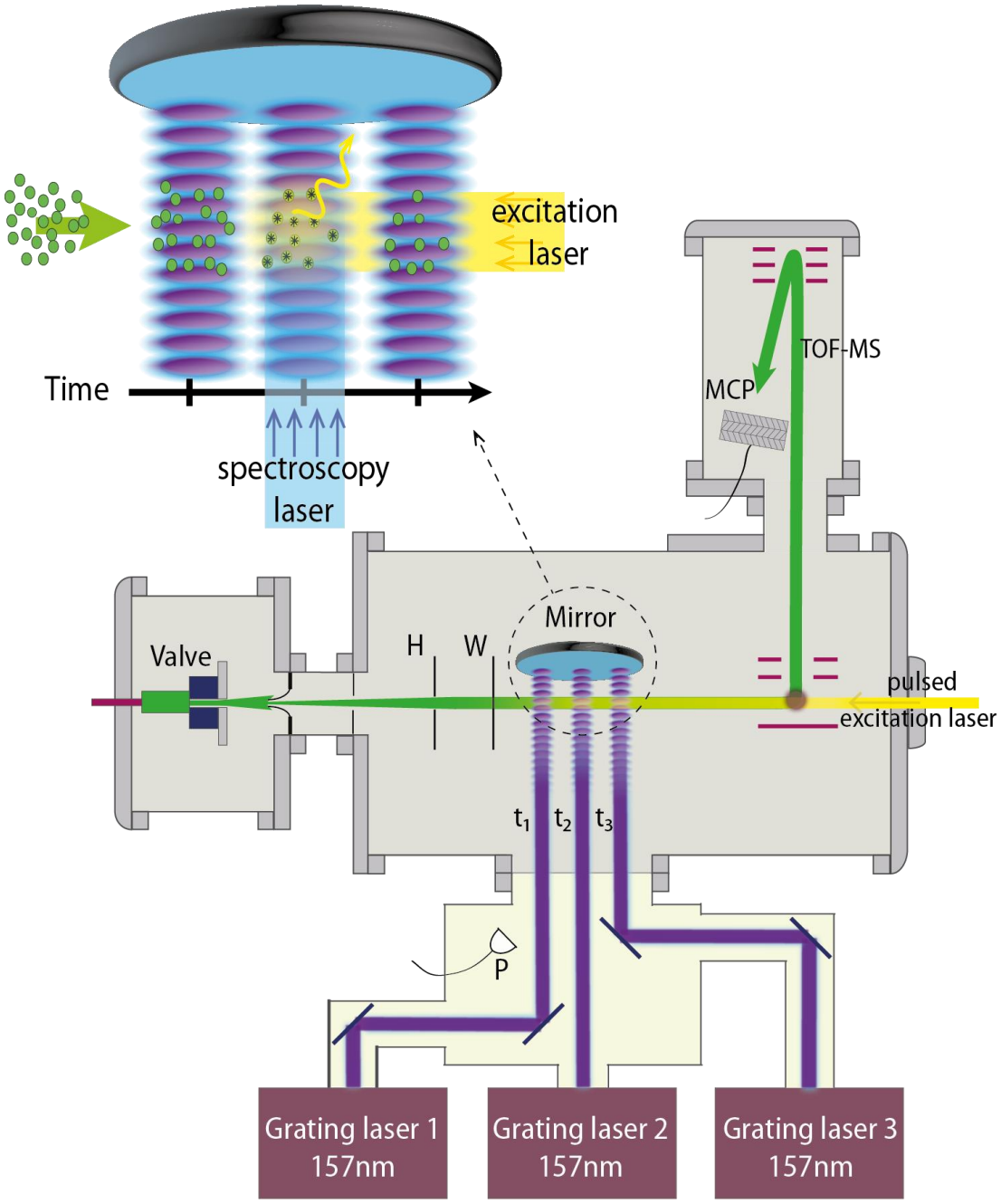

Figure 4-1 Experimental overview of the OTIMA interferometer with two additional lasers. *Spectroscopy laser (blue):* The OTIMA interferometer is able to resolve the shift due to the photon absorption recoil (see 4.1.4) *Excitation laser (yellow):* The absorption of an oncoming photon (perpendicular to the grating period) doesn´t shift the interference pattern but may lead to several other effects: it may excite the particle and change the optical polarizability (see 4.1.2); fluorescence; fragmentation of the particle (see 4.2.1). Picture modified from [6].

4.1 Metrology

Various experiments in our group have already shown that matter-wave interferometry can enhance the precision in measurements of particle properties [84,85]. This improvement was mainly achieved by the high spatial resolution with a grating period of down to 266 nm (in KDTL interferometry [21,84]) and the quantum enhanced molecular pattern.
In the OTIMA interferometer the grating period is even smaller (78.5 nm). Another big advantage is that all deflection experiments can be done in the time-domain. The interference pattern is only influenced by deflections between the first and the third light grating and shows no sensitivity to forces that act before and after the interferometer. A pulsed interferometer has therefore the great advantage that all particles spend the same time in the interferometer which leads to a velocity independent deflection of the interference pattern. In other words, the interaction time of all particles is the same regardless of their velocities. That is the first experimental deflection scheme for complex particles where fringe shifts can be recorded independent of the particles' velocities.

4.1.1 Static polarizability

Static polarizabilities of biomolecules and their clusters are of great interest. Polarizabilities provide information about molecular structures, conformation and cluster geometry [86]. The interaction of particles with static electric fields is given by their dipole moment and the induced dipole moment, the polarizability [86,87]. Interferometric [50] as well as classical deflection [88] measurements have already provided high accuracy data of the polarizability of various atoms. Talbot-Lau interferometers can easily be modified to become sensitive to static polarizabilities [84,85,89] . In the OTIMA interferometer the 2-inch interferometer mirror can be easily placed above two electrodes. These electrodes form a deflector by applying an electric field gradient on the interfering particles.

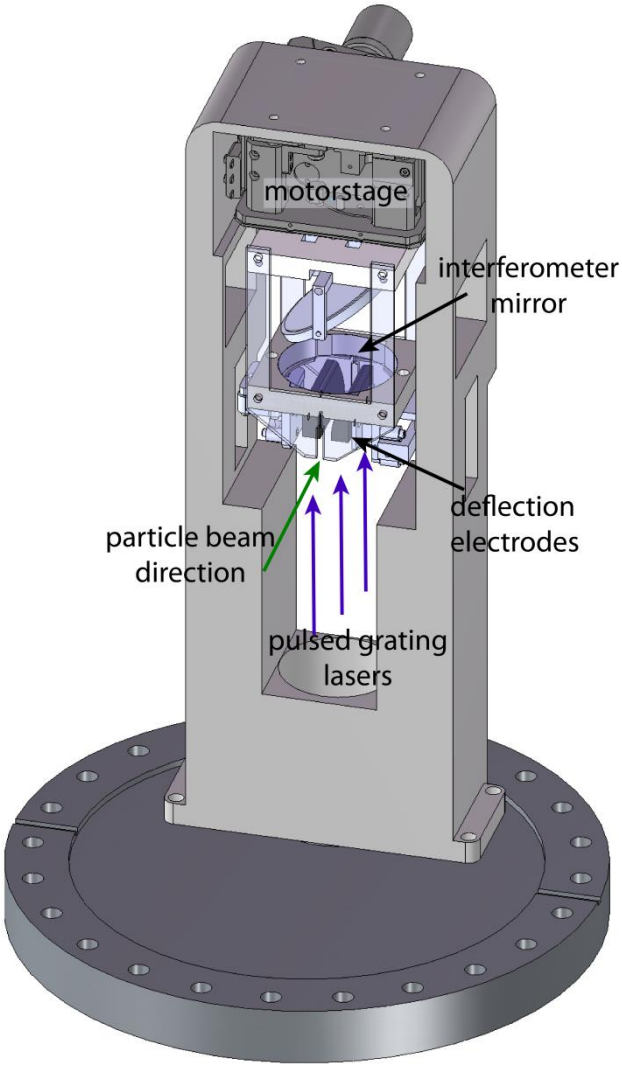

Figure 4-2 Sketch of the OTIMA interferometer for future metrology. The interferometer mirror is placed above tow deflector electrodes. These electrodes form an inhomogeneous electrical field, which couples on their static polarizability, and deflect the particles.

The force $F = \alpha(\boldsymbol{E}\nabla)\boldsymbol{E}$ is proportional to the static polarizability α of the particles. The resulting deflection is given by

$$\Delta x \propto \frac{\alpha}{m}(\boldsymbol{E}\nabla)\boldsymbol{E}\left(\frac{d_{elec}}{v}\right)^2 + \Delta x_s$$

Here v denotes the longitudinal velocity of the particles and limits the interaction time with the electrodes of length d_{elec}. The deflection over the whole device is

velocity dependent and difficult to calculate due to the shifts Δx_s by stray fields before and after the electrodes.

However, the deflection of the interference pattern in the OTIMA interferometer just depends on

$$\Delta x \propto \frac{\alpha}{m}(\boldsymbol{E}\nabla)\boldsymbol{E}\, T_T{}^2$$

the electric field $(\boldsymbol{E}\nabla)\boldsymbol{E}$ between the first and the third laser grating, the laser grating delay T_T and shows no dependence on the particles velocities.

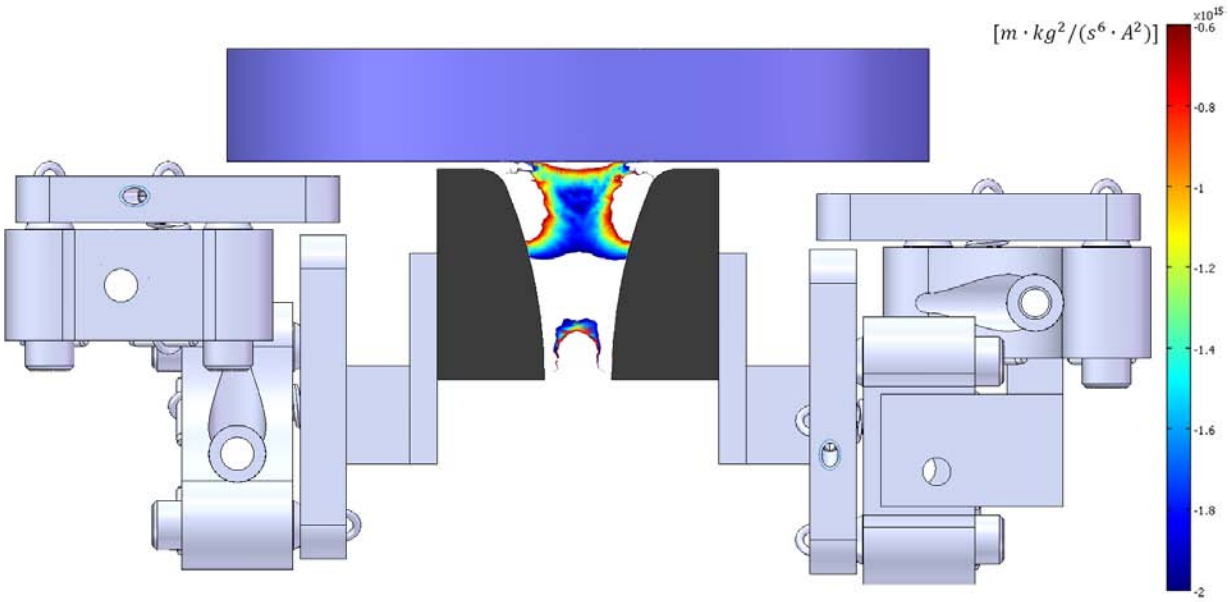

Figure 4-3 Assembly (SolidWorks) and simulation (COMSOL) of the electrodes. The electrodes are at a potential of ±15 kV. The electrodes are aligned with micrometer screws (right and left). The simulated field is $(\boldsymbol{E}\nabla)\boldsymbol{E} \approx 1.8 \cdot 10^{15}\ [V^2/m^3]$ with a variation of less than 5% in the area of the molecular beam. Particles with the same mass to polarizability ratio as Anthracene molecules [77] with $\alpha = 4\pi\epsilon_0 \times 25.4\,\dot{A}^3$ and $m = 178\,amu$ are deflected in this field within 25 µs (corresponds to a velocity of 960m/s) by 10.8 nm, that is more $1/8$ of the grating period.

4.1.2 Optical polarizability at 157 nm

The measurement of the optical (AC) polarizabilities of clusters or other particles that cannot be measured in vapour cells (e.g. thermal instable,..) has been developed in the last years by optical deflection technics [31,90–92].
The OTIMA interferometer is highly sensitive to the optical polarizability at the grating laser wavelength. During the interaction with the second light grating, the matter-waves accumulate a spatially dependent phase shift due to their optical polarizability $\alpha_{\lambda L}$ (see 2.2.2).

$$\phi(x) = \frac{16 P_L \alpha_{\lambda L} t}{\hbar c \omega_y \omega_z} \sin^2\left(\frac{\pi x}{d}\right) = V_0 \sin^2\left(\frac{\pi x}{d}\right)$$

The optical polarizability depends on the particles' electron density and delocalization. As shown in Figure 4-1, an additional pulsed laser (yellow) could provide photons to excite the particles right before the second light grating with high timing accuracy. The absorption of a photon excites the particle and changes the electron density distribution and therefore the optical polarizability. If this excited state lifetime is long enough (a few ns), the change in polarizability influences the visibility of the interference pattern, which depends on the β-parameter ((E 2-1)). The β-parameter can be determined by varying the laser power of the second light grating, as already discussed in section 2.4. Figure 2-6 plots the visibility as a function of the power of the second light grating for different β-parameters.

4.1.3 Magnetometry

The deflection scheme for the static polarizability in of 4.1.1 can also be applied for magnetometry to measure magnetic properties like the magnetic susceptibility$\boldsymbol{\chi}$ in a Stern-Gerlach experiment [93–95]. In the OTIMA interferometer a strong permanent magnet can be placed on top of the interferometer mirror to create an inhomogeneous magnetic field **B** below the mirror that deflects the particles in grating direction and shifts the interferogram by

$$\Delta x \propto \frac{\boldsymbol{\chi}}{m}(\boldsymbol{B}\nabla)\boldsymbol{B}\, T_T^{\,2}$$

4.1.4 Spectroscopy - Absolute absorption cross section σ from UV- far IR

Optical spectroscopy is a technology as old as the human eye and it is of significant importance for various fields of science like astronomy, physics, chemistry and biology. In the last century spectroscopic techniques have improved enormously [60,96–98]. Optical spectroscopy provides information about electronic, vibrational, rotational and structural properties of particles. However, it is still challenging to determine the absolute absorption cross section [97] for molecular clusters [96] below their ionization energies. Other techniques such as resonant two-photon ionization spectroscopy (R2PI) [99–102] or laser induced fluorescence spectroscopy (LIF) [103–105] had to be developed to get access to absolute absorption cross-sections. However, also these methods are limited in the presence of fast radiation-less relaxations of excited states, especially for large clusters. Radiating processes are necessary for LIF but inappropriate for R2PI. Here a long-lived excited state is needed to ionize the particles with an additional tuneable laser beam. Another spectroscopic approach makes use of the photon induced dissociation of a particle or an attached daughter fragment. A molecular beam is probed with a laser beam. Depending on the absorption of the photon, a subsequent heating of the complex results in the dissociation of weakly bound rare gas atoms of the particle or other

parts of it. A mass spectrometer analyses the remaining particle masses depending on the applied laser frequency and depicts the photo-induced fragmentation. Photo depletion spectroscopy has been applied to neutral [106–109] as well as to ionic [110] particles and is most efficient for small clusters with weakly bound rare gas atoms [106,111,112]. For bigger cluster sizes, the deposited photon energy is better distributed all over the particle which causes larger dissociation lifetimes that eventually exceed the timescale of the free propagation.

Thanks to its high spatial resolution and velocity independence the OTIMA interferometer offers a new approach for absorption spectroscopy (see Figure 4-2). The high spatial resolution allows to resolve the shift caused by the recoil $\hbar k$ of an absorbed photon [113]. This is a technique which is independent of other following actions like dissociation in depletion spectroscopy [114] or fluorescence in LIF, or ionization in R2PI. This spectroscopic method requires nothing else but the absorption of the photon. The biggest deflection is achieved when the photon is absorbed at the time of the second light grating (see (E 3-1)).

The deflection of a particle of mass m caused by the absorption of a photon of wavelength λ_{abs} is given by

$$\Delta x = \frac{h}{m\,\lambda_{abs}} t$$

By setting t to the Talbot time (E 1-5) the shift can be rewritten as a function of the Talbot time. (n represents the Talbot-Lau order)

$$\Delta x = n \frac{(78.5 \cdot 10^{-9} m)^2}{\lambda_{abs}}$$

A photon of 400 nm thus deflects a particle during its Talbot-time by 15.4 nm. This tiny shift is about 1/5 of the grating period and can be easily resolved.

4.2 Decoherence of matter-waves

In matter-wave interferometry particles are in a superposition state of two or more spatially separated locations. But with the increase of mass and complexity the particle interacts more with the environment and the lifetime of this quantum system normally decreases until the particle can be described classically. A future realization of Schrödinger's cat gedanken experiment, maybe with smaller objects like a virus, depends also on the suppression of mechanisms which destroy quantum effects and render matter-waves to matter (classical objects). This points out the need of studying decoherence mechanisms. Decoherence is caused by the interaction of quantum systems with its environment. This interaction can for instance be absorption/emission of photons [115–118], collisions with residual gas [80] or evaporation of parts of the molecular matter-wave itself. The first two mechanisms are well studied but evaporation processes have never been investigated. Nevertheless, they play an important role in forcing objects to act classically.

In the OTIMA interferometer, the timing of evaporation can, in principle, be controlled with an additional laser pulse (see Figure 4-1, yellow laser) with nanosecond accuracy. In contrast to the emission of a massless photon, which will localize the matter-wave to an area with a diameter of λ/2 (Heisenberg microscope), the evaporated matter has a de Broglie wavelength much smaller than the photon and therefore transfers a much larger momentum kick. Even the lightest atom (hydrogen at its boiling point 21.15 K) will leave the particle with a momentum of about $7 \cdot 10^{-25}$ [kg · m/s] and a de Broglie wavelength of $\lambda_{dB} \approx 0.7\,nm$. The momentum of a photon with the same thermal energy is only $1.5 \cdot 10^{-31}$ [kg · m/s] corresponding to a wavelength of $\lambda \approx 0.7\,mm$. In both cases, the parent particle will be kicked due to momentum conservation.

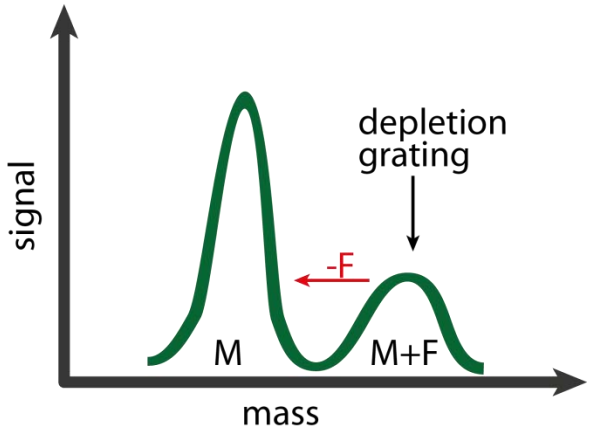

Figure 4-4 Sketch of the depletion grating scheme. Particle M shows insufficient photon ionization efficiency and is thermally stable. Attaching a weakly bound molecule F, the absorbed photon has the possibility to mark the particle M by depleting F.

For the investigation of decoherence by ligand evaporation in an experiment one has to find the right particles (see Table 4-1). The particle of choice should evaporate below 570 K (for use in the Even-Lavie see 3.1.2) without significant fragmentation into the same particles which are afterwards produced by photo-dissociation using radiation in the range of 1000 – 266 nm (1.2 – 5 eV). We assume the fragmentation process to be thermal. The relation between the internal energy U and the internal particle temperature T is given by the caloric curve $U = U(T)$ [119]. The change of U with T is measured by the heat capacity $c(T) = \partial U/\partial T$. From a classical point of view we can calculate the heat capacity $c = \frac{f}{2}k_B$. All independent degrees of freedom of the atoms n sum up to $f \approx 3n$, and k_B being the Boltzmann constant. This formula shows that all particles and their degrees of freedom equally share the total energy. Here, the temperature indicates the average energy of every single degree of freedom of an object.

In this case, we can approximate the internal temperature increase of a particle after photon absorption with:

$$\Delta T_{int} = \frac{2h\nu}{f k_B}$$

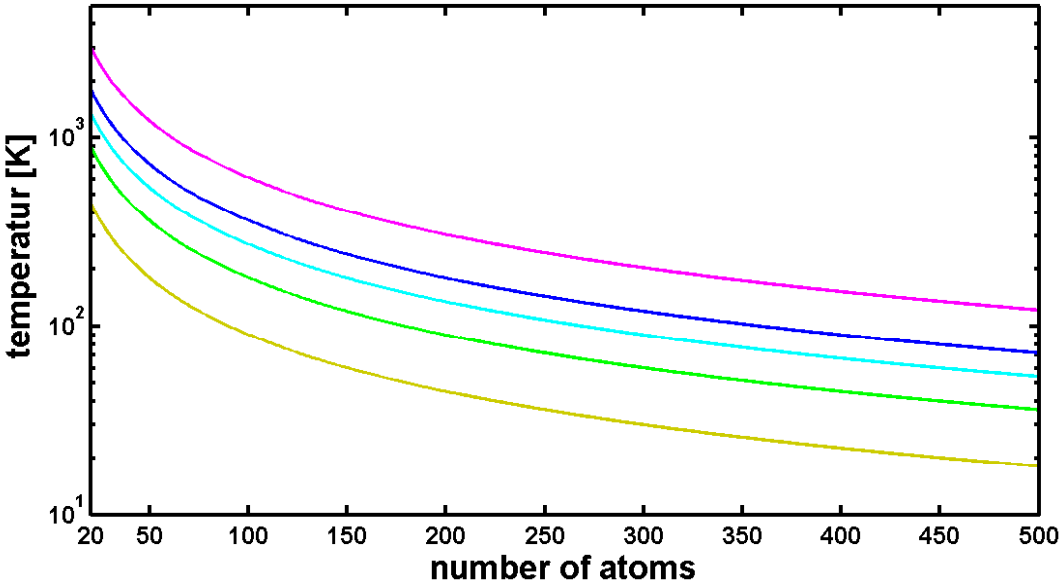

Figure 4-5 The internal temperature change after photon absorption increases with decreasing number of atoms per particle: 1064 nm (yellow), 532 nm (green), 355 nm (cyan), 266 nm (blue), 157 nm (violet)

The reduction factor of the visibility R_{Vis} due to the emission of photons has been calculated by Hornberger et al. [120] and can be generalized to the emission of a particle.

$$R_{Vis} = \int_0^\infty 4\pi \left(\frac{m_2}{2\pi k_B T}\right)^{3/2} v^2 e^{-\left(\frac{m_2 v^2}{2k_B T}\right)} sinc(2\pi \frac{vt}{d} \frac{m_2}{m_1}) dv$$

$$R_{Vis} = \exp(-2\pi^2 \frac{m_2 t^2 2k_B T}{m_1^2 d^2})$$

The first part of this equation is the Maxwell-Boltzmann distribution, which describes the evaporation process of the fragment with mass m_2 at a certain temperature T from the mother particle m_1. The sinc-function evaluates the momentum corresponding to the mass ratio $\frac{m_2}{m_1}$, of the fragment m_2 to the mother

particle m_1, with respect to the grating constant d. This integral can be solved analytically [121].

Figure 4-6 shows the visibility reduction calculated for a particle with a mass of 1000 amu depending on the delay between the first laser grating and the fragmentation. In this simulation the fragmentation is a thermal evaporation at temperatures from 10 K (right) to 110 K in steps of 10 K. The red curve shows the visibility reduction for an evaporated particle of 2 amu (e.g. H_2), the blue curve for a 40 amu particle like Argon or CO_2 (44 amu).

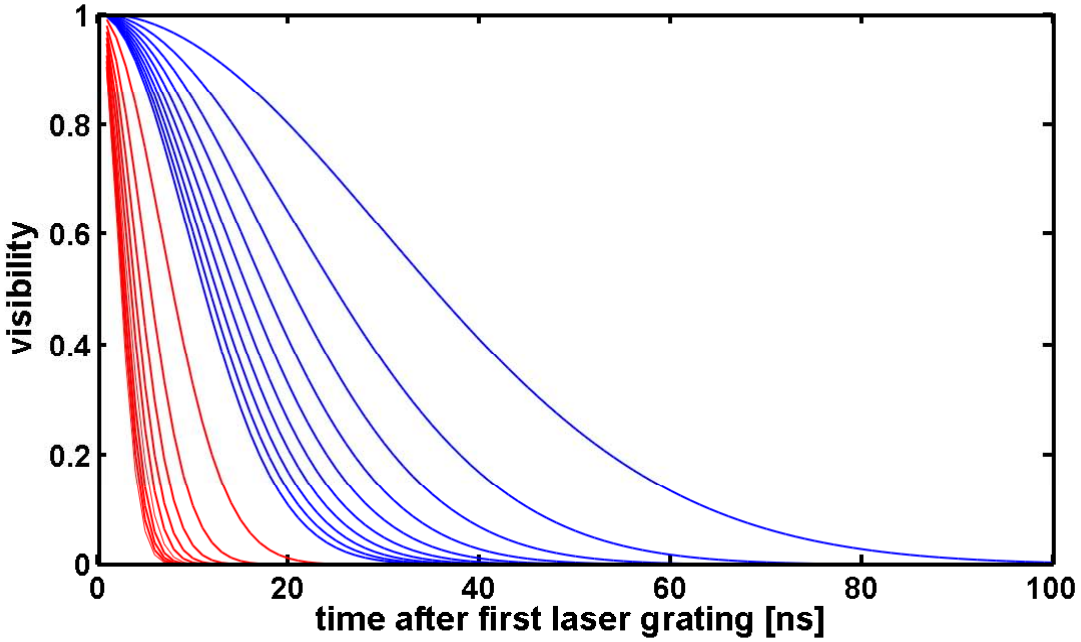

Figure 4-6 A particle of 1000 amu loses via thermal evaporation at 10 K (right) to 110 K (left) 2 amu (H_2 blue) or 40 amu (Ar, ~CO_2 red). This process leads to a visibility reduction depending on the delay between the first laser grating and fragmentation. At the time of the first grating the interference is not sensitive on the initial particle's momentum distribution. Depending on the delay to the second grating the sensitivity grows until it shows the maximum effect at the time of the second grating.

The fragmentation can also be a photo-induced event that occurs within picoseconds after absorption. Special molecules containing a nitrite compound show strong photo-dissociation of the NO group in the UV range [122]. The flight direction of the fragment depends on the polarization of the light and the wavelength. Nitrobenzene, for example: at 248 nm, 53±2 % of the available 3.2 eV (photon

energy minus 1.8 eV dissociation energy) is transformed to the kinetic energy of the fragments [123], the rest of the energy is split into vibrational and rotational excitations.

With that knowledge one can think of a decoherence experiment with kinetic control of the photo-dissociated particles.

4.2.1 Depletion grating

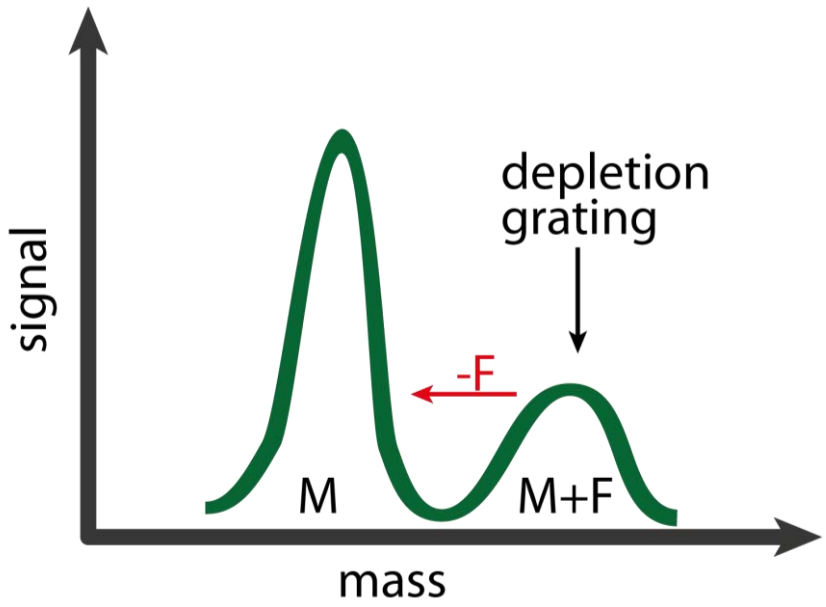

Figure 4-7 Sketch of the depletion grating scheme. Particle M shows insufficient photon ionization efficiency and is thermally stable. Attaching a weakly bound molecule F, the absorbed photon has the possibility to mark the particle M by depleting F.

Depletion spectroscopy is a well-established technique to access absorption lines and their cross-sections at wavelengths starting from far infrared [112] to the optical [124] range, which are below the ionization energy of the particle. The particles are usually co-expanded with a mixture of noble gases such as 1% Kr or Ar in He in order to form van der Waals bonds of Kr or Ar with the internally cold particles [125]. The lighter noble gas is needed to sufficiently cool the molecules or clusters

below the "boiling point" of the ligand. The particle beam is then hit by a wavelength tuneable laser beam. Photon absorption leads to a thermal heating of the particles which causes evaporation of the ligand. The signal of the particles with a ligand is now measured as a function of the laser wavelength. Other photo dissociated particles shouldn´t fragment to our considered particles, as shown in Figure 4-7.

Table 4-1 Experimental requirements of emitted particle induced decoherence compared to depletion gratings. Both need photon-induced fragmentation.

	Decoherence	**Depletion grating**
Dissociation @	532 nm	157 nm
Fragmented mass	1 - 4 amu	unimportant
Dissociation time scale	Fast (ns)	Slow (µs) before detection
Ionization cross section @ 157 nm [12]	high	low
Absorption cross section @ 157 nm	high	high
	$\sigma_A = \sigma_I$	$\sigma_A > \sigma_I$
Ionization cross section parent particle @ 157 nm	high	unimportant

In analogy to the ionization gratings where the particles lose an electron, this marker scheme can be used to implement a grating where particles get rid of a ligand. The interference is detected for those particles that have not absorbed a photon. This depletion grating scheme has a main advantage since it doesn´t require laser grating photon energies above the particle's ionization energy nor a high ionization yield.

[12] similar to Ac_6. The cross-section of Ac_6 perfectly fits for interferometry to the power of the F_2-Excimer laser (EX50 GAM).

By choosing the right ligand one may also enhance the absorption cross-section of the whole cluster or molecule at the grating wavelength. In that case, the ligand with its high cross-section acts like a guide dog and leads the particle in a quantum mechanical way through the interferometer. Such guide dog molecules may be Ethene (C_2H_4) with $\sigma_{157} = 30\ Mbarn$ or Pyrazine ($C_4H_4N_2$) $\sigma_{157} = 55\ Mbarn$ (see Table 4-2), which have at 157 nm an absorption line and ionization energies of 10.5 eV [126] and 9.3 eV [127].

Table 4-2 Comparison of different ligand molecules

Ligand	Dissociation temp. [K]	Mass [amu]	Cross section @ 157nm [10^{-18} cm^2]
Argon	87	40	0
CO_2	193	44	0.2 - 0.3 [128],[129]
C_2H_4	169	28	30 [130]
$C_4H_4N_2$	388	80	55 [131]

5 Influence of Coriolis force in matter wave interferometry

Matter-wave interferometry is very sensitive to all kinds of perturbations [55,132–134] as described in 4.1 as well as to fictitious forces like the Coriolis force. Since we are preforming our experiments on earth, which is spinning[13] with $\omega_E = 7.2921 \cdot 10^{-5} sek^{-1}$, our frame of reference is not an inertial system. The Coriolis force [135] is given by

$$\vec{F}_C = -2m(\vec{\omega}_E \, x \, \vec{v})$$

Here m denotes the mass and $\vec{v}$ the velocity vector of the particle.

The effect of the Coriolis force can especially be seen with large space-time interferometers, where it deflects the coherently split matter-waves in opposite directions. As a consequence of Earth rotation the interferometer doesn´t close precisely in the end. The matter waves cannot overlap with the needed accuracy and no superposition is observed.

One of these large space-time interferometers is a "simultaneous conjugated Ramsey-Bordé interferometers". We have performed such an interferometer [5,44,136] with caesium atoms and multiple photon beam splitters during a research stay at the University of California, Berkeley. The atoms are trapped and cooled in a magneto-optical trap (MOT). A moving optical molasses accelerates the cold atoms upwards and releases them into an about 3 meter high ballistic free fall. Now the atoms are coherently split and recombined by multi photon Bragg diffraction [137] as shown in Figure 5-1.

[13] Earths needs for a whole rotation in average 23 hours, 56 minutes, 4.0916 seconds (sidereal time)

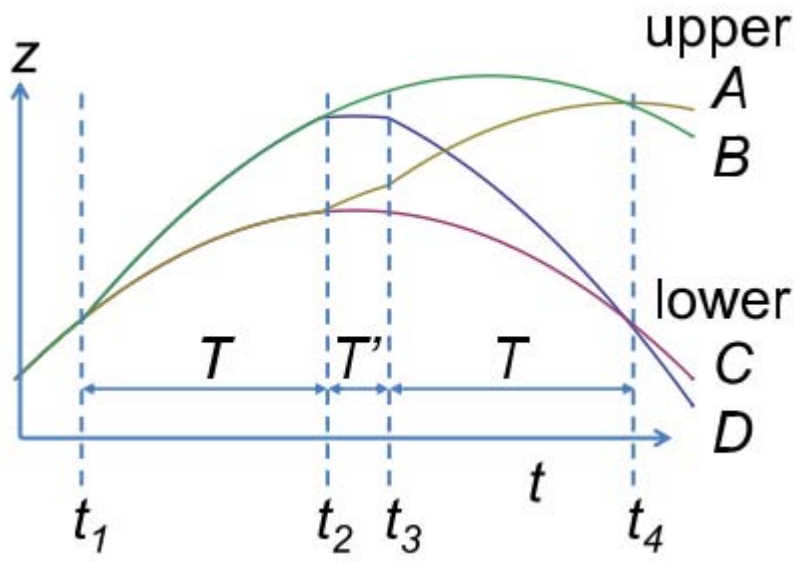

Figure 5-1 Sketch of simultaneous conjugate Ramsey-Bordé interferometers. The atoms are split at t_1, t_2, t_3, t_4 with $\pi/2$ pulses which split and recombine the atomic wave functions with a probability of 0.5. At each $\pi/2$ pulse, a momentum of several photons $n\hbar k$ can be transferred [136,138]. The non-interfering outputs of the last two beam splitters are not shown. Figure from [5].

After the last recombination laser pulses, the outputs A, B and C, D show a correlated interference patterns. Interferometers with large space-time areas are extremely sensitive to vibrations. To suppress their influence, the setup consists of a pair of simultaneous conjugate Ramsey-Bordé interferometers [75]. These two interferometers accumulate the same phase regarding to space like homogenous accelerations but with reversed signs. Therefore vibrations cancel out.

Nevertheless the Coriolis force causes a special deflection of the two coherently split wave packets which prevents them from interference. Let´s consider one of the two paths with an inertial reference frame (which is not rotating with the Earth). The x-axis is pointing westwards, the y-axis is pointing southwards and the z-axis is the direction in which the particles are coherently split. The velocity v (between the $\pi/2$ pulses at t_1, t_2, t_3, t_4) of this wave packet in one path in respect to the other one is given by the photon recoil velocity $v_r = \hbar k/m$ and the deflection by the Coriolis force (calculated with a first order approximation)

$$v_{12} = 2nv_r(0,0,1) \qquad v_{23} = 2nv_r(\omega_E T\cos\vartheta\,,0,0)$$

$$v_{34} = 2nv_r(\omega_E(2T+T')\cos\vartheta\,,0,-1) \qquad v_{4\infty} = 0$$

The experiment was built up in Berkeley, California at latitude $\vartheta = 37.87°$.
This leads to a mismatch at t_4 of

$$\Delta d = 4nv_r\omega_E T(T+T')\cos\vartheta\,(1,0,0)$$

A good approximation of the size of the atomic matter waves is given by the thermal de Broglie wavelength

$$\lambda_{dB} = \frac{h}{\sqrt{2\pi m k_B T}} \qquad \text{(E 5-1)}$$

where k_B denotes the Boltzmann constant. The typical temperature T of the interfered caesium atoms in this experiment is 2 µK, which leads to a size of about 100 nm. At pulse separation times of 250 ms and with a multi photon beam splitter of $n = 10$, the Coriolis induced displacement of the wave packets amounts to $\Delta d = 330\ nm$ and reduces the interference contrast.
To compensate for the Earth's rotation we tilt the main mirror which retro-reflects the laser beams to create the π/2 pulses. The interference contrast becomes maximal at an angular tilting velocity[14] of around $\omega_{x'} = 5\cdot 10^{-5} sek^{-1}$ and $\omega_{y'} = 2.62\cdot 10^{-5} sek^{-1}$ which roughly matches the Earth's rotation at latitude $\vartheta = 37.87°$. (see Figure 5-2).

[14] Due to experimental limitations the x´-axis is pointing roughly west and the y´-axis is pointing south, enclosing an angle of 82°.

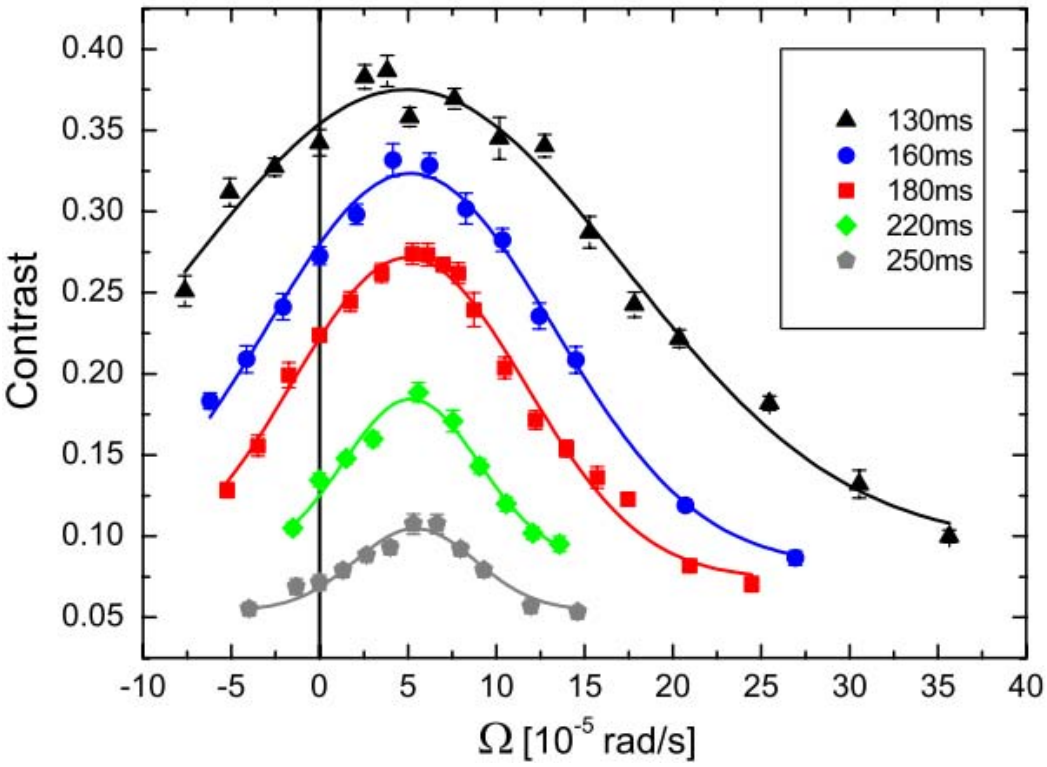

Figure 5-2 Interference contrast depending on the tip-tilt mirror rotation rate in y´ direction recorded for various pulse separation times. The x´-directions rotation rate is fixed at -26,2 µ rad/s. Figure from [5].

The Coriolis induced shift at the OTIMA interferometer [59] is given by

$$\Delta d = 4 v_r \omega_E T^2 \cos\vartheta \, (1, 0, 0)$$

Δd depends on the mass of the particles because $v_r = \hbar k/m$. At a pulse separation time of 25.9 µs (see Figure 3-12), particles of a mass of 2000 amu separate their wave functions due to the Earth rotation by about 0.15 fm, 200 amu particles by already 1.5 fm. This influence can be neglected since the lower limit of the wave function size can be estimated by equation (E 5-1) with 4 pm (2000 amu at 100 K). This estimation gives a lower bound because our molecular beam is spatially restricted by slits which enhance the size of the wave functions. (see Figure 2-1).

However, the Coriolis force influences the interferometer pattern also in another way. It deflects particles depending on their velocities. These deflections also occur in grating direction and lead to dispersive shifts of the interference pattern, which will reduce the visibility. In pulsed molecular beam experiments, velocities can be selected by collimating the beam in the transversal direction as well as by pulsed detection in the longitudinal direction (see Figure 2-1)

Future interference experiments may start with clouds of trapped cold particles (see 6.2) which will expand in all directions. A deflection caused by Earth's rotation will shift the interference pattern. The trajectories of the particles will be similar to the ones of rain clouds around a high atmospheric pressure area, but on nanometer scale. However, an interferometer in the time-domain can avoid this dephasing [7,21] by orientating the normal vector of the mirror, which gives the boundary condition for the light gratings, parallel to ω_E. This reorientation will change deflections in the direction of the grating vector to shifts parallel to the mirror surface.

6 Outlook

"Prediction is very difficult, especially if it's about the future" [15]

In this short chapter I will talk about future experiments which may push the mass limit further.

6.1 OTIMA with pulsed thermal laser evaporation

In order to increase the pulse separation delay which is limited by the transit time of the particles flying along the mirror, we will use a pulsed thermal laser evaporation source (see 3.1.3). The most probably thermal velocity is given by

$$v_{max} = \sqrt{\frac{2k_B T}{m}}$$

Between each applied light grating the particles can fly about 2 cm. Now, one can set the maximal passage time $\frac{0.02}{v_{max}}$ equal to the Talbot-Lau time $T_T = \frac{md^2}{h}$, and extract the product of T (temperature) and m (mass)

$$T \cdot m = \frac{(0.02 \cdot h)^2}{2d^4 k_B \cdot amu} \approx 1 \cdot 10^8$$

[15] Quote attributed to both Niels Bohr and Mark Twain [152]

If this product $T \cdot m$ is smaller than $10^8[K \cdot kg]$, particles of the most probable velocity at temperature T fulfill the Talbot-Lau condition and have enough time to form an interference pattern. Figure 6-1 shows this limitation from the first until the 7th Talbot-Lau order.

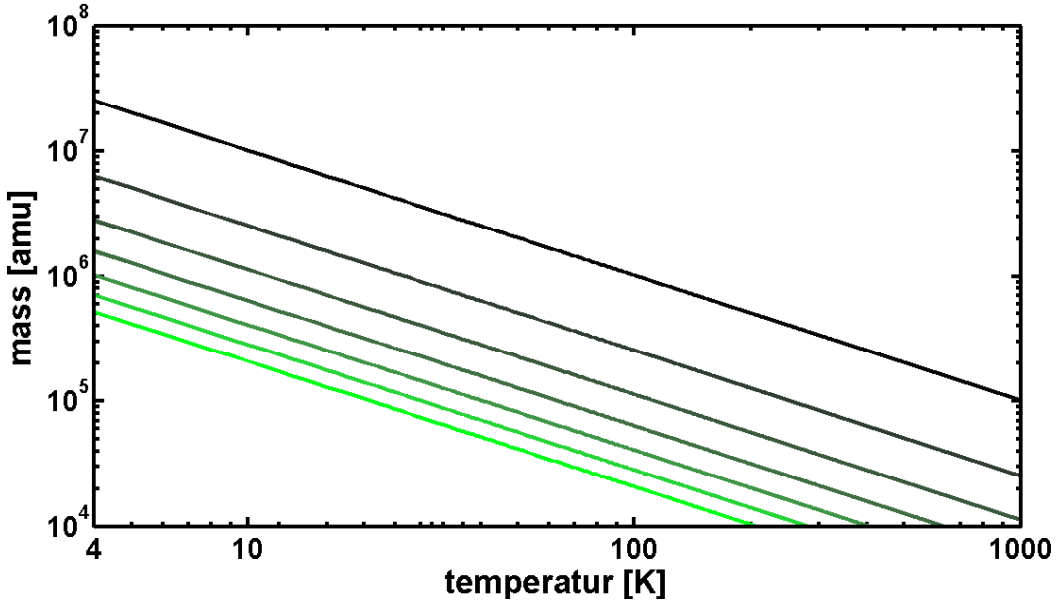

Figure 6-1 The lines set the upper limit for particles, with certain masses and a given most probably thermal velocity, to fulfill the Talbot-Lau condition. The border for the 1st order Talbot-Lau condition is the black line until the border of the 7th order in bright green.

6.2 OTIMA - interferometry in an ion-trap

To decrease the velocity of heavy particles one can trap them as negative ions in a RF-multi-pole trap [139,140] and reduce their temperature by buffer gas cooling [141,142]. The minimum temperature which can be reached using a suitable cold head or liquid helium is around 4 K.
At temperatures of 4 K, as shown in Figure 6-1, particles are slow enough to realize pulse separation times suitable for interference of particles with masses of more than 10^7 amu. Metal clusters show a good size to mass scaling since they can form spherical particles with high density, for example of gold with a mass density of 19320 kg/m³. A 10^7 amu gold cluster has a diameter of 11.8 nm. Biologically relevant molecules or already living matter in this mass range, like a tobacco mosaic virus have an extension of 300 nm [10]. Objects of sizes comparable to the grating constant would average over the standing light wave photon distribution and photo-ionize everywhere.

10^7 amu corresponds to a total interference time of about 300 ms. During this time particles fall already 45 cm in gravity, which is still a manageable distance for table top experiments. In this case one may have to think about a particle fountain similar to the experimental setup described in chapter 5 but for ions. The requirements regarding environmental decoherence become important [143] (see Figure 6-2). The main environmental decoherence sources are given by collisions with background particles [80] and by absorption/emission and scattering of thermal blackbody photons [81,118]. Elastic scattering of laser grating photons can be neglected until 10^9 amu [7].

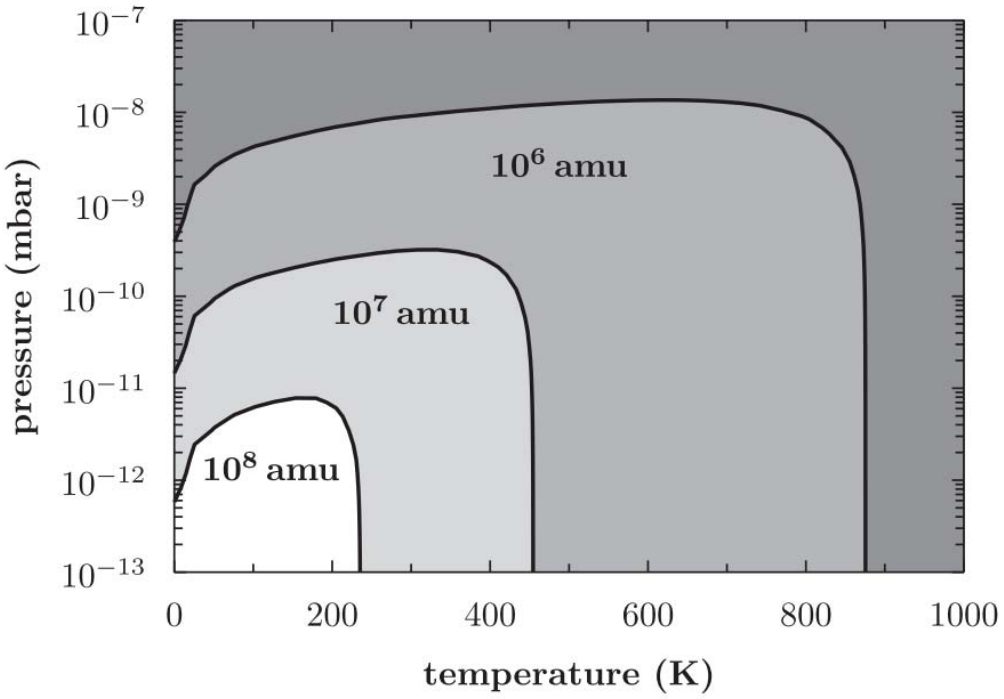

Figure 6-2 The contour lines set the border at which visibility is reduced through residual gas pressure and blackbody radiation (absorption/emission) by a factor 2. The temperature of the interfering particles is in equilibrium with the environment. The simulations are assuming clusters with gold properties and the residual gas consisting of N_2. Figure form [143].

A possible experimental scheme:

Negatively charged ions are cooled, mass selected and trapped in a RF-multi-pole trap. In the moment when the trap is switched off, the first pulse of the grating laser is applied and neutralizes the particles by single photon detachment in the antinodes of the standing light wave. This grating works in an inverse way to the ionizing light grating but still fulfills all requirements of a required transmission grating [7]. The remaining negative or the already positively photo-ionized particles are deflected by a small electrical potential. After one Talbot-Lau time, the second laser grating diffracts the neutral particles like in the previous OTIMA scheme and the third light grating photo ionizes and resolves the appearing interference pattern. After the last

grating, the now positively charged ions are trapped in the same RF-multi-pole trap and detected by fluorescence detection [144,145], counted with a channeltron or with a super conducting detector [146].

This experimental scheme consists of components and uses experimental techniques which are well established. Ion traps are therefore a promising tool to provide a cold suitable source and improved detection techniques for matter-wave interferometry with very massive particles.

7 Conclusion

During my thesis we have built up the OTIMA interferometer starting from a nearly empty lab. The now existing setup is the first interferometer for massive and complex particles in the time-domain. We have proven the quantum wave behavior for Anthracene clusters [6] as well various other clusters consisting of pure Vanillin, Caffeine or Ferrocene [147].

The use of only optical pulsed light gratings overcomes the restrictions of van der Waals interactions with material grating structures and offers a grating period of 78.5 nm. This pulsed interferometer accesses to study decoherence mechanisms for complex particles (e.g. evaporation of matter (4.2)) with unreached temporal and spatial precession. Also applications in metrology will benefit of the velocity independent character of the OTIMA setup [85,113].

Quantum mechanics is one of the best tested theories in physics but it is still an unresolved question if it still holds for macroscopic systems. Continuous spontaneous localization (CSL) theories like carried out by Ghirardi, Rimini and Weber [148] as well as [149,150] predict a random wave function "collapse" to a size of about 100 nm. The rate of this localization collapse scales with the mass of the object. In [143] we proposed a feasible test of the CSL model with the OTIMA interferometer with masses starting from 10^6 amu where recent estimations predict standard quantum mechanics to fail [151].

8 Pictures of the experiment

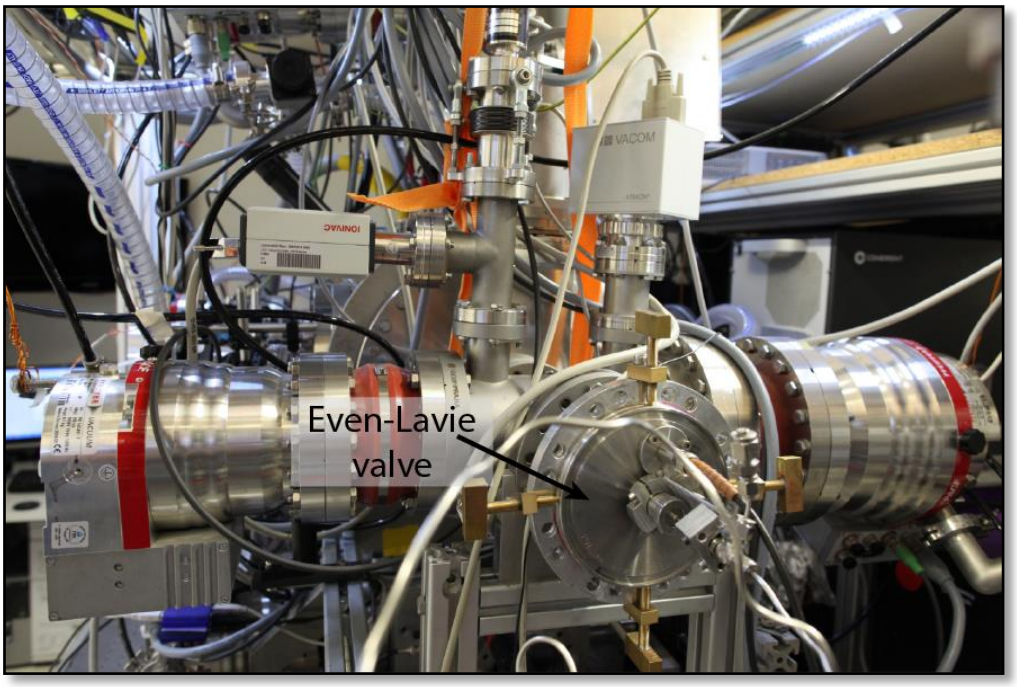

Figure 8-1 Setup view from the source side.

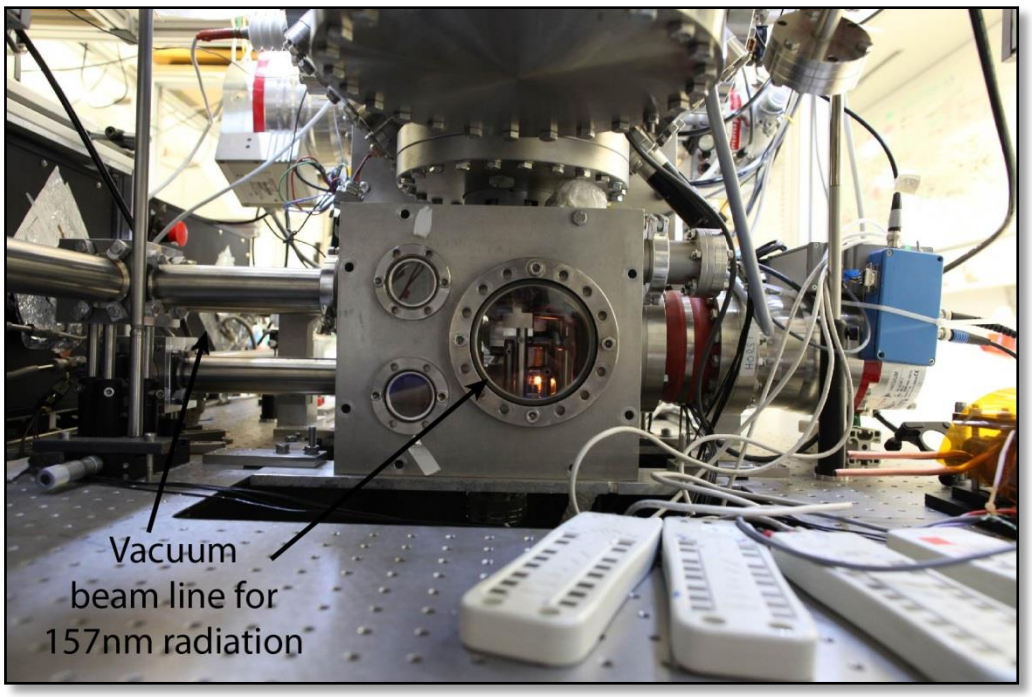

Figure 8-2 Setup view from below. Vacuum assembly for beam line purging; optics box and beam line tubes.

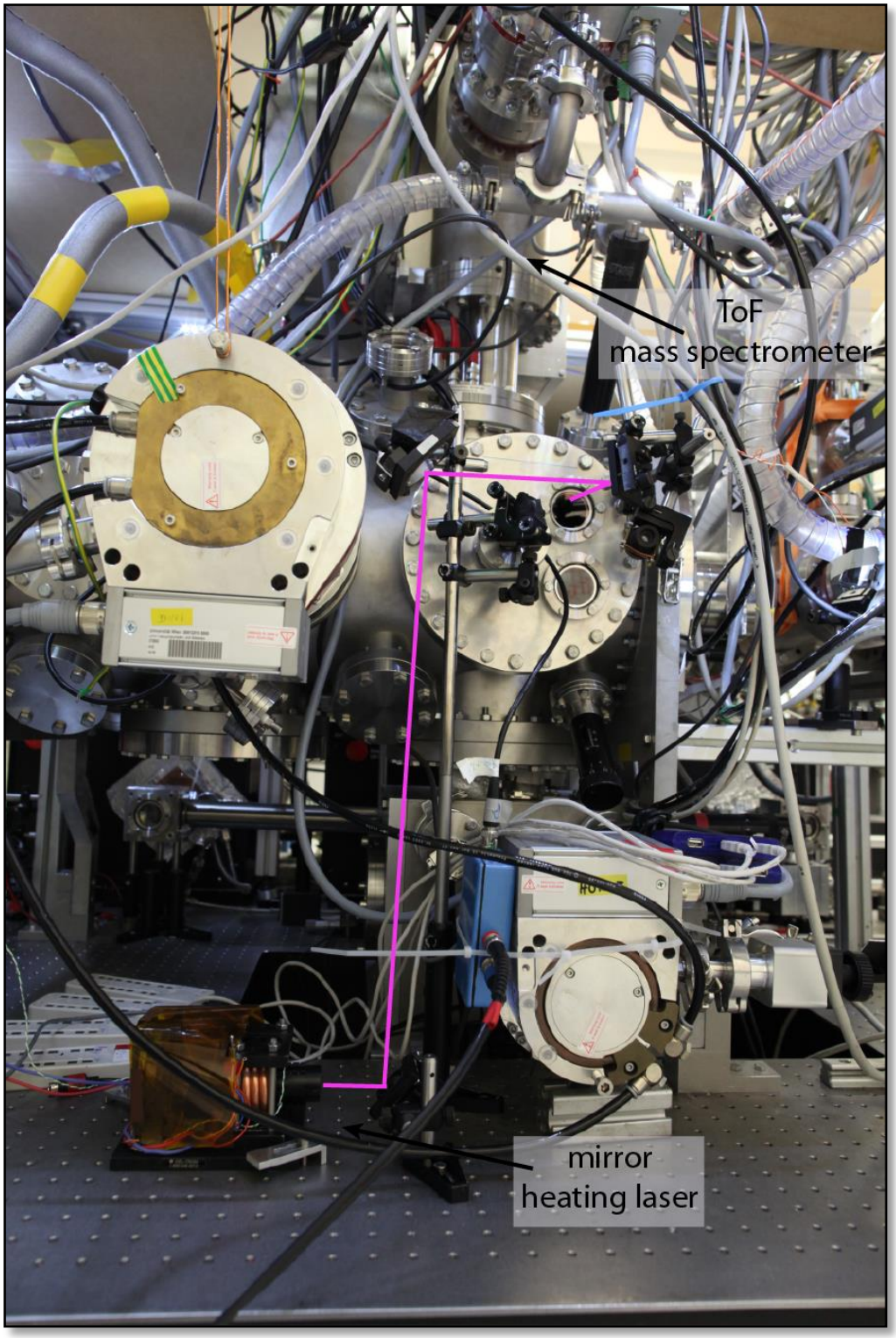

Figure 8-3 Setup view from the side. The 2-inch interferometer mirror is mounted where the violet laser beam enters the chamber.

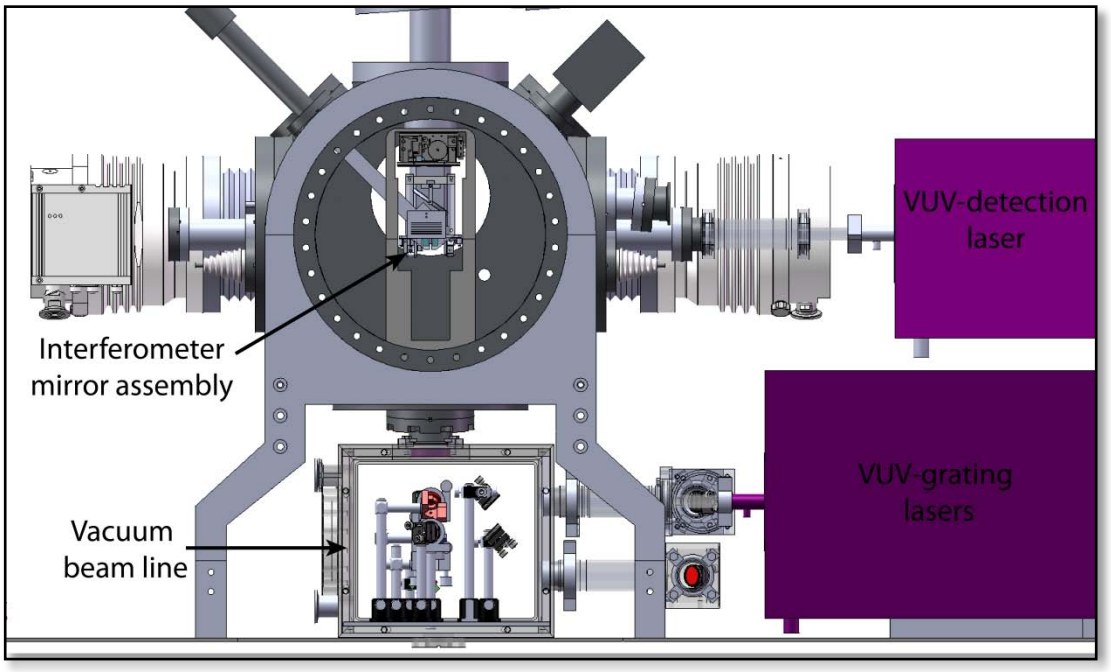

Figure 8-4 Setup in a schematic front view (SolidWorks).

9 Publications

All publications to which I could contribute during my PhD:

- Philipp Haslinger, Nadine Dörre, Philipp Geyer, Jonas Rodewald, Stefan Nimmrichter, Markus Arndt
  A universal matter-wave interferometer with optical ionization gratings in the time domain
  Nature Physics **9**, 144–148 (2013)

- Shau-Yu Lan, Pei-Chen Kuan, Brian Estey, Philipp Haslinger, Holger Müller
  Influence of the Coriolis force in atom interferometry
  Phys. Rev. Lett. **108**, 090402 (2012)

- Klaus Hornberger, Stefan Gerlich, Philipp Haslinger, Stefan Nimmrichter, Markus Arndt
  Colloquium: Quantum interference of clusters and molecules
  Rev. Mod. Phys. **84**, 157-173 (2012)

- Stefan Nimmrichter, Klaus Hornberger, Philipp Haslinger, Markus Arndt
  Testing spontaneous localization theories with matter-wave interferometry
  Phys. Rev. A **83**, 043621 (2011)

- Stefan Nimmrichter, Philipp Haslinger, Klaus Hornberger, Markus Arndt
  Concept of a time-domain ionizing matter-wave interferometer
  New J. Phys. **13**, 075002 (2011)

- Markus Marksteiner, Alexander Divochiy, Michele Sclafani, Philipp Haslinger, Hendrik Ulbricht, Alexander Korneev, Alexander Semenov, Gregory Gol'tsman, Markus Arndt
  Superconducting NbN detector for neutral nanoparticles
  Nanotechnology **20**, 455501 (2009)

LETTERS
PUBLISHED ONLINE: 10 FEBRUARY 2013 | DOI: 10.1038/NPHYS2542
nature physics

A universal matter-wave interferometer with optical ionization gratings in the time domain

Philipp Haslinger, Nadine Dörre, Philipp Geyer, Jonas Rodewald, Stefan Nimmrichter and Markus Arndt*

Matter-wave interferometry with atoms[1] and molecules[2] has attracted a rapidly growing level of interest over the past two decades, both in demonstrations of fundamental quantum phenomena and in quantum-enhanced precision measurements. Such experiments exploit the non-classical superposition of two or more position and momentum states that are coherently split and rejoined to interfere[3–11]. Here, we present the experimental realization of a universal near-field interferometer built from three short-pulse single-photon ionization gratings[12,13]. We observe quantum interference of fast molecular clusters, with a composite de Broglie wavelength as small as 275 fm. Optical ionization gratings are largely independent of the specific internal level structure and are therefore universally applicable to different kinds of nanoparticle, ranging from atoms to clusters, molecules and nanospheres. The interferometer is sensitive to fringe shifts as small as a few nanometres and yet robust against velocity-dependent phase shifts, because the gratings exist only for nanoseconds and form an interferometer in the time domain.

Recent progress in atom interferometry has been driven by the development of wide-angle beam splitters[14], large interferometer areas[15] and long coherence times[16]. Most interferometers operate in a Mach–Zehnder[5,17], Ramsey–Bordé[18] or Talbot–Lau[19] configuration, some of them also in the time domain[20,21]. Here we ask how to generalize these achievements to atoms, molecules, clusters or nanoparticles—irrespective of their internal states.

Mechanical nanomasks[22] could be considered as universal if it were not for their van der Waals attraction on the traversing matter waves, which induces sizable dispersive, that is, velocity-dependent, phase shifts even for gratings as thin as 10 nm.

Optical[9,14] or measurement-induced[23] gratings eliminate this effect, but most methods so far relied on closed transitions and required an individual light source for every specific kind of atom or molecule.

It is possible to circumvent this restriction by using the spatially periodic electric dipole potential in an off-resonant standing light wave. Its field then modulates the phase of the matter wave rather than the amplitude. This implies, however, that the spatial coherence of the incident matter wave needs to be prepared by other means before—such as by collimation, cooling[24] or the addition of another absorptive (material) mask[2].

Here, we demonstrate a new method for coherence experiments with a wide class of massive particles and show how a sequence of ionizing laser grating pulses[12] can form a generic matter-wave interferometer in the time domain[13].

Figure 1 shows a schematic of the layout of our experiment, which we here realize specifically for clusters of anthracene (Ac) molecules. The molecules are evaporated in an Even–Lavie valve[25] that injects the organic vapour with a pulse width of about 30 µs into the vacuum chamber. The adiabatic co-expansion with a noble gas cools the molecules and fosters the formation of organic clusters—here typically up to Ac_{15}.

The bunch of neutral nanoparticles passes a differential pumping stage, enters the interferometer chamber and flies in a short distance (0.1–4 mm) from the surface of a super-polished CaF_2 mirror before it reaches the laser ionization region of a time-of-flight mass spectrometer (TOF-MS) where it creates the signal peaks.

The pulsed beams of three synchronized F_2-excimer lasers ($\lambda = 157.63$ nm) hit the mirror surface and the cluster beam under normal incidence with a variable pulse energy of 1–3 mJ and a duration of about 7 ns. The laser beams are separated in space by ~20 mm along the cluster trajectory. Their mutual time delay is adjusted with an accuracy of a few nanoseconds. We choose the laser beam diameters (~1 mm × 10 mm rectangular flat top, extended along the cluster beam) to cover a wide particle bunch emitted by the source, whereas the detection laser beam is narrow enough to post-select only those clusters that have interacted with all three laser light pulses.

All three laser gratings interact with the matter waves in two different ways[13]: they imprint a periodic phase and, more importantly, they act as transmission gratings because the photon energy of ~7.9 eV exceeds the ionization energy of the nanoclusters. Particles that traverse the antinodes of a laser grating ionize with high probability after absorption of one or more photons and a weak electric field removes them from the beam. Close to the nodes of the standing light waves the clusters remain neutral and move on in the interferometer. This process imprints a periodic modulation onto the matter-wave amplitude—as if the clusters had passed a mechanical nanomask.

A strong spatial localization inside the first laser grating is important for preparing a comb of emergent wavelets whose transverse coherence will cover a few antinodes in the second light grating further downstream. This is a prerequisite for interference to occur, that is, for the formation of a free-flying cluster density pattern at precisely defined moments in time, which is probed with nanosecond precision by the third ionizing standing wave.

The three laser pulses form a Talbot–Lau interferometer in the time domain, which exhibits transmission resonances when the delay between two subsequent pulses is close to the Talbot time $T_m = md^2/h$, where m is the cluster mass and h is Planck's constant. In our setting, the grating period $d = \lambda/2 = 78.8$ nm results in $T_m = 15$ ns AMU^{-1}. All particles see the same gratings at the same time irrespective of their velocity. Even though they may enclose different areas in real space (x–z), they will accumulate the same phase and contribute constructively to the same interferogram for each given mass (Fig. 1b).

Faculty of Physics, University of Vienna, VCQ, Boltzmanngasse 5, A-1090 Vienna, Austria. *e-mail: markus.arndt@univie.ac.at.

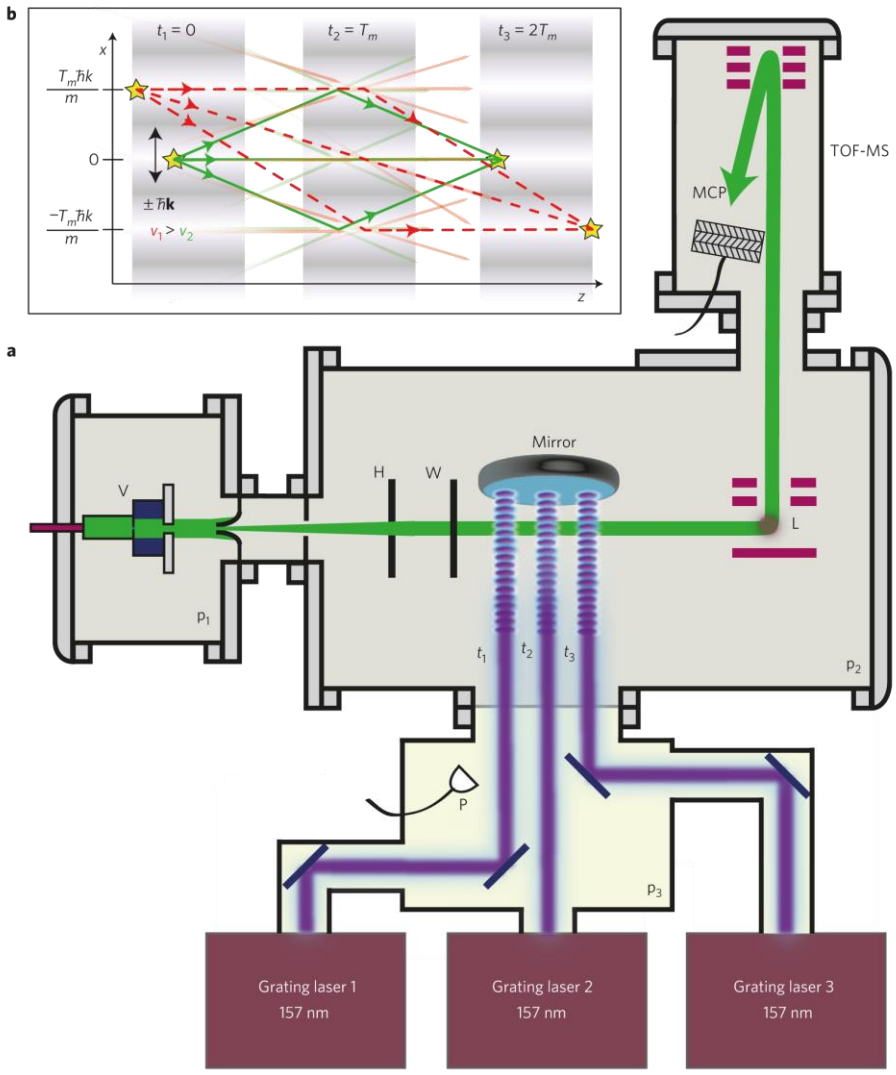

Figure 1 | Layout of the OTIMA interferometer. a, Set-up for nanoparticle interferometry with three short-pulse optical ionization gratings. From left to right: the Even–Lavie valve (V) produces a 30 μs pulse of neutral Ac clusters that are cooled in an adiabatic co-expansion with a noble gas jet. The cluster beam is delimited by two slits that are variable in height (H) and width (W). The laser pulses at $t_1 = 0, t_2 = T$ and $t_3 = 2T$ are back-reflected by a single 2-inch mirror to form three standing light waves. These are responsible for preparing the initial spatial coherence, for matter-wave diffraction and for spatially filtering the emerging cluster interferogram. The detection laser (L) ionizes the transmitted neutral clusters for TOF-MS. A photodiode (P) is used to monitor the laser timing with nanosecond accuracy. MCP, micro-channel plate. **b**, The interferogram is formed by multiple paths from the first to the third grating that correspond to an effective momentum transfer of $n\hbar k$ in each grating, with $n \in \mathbb{Z}$. Accurate timing ensures that the interfering paths branch and close at the same points on the grating axis x, irrespective of the cluster's initial velocities v_1 (red) > v_2 (green). The stars indicate the localization of the matter waves.

We trace the emergent interference pattern in four different ways: its mass characteristics, its dependence on the pulse separation and pulse sequence asymmetry, and by visualizing its structure in position space.

We start by monitoring the TOF-MS signal and toggle between a resonant and a non-resonant setting. In the resonant mode the delays $t_2 - t_1 = T$, $t_3 - t_2 = T + \Delta T$ between two subsequent laser pulses are equal, $\Delta T = 0$, and quantum interference is expected to modulate (enhance or reduce, depending on the phase) the transmission for the mass whose Talbot time matches the pulse separation T. In the off-resonant mode, the pulse delays are imbalanced by $\Delta T = 200$ ns and this tiny mismatch suffices to destroy the interferometric signal. We extract the interference contrast from the normalized difference $\Delta S_N = (S_R - S_O)/S_O$ between the resonant signal S_R and the off-resonant signal S_O and plot it as a function of mass in Fig. 2. The experimental mass spectra and ΔS_N bars (green) can be well understood by a quantum mechanical model (violet bars), as described in Methods, and both are in marked discrepancy with a classical model (grey bars)[13].

The role of the pulse separation T is demonstrated by changing the seed gas from argon to neon. Shifting the most probable jet velocity from 690 to 925 m s^{-1} allows us to decrease T. The quantum model then predicts the highest contrast to occur at smaller masses, as confirmed by the experimental data in Fig. 2b.

LETTERS NATURE PHYSICS DOI: 10.1038/NPHYS2542

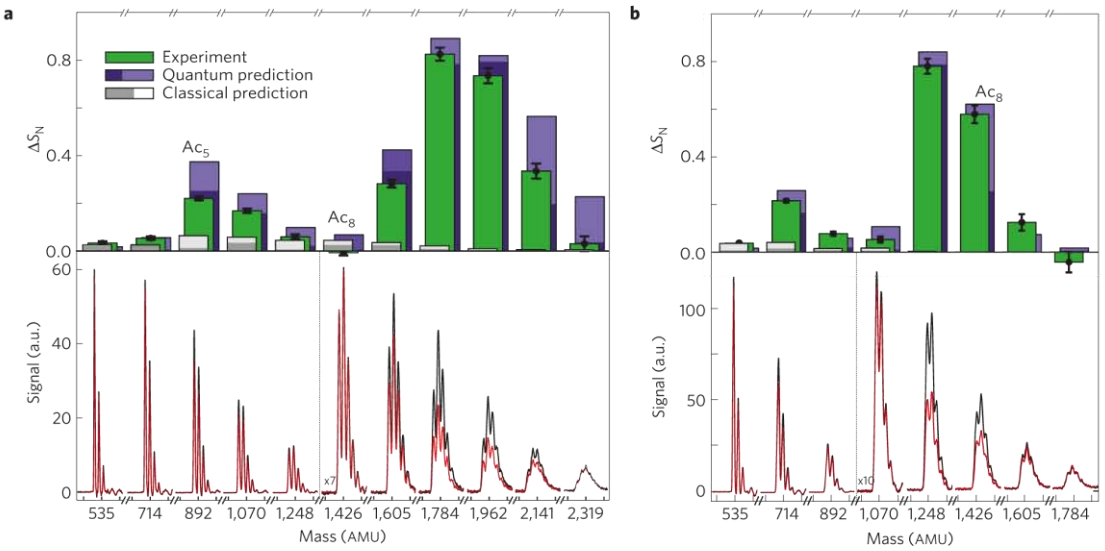

Figure 2 | Cluster interference visualized by means of the mass spectrum, for two pulse separation times. a, Lower panel: mass spectra recorded for a resonant (black line) and off-resonant ($\Delta T = 200$ ns, red line) pulse separation of $T = 25.9$ μs (clusters seeded in an argon jet). Each cluster signal splits into isotopic sub-peaks. The *x*-ticks correspond to a mass separation of 4 AMU. The two spectra differ for masses that fulfil $T_m \simeq T$. Upper panel: histogram of the cluster interference contrast, as measured by the signal difference ΔS_N integrated over the main isotopes of a given cluster. The predictions of the quantum/classical model[13] are shown in violet/grey. The light violet/grey regions indicate the variation of the fringe contrast with a ±30% variation of the cluster polarizability α_{157}. For further details, see Methods and Supplementary Information Se. **b**, The same as in **a** but with neon seeding and $T = 18.9$ μs. The error bars represent 1 s.d. of statistical error (see Supplementary Information Sh).

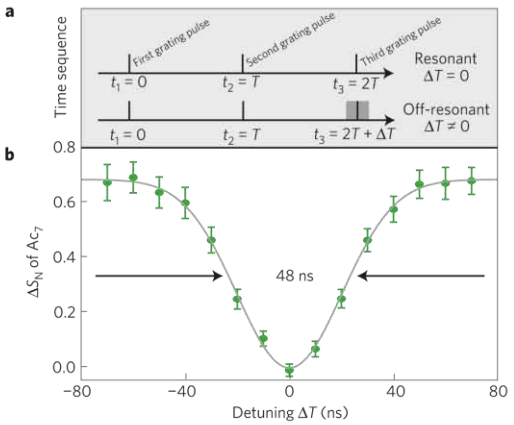

Figure 3 | Interferometric resonance and timing precision. Cluster self-imaging in a pulsed near-field interferometer is a resonant process with a short acceptance window for the matter waves to rephase. **a**, Pulse sequence. **b**, Difference ΔS_N between the resonant and off-resonant signals detected at a mass of Ac_7 as a function of ΔT. In our set-up and for a pulse separation time T of 18.9 μs, interference occurs during a time window of 48 ns (full-width at half-maximum). The error bars represent 1. s.d. of statistical error (see Supplementary Information Sh).

Figure 3 shows a clear resonance in ΔS_N as a function of the time imbalance $\Delta T \in [-70, +70]$ ns with a width determined by the transverse momentum distribution of the cluster beam[13]. The momentum spread inferred from a Gaussian fit to the data in Fig. 3 corresponds to a divergence angle along the grating of 2.1 mrad, in good agreement with the experimental settings.

In our set-up, the pulsed supersonic expansion determines the cluster velocity distribution and the pulsed mass detection post-selects its relative width to $\Delta v/v \simeq 3\%$. It is then justified to interpret the observations in position space: with the de Broglie wavelength given by $\lambda_{dB} = h/mv$, the mass distribution also represents a wavelength spectrum. The most prominent interference peak in Fig. 2b at 1,248 AMU corresponds to the heptamer Ac_7 with $\lambda_{dB} \simeq 345$ fm, at $v \simeq 925$ m s^{-1}. The highest mass peaks in the spectrum reach down to below $\lambda_{dB} \simeq 275$ fm.

Finally, we can also prove the formation of an interference pattern in real space by modifying the period of the central grating: whereas all laser beams had originally been set to normal incidence on the interferometer mirror—with an uncertainty of about 200 μrad—we now explicitly tilt the central laser beam by 5.1 mrad along the cluster beam. The direction of the standing-light-wave grating remains defined by the orientation of the mirror surface, but an increasing tilt angle θ reduces the modulus of the wave vector perpendicular to the surface, $k_p = k \cdot \cos\theta$. We can shift the interference pattern by half a grating period when the clusters pass the mirror surface at an average distance of 1.5 mm. We plot the fringe shift as a function of the separation between the beam and the mirror in Fig. 4 and find a damped sinusoidal transmission curve for all clusters with the expected period. The overall damping results from the limited coherence of the laser system and the vertical extension of the Ac cluster beam.

All tests presented here confirm the successful experimental realization of an optical time-domain ionizing matter-wave (OTIMA) interferometer[2,13], which exploits pulsed ionization gratings. This versatile tool for quantum interferometry will be applicable to a large class of nanoparticles.

Owing to the pulsed gratings, all phase shifts caused by constant external forces become velocity-independent and leave the contrast unaffected. The dispersive Coriolis shift[15] can be well compensated by a suitable orientation of the interferometer, if needed.

The wide applicability and non-dispersive nature of pulsed ionization gratings make the OTIMA design particularly appealing for quantum experiments with highly complex particles, eventually

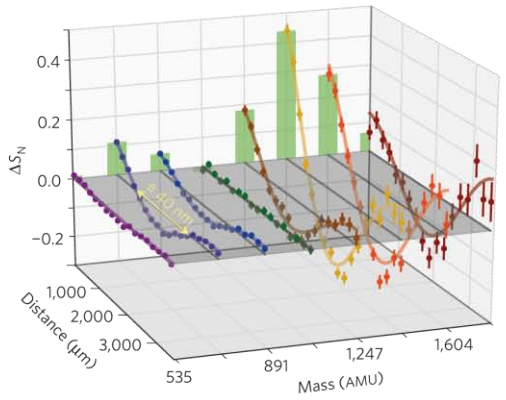

Figure 4 | ΔS_N as a function of the mirror displacement for different clusters. The second grating laser beam was tilted by 5.1 ± 0.3 mrad in the direction of the molecular beam to stretch the effective grating period by about 0.013 per mille. This suffices to induce a fringe shift of half a grating period for molecules travelling around 1.5 mm distance from the mirror surface. The mirror height is varied to effectively shift the second grating with regard to the other two, which allows us to scan the cluster interference pattern. We extract the periodicity for ΔS_N as a function of the mirror distance by fitting a damped sine curve to the experimental data. This periodicity corresponds to the expected effective period[13] of the interferogram of about 78.8 nm. The error bars represent 1 s.d. of statistical error (see Supplementary Information Sh).

even with nanoparticles at the length scale of the grating period. As high-mass interferometry requires coherence of the order of the Talbot time, practical mass limits are imposed by free fall in the gravitational field on Earth in combination with the limited coherence of vacuum ultraviolet lasers and the finite phase-space density of the available particle sources. However, none of them is fundamental. Even in the presence of thermal radiation at room temperature (particle and environment) and collisional decoherence at a background pressure of 10^{-9} mbar, the OTIMA design is predicted to enable new tests of quantum physics, such as tests of spontaneous localization, with particle masses around 10^6 AMU and beyond[26].

On the applied side, the OTIMA set-up is expected to improve the accuracy of molecule and cluster deflectometry because it ensures the same interaction (phase accumulation) time for all particles with the external fields[27] and a position readout at the nanometre scale. Our interferometer concept therefore establishes also the basis for a new class of quantum-enhanced precision metrology experiments.

Methods

Absorption and optical polarizability. The central grating influences the propagation of the coherent matter wave by modulating both its amplitude and phase. It does this by removing particles from the anti-nodes of the standing light field and by imprinting a phase onto the matter wave in proportion to the clusters' optical polarizability at 157 nm. In the first and third grating the phase modulation has no effect, because the clusters enter with random phases, and because the last grating merely acts as a transmission mask. Neither the absorption cross-sections $\sigma_{157}(N)$ nor the polarizabilities $\alpha_{157}(N)$ are known, a priori, for each cluster of N molecules in the vacuum ultraviolet wavelength range. However, $\sigma_{157}(N)$ enters the model only through the mean number of photons absorbed $n_0(N)$ in each grating, which we can determine by monitoring the cluster loss rate. Whereas this parameter influences the general shape of the interference curve as a function of mass, the polarizability may modify the predicted contrast of each individual cluster. We assume the polarizability and the absorption cross-section to exhibit the same N-scaling as retrieved from our $n_0(N)$ measurements and we allow the polarizability to vary by ±30% (light violet confidence areas in Fig. 2) around the single-molecule value. We use the polarizability $\alpha_{157}(1) = 25.4 \times 10^{-30}$ m^3 from ref. 28 and we extract an absorption cross-section of $\sigma_{157}(1) = 1.1 \times 10^{-20}$ m^2 from ref. 29.

This yields the quantum and classical theory curve in Fig. 2. Apart from the uncertain polarizability, the deviations from the experimental data may be attributed to a limited efficiency of single-photon ionization and contributions by fragmentation processes. Although the absolute interference contrast is sensitive to a variety of different cluster properties that are still to be extracted in combination with more refined cluster theory, the fringe shift will become valuable for precisely measuring the interplay between internal cluster properties and external forces.

Received 2 November 2012; accepted 24 December 2012; published online 10 February 2013

References

1. Cronin, A. D., Schmiedmayer, J. & Pritchard, D. E. Optics and interferometry with atoms and molecules. *Rev. Mod. Phys.* **81,** 1051–1129 (2009).
2. Hornberger, K., Gerlich, S., Haslinger, P., Nimmrichter, S. & Arndt, M. Colloquium: Quantum interference of clusters and molecules. *Rev. Mod. Phys.* **84,** 157–173 (2012).
3. Estermann, I. & Stern, O. Beugung von Molekularstrahlen. *Z. Phys.* **61,** 95–125 (1930).
4. Keith, D. W., Schattenburg, M. L., Smith, H. I. & Pritchard, D. E. Diffraction of atoms by a transmission grating. *Phys. Rev. Lett.* **61,** 1580–1583 (1988).
5. Kasevich, M. & Chu, S. Atomic interferometry using stimulated Raman transitions. *Phys. Rev. Lett.* **67,** 181–184 (1991).
6. Bordé, C. Atomic interferometry with internal state labelling. *Phys. Lett. A* **140,** 10 (1989).
7. Rasel, E. M., Oberthaler, M. K., Batelaan, H., Schmiedmayer, J. & Zeilinger, A. Atom wave interferometry with diffraction gratings of light. *Phys. Rev. Lett.* **75,** 2633–2637 (1995).
8. Fray, S., Diez, C., Hänsch, T. & Weitz, M. Atomic interferometer with amplitude gratings of light and its applications to atom based tests of the equivalence principle. *Phys. Rev. Lett.* **93,** 240404 (2004).
9. Müller, H., Chiow, S-w., Long, Q., Herrmann, S. & Chu, S. Atom interferometry with up to 24-photon-momentum-transfer beam splitters. *Phys. Rev. Lett.* **100,** 180405 (2008).
10. Moskowitz, P. E., Gould, P. L., Atlas, S. R. & Pritchard, D. E. Diffraction of an atomic beam by standing-wave radiation. *Phys. Rev. Lett.* **51,** 370–373 (1983).
11. Giltner, D. M., McGowan, R. W. & Lee, S. A. Atom interferometer based on Bragg scattering from standing light waves. *Phys. Rev. Lett.* **75,** 2638–2641 (1995).
12. Reiger, E., Hackermüller, L., Berninger, M. & Arndt, M. Exploration of gold nanoparticle beams for matter wave interferometry. *Opt. Commun.* **264,** 326–332 (2006).
13. Nimmrichter, S., Haslinger, P., Hornberger, K. & Arndt, M. Concept of an ionizing time-domain matter–wave interferometer. *New. J. Phys.* **13,** 075002 (2011).
14. Chiow, S., Kovachy, T., Chien, H. C. & Kasevich, M. A. 102$\hbar k$ large area atom interferometers. *Phys. Rev. Lett.* **107,** 130403 (2011).
15. Lan, S-Y., Kuan, P-C., Estey, B., Haslinger, P. & Müller, H. Influence of the coriolis force in atom interferometry. *Phys. Rev. Lett.* **108,** 090402 (2012).
16. Müller, H., Chiow, S., Herrmann, S., Chu, S. & Chung, K. Y. Atom-interferometry tests of the isotropy of post-Newtonian gravity. *Phys. Rev. Lett.* **100,** 31101 (2008).
17. Keith, D. W., Ekstrom, C. R., Turchette, Q. A. & Pritchard, D. E. An interferometer for atoms. *Phys. Rev. Lett.* **66,** 2693 (1991).
18. Bordé, C. J., Courtier, N., Burck, F. D., Goncharov, A. N. & Gorlicki, M. Molecular interferometry experiments. *Phys. Lett. A* **188,** 187–197 (1994).
19. Clauser, J. F. & Li, S. Talbot–von Lau atom interferometry with cold slow potassium. *Phys. Rev. A* **49,** R2213 (1994).
20. Szriftgiser, P., Guéry-Odelin, D., Arndt, M. & Dalibard, J. Atomic wave diffraction and interference using temporal slits. *Phys. Rev. Lett.* **77,** 4–7 (1996).
21. Cahn, S. B. *et al.* Time-domain de Broglie wave interferometry. *Phys. Rev. Lett.* **79,** 784–787 (1997).
22. Juffmann, T. *et al.* Real-time single-molecule imaging of quantum interference. *Nature Nanotech.* **7,** 297–300 (2012).
23. Storey, P., Collett, M. & Walls, D. Measurement-induced diffraction and interference of atoms. *Phys. Rev. Lett.* **68,** 472–475 (1992).
24. Deng, L. *et al.* Temporal, matter–wave-dispersion Talbot effect. *Phys. Rev. Lett.* **83,** 5407–5411 (1999).
25. Even, U., Jortner, J., Noy, D., Lavie, N. & Cossart-Magos, C. Cooling of large molecules below 1 K and He clusters formation. *J. Chem. Phys.* **112,** 8068–8071 (2000).
26. Nimmrichter, S., Hornberger, K., Haslinger, P. & Arndt, M. Testing spontaneous localization theories with matter–wave interferometry. *Phys. Rev. A* **83,** 043621 (2011).

27. De Heer, W. A. & Kresin, V. V. in *Handbook of Nanophysics: Clusters and Fullerenes* (ed. Sattler, K. D.) Ch. 10 (CRC Press, 2011).
28. Marchese, F. T. & Jaffé, H. H. The calculation of ground and excited state molecular polarizabilities: A simple perturbation treatment. *Theor. Chim. Acta* **45,** 241–247 (1977).
29. Malloci, G., Mulas, G. & Joblin, C. Electronic absorption spectra of PAHs up to vacuum UV Towards a detailed model of interstellar PAH photophysics. *Astron. Astrophys.* **117,** 105–117 (2004).

Acknowledgements

We acknowledge support by the Austrian science funds (FWF-Z149-N16 Wittgenstein and DK CoQuS W1210-2) as well as infrastructure funds by the Austrian ministry of science and research BMWF (IS725001). We thank U. Even and O. Cheshnovsky for emphasizing the benefits of organic molecules with the Even–Lavie valve and K. Hornberger for collaborations on the modelling of the OTIMA interferometer. We thank B. von Issendorff for discussions on cluster sources.

Author contributions

P.H., N.D., P.G. and J.R. built the interferometer and performed the measurements. P.H. contributed the initial experimental layout and the time-domain perspective of the experiment. P.G. developed the customized software and data acquisition system in feedback with the team. Data analysis was done by N.D., J.R. and P.H. S.N. contributed the theoretical description. M.A. initiated and supervised the experiment. P.H., N.D., J.R., S.N. and M.A. wrote the paper with input by all co-authors.

Additional information

Supplementary information is available in the online version of the paper. Reprints and permissions information is available online at www.nature.com/reprints. Correspondence and requests for materials should be addressed to M.A.

Competing financial interests

The authors declare no competing financial interests.

Influence of the Coriolis Force in Atom Interferometry

Shau-Yu Lan,[1,*] Pei-Chen Kuan,[1] Brian Estey,[1] Philipp Haslinger,[2] and Holger Müller[1,3]
[1]*Department of Physics, University of California, Berkeley, California 94720, USA*
[2]*VCQ, Faculty of Physics, University of Vienna, Boltzmanngasse 5, A-1090 Vienna, Austria*
[3]*Lawrence Berkeley National Laboratory, One Cyclotron Road, Berkeley, California 94720, USA*
(Received 31 October 2011; published 27 February 2012)

In a light-pulse atom interferometer, we use a tip-tilt mirror to remove the influence of the Coriolis force from Earth's rotation and to characterize configuration space wave packets. For interferometers with a large momentum transfer and large pulse separation time, we improve the contrast by up to 350% and suppress systematic effects. We also reach what is to our knowledge the largest space-time area enclosed in any atom interferometer to date. We discuss implications for future high-performance instruments.

DOI: 10.1103/PhysRevLett.108.090402 PACS numbers: 03.75.Dg, 06.30.Gv, 37.25.+k, 67.85.−d

Light-pulse atom interferometers use atom-photon interactions to coherently split, guide, and recombine freely falling matter-waves [1]. They are important in measurements of local gravity [2], the gravity gradient [3], the Sagnac effect [4], Newton's gravitational constant [5], the fine structure constant [6], and tests of fundamental laws of physics [7–9]. Recent progress in increased momentum transfer led to larger areas enclosed between the interferometer arms [10–12] and, combined with common-mode noise rejection between simultaneous interferometers [13,14], to strongly increased sensitivity. With these advances, what used to be a minuscule systematic effect now impacts interferometer performance: The Coriolis force caused by Earth's rotation has long been known to cause systematic effects [2]. In this Letter, we not only demonstrate that it causes severe loss of contrast in large space-time atom interferometers, but also use a tip-tilt mirror [15] to compensate for it, improving contrast (by up to 350%), pulse separation time, and sensitivity, and characterize the configuration space wave packets. In addition, we remove the systematic shift arising from the Sagnac effect [16]. This leads to the largest space-time area enclosed in any atom interferometer yet demonstrated, given by a momentum transfer of $10\hbar k$, where $\hbar k$ is the momentum of one photon, and a pulse separation time of 250 ms.

Figure 1 shows the atom's trajectories in our apparatus. We first consider the upper two paths: At a time t_0, an atom of mass m in free fall is illuminated by a laser pulse of wave number k. Atom-photon interactions coherently transfer the momentum of a number $2n$ of photons to the atom with about 50% probability, placing the atom into a coherent superposition of two quantum states that separate with a relative velocity of $2nv_r$, where $v_r = \hbar k/m$ is the recoil velocity. An interval T later, a second pulse stops that relative motion and another interval T' later, a third pulse directs the wave packets towards each other. The packets meet again at $t_4 = t_1 + 2T + T'$ when a final pulse overlaps the atoms. The probability of detecting an atom in a particular output of the interferometer is given by $\cos^2(\Delta\phi/2)$, where $\Delta\phi$ is the phase difference accumulated by the matter wave between the two paths. It can be calculated to be $\Delta\phi^{\pm} = 8n^2(\hbar k^2/2m)T \pm nkgT(T + T')$, the sum of a recoil-induced term $8n^2(\hbar k^2/2m)T$, and a gravity-induced one, $nkgT(T + T')$, where g is the acceleration of free fall and $\pm$ correspond to the upper and lower interferometer, respectively (Fig. 1) [14].

Because of Earth's rotation, however, the interferometer does not close precisely. We adopt Cartesian coordinates in an inertial frame, one that does not rotate with Earth. We take the x axis horizontal pointing west, the y axis pointing south, and the z axis such that the laser, pointing vertically upwards, coincides with it at t_1, see Fig. 2. Later, at t_2, t_3, and t_4, the laser is rotated relative to the inertial frame, changing the direction of the momentum transfer. As a result, the wave packet's relative velocities during the intervals $[t_1, t_2]$, $[t_2, t_3]$, $[t_3, t_4]$, and $[t_4, \infty]$ are, to first order in $\Omega_\oplus$,

$$v_{12} = 2nv_r(0, 0, 1), \qquad v_{23} = 2nv_r(\Omega_\oplus T\cos\vartheta, 0, 0),$$
$$v_{34} = 2nv_r(\Omega_\oplus(2T + T')\cos\vartheta, 0, -1), \qquad v_{4\infty} = 0, \tag{1}$$

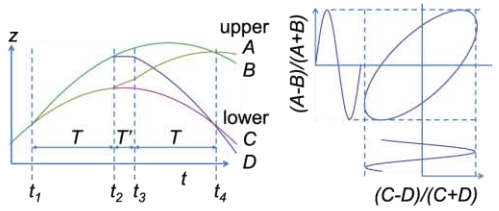

FIG. 1 (color online). Simultaneous conjugate Ramsey-Bordé interferometers. Left: atomic trajectories. Beam splitters ($\pi/2$ pulses) split and recombine the wave packets. Right: plotting the populations A through D at the outputs of the interferometers versus each other yields an ellipse whose shape is determined by $\Delta\phi^+ - \Delta\phi^- = 16n^2(\hbar k^2/2m)T$.

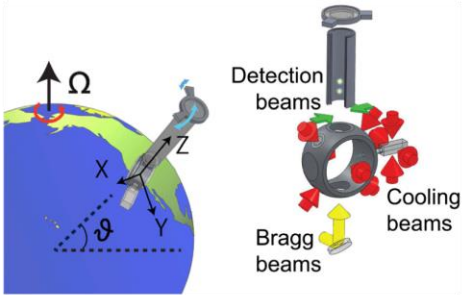

FIG. 2 (color online). Left: Location of the experiment relative to Earth's rotation. Right: Experimental setup. The wave packets in the interferometer are separated by up to 8.8 mm with $2n = 10$, $T = 250$ ms.

respectively, where $\Omega_\oplus$ is the angular frequency of Earth's rotation and $\vartheta = 37.87°$, the latitude of the laboratory in Berkeley, California. Thus, at t_4, the wave packets miss each other by

$$\vec{\delta} = 4n v_r \Omega_\oplus T(T + T') \cos\vartheta (1, 0, 0). \quad (2)$$

An estimate of the size of the atomic wave packets is provided by the thermal de Broglie wavelength $h/\sqrt{2\pi m k_B T}$, where k_B is the Boltzmann constant. For cesium atoms at a temperature T of 2 μK (typical of a moving molasses launch), this is about 100 nm. For typical parameters, e.g., $T = 100$ ms, $T' = 5$ ms, and $2n = 2$, we find $\delta = 13$ nm. Even though this will not lead to a substantial loss of contrast, it will still lead to systematic errors that we discuss below. For large momentum transfer beam splitters and longer pulse separation times, however, $\delta = 0.33$ μm (at $2n = 10$, $T = 250$ ms), giving rise to a significant contrast reduction. (Use of condensed atoms increases wave-packet size [17], but does not reduce the systematic effects arising from rotation.)

Our experiment is based on a 1.5 m tall fountain of cesium atoms in the $F = 3$, $m_F = 0$ quantum state, launched ballistically using a moving optical molasses. The launched atoms have a three-dimensional temperature of 1.2 μK, determined by a time-of-flight measurement. A Doppler-sensitive two-photon Raman process selects a group of atoms having a subrecoil velocity distribution along the vertical launching axis.

Because of the extreme sensitivity of interferometers with large momentum transfer and long pulse separation time, suppression of the sensitivity to vibrations is important. For this reason, we operate a pair of simultaneous conjugate Ramsey-Bordé interferometers [14], see Fig. 1. The direction of the recoil is reversed between them, reversing the sign of the gravity-induced term in their phases $\Delta\phi^{\pm}$. The influence of gravity and vibrations cancels out, and the signal can be extracted even when vibrations lead to zero visibility of the fringes for each interferometer. For beam splitting, we use multiphoton Bragg diffraction [10,18]: An atom absorbs a number n of photons from a first laser beam with wave vector $\vec{k}_1$ while being stimulated to emit the same number of photons having a wave vector $\vec{k}_2$ by a second, antiparallel, laser beam, without changing its internal quantum state. The process transfers a momentum $n\hbar(\vec{k}_1 - \vec{k}_2)$ to the atom and thus a kinetic energy of $n^2\hbar^2(\vec{k}_1 - \vec{k}_2)^2/(2m)$. Energy-momentum conservation selects one particular Bragg diffraction order n, depending on the laser's frequency difference ω_1–ω_2. We generate the two laser beams from a common 6 W titanium:sapphire laser and use acousto-optical modulators to shift the frequency of the laser [19] and optimize the efficiency of the Bragg diffraction beam splitter by adjusting Gaussian pulse width to about 100 μs [11,14]. The beam is collimated at a $1/e^2$ intensity radius of 3.6 mm and sent vertically upwards to a retroreflection mirror inside the vacuum chamber. The Doppler effect due to the free fall of the atoms singles out one pair of counter-propagating frequencies that satisfy the above resonance condition.

The retroreflection mirror is flexibly mounted on the top of the vacuum chamber with a bellows and can be rotated by piezoelectric actuators, see Fig. 2. The rotation axes are roughly pointing west (x') and south (y'), enclosing an angle of 82°. In order to rotate the mirror, a linear electrical ramp is applied to the piezoelectric actuators. The sensitivity of the actuators has been calibrated against an Applied Geomechanics 755-1129 tilt sensor. We can use this to give the momentum transfer $\vec{k}_1 - \vec{k}_2$ a constant direction as seen from the inertial frame, in spite of Earth's rotation, to compensate for the Coriolis force.

Figure 3 shows data obtained with and without Coriolis compensation. The increase in contrast is obvious. We fit the data with an ellipse [14] and determine the contrast by the length of the projection of the fitted ellipse onto the axes, separately for the upper and lower interferometer. For the remainder of the Letter, data are quoted for the upper interferometer. By grouping the data into bins of 20 points,

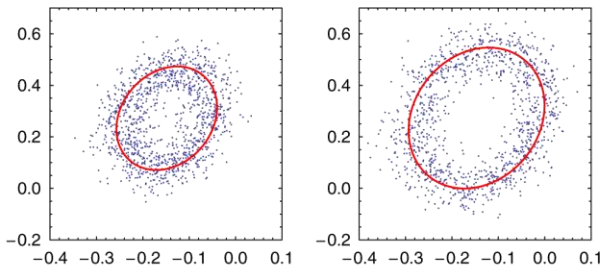

FIG. 3 (color online). Raw data obtained without Coriolis compensation (left) and with (right) at $T = 180$ ms, $T' = 2$ ms, and $10\hbar k$ momentum transfer. The axes are normalized population difference as shown in Fig. 1. The contrast of the upper interferometer are 20% and 27% for the left and right figure, respectively.

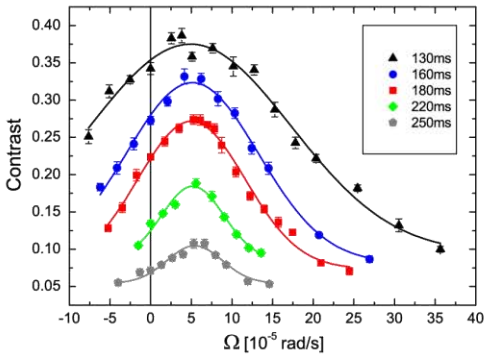

FIG. 4 (color online). Contrast versus tip-tilt mirror rotation rate for various pulse separation times ($T = 130$, 160, 180, 220, 250 ms; $T' = 2$ ms). The y'-axis rotation rate is varied, the x'-axis rotation rate is fixed at -26.2μ rad/s. The loss of contrast for larger T is mainly due to the thermal expansion of the atomic cloud and wave front distortion in the interferometer beam.

the contrast and its standard error is determined by statistics over the bins. Figure 4 shows the contrast as a function of the tip-tilt rotation rate around the y' axis for various pulse separation times. A Gaussian function of the rotation rate (with the center Ω_{opt}, width σ_Ω, amplitude and offset as fit parameters) fits the data within the standard error. The fit results are tabulated in Table I. A weighted average for the optimum tip-tilt rotation rate is $\Omega_{\text{opt}} = (51.3 \pm 0.8)\ \mu$rad/s. We also performed a similar measurement for the x' axis, Fig. 5 (left). From both measurements, we compute the magnitude of the rotation rate, $(58.5 \pm 1.0)\ \mu$rad/s (taking into account the actual angle of 82° between x' and y'). This agrees with $\Omega_\oplus \cos\theta = 57.4\ \mu$rad/s within a $\sim 1\sigma$ error.

To model this loss of contrast, we calculate the overlap integral $\langle\psi'(\vec{x})|\psi(\vec{x})\rangle$ of the interfering wave packets at $t = t_4$. Since the free time evolution of a wave packet is given by a unitary operator $U(t, t_0)$, the overlap integral of the wave packet $\langle\psi'(t)|\psi(t)\rangle = \langle\psi'(t_0)U^\dagger(t, t_0)|U(t, t_0)\psi(t_0)\rangle = \langle\psi'(t_0)|\psi(t_0)\rangle$ is independent of the free time evolution and depends on the relative position only. For example, the atom may initially be represented by a Gaussian wave packet

TABLE I. Ω_{opt} and σ_Ω are the fitting center and width from Fig. 4. σ is calculated from σ_Ω and Eq. (4).

T [ms]	Ω_{opt} [μrad/s]	σ_Ω [μrad/s]	σ [nm]
130	49 ± 4	124 ± 8	106 ± 7
160	51 ± 2	81 ± 4	105 ± 5
180	50 ± 2	66 ± 3	108 ± 5
220	52 ± 2	38 ± 5	92 ± 12
250	54 ± 2	34 ± 4	107 ± 13

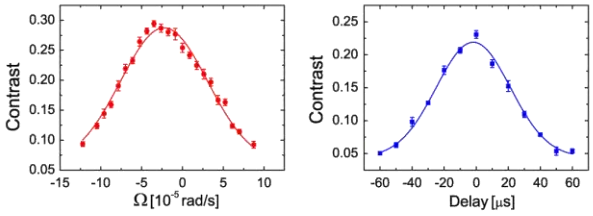

FIG. 5 (color online). Left: Contrast versus tip-tilt mirror rotation rate in x' direction ($T = 180$ ms, $T' = 2$ ms). The y'-axis rotation is fixed at 69.8μ rad/s. The Gaussian fit has its maximum at $(-22 \pm 1)\mu$ rad/s with a width of $53 \pm 4\mu$ rad/s, which leads to an estimate of $\sigma_y = (86 \pm 7)$ nm. Right: Contrast versus delay of t_4 in Fig. 1. The width of the fit is $(23.1 \pm 0.6)\ \mu$s.

$$\psi = \left(\frac{\det A}{\pi^3}\right)^{1/4} e^{-(1/2)\vec{x}A\vec{x}}, \tag{3}$$

where the matrix A can be taken as symmetric. In its principal frame, A is diagonal with elements σ_1^{-2}, σ_2^{-2}, and σ_3^{-2}. The overlap integral is independent of time,

$$\int d^3r\psi^*(\vec{r} + \vec{\delta})\psi(\vec{r}) = e^{-(1/4)\vec{\delta}A\vec{\delta}}, \tag{4}$$

where δ is given by Eq. (2). The experiment validates this model: Figs. 4 and 5, show that the data are well described by Gaussian functions. According to Table I, the measured widths of the overlap integral agree with one another for all measured T. From the data, we can determine the parameters of the overlap integral. The symmetry of the atomic fountain suggests that the principal axes of the matrix A coincide with the x, y, z laboratory frame. In what follows, we neglect the small difference of the x, x' and y, y' directions. The weighted average of the numbers in the last column of Table I is $\sigma_x = (105 \pm 3)$ nm. The fit shown in Fig. 5, left, yields $\sigma_y = (86 \pm 7)$ nm. To determine σ_z, we vary the time interval between t_3 and t_4 (Fig. 1), see Fig. 5, right. The fitted width corresponds to $\sigma_z = (813 \pm 21)$ nm.

Because each atom interferes only with itself, these measured quantities are properties of individual atoms, averaged over the atomic ensemble. They need not be related to the temperature of the ensemble. This is illustrated by the data: The expectation value of the squared momentum along the ith coordinate $\langle p_i^2\rangle$ of the wave packet Eq. (3) allows one to compute an expectation value $\langle\psi|p_i^2/2m|\psi\rangle = \hbar^2/(2m\sigma_i^2)$. If we set this equal to $k_B T_i/2$, where T_i has the dimension of temperature, we obtain $T_x = (0.33 \pm 0.02)\ \mu$K and $T_y = (0.49 \pm 0.07)\ \mu$K. Since our atomic ensemble is not a Bose-Einstein condensate, these values are unrelated to (specifically, lower than) the 1.2 μK ensemble temperature. For T_z, we obtain (5.5 ± 0.3) nK. This low value results from the velocity selection in our atomic fountain: The Fourier

width of the $1/\sqrt{e}$ pulse duration σ_{vs} of the Gaussian velocity selection pulse corresponds to a Doppler velocity width of $c/(\omega\sigma_{vs})$ and, per $\Delta x\Delta p = \hbar/2$ (the minimum uncertainty product applies to Gaussian wave packets), a position envelope function having a $1/\sqrt{e}$ width of $v_r\sigma_{vs}/2$, where $v_r = \hbar k/m$. For $\sigma_{vs} = 500\ \mu$s, this evaluates to 880 nm, in reasonable agreement with the observed value.

Uncompensated rotation also causes systematic effects [2]. For a Mach-Zehnder interferometer, e.g., the resulting phase shift is given by $\Delta\phi = 2\vec{\Omega}_\oplus \cdot (\vec{v}_0 \times \vec{k})T^2$, where $\vec{v}_0$ is the atom's initial velocity. If the interferometer is used for gravity measurements, the corresponding gravity offset is $\Delta g = 2\vec{\Omega}_\oplus \cdot (\vec{v}_0 \times \hat{k})$, where $\hat{k}$ is a unit vector pointing along the laser beams. This is zero when the launch has no horizontal velocity component, but in practice a small horizontal component is inevitable due to alignment error. If, e.g., we assume a horizontal velocity of 1 cm/s typical of a laser-cooled atomic fountain, $\Delta g = 6 \times 10^{-8} g$ due to Earth's rotation, a dominant contribution to the accuracy of atom interferometers [2]. Coriolis compensation as employed here can remove it without a need to know $\vec{v}_0$. The accuracy from our rotation measurement, $\Delta\Omega/\Omega \sim 0.017$, would reduce Δg to $1 \times 10^{-9} g$ and, thus, below the precision of state-of-the-art instruments. A tip-tilt mirror using actuators with active feedback could easily increase this accuracy further, and maximizing the contrast provides an independent verification of successful compensation. Possible remaining imperfections of the overlap of the wave packets are due to the vibration of the retroreflection mirror and the gravity gradient. We note that Coriolis compensation removes the leading order effect of Earth's rotation but higher order effects remain [15]. However, they are negligible here.

We have used a tip-tilt mirror to compensate the influence of Earth's rotation in atom interferometry, and also to characterize the overlap integral of the interfering atomic wave packets. The observations are well described by Gaussian wave packets, whose properties were determined from the data. Coriolis compensation allows us to reach better contrast, larger space-time enclosed area, and reduce systematic effects in atom interferometry. For example, from the measured width of the overlap integral (Table I) together with the displacement Eq. (2), an uncompensated Coriolis force would reduce the contrast by a factor of $\exp[-(\Omega_\oplus \cos\vartheta)^2/(2\sigma^2)] = 0.28$, for $2n = 10$ and $T = 250$ ms. At $T = 130$ ms, we reach a contrast of 40%. Coriolis compensation is, thus, crucial for the most sensitive large-area, large momentum transfer atom interferometers. We also note that Coriolis compensation has allowed us to experimentally demonstrate the atom interferometer with the largest enclosed space-time area thus far: The gravitationally induced phase $2nkgT(T + T')$ in our interferometer is 6.3×10^7 rad ($2n = 10$ and $T = 250$ ms), compared to 3.2×10^7 rad in Ref. [9]. (Other work [20] has reached higher momentum transfer but substantially smaller T and thus lower overall phase shift.) The recoil-induced phase $16n^2(\hbar k^2/2m)T$ between our simultaneous conjugate interferometers is 1.2×10^6 rad, compared to 5×10^5 rad in Ref. [14] or 2×10^6 rad in Ref. [6]. Such a measurement can be used to determine the fundamental constants $\hbar/m$ and α, the fine structure constant. Our data allow a resolution in $\hbar/m$ of 12 ppb within 42 minutes (10 ppb$\sqrt{\text{hr}}$), twice as good as in Ref. [14]. We expect that Coriolis compensation will enhance future high-performance interferometers, e.g., in gravity wave detection [21], measurements of $\hbar/m$, α [6], Avogadro constant N_A, new tests of general relativity [22], and inertial sensing, with applications in navigation and geophysics. The technique will be especially important for achieving high performance in mobile and space-borne atom interferometers [23,24], which must cope with rotation rates that are orders of magnitude larger than Earth's rotation.

We thank Justin Brown, Paul Hamilton, Michael Hohensee, Gee-Na Kim, and Achim Peters for discussions, and the Alfred P. Sloan Foundation, the David and Lucile Packard Foundation, the National Aeronautics and Space Administration, the National Institute of Standards and Technology, and the National Science Foundation for support.

*sylan@berkeley.edu

[1] A. D. Cronin, J. Schmiedmayer, and D. E. Pritchard, Rev. Mod. Phys. **81**, 1051 (2009).
[2] A. Peters, K.-Y. Chung, and S. Chu, Nature (London) **400**, 849 (1999); Metrologia **38**, 25 (2001).
[3] M. J. Snadden *et al.*, Phys. Rev. Lett. **81**, 971 (1998).
[4] T. L. Gustavson, P. Bouyer, and M. A. Kasevich, Phys. Rev. Lett. **78**, 2046 (1997); J. K. Stockton, K. Takase, and M. A. Kasevich, Phys. Rev. Lett. **107**, 133001 (2011); B. Canuel *et al.*, Phys. Rev. Lett. **97**, 010402 (2006).
[5] J. B. Fixler *et al.*, Science **315**, 74 (2007); G. Lamporesi *et al.*, Phys. Rev. Lett. **100**, 050801 (2008).
[6] R. Bouchendira *et al.*, Phys. Rev. Lett. **106**, 080801 (2011).
[7] H. Müller, A. Peters, and S. Chu, Nature (London) **463**, 926 (2010).
[8] M. A. Hohensee, S. Chu, A. Peters, and H. Müller, Phys. Rev. Lett. **106**, 151102 (2011).
[9] H. Müller *et al.*, Phys. Rev. Lett. **100**, 031101 (2008); K.-Y. Chung *et al.*, Phys. Rev. D **80**, 016002 (2009).
[10] H. Müller *et al.*, Phys. Rev. Lett. **100**, 180405 (2008).
[11] H. Müller, S.-w. Chiow, S. Herrmann, and S. Chu, Phys. Rev. Lett. **102**, 240403 (2009).
[12] P. Cladé *et al.*, Phys. Rev. Lett. **102**, 240402 (2009).
[13] J. M. McGuirk *et al.*, Phys. Rev. A **65**, 033608 (2002).

[14] S.-w. Chiow, S. Herrmann, S. Chu, and H. Müller, Phys. Rev. Lett. **103**, 050402 (2009).
[15] J. M. Hogan, D. M. S. Johnson, and M. A. Kasevich, in *Proceedings of the International School of Physics Enrico Fermi Course CLXVIII on Atom Optics and Space Physics*, edited by E. Arimondo, W. Ertmer, W. P. Schleich, and E. M. Rasel (IOS Press, Oxford, 2007), p. 411.
[16] A. Louchet-Chauvet *et al.*, New J. Phys. **13**, 065025 (2011).
[17] J. E. Debs *et al.*, Phys. Rev. A **84**, 033610 (2011).
[18] H. Müller, S.-w. Chiow, and S. Chu, Phys. Rev. A **77**, 023609 (2008).
[19] S.-w. Chiow *et al.*, Opt. Express **17**, 5246 (2009).
[20] S.-w. Chiow, T. Kovachy, H.-C. Chien, and M. A. Kasevich, Phys. Rev. Lett. **107**, 130403 (2011).
[21] S. Dimopoulos *et al.*, Phys. Rev. D **78**, 122002 (2008); M. A. Hohensee *et al.*, Gen. Relativ. Gravit. **43**, 1905 (2010).
[22] S. Dimopoulos, P. W. Graham, J. M. Hogan, and M. A. Kasevich, Phys. Rev. D **78**, 042003 (2008).
[23] J. M. Hogan *et al.*, Gen. Relativ. Gravit. **43**, 1953 (2011).
[24] W. Ertmer *et al.*, Exp. Astron. **23**, 611 (2008); R. Geiger *et al.*, Nature Commun. **2**, 474 (2011).

REVIEWS OF MODERN PHYSICS, VOLUME 84, JANUARY–MARCH 2012

Colloquium: Quantum interference of clusters and molecules

Klaus Hornberger

University of Duisburg-Essen, Faculty of Physics, Lotharstraße 1-21, 47048 Duisburg, Germany

Stefan Gerlich, Philipp Haslinger, Stefan Nimmrichter, and Markus Arndt

University of Vienna, Vienna Center for Quantum Science and Technology VCQ, Faculty of Physics, Boltzmanngasse 5, A-1090 Vienna, Austria

(published 8 February 2012)

Recent progress and future prospects of matter-wave interferometry with complex organic molecules and inorganic clusters are reviewed. Three variants of a near-field interference effect, based on diffraction by material nanostructures, at optical phase gratings, and at ionizing laser fields are considered. The theoretical concepts underlying these experiments and the experimental challenges are discussed. This includes optimizing interferometer designs as well as understanding the role of decoherence. The high sensitivity of matter-wave interference experiments to external perturbations is demonstrated to be useful for accurately measuring internal properties of delocalized nanoparticles. The prospects for probing the quantum superposition principle are investigated in the limit of high particle mass and complexity.

DOI: 10.1103/RevModPhys.84.157 PACS numbers: 03.75.Dg

CONTENTS

I. INTRODUCTION

The wave nature of matter, most conspicuously revealed in interference studies such as the double slit experiment, is a paradigm of quantum mechanics. According to Richard Feynman, it even ''contains the only mystery'' of quantum physics (Feynman, Leighton, and Sands, 1965). And indeed, the spatial delocalization of objects composed of hundreds of atoms, over extensions that exceed the particle size by orders of magnitude, clearly defies our common intuition. In spite of that, such highly nonclassical states have been created repeatedly in the laboratory and are used for fundamental science.

Recent matter-wave experiments with nanometer-sized particles have opened a new field of research at the interface between the foundations of physics, quantum optics, and physical chemistry. Here we mainly focus on near-field interference experiments, since they exhibit a number of advantages over the conceptually simpler far-field arrangements, if one is interested in massive and internally complex particles. An overview of earlier experiments with more elementary particles can be obtained from the comprehensive reviews on interference with electrons (Tonomura, 1987; Batelaan, 2007; Hasselbach, 2010), neutrons (Rauch and Werner, 2000), and atoms (Berman, 1997; Cronin, Schmiedmayer, and Pritchard, 2009).

There are two main motivations for probing the wave nature of complex particles. First, we explain how it can be exploited to study the internal properties and dynamics of quantum delocalized particles. Quantum-assisted molecule metrology is now becoming a viable tool for molecular physics with prospects to outperform classical measurements in the near future. Second, nanoparticle interference is well suited for studying the quantum superposition principle in a mass regime that has not been accessible hitherto. We show how recent studies can quantitatively validate the predictions made by decoherence theory, and we argue that matter-wave experiments will set bounds to theories predicting a modification of the Schrödinger equation at the quantum-classical borderline.

We start in Sec. II by discussing the general requirements for de Broglie wave interferometry and the advantages of near-field experiments. Section III describes three recent near-field interferometer developments, their merits, and drawbacks. The highly nonclassical states in these instruments enabled studies of environmental decoherence, which are reviewed in Sec. IV. While some types of interactions with the environment induce the emergence of classical behavior, others can be exploited to measure internal molecular properties, as explained in Sec. V.

In Sec. VI we present some challenges encountered in the attempt to extend matter-wave interferometry to ever more complex objects. This includes requirements for molecular beam sources, detection schemes, and ways to cope with phase averaging. A quantitative theoretical approach to describe all of these experiments is briefly introduced in Sec. VII. To date, there has been no experimental indication that the quantum superposition principle may fail at any mass or length scale. However, as discussed in Sec. VIII, a number of modifications of the Schrödinger equation have been suggested, and, in particular, the model of continuous spontaneous localization may be the first alternative that can be put to a definitive test in matter-wave experiments with very massive clusters. We close in Sec. IX with our conclusions and an outlook.

II. FROM FAR-FIELD TO NEAR-FIELD INTERFEROMETRY

From a conceptual point of view, far-field diffraction is by far the simplest and most palpable matter-wave phenomenon: When a collimated and sufficiently slow particle beam impinges on a mask perforated by equidistant slits the particle density farther downstream exhibits a fringe pattern, whose period is determined by the ratio λ_{dB}/d of the de Broglie wavelength λ_{dB} and the slit separation d. Such experiments have been implemented with electrons (Jönsson, 1961), neutrons (Zeilinger *et al.*, 1988), and atoms (Keith *et al.*, 1988; Carnal, Faulstich, and Mlynek, 1991; Shimizu, Shimizu, and Takuma, 1992). More recently, also beams composed of cold helium clusters (Schöllkopf and Toennies, 1994; Brühl *et al.*, 2004), and hot fullerenes (Arndt *et al.*, 1999) have shown such far-field interference patterns, in complete agreement with quantum expectations, including the subtle but significant role of van der Waals forces between the molecules and the material grating structures.

A number of alternative interferometer concepts have been studied also with diatomic molecules: This includes Mach-Zehnder interferometry with Na_2, using three nanofabricated gratings (Chapman, Hammond *et al.*, 1995), Ramsey-Bordé interference experiments, exploiting the near-resonant interaction with four running laser waves, with I_2 (Bordé *et al.*, 1994) and K_2 (Lisdat *et al.*, 2000), and the observation of the Poisson spot behind a circular obstacle with D_2 (Reisinger *et al.*, 2009). The scattering of fast H_2, as first studied by Estermann and Stern (1930), has recently been extended to quantum reflection studies with He_2 by Zhao, Meijer, and Schöllkopf (2011).

Most of these experiments operate in the far field, thus requiring a collimation of the molecular beam that is significantly narrower than the diffraction angle. This condition is the reason why it is difficult to extend these far-field schemes to objects composed of, say, several hundred thousand atoms: Their requirements with regard to source brilliance and coherence, interferometer size and stability, as well as detection efficiency still necessitate the development of new experimental methods for controlling nanoparticles.

In contrast, near-field phenomena, such as the Talbot-Lau effect, allow one to operate with particle beams of modest coherence, without the need for a spatially resolving particle detector, and one can draw on favorable length and mass scaling properties. In order to show this, we start by introducing some elementary coherence considerations and the basic idea behind Talbot interference.

A. Coherence considerations

In the absence of external forces, the stationary Schrödinger equation of quantum mechanics is formally equivalent to the Helmholtz equation that governs the propagation of light. This explains why many phenomena from classical wave optics, such as diffraction and interference, find a close analogy in nonrelativistic quantum mechanics. Indeed, Huygens' principle of elementary wavelets and the Kirchhoff-Fresnel integral formula are closely related to a Feynman path integral formulation of the dynamics of matter waves (Storey and Cohen-Tannoudji, 1994).

Both in classical optics and in quantum mechanics the ability to observe wave phenomena relies on the preparation of sufficient spatial and temporal coherence, i.e., of stable correlations between separate space-time points of the complex wave field. They should be appreciable over a significant portion of the diffracting element, e.g., over at least two slits of a diffraction grating.

Most matter-wave experiments are operated with a particle beam propagating in a well-defined longitudinal direction. In many cases it is then justified to decouple the forward direction from the transverse state of motion. If we assume an initially incoherent particle source, its spatial (transverse) coherence depends on the effective width a of the source aperture. According to the *van Cittert–Zernike theorem* the spatial coherence behind an incoherent source is described by the same functional form that also quantifies the intensity pattern due to diffraction behind the same aperture under coherent plane wave illumination (Born and Wolf, 1993). The coherence width at a distance L behind the intrinsically incoherent particle source can therefore be estimated as $2L\lambda_{\mathrm{dB}}/a$. This illustrates that for massive particles with small de Broglie wavelengths λ_{dB} we will need either a narrow source opening a or a long propagation distance L to prepare the required spatial coherence.

Similarly, the *Wiener-Khinchin theorem* describes the longitudinal coherence function as the Fourier transform of the beam spectral density (Born and Wolf, 1993). A narrow distribution of de Broglie wavelengths, i.e., a good momentum selection, is therefore required if we want to prepare longitudinally extended matter-wave coherence. This is a source property that cannot be improved by increasing the distance between the source and the grating.

B. Entering the near field

Many textbooks on classical optics restrict themselves to far-field interference patterns described by the Fourier transform of the diffraction mask. Also the first diffraction experiments with C_{60} fullerenes were performed in this regime: an effusive molecular beam with a velocity of about 100 m/s was sent onto a nanomechanical grating with a slit separation of 100 nm (Arndt *et al.*, 1999). Given the de Broglie wavelength of 5 pm, sufficient transverse coherence could be prepared only by reducing the effective source width to smaller than 10 μm. Since the first order interference fringes were separated by only 50 μm at a distance of 1 m behind the grating, a second 10 μm slit was placed immediately in front of the grating to collimate the beam width to smaller than the diffraction angle. This concept clearly worked, but at the expense of reducing the detected particle flux by many orders of magnitude. Experiments with more massive species must cope with even smaller de Broglie wavelengths and even stricter coherence requirements. Several strategies are conceivable to fulfill them.

Novel source methods may serve to improve the coherence and to increase λ_{dB}. However, slowing of the particle beam alone does not solve the problem, since it reduces only the forward velocity and therefore increases the beam divergence by the same factor. Genuine cooling would reduce the mean velocity, the velocity spread in all directions, and eventually also the number of internal excitations. But cooling schemes for interferometry with massive particles are still in an early development stage (see Sec. VI). Improved detectors with true single-particle sensitivity may allow one to compensate for the small fluxes associated with a tight collimation. We focus here on a third aspect, the implementations of novel near-field interferometer schemes which relax the coherence requirements and at the same time parallelize the diffraction effect thousandfold.

Coherent diffraction at an arbitrary aperture is generally described by the Kirchhoff-Fresnel integral (Born and Wolf, 1993). It can be viewed as a decomposition of the diffraction pattern into spherical waves emanating from all points in the aperture surface. Each contributes a phase $2\pi R/\lambda_{\mathrm{dB}}$ with R the distance between an aperture point and an image point on a screen. The paraxial approximation holds if the latter is located at a distance L large compared to the extension of the aperture. The contributing phases can then be expanded to second order in the lateral coordinates of aperture and screen, $\phi = \pi(x_a - x_s)^2/\lambda_{\mathrm{dB}}L$.

One can further distinguish between far-field and near-field interference based on the importance of the propagating wave front curvature in ϕ (Born and Wolf, 1993; Berman and Malinovsky, 2010). In the Fraunhofer, or far-field approximation, the quadratic terms x_a^2 and x_s^2 may be neglected in ϕ, while they are required for Fresnel, or near-field diffraction. Figure 1 shows the transition from the near-field to first features of the far-field regime for diffraction at a grating of ten slits. The proper far-field limit is then reached at the characteristic distance $a^2/\lambda_{\mathrm{dB}}$, where the wave pattern is already expanded to well beyond the size of the aperture a, so that spherical waves can already be locally approximated as plane waves.

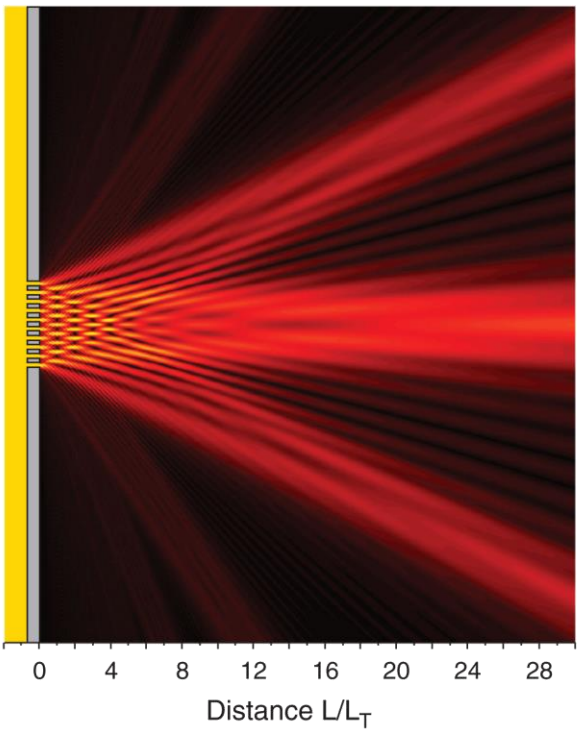

FIG. 1 (color). Transition from near-field to far-field interference for a plane wave illuminating a grating with ten equidistant slits from the left. The brightness is scaled to be proportional to the wave amplitude. In the near field, at integer multiples of the Talbot length $L/L_{\mathrm{T}} = 1$, 2, and 3, one observes partial recurrences of the intensity distribution in the slits, while at greater distances the main diffraction orders of far-field interference start to emerge. The calculation is done in the paraxial approximation, assuming ideal gratings with a slit width of one-half the slit separation. Note that the axes are not to scale.

Our near-field interferometers are based on the principle of *coherent lenseless self-imaging*. This concept was first developed for light optics (Talbot, 1836) and it is nowadays often employed in situations where refractive optical elements are unavailable, such as with molecules (Brezger *et al.*, 2002) or x rays (Pfeiffer *et al.*, 2006).

The effect, which can already be recognized in the near-field region of Fig. 1, is illustrated in its idealized form in Fig. 2: When a monochromatic plane wave illuminates a wide grating of period d, interference of all diffraction orders will reproduce a self-image of the intensity distribution in the mask, at the distance

$$L_{\mathrm{T}} = d^2/\lambda_{\mathrm{dB}} \tag{1}$$

further downstream. The Talbot length L_{T} is named after Henry Fox Talbot who discovered the effect with light (Talbot, 1836). Self-imaging recurs at integer multiples of L_{T} up to the point where diffraction at the edges of the grating window becomes relevant. At odd multiples of L_{T} the grating image is shifted by half a fringe period, while it appears

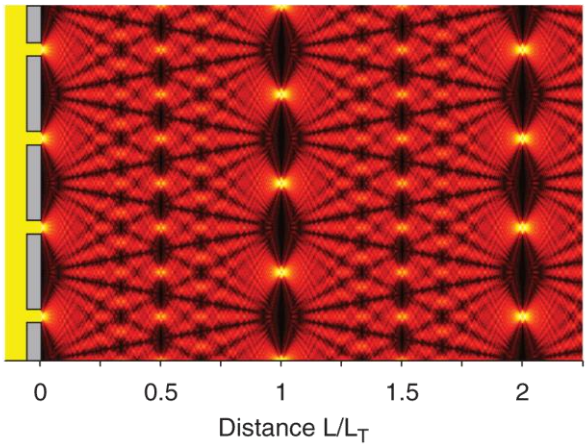

FIG. 2 (color). Detail of a Talbot carpet in the near-field region of an extended grating generated by a plane wave from the left. As in Fig. 1 bright colors indicate large wave amplitudes. At integer multiples of the Talbot length L_T it displays an exact image of the intensity distribution in the grating (shifted by one-half a grating period for odd multiples). To highlight the fractional recurrences at rational multiples of L/L_T the calculation was done (in the paraxial approximation) with a small slit width of 15% of the grating period. The Talbot-Lau interferometers described below are based on the same resonant interference effect which gives rise to these structures.

unshifted at even multiples; some therefore prefer to define $2d^2/\lambda_{dB}$ as the Talbot length. Figure 2 also reveals fractional revivals with smaller periods in distances which are rational fractions of L_T. The observed intensity distribution is an example of wave physics and clearly incompatible with the assumption of ray optics (Berry, Marzoli, and Schleich, 2001; Case *et al.*, 2009).

C. Concept of Talbot-Lau interferometry (TLI)

The implementation of the Talbot effect still requires a high degree of coherence and has so far been observed with atoms (Chapman, Ekstrom *et al.*, 1995; Nowak *et al.*, 1997) and electrons (McMorran and Cronin, 2009) but not yet with molecules. We can extend this concept to spatially incoherent sources by adding a second grating of the same period. This leads to the configuration of array illuminators which was proposed by Lau (1948) and is nowadays widely used in light optics (Patorski, 1989).

The intuitive picture behind this scheme is the following: The first grating G_1 acts as a periodic spatial mask which prepares transverse coherence by slicing the incident wave field into numerous wavelets. There is no phase coherence between the waves emerging from neighboring slits. However, each of the individual wavelets emanating from any of the slits of G_1 develops sufficient transverse coherence on its way toward the second grating G_2 to cover two or more slits with a well-defined phase relation. This requires G_2 to be at a distance comparable to L_T away from G_1. Diffraction at the second grating followed by the free evolution over the Talbot distance then leads to the formation of a spatially periodic intensity pattern whose period equals that of the two gratings. This way, each slit in G_1 gives rise to a fringe pattern at the detection screen. All interferograms associated with the individual source slits are synchronized in their phase position such that they add up to a high-contrast density pattern. A formal treatment shows that the fringe visibility may actually have a minimum when the grating distance exactly matches the Talbot length (Dubetsky and Berman, 1997a; Nimmrichter and Hornberger, 2008), but it reaches a maximum in the close vicinity of L_T.

A direct way to visualize the final molecular density pattern is to capture and image the molecules on a clean surface (Juffmann *et al.*, 2009). Alternatively, one can scan the interferogram with a third grating G_3 of the same period (Brezger *et al.*, 2002). In this case the spatial resolution is provided by the grating, so that the integration over a large area leads to a significant gain in signal and a reduction of the measurement time. This is of a particular advantage for sources with a small flux and limited coherence. It also provides a fast signal readout which is often required for feedback and alignment purposes.

In Talbot-Lau interferometry the required grating period $d = \sqrt{\lambda_{dB} L} \propto m^{-1/2}$ is determined by the de Broglie wavelength and the size of the interferometer L, independently of the molecular beam width D. This scaling is much less demanding than that of far-field diffraction $d \leq L\lambda_{dB}/D \propto m^{-1}D^{-1}$. In comparison to single-grating far-field diffraction, Talbot-Lau interferometry with three masks imposes more stringent alignment requirements since both the rotation and the longitudinal position of the gratings are important. On the other hand, the arrangement of thousands of parallel slits increases the signal by several orders of magnitude over far-field experiments.

III. NEAR-FIELD INTERFERENCE WITH NANOPARTICLES

Both the short de Broglie wavelength and the limited coherence of available molecular beam sources are the reasons why interferometry with large molecules started off with only the advent of near-field interferometers. The concept was first demonstrated for potassium atoms by Clauser and Li (1994) and it was further explored in a number of theoretical papers (Clauser, 1997; Dubetsky and Berman, 1997b; Rohwedder, 1999). Macromolecule interferometry was then realized in the following steps.

A. Talbot-Lau interferometry

The first fullerene interferometer was implemented in a Talbot-Lau (TL) configuration with three microfabricated gold gratings, as illustrated in Fig. 3(a). The microstructures were written with a period of 991 nm and an open slit width of about 470 nm into 16 mm wide and 500 nm thin gold membranes. Three identical gratings were adjusted with a separation of 22 cm (Brezger *et al.*, 2002).

In the experiment care was taken to align all grating slits with an accuracy of about 1 mrad with respect to each other and to the Earth's gravitational field. The interferometer was placed in a high-vacuum chamber evacuated to better than

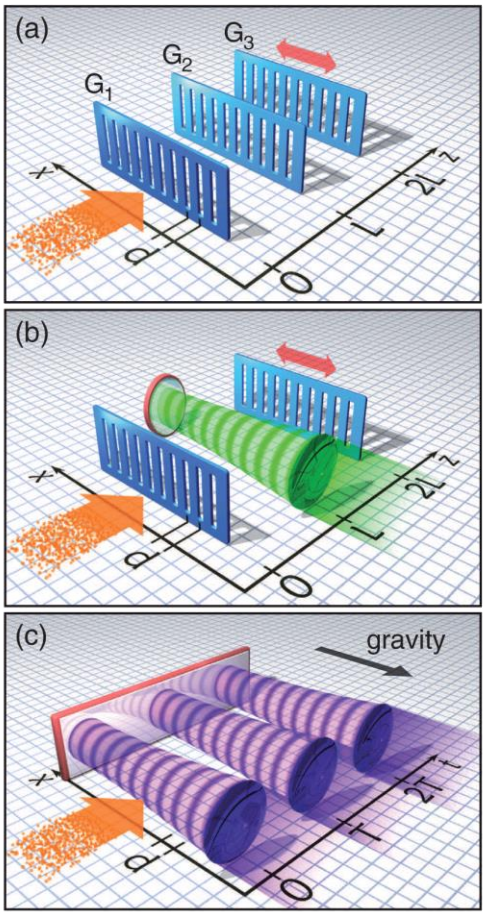

FIG. 3 (color). Near-field interferometers are optimized for beams of low flux and limited coherence: (a) The Talbot-Lau interferometer (TLI) uses three nanofabricated gratings. G_1 prepares the required spatial coherence, G_2 diffracts the wavelets so that they will form an interferogram, and G_3 is scanned to sample the fringe pattern (Clauser and Li, 1994; Brezger *et al.*, 2002). (b) The Kapitza-Dirac-Talbot-Lau interferometer (KDTLI) eliminates the dispersive van der Waals interactions between the molecules and the grating walls inside the TLI, since the central diffraction element is realized as an off-resonant standing light wave (Gerlich *et al.*, 2007). (c) An optical time-domain ionizing matter (OTIMA) interferometer, which has yet to be realized, consists of three ultraviolet laser beams. Single-photon ionization in the antinodes of the standing wave removes clusters from the incident particle cloud, acting similarly as the massive bars of a material grating. Operated in the time domain and using short and precisely timed laser pulses, the OTIMA concept avoids many phase averaging effects. From Nimmrichter, Haslinger *et al.*, 2011.

10^{-7} mbar and isolated from floor vibrations by an inflated optical table. A sublimation source emitted a thermal beam of molecules, with an internal and motional temperature of up to 900 K, in the case of C_{60} and C_{70} fullerenes. The thermal distribution contained a broad range of initial velocities. A velocity band of $\Delta v/v \simeq 20\%$ was filtered out by selecting the molecular free-fall parabola. In this interferometer arrangement, high-contrast interference could be observed both

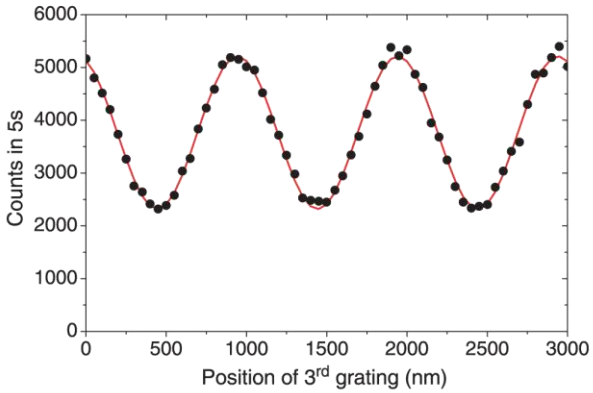

FIG. 4 (color online). Talbot-Lau interference of C_{70} as seen in experiments by Brezger *et al.* (2002). The data set is well reproduced by a sinusoidal curve with a fringe visibility of 38%.

for the fullerenes by Brezger *et al.* (2002) and for the biodye tetraphenylporphyrin (TPP) by Hackermüller *et al.* (2003). In Fig. 4 we show an interferogram of C_{70} displaying high contrast and a good signal-to-noise ratio. As in light optics, we define the fringe visibility of a sine wave pattern as the ratio of its amplitude over its offset.

In contrast to far-field diffraction, which is an unambiguous wave phenomenon without any ray optics analog, the appearance of molecular density fringes in a two-grating experiment might also be explained by a classical moiré shadow, to a certain degree. Fortunately, quantum diffraction and moiré effects can be well distinguished by studying the fringe visibility as a function of the particle velocity, as done in Fig. 5. If molecules were classical particles traveling along straight trajectories, their velocity would not influence the moiré visibility. They should, therefore, all exhibit a visibility of only 4% in our settings. In contrast to that, the de Broglie wavelength of a quantum object is inversely proportional to its velocity and we expect a periodic recurrence of the fringe visibility with the velocity.

Interestingly, this idealized quantum wave picture (dotted line in Fig. 5) does not reproduce the fullerene interference experiment at all (black circles), since it ignores the van der Waals interaction of the polarizable molecule with the grating walls. Although the effect of grating interactions was already observed in far-field diffraction at thin SiN masks (Grisenti *et al.*, 1999; Nairz, Arndt, and Zeilinger, 2003), it becomes much more dominant in near-field interference, as discussed in Sec. VII.

The C_{70} experiment can be better described by a quantum model that includes the van der Waals attraction as in Fig. 5. The solid line assumes the nonretarded van der Waals potential $V = -C_3/r^3$, with $C_3 = 10$ meV nm^3 (Jacob, 2011), and the dashed line the asymptotic long-distance form of the Casimir-Polder potential $V = -3\hbar c\alpha_{\rm stat}/32\pi^2\varepsilon_0 r^4$, with the static polarizability $\alpha_{\rm stat}/4\pi\varepsilon_0 = 102 \times 10^{-30}$ m^3 for C_{70} (Compagnon *et al.*, 2001). The exact potential according to Casimir and Polder (1948) leads to a curve close to that of the nonretarded form in the present case. An explanation of the remaining discrepancy between experiment and theory requires future experiments with gratings of

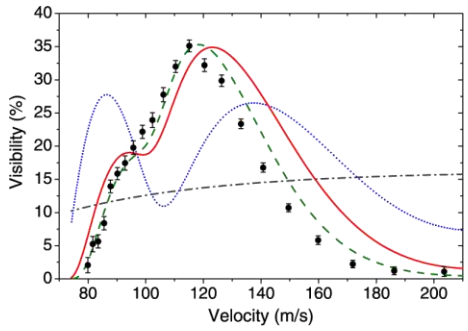

FIG. 5 (color online). Interference in the Talbot-Lau configuration leads to near-sinusoidal fringes when the open fraction is approximately 48%. The qualitative and quantitative dependence of the fringe visibility of the molecular velocity is important for discriminating the quantum wave behavior from classical moiré patterns (Brezger *et al.*, 2002). Full circles: experimental data with statistical error bars; dotted line: quantum wave model, ignoring the molecular polarizability; solid line: quantum wave model including the attractive van der Waals interaction between the polarizable C_{70} molecule and the gold grating wall; dashed line: replacing the van der Waals attraction by the asymptotic form of the Casimir-Polder interaction; dash-dotted line: classical shadow contrast in the presence of van der Waals forces. All theoretical curves include an average over the measured velocity distribution in the beam.

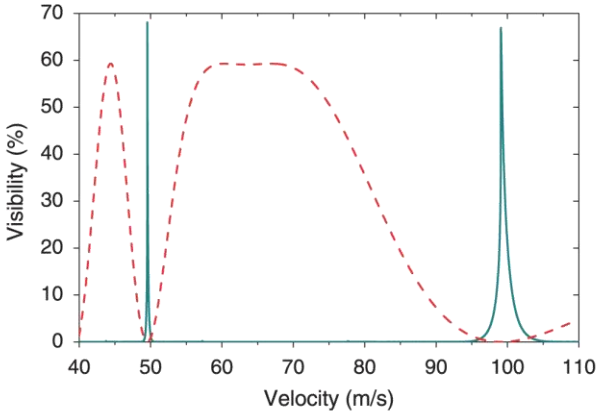

FIG. 6 (color online). Interference fringe visibility vs molecular velocity for molecules of high polarizability. Dashed line: KDTLI prediction for the perfluoralkylated nanosphere PFNS8 with a polarizability of $\alpha_{\rm opt}/4\pi\varepsilon_0 = 2\times10^{-28}$ m^3; solid line: TLI prediction for the same experimental arrangement, except for the laser grating being replaced by a 200-nm-thick SiN wafer with a grating period of 266 and 90 nm open slits. Even though the use of mechanical gratings may allow one to achieve a high interference contrast at a few selected velocities, real-world sources have a finite velocity spread and the effective visibility in a TL interferometer can be dramatically reduced when the velocity spread exceeds 1%. From Gerlich *et al.*, 2007.

variable thickness and different materials, as well as better velocity selection. We note that also the classical treatment must include the attractive force in the grating slit. The expected visibility then follows a monotonic curve in the same diagram (dash-dotted line in Fig. 5), but never exceeds 16% in our setting. This is clearly different from both the quantum description and the experimental observation.

The polarizability of a mesoscopic particle is roughly proportional to its volume. Therefore Casimir-Polder forces have an even more significant effect on larger particles. This explains why in a Talbot-Lau interferometer with material gratings quantum interference may be difficult to observe for more massive particles, unless we are able either to prepare a sufficiently intense molecular beam with a narrow velocity spread below 1% or to fabricate an atomically thin diffraction mask, for instance, from graphene (Geim and Novoselov, 2007).

B. Kapitza-Dirac-Talbot-Lau interferometry (KDTLI)

The problem of van der Waals forces can be eliminated by another interferometer scheme: Following the demonstration of an optical phase grating for fullerenes by Nairz *et al.* (2001) a new interferometer was proposed by Brezger, Arndt, and Zeilinger (2003) and implemented by Gerlich *et al.* (2007). This KDTLI combines the idea of TL near-field parallelization with the concept of matter diffraction at a standing light wave as originally proposed by Kapitza and Dirac (1933) for electrons and first realized with atoms by Moskowitz *et al.* (1983) in the Bragg regime.

The KDTLI evolves from a TLI if we replace the central diffraction grating G_2 by a standing laser light wave with the same grating period; see Fig. 3. We still keep the mechanical masks G_1 and G_3 for coherence preparation and interference imaging. The van der Waals phases at these stages do not perturb the final pattern since G_1 and G_3 act only as spatially periodic transmission filters (each thinning out the beam by about two-thirds).

The new optical phase grating G_2 does not remove any particles from the beam. Instead, the electric laser field E interacts with the molecular optical polarizability $\alpha_{\rm opt}$ to induce a rapidly oscillating electric dipole moment which interacts again with the laser field. In a standing light wave, the resulting dipole potential $W = -\alpha_{\rm opt}E(x,t)^2/2$ is spatially modulated, and so is the imprinted molecular phase. Given that its period is the same as that of G_1, the free evolution of the de Broglie waves behind the grating then results in an observable molecular fringe pattern with the same periodicity. As illustrated by Fig. 6, the elimination of the molecule wall interaction at G_2 significantly reduces the monochromaticity requirement on the incident matter waves.

In our experiment the optical phase grating is realized by retroreflecting a 532 nm laser of up to 18 W at a flat mirror. Since the incident molecular beam has a divergence of about 1 mrad, it is important to orient the standing light wave such that no semiclassical molecular trajectory crosses more than a single node or antinode of the green light field. In order to meet this condition the laser is focused along the molecular beam axis to a narrow waist of $w = 20$ μm. The period of the mechanical masks G_1 and G_3 was also carefully matched to that of the laser grating (266 nm) since already a deviation exceeding 0.05 nm would significantly reduce the interference fringe visibility.

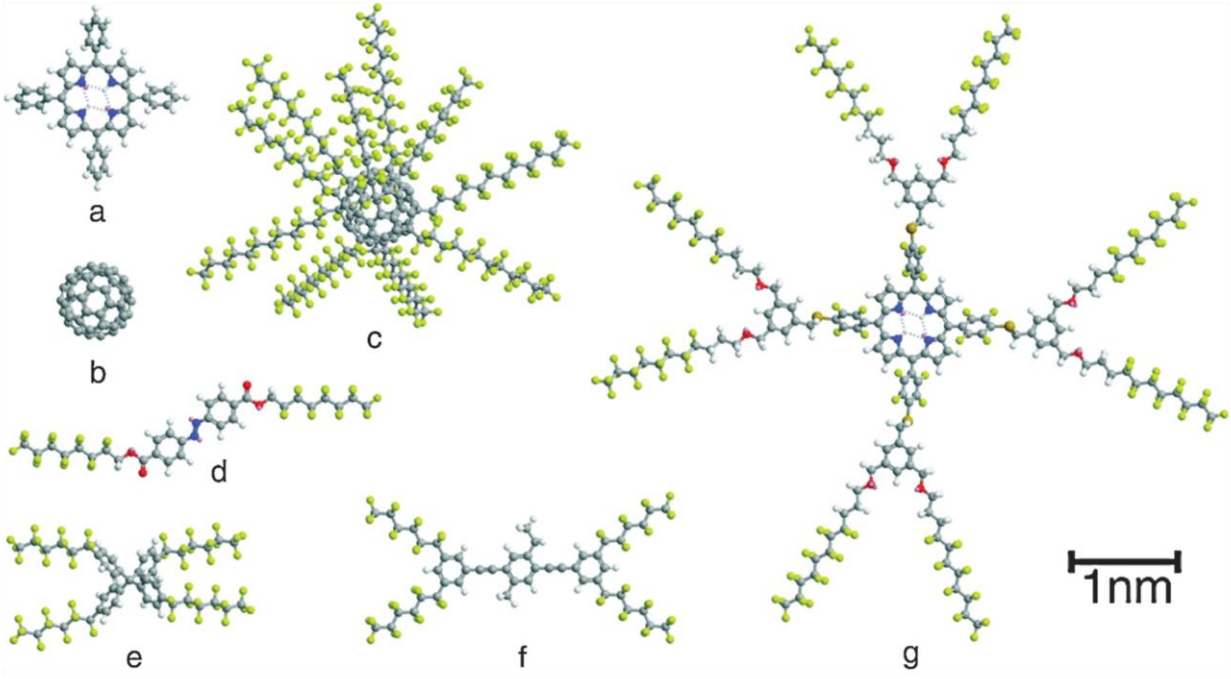

FIG. 7 (color). Gallery of molecules that showed quantum interference in the KDTL interferometer. (a) Tetraphenylporphyrin (TPP); (b) C_{60} fullerene; (c) PFNS10, a carbon nanosphere with ten perfluroalkyl chains; the variant PFNS8 with eight side arms was also used; (d) a perfluoroalkyl-functionalized diazobenzene (Gerlich *et al.*, 2007); (e), (f) two structural isomers with equal chemical composition but different atomic arrangement (Tüxen *et al.*, 2010); (g) TPPF152, a TPP derivative with 152 fluorine atoms (Gerlich *et al.*, 2011).

The gratings are mounted on a common base with a mutual distance of 105 mm. This allows operating with a de Broglie wavelength down to 1 pm, for instance, with particles of 10 000 amu at a velocity of 40 m/s or correspondingly higher masses at lower velocities. This design was experimentally validated in our laboratory with a variety of organic molecules, as shown in Fig. 7. We demonstrate high-contrast quantum interference for many molecular shapes, symmetries, masses, and internal excitations. Some of these molecules contained more than 400 atoms, weighed about 7000 amu, were thermally excited to 1000 K, or measured more than 6 nm in diameter, and still they all exhibited clear quantum interference (Gerlich *et al.*, 2011). In Fig. 8 we present the evolution of the fringe visibility for the perfluoroalkylated nanosphere PFNS8 (356 atoms, 5672 amu) as a function of the diffracting laser power in G_2. The experimental data (full circles) show a visibility of up to 50% and they are well described by the quantum predictions (heavy line) and cannot be reproduced by classical physics (thin line). The relatively large error bars in this experiment are due to the short measurement time resulting from the thermal instability of the species and from the fact that they are available only in small amounts.

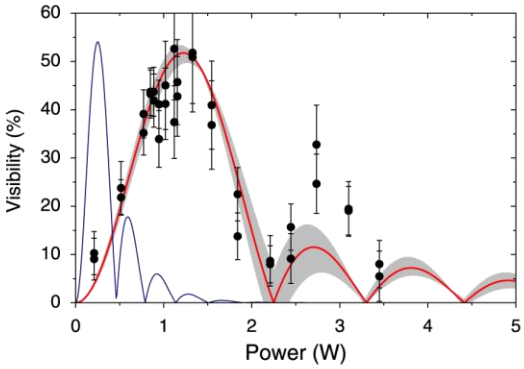

FIG. 8 (color online). Fringe visibility of PFNS8 in the KDTLI as a function of diffracting laser power at a mean molecular velocity of 75 m/s and a velocity spread of 10%. Experimental data are represented by full circles; the error bars correspond to a 68% confidence interval of the sinusoidal fit of the interference pattern. The heavy line is the quantum prediction based on the expected polarizability of $\alpha_{\rm opt}/4\pi\varepsilon_0 = 2\times10^{-28}$ m^3. The shaded area displays the effect of a ±2 m/s variation of the mean molecular velocity. The thin line gives the classically expected visibility. From Gerlich *et al.*, 2011.

C. Interferometry with pulsed optical gratings (OTIMA)

Although KDTLI is compatible with high molecular masses, van der Waals forces in G_1 and G_3 may eventually lead to a blockage of the grating due to adsorbed molecules clogging the slits. It is therefore useful to consider an all-optical setup, such as the optical time-domain ionizing matter (OTIMA) interferometer we describe below.

As long as we are limited to incoherent sources, the first grating must act as an absorptive mask to prepare the required spatial coherence. Optical amplitude gratings were already realized by Abfalterer *et al.* (1997) for metastable atoms by

inducing transitions to undetected states. Since the high level density in clusters and molecules usually precludes this resonant excitation scheme, Reiger *et al.* (2006) proposed photoionization gratings as a universal tool for complex nanoparticles, where a single photon suffices to ionize and remove the particles from the antinodes of a standing light wave. The intensity maxima thus play the role of the grating bars, but their transmission, periodicity, and the additionally imprinted phase can be tuned by varying the pulse energy and the laser wavelength. In variance to the TLI and KDTLI designs, the second pulse G_2 acts as a combination of both an absorptive and a phase grating.

The use of pulsed optical gratings also allows one to implement an interferometer in the time domain as discussed in detail by Nimmrichter, Haslinger *et al.* (2011). Time-domain interferometry was first proposed by Moshinski (1952) for neutrons. Since then it has been implemented in various atom experiments, for instance, by Kasevich *et al.* (1991), Szriftgiser *et al.* (1996), Cahn *et al.* (1997), Fray *et al.* (2004), and Turlapov, Tonyushkin, and Sleator (2005). It permits one to eliminate many velocity-dependent dispersive effects since all particles interact with all perturbations for the same period of time.

A possible implementation for clusters is illustrated in Fig. 3(c), where a cluster package passes along a plane mirror surface. It is subjected to three retroreflected UV laser pulses which form standing light waves. These pulses are separated in time by a pulse delay of several tens of microseconds for low-mass clusters and up to tens of milliseconds for clusters around 10^6 amu. The time-domain analog of the Talbot length is the Talbot time $T_T = md^2/h$, proportional to the particle mass. For light with a wavelength of $2d = 157$ nm as generated by an F_2-excimer laser it amounts to $T_T/\mathrm{ns} = 15m/\mathrm{amu}$. F_2 lasers have a coherence length of about 1 cm (Sansonetti, Reader, and Vogler, 2001) and a pulse width of about 10 ns, which suffices to form a laser grating up to a few millimeter distance from the mirror surface. Other light sources, such as high harmonics of solid state lasers, are similarly conceivable.

One can scan the interference fringes, for instance, by allowing the particles to fall freely in the gravitational field. Since the delay time is the same for all clusters, they will fall by the same distance, and will thus be effectively scanned by laser grating G_3, independent of their velocities. The simulation presented in Fig. 9 shows that the quantum visibility in such a scheme could reach as much as 100% for a given mass.

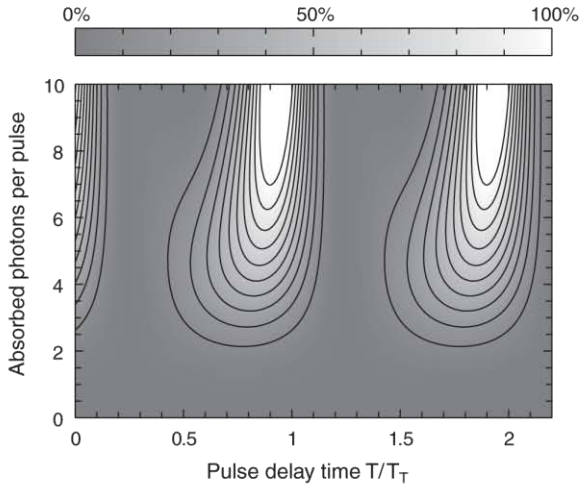

FIG. 9. Predicted fringe visibility as a function of both the pulse delay time and the mean number of absorbed UV photons. Matter-wave self-imaging occurs at multiples of the Talbot time T_T. Each single-photon ionization grating leads to a spatially periodic removal of clusters from the beam. The antinodes of the standing light waves thus play the role of the mechanical bars in a nanofabricated grating. By increasing the laser pulse energy one broadens the zones from which the clusters can be efficiently extracted. This corresponds to a reduction of the effective open slit width in a mechanical grating. All gratings are not only ionizing, but are accompanied by an additional phase modulation arising from the interaction between the polarizable molecules and the laser field. This intensity dependent phase gives rise to the predicted asymmetry of this figure.

IV. PROBING ENVIRONMENTAL DECOHERENCE

The experiments described in the previous section demonstrate that complex particles can be delocalized over hundreds of nanometers, a distance exceeding their size by orders of magnitude. Given this clear confirmation of quantum mechanics, how can one understand that under normal circumstances molecules appear as well-localized objects? This distinction of states with well-defined position can be explained within the framework of quantum mechanics by the concept of environmental decoherence (Joos *et al.*, 2003; Zurek, 2003; Schlosshauer, 2007).

The theory accounts for the crucial influence of practically unobservable environmental degrees of freedom, such as ambient gas particles or the radiation field. The interaction correlates the environmental quantum state with that of the molecular motion, implying that some information on the molecule's whereabouts could be obtained in principle by an appropriate measurement of the environment. Even though this cannot be done in practice, the mere fact that which-way information remains in the environment suffices to affect the reduced state of the molecule in the same way as if the particle position was continuously monitored by a coarse-grained detector and the outcome discarded. This leads to the effective localization of the particle, i.e., to the reduction of spatial coherence, prohibiting its wave behavior in agreement with the complementarity principle (Bohr, 1949). Equivalently, one can view the environment as exerting random momentum kicks on the molecule, which blur the molecular state in the momentum representation.

The near-field interference setups discussed in Sec. III are particularly well suited for quantitative decoherence studies since a molecule will typically not be scattered out of the detected beam after an environmental interaction. This enabled the first studies of thermal and collisional decoherence, two paradigmatic mechanisms, which can be experimentally well controlled and where the observed reduction of the interference visibility can be compared with the quantitative predictions of decoherence theory.

It should be emphasized that the fringe visibility may also be degraded by more mundane effects which cannot be related to the dissemination of which-way information, even though they may be hard to distinguish from proper decoherence. In practice the most relevant of these is the blurring of the observed interference pattern due to the phase averaging caused by vibrations and due to thermal drifts of the grating positions and their alignment; also fluctuations of electromagnetic field gradients can reduce the recorded interference visibility. Such classical noise effects were sufficiently suppressed in the experiments on thermal and collisional decoherence.

A. Endogenous heat radiation

Every complex particle with a finite temperature emits thermal radiation. The localization due to that radiation is thus a basic decoherence effect expected to occur in any thermal object. It can be studied conveniently with fullerenes since they behave in many ways similar to a small solid when heated to high internal energies.

At temperatures exceeding 1000 K fullerenes radiate in a continuous optical spectrum, similar to a blackbody (Hansen and Campbell, 1998). They also start to evaporate C_2 subunits and to emit thermal electrons. All of these processes can occur while the hot molecules traverse the Talbot-Lau interferometer. However, ionization and fragmentation lead to a complete loss of the molecules and thus do not contribute to the recorded signal.

In the experiment the fullerenes were heated by several intense laser beams in front of the interferometer (Hackermüller *et al.*, 2004). Both the ionization yield in the excitation region and the increased final detection efficiency are recorded as a function of the heating laser power and the particle velocity, providing a temperature calibration. The agreement of these measurements with a model calculation yields the distribution of microcanonical temperatures in the molecular ensemble (Hornberger, Hackermüller, and Arndt, 2005). Photoemission is the fastest and most efficient cooling process, and a good portion of the internal energy is emitted before the molecules enter the interferometer. However, it still is probable for the molecules to emit several near-infrared or even visible photons during their transit between the first and the third grating.

The theoretical account of the expected decoherence must consider the fact that fullerenes differ from ideal blackbody emitters. A microscopically realistic description of the spectral emission rate is obtained by including their known frequency-dependent absorption cross section, their finite heat capacity, and the fact that they are not in thermal equilibrium with the radiation field (Hornberger, Hackermüller, and Arndt, 2005).

As shown in Fig. 10, the prediction from decoherence theory is well confirmed by the experimental observation: The interference visibility is gradually reduced with increasing molecular temperature until it vanishes completely. The upper scale gives the mean microcanonical temperature in the molecular beam, showing that at 1500 K the fullerenes still behave as quantum waves in this experimental arrangement, while they are indistinguishable from classical particles when close to 3000 K. The calculation shows that between three and four photons are typically required to reduce the visibility by one-half. This is consistent with the emitted wavelength being comparable to the spatial delocalization of the molecular matter waves.

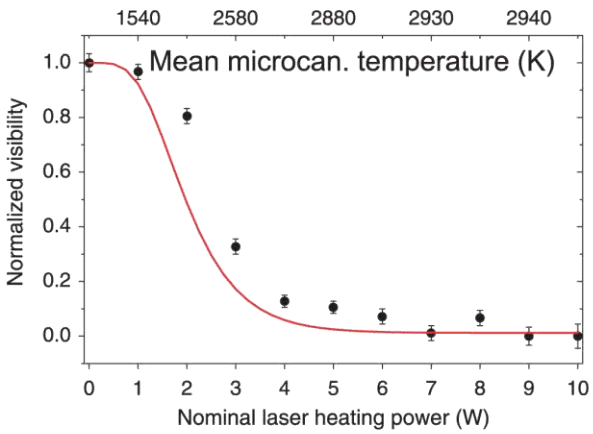

FIG. 10 (color online). Observation of thermal decoherence in a Talbot-Lau interferometer. The expected visibility reduction (solid line) is in good agreement with the experimental observation (points). The bottom scale gives the heating laser power, and the top scale shows the mean molecular temperature at the interferometer entrance. The maximal interference path separation of 990 nm is comparable to the wavelengths of the thermal photons, implying that more than a single photon has to be emitted to fully destroy the fringe visibility. Combined with the highly nonlinear temperature dependence of the emission probability, this explains the particular form of the curve. In the experiment the gratings are separated by 38 cm and the mean beam velocity is 100 m/s. From Hackermüller *et al.*, 2004.

These studies imply that thermal decoherence can turn into a serious obstacle for interferometry with very complex particles. In particular, the effect suffices to explain the localization of truly macroscopic objects, since the critical temperature for the effective quantum-to-classical transition decreases with increasing size (Joos *et al.*, 2003; Hornberger, 2006). At the same time, thermal decoherence should be avoidable for particles with masses up to 10^9 amu by cooling them to their vibrational ground state, i.e., below 77 K; at these masses also the vacuum chamber containing the setup needs to be cooled to avoid decoherence due to blackbody radiation (Nimmrichter, Hornberger *et al.*, 2011).

B. Collisional decoherence

A second fundamental decoherence effect is related to the scattering of ambient gas particles off the delocalized molecule. Using a Talbot-Lau interferometer one can study this effect quantitatively by the gradual admission of different gases into the vacuum chamber. At room temperature, the collisional momentum and information transfer is so high that already a single scattering event per molecule suffices to fully destroy the interference. On the other hand, because of the

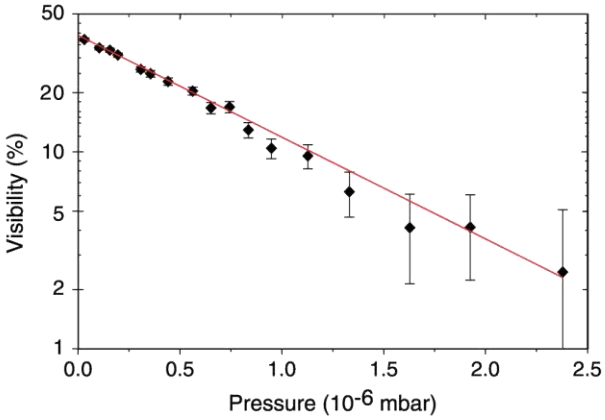

FIG. 11 (color online). Interference fringe visibility of C_{70} fullerenes as a function of the methane gas pressure in a TLI (semilogarithmic scale). The exponential decay indicates that already a single collision leads to a complete loss of coherence. Good agreement is found with the prediction of decoherence theory (solid line), which is based on the microscopic scattering dynamics. From Hornberger *et al.*, 2003.

high mass of the interfering particles and the wide detection area there is no dominant beam depletion due to collisions within the interferometer.

As shown in Fig. 11 an exponential decay of the fringe visibility can be observed as the gas pressure increases (Hornberger *et al.*, 2003). This is consistent with assuming that a single collision process is able to resolve the molecular position, or equivalently to blur the interference pattern by the random momentum transfer. We note that also the molecular transmission decreases exponentially, though this is mainly due to collisions outside the interferometer.

We find a good quantitative agreement with decoherence theory, as indicated by the solid line in Fig. 11. The calculation is based on a semiclassical approximation for the velocity-dependent total scattering cross section, which is determined by the interparticle van der Waals potential, and which must be averaged over the velocity distribution in the gas; see Hackermüller *et al.* (2003). This experiment serves also to confirm the short time limit of the quantum linear Boltzmann equation for a tracer particle in a gas (Vacchini and Hornberger, 2009).

The interference of fullerenes yields substantial visibilities even at moderate pressures of 10^{-7} mbar (and an interferometer transit time of 5 to 10 ms). However, we estimate that quantum interference with gold nanoclusters of 10^6 amu will require a pressure of less than 10^{-9} mbar (Nimmrichter, Haslinger *et al.*, 2011).

V. INTERFERENCE-ASSISTED MEASUREMENTS

The narrow spacing of the quantum interference fringes and the high sensitivity of their position to external forces allows one to turn molecule interferometry into a viable tool for quantum-enhanced metrology. The high potential of interference-assisted measurements has already been demonstrated with atoms. Static polarizabilities (Ekstrom *et al.*, 1995; Miffre *et al.*, 2006a; Holmgren *et al.*, 2010), the ratio $\hbar/m_{Cs}$ (Weiss, Young, and Chu, 1993), the gravitational acceleration (Peters, Chung, and Chu, 1999), and Earth's rotation (Gustavson, Bouyer, and Kasevich, 1997) have been measured interferometrically, to name a few.

Here we focus our discussion on the combination of Kapitza-Dirac-Talbot-Lau interferometry with conventional Stark deflectometry (De Heer and Kresin, 2010) to determine the internal properties of large organic molecules. This provides valuable insight into physical chemistry, and it is also important for future interference experiments since the coupling of the molecule to the environment depends on these parameters.

A. Optical polarizability

In KDTLI the light grating G_2 interacts with the molecular optical polarizability α_{opt} and modulates the de Broglie phase shift. The influence of the laser power P on the fringe visibility V was already illustrated in Fig. 8 for the perfluoralkylated nanosphere PFNS8. For smaller molecules with a higher signal-to-noise ratio, such as the fullerenes, Hornberger *et al.* (2009) found that the excellent agreement between theory and experiment permits the determination of α_{opt} with an accuracy of around 10% (dominated by the systematic uncertainties in the power and the vertical waist of the diffracting laser). This allows, for instance, a clear distinction between C_{60} and C_{70}, directly from the power dependence of their fringe visibility. KDTLI may thus be used for identifying properties which cannot be discriminated by a mass spectrometer alone (Gerlich *et al.*, 2008).

B. Electric polarizability

The KDTLI can be extended by a pair of electrodes (Stefanov, Berninger, and Arndt, 2008) in front of G_2, as shown in Fig. 12, to access the static polarizabilities. The inhomogeneous electric field $\mathbf{E}$ produced by the electrodes provides a homogenous transverse force on a polarizable particle of polarizability α_{stat}. The magnitude of the final quantum fringe shift

$$\Delta x = K \frac{\alpha_{stat}}{2mv^2} \frac{\partial}{\partial x}(\mathbf{E}^2) \tag{2}$$

is identical to the displacement of a classical particle beam of mass m and velocity v. K is a constant defined by the geometry of the electrodes. Matter-wave interferometry, however, additionally imprints a nanosized, high-contrast fringe pattern whose shift can be monitored with a resolution of a few nanometers. This exceeds the spatial resolution of typical classical experiments by orders of magnitude. Because of that, quantum experiments can operate at lower fields and be less intrusive. At present, the experimental uncertainty in quantum deflectometry is still comparable to its classical analog (Berninger *et al.*, 2007), since the experimental precision is currently limited by the uncertainty of the velocity measurement and the error of the geometry factor K. Future experiments featuring an improved velocity selection and a better calibration, for

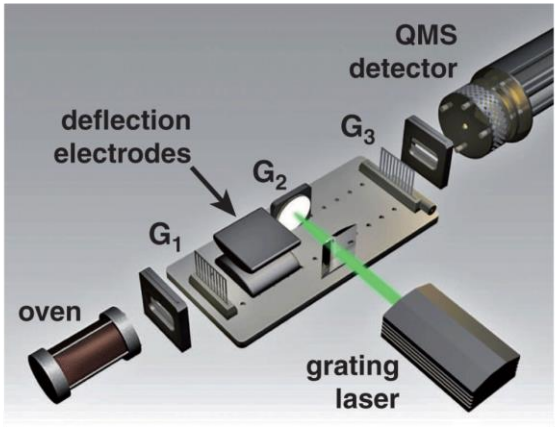

FIG. 12 (color online). Interferometric Stark deflectometry combines the high spatial resolution of the KDTL experiment [see Fig. 3(b)] with the fringe deflection in an electric force field. Beam shifts as small as 10 nm can easily be resolved and be used to evaluate both intramolecular properties and external forces. From left to right: A thermal source emits an intense beam of neutral molecules. A pair of electrodes, placed in between G_1 and G_2, provides the deflection field. An electron impact ionization quadrupole mass spectrometer (QMS) serves as detector.

instance using an atom beam, are expected to achieve an accuracy of better than 1%. This is close to the intrinsic limit for thermally excited molecules undergoing state changes on a rapid time scale, as shown later.

C. Structural isomers

The molecular polarizability is also closely linked to the intramolecular atomic arrangement. Stark deflectometry therefore allows one to distinguish structural isomers, i.e., molecules which have the same chemical composition and mass but a different atomic arrangement. This is the case for the compounds in Figs. 7(e) and 7(f) which were tailor made by Tüxen *et al.* (2010). Molecular beams of both species are prepared under equal conditions and delocalized over similar areas in the same interferometer. The stretched compound in Fig. 7(f), however, contains a delocalized π-electron system which enhances the electronic polarizability with respect to the value of the compound in Fig. 7(e) with a tetrahedral core. Interferometric deflectometry can then distinguish between these two species and in principle even sort them spatially (Ulbricht *et al.*, 2008). This occurs without the exchange of any which-path information, since the interaction of the molecules with the external field is conservative and reversible.

D. Thermal dynamics

In contrast to atoms, whose interaction with an electric field is determined by the static atomic polarizability alone, complex molecules are bestowed with many additional degrees of freedom. Even intrinsically nonpolar particles, with a point-symmetric thermal ground state, may develop vibrationally induced electric dipole moments which fluctuate on a short time scale. The beam shift in an external field is then again determined by a polarizability as in Eq. (2). However, in place of only the static polarizability, which describes the response of the electron cloud, we must use the sum of α_{stat} and a temperature dependent nuclear term accounting for the nuclear motion. It is determined by the thermal average $\langle d^2\rangle$ of the squared electric dipole component (Compagnon *et al.*, 2002):

$$\alpha_{\mathrm{tot}} = \alpha_{\mathrm{stat}} + \frac{\langle d^2\rangle}{3k_{\mathrm{B}}T}. \tag{3}$$

Although the underlying conformation changes occur on a subnanosecond time scale and average the expectation value of the dipole moment to zero, the squared dipole remains finite at finite temperatures. This picture was experimentally tested with hot perfluoroalkylated azobenzene molecules, shown in Fig. 7(d). At 500 K they undergo rapid fluctuations with dipole variations between 0.8 and 3.6 D. Interferometric deflectometry yields a total polarizability of $\alpha_{\mathrm{tot}}/4\pi\varepsilon_0 = (95 \pm 3 \pm 8) \times 10^{-30}$ m^3, which is larger than the value for the electronic polarizability $\alpha_{\mathrm{stat}}/4\pi\varepsilon_0 = (61 \pm 1 \pm 7) \times 10^{-30}$ m^3, as taken from a visibility-versus-power curve. Here the first uncertainty values give the statistical error, and the second ones give the systematic error. The observed total polarizability is numerically consistent with the sum of the electronic polarizability and the temperature dependent term in Eq. (3) (Gring *et al.*, 2010).

E. Permanent electric dipole moments

While all measurements described so far are contrast preserving at a fixed molecular velocity, the interaction between a static molecular moment and an external field may eventually lead to a loss of the fringe visibility due to the molecular rotation. If a polar molecule is exposed to an external field gradient, a deflection force $\mathbf{F} = -\boldsymbol{\nabla}(\mathbf{d}\cdot\mathbf{E})$ will displace the interference pattern in dependence of the molecular orientation with respect to the field. Thermally excited molecules will generally leave the source with a random orientation, rotating at frequencies around 10^{10} Hz. The fringe shift then varies not only in magnitude but also in direction such that the interference pattern washes out already at moderate external field strengths. This is a typical example where the fringe visibility is reduced by phase averaging instead of genuine decoherence, i.e., without the dissemination of which-path information into the environment (Eibenberger *et al.*, 2011).

F. Absolute absorption cross sections

The experiments of Sec. IV illustrated how the emission of photons can lead to the decoherence of matter waves. This sensitivity to the recoil of a single photon can be brought to practical use in an interferometric measurement of the absolute molecular photoabsorption cross section (Nimmrichter *et al.*, 2008). Photon absorption may be induced by the running wave of an additional laser beam crossing the molecular beam in the direction of the grating vector. Given the Poissonian photon number statistics, a small discrete number of photons can be absorbed, and the corresponding

interferograms are shifted in discrete steps which add up to an interference pattern with reduced visibility. By a judicious choice of the laser position the interference visibility is maximally blurred already if a single photon is absorbed on average. It is thus possible to determine the absorption cross section without knowing the molecular density in the beam, a frequent challenge in physical chemistry. This exemplifies the fact that quantum decoherence phenomena can become a tool for molecular metrology.

VI. EXPERIMENTAL CHALLENGES

Interference experiments are only as good as their beam sources and detectors. In the following, we briefly describe some schemes which are currently available or under investigation for matter-wave interferometry. For brevity we limit the discussion to neutral clusters and molecules.

A. Molecular beam sources

An ideal source emits velocity- and mass-selected particles at low internal and external temperatures in a well-defined direction into ultrahigh vacuum. Up to now, molecular interference experiments had to rely on either supersonic sources or thermal beams. Effusive sources are particularly appealing for matter-wave experiments as they are fully vacuum compatible, simple, and have the capability of generating beams of molecules exceeding 10 000 amu with velocity distributions that have significant components at velocities as low as 10 m/s. Supersonic sources, on the other hand, generate beams which emerge at much higher velocities, but exhibit much smaller velocity spreads and internal temperatures (Scoles, 1988), which makes them still suitable for interferometric metrology experiments with polypeptides and oligonucleotides. Mechanical slowing mechanisms (Gupta and Herschbach, 1999; Narevicius *et al.*, 2007) and electromagnetic slowing mechanisms (Bethlem, Berden, and Meijer, 1999; Fulton, Bishop, and Barker, 2004; Narevicius *et al.*, 2008) have been used to decelerate molecules around 100 amu. Molecules beyond the size of a single virus may be volatilized by matrix assisted laser desorption ionization (Tanaka *et al.*, 1988) or electrospray ionization (Fenn *et al.*, 1989).

Large clusters of metals and semiconductors can be prepared using aggregation sources (Martin, 1984; Haberland, Karrais, and Mall, 1991; von Issendorff and Cheshnovsky, 2005) with diameters up to several nanometers, both as neutrals as well as ions, and with a base velocity of about 200 to 300 m/s in a carrier gas at 77 K. Further slowing and internal state cooling can be achieved using a cold buffer gas or cryogenic ion traps.

Low molecular beam velocities are expected via sympathetic cooling by laser cooled ions (Molhave and Drewsen, 2000) or by cooling in an off-resonant cavity (Horak *et al.*, 1997; Chang *et al.*, 2010; Nimmrichter *et al.*, 2010; Romero-Isart, Pflanzer, Blaser *et al.*, 2011). However, many experimental challenges still have to be overcome to turn any of these sources into a reliable method for nanoparticle quantum optics.

B. Detection methods

All experiments described in this review were carried out using either thermal laser ionization or electron impact quadrupole mass spectrometry. Thermionic emission of electrons is an efficient and fast detection method for stable particles, such as fullerenes, which exhibit thermal photon emission rather than fragmentation when heated to high temperatures (Campbell, Ulmer, and Hertel, 1991; Hansen and Campbell, 1998).

Electron impact ionization quadrupole mass spectrometry, on the other hand, is more universal at low masses, but limited to a typical detection efficiency of 10^{-4} and often compromised by uncontrolled fragmentation at high mass. Complementary to that, single-photon or two-photon methods seem to be adapted for the detection of clusters of almost any size, yet they often fail for large organic molecules (Hanley and Zimmermann, 2009).

This is why scanning tunneling microscopy (Juffmann *et al.*, 2009) or fluorescence methods (Stibor, Stefanov *et al.*, 2005) have been established to image surface deposited interferograms. Their high detection efficiency, however, has to be weighed against the difficulty of distinguishing molecules from their fragments.

C. External perturbations

Classical noise phenomena, which should be distinguished from the decoherence processes described in Sec. IV, are conceptually less intriguing, but are in practice often more relevant to the experiment. A theoretical discussion in the context of atom interferometry was given by Schmiedmayer *et al.* (1997) and Miffre *et al.* (2006b), and for molecule experiments by Stibor, Hornberger *et al.* (2005).

In a three-grating interferometer the fringe shift Δx depends on the relative position of all gratings as given by $\Delta x = \Delta x_1 - 2\Delta x_2 + \Delta x_3$. Grating vibrations may destroy the interference fringes already at amplitudes as small as a few nanometers. In the presence of a constant acceleration a the fringe shift is $\Delta x = -2(aT^2/2) + a(2T)^2/2 = aT^2$, with T the free evolution time between two subsequent gratings. This applies to the Earth's gravitational acceleration $a_g = 9.81\ \mathrm{m/s^2}$, the Coriolis acceleration $a_c = 2\mathbf{v} \times \mathbf{\Omega}_E$, or any constant electromagnetic acceleration.

An overall fringe shift will not destroy the interference pattern. However, if different particles experience different shifts due to different transit times the final molecular pattern will be a mixture of differently shifted interferograms, and the visibility can be drastically reduced. An interferometer in the time domain (see Sec. III.C) can eliminate all phase shifts that depend on transit times. Even the intrinsically velocity-dependent Coriolis force can be compensated then by a reorientation of the interferometer grating vector parallel to $\mathbf{\Omega}_E$.

VII. THEORY OF TALBOT-LAU NEAR-FIELD INTERFERENCE

We now provide an overview of the theory, which permitted us to design the interferometers such that the quantum mechanically predicted fringe visibility is always

considerably larger than of the moiré-type shadows expected by classical physics.

In Talbot-Lau near-field interference, many different diffraction orders contribute to a resonant interference effect. Even small distortions of the various wave fronts can therefore result in large effects. This applies, in particular, to the influence of the dispersion forces between the polarizable molecules and the grating walls. An accurate description must also account for the finite longitudinal coherence in the initial beam, as well as the incoherent effects of photon absorption and Rayleigh scattering in the standing laser light wave. For precise predictions also the finite width and the transverse coherence of the molecular beam entering the interferometer must be included, as well as the effects of grating vibrations and inertial forces due to gravity and the rotation of the Earth.

All this can be accounted for in a transparent and largely analytical fashion by expressing the state of the particle beam and its evolution in phase space in terms of the Wigner function (Wigner, 1932; Schleich, 2001). This also facilitates the incorporation of decoherence effects caused by the emission of thermal radiation or the scattering of particles. Comparison with the classical prediction, including all forces and environmental effects, then simply requires one to replace the Wigner function by the classical phase-space distribution.

A. Phase-space formulation

A quantum phase-space theory of Talbot-Lau interferometry was developed by Hornberger, Sipe, and Arndt (2004) and refined to the treatment of grating dispersion forces beyond the eikonal approximation by Nimmrichter and Hornberger (2008). It is based on earlier treatments using wave functions (Patorski, 1989; Clauser and Reinsch, 1992; Berman, 1997; Brezger, Arndt, and Zeilinger, 2003). The concept was later extended to Kapitza-Dirac-Talbot-Lau interferometry (Hornberger *et al.*, 2009) and to time-domain interferometry with ionizing laser beams (Nimmrichter, Haslinger *et al.*, 2011).

We assume a coarsely collimated molecular beam where the longitudinal speed exceeds the transversal velocity. The change of the longitudinal velocity component v_z may then be neglected as the particles pass the interferometer, and the description can be confined to the transverse state of motion in a longitudinally comoving frame. One considers how the transverse Wigner function transforms under the sequential steps of passages through the gratings and the stretches of free propagations, and includes the longitudinal coherence only in the end by averaging over the velocity distribution in the beam. The classical prediction can be obtained in much the same way, since the Wigner function and the classical phase-space distribution exhibit the same shearing transformation during the free motion in between the gratings.

To keep the presentation simple we focus here on the results for the special case of equidistant gratings with equal period d, and we assume a transversally extended and incoherent initial beam. The periodic nature of the diffraction masks then allows us to expand the expected periodic fringe pattern in a Fourier series,

$$w_{\mathrm{TL}}(x) = \sum_{m=-\infty}^{\infty} B_m^*(0) B_{2m}\left(m\frac{L}{L_{\mathrm{T}}}\right) \exp\left(2\pi i m \frac{x}{d}\right). \tag{4}$$

It involves the Talbot-Lau coefficients

$$B_m(\xi) = \sum_{j=-\infty}^{\infty} b_j b_{j-m}^* \exp[i\pi(m-2j)\xi]. \tag{5}$$

The b_j components are the Fourier coefficients of the transmission function of the second grating G_2,

$$t(x) = b(x)\exp\left(\frac{-i}{\hbar v_z}\int V(x,z)dz\right) = \sum_{j=-\infty}^{\infty} b_j \exp\left(2\pi i j \frac{x}{d}\right). \tag{6}$$

They are determined by the aperture amplitude $0 \le b(x) \le 1$, and they also involve a complex phase if the grating potential $V(x, z)$ caused by dispersion forces or optical dipole forces is included.

It follows from Eq. (5) that for integer $\xi = n$ the $B_m(n)$ reduce to the Fourier coefficients of the transmission probability $|t(x)|^2$ (shifted by half a grating period for odd n). This is the same self-imaging phenomenon encountered if a plane wave illuminates a single grating; see Sec. II.B. Indeed, the density pattern of the basic Talbot effect consists of the same coefficients (5), and reads as (Nimmrichter and Hornberger, 2008)

$$w_{\mathrm{T}}(x) = \sum_{m=-\infty}^{\infty} B_m\left(m\frac{L}{L_{\mathrm{T}}}\right) \exp\left(2\pi i m \frac{x}{d}\right). \tag{7}$$

At integer multiples of the Talbot length, i.e., $L = nL_{\mathrm{T}}$, one indeed recovers the grating profile $|t(x)|^2 = |b(x)|^2$. At fractional multiples, $L/L_{\mathrm{T}} = n/m$, smaller periods appear in the interferogram. This can be clearly seen, e.g., for $n/m = 1/2$, $1/3$, $1/4$, in the carpet of Fig. 2, which was produced with this formula for $V = 0$.

The comparison with Eq. (4) shows that in an incoherently illuminated TLI or KDTLI the density pattern $w_{\mathrm{TL}}(x)$ at the position of the third grating is given by a convolution of the Talbot pattern (7) with the first grating mask $|t(x)|^2$. If a third grating is used to scan the interferogram, another convolution of Eq. (4) with the transmission probability $|t(x)|^2$ produces the same form as Eq. (4) with another factor of $B_m^*(0)$, such that the transmitted signal has the Fourier components $S_m = [B_m^*(0)]^2 B_{2m}(mL/L_{\mathrm{T}})$. The fringe visibility of a sinusoidal fit to the density pattern, as done in the experiment, is then obtained as the ratio of the first and zeroth Fourier components, $\mathcal{V}_{\sin} = 2|S_1/S_0|$. The general form of the visibility curves of Figs. 5, 6, and 8 can be reproduced with these formulas.

The time-domain interferometer of Sec. III.C can be described by the same formalism, if we replace the longitudinal position of the comoving frame of reference by the evolved time. The length ratio of L/L_{T} is then replaced by the time ratio T/T_{T}.

B. Incorporating decoherence

Our phase-space formulation also allows one to easily incorporate the effects of decoherence discussed in Sec. IV. During the free propagation of the matter wave any scattering or emission event will reduce the off-diagonal elements of the motional density matrix in position representation, $\langle \mathbf{x}|\rho|\mathbf{x}'\rangle \to \eta(\mathbf{x}-\mathbf{x}')\langle \mathbf{x}|\rho|\mathbf{x}'\rangle$. The decoherence function η describes the reduction of the fringe visibility, satisfying $|\eta| \le 1$ and $\eta(0) = 1$. It can be calculated for various decoherence processes based on their detailed microscopic physics (Hornberger, Sipe, and Arndt, 2004).

Given the rate $R(t)$ of interaction events with the environment, the effect of decoherence is accounted for by replacing the Talbot-Lau coefficients $B_m(\xi)$ in Eq. (4) by

$$B_m(\xi)\exp\left\{-\int_{-L/v_z}^{L/v_z} R(t)\left[1-\eta\left(\frac{md}{2}\frac{|v_z t|-L}{L_T}\right)\right]dt\right\}.$$

The $m = 0$ coefficient, describing the mean particle current, remains unaffected. The $m = 2$ coefficient, on the other hand, which determines the sinusoidal visibility gets reduced by an exponential factor. It is determined by an integral over the decoherence function, whose argument is the effective separation between two neighboring interference paths. We observe that decoherence is most effective at the position $v_z t = 0$ of the central grating, whereas there is no effect at $v_z t = -L$ and $v_z t = L$ where all interference paths coalesce. This agrees with the intuitive picture that decoherence is related to the degree of information gained by the environment in the interaction process: Which-path information is best available where the interference paths are farthest apart, i.e., at the central grating.

In the case of decoherence due to collisions between delocalized molecules and residual gas particles, the decoherence function η is given by an angular integration involving the scattering amplitude f, the total cross section σ, and an average over the distribution of gas velocities v_g (Hornberger, Sipe, and Arndt, 2004),

$$\eta(x) = \left\langle \int d\Omega \frac{|f(\cos(\theta))|^2}{\sigma(v_g)} \operatorname{sinc}\left[\sin\left(\frac{\theta}{2}\right)\frac{2v_g m_g x}{\hbar}\right]\right\rangle_{v_g}.$$

The argument of the function $\operatorname{sinc}(z) = \sin(z)/z$ compares the distance x between the interference paths to the wavelength associated with the momentum exchange experienced if the gas particle scatters with angle θ. Thus, the better the probing gas particles can resolve the separation between the interference paths, the stronger the reduction of the fringe visibility. This is analogous to the case of a Heisenberg microscope, where the spatial resolution is determined by the wavelength of the probe particles.

VIII. EXPLORING NEW PHYSICS WITH MESOSCOPIC MATTER WAVES

So far, we discussed the recent progress in high mass interferometry, as well as the challenges related to extensions into the mass range beyond 10^6 amu. Complementary to that, various theories have been put forward over the last decades for an objective modification of the quantum superposition principle for macroscopic objects. Such speculations range from nonlinear extensions of the Schrödinger equation (Bialynicki-Birula and Mycielski, 1976; Großardt and Giulini, 2011), dephasing due to space-time fluctuations (Wang, Bingham, and Mendonca, 2006), and gravitational collapse models (Karolyhazy, 1966; Diosi, 1989; Penrose, 1996), to spontaneous localization theories (Ghirardi, Rimini, and Weber, 1986; Pearle, 1989; Ghirardi, Pearle, and Rimini, 1990). These models have in common the fact that they modify the motional dynamics of quantum objects in such a way that the quantum superposition principle fails above a certain mass scale of the objects. This way they lead to a macrorealist description (Leggett, 2002), where nonclassical delocalized quantum states of macroscopic objects are excluded.

While most of the suggested models provide at most rough estimates of the critical mass range, the theory of continuous spontaneous localization (CSL) by Ghirardi, Pearle, and Rimini (1990) has been extensively studied (Bassi and Ghirardi, 2003) and yields quantitative predictions. In the CSL model a stochastic term is added to the many-particle Schrödinger equation which randomly collapses the wave function to a length scale given by the localization length parameter, commonly estimated as $r_c = 100$ nm. The rate of the localization events grows quadratically with the mass of the composite object. In the CSL literature the rate parameter λ_0 is specified as the localization rate for a single nucleon ($m = 1$ amu). Current estimates of the strength of the CSL effect by Adler (2007) and Bassi, Deckert, and Ferialdi (2010) locate its value between 10^{-12} and 10^{-8} Hz, which also ensures that the CSL predictions are consistent with all currently known microscopic and mesoscopic quantum phenomena.

Nimmrichter, Haslinger *et al.* (2011) showed that the OTIMA interference experiment outlined in Sec. III.C should be able to test the predictions of CSL with nanoparticles in the mass range between 10^6 and 10^8 amu. This is illustrated

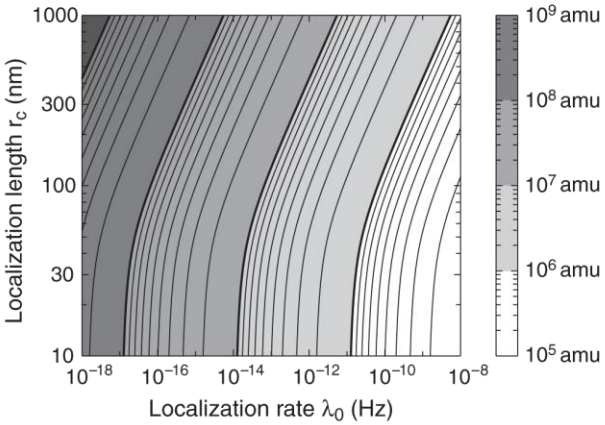

FIG. 13. Critical mass for testing the continuous spontaneous localization model (Ghirardi, Pearle, and Rimini, 1990) in the OTIMA interferometer (Nimmrichter, Haslinger *et al.*, 2011) with gold clusters. For a mass beyond 10^6 amu the experiments already rule out a significant value range of the localization parameters λ and r_c of the model. High-contrast interferometry with $m = 10^8$ amu largely exclude the validity of all current estimates of the CSL model.

in Fig. 13, where the critical mass for testing the continuous spontaneous localization is plotted for reasonable values of the free localization parameters λ_0 and r_c. Observing interference at 10^8 amu in this setting would largely rule out the CSL model in its currently estimated strength.

IX. CONCLUSIONS

Matter-wave interferometry with nanoscale objects is still a young discipline at the interface between the foundations of quantum physics, atomic, molecular and cluster physics, and the nanosciences. We have seen that the de Broglie wave well describes the center-of-mass motion of even very complex particles, giving rise to interference phenomena which can be surprisingly robust against a large variety of internal state transformations and against interactions between external force fields and internal particle dynamics.

In the coming years we expect to exploit the finesse of quantum effects for measuring electromagnetic and structural properties of nanosized objects with growing sensitivity. It is important to do so, not only to obtain insights about nanoparticles, but also to assess the feasibility of quantum experiments with ever more complex compounds. Future explorations should also study the effect of atomic or molecular adducts to the interfering nanoparticles, and the role of thermal, optical, or magnetic properties of the diffracted species.

We also indicated the interesting prospects for matter-wave interferometry with particles in the mass range of 10^6 amu and beyond. Various experimental challenges are still to be overcome to get there, but they will enable new tests of decoherence mechanisms and experimental explorations of standing hypotheses on modifications of established quantum physics.

Cluster interferometry can be contrasted with the enormous progress seen in the development of ultracold Bose-Einstein condensates (BEC), which have opened a new class of atomic quantum coherence experiments (Anderson *et al.*, 1995; Davis *et al.*, 1995). BEC experiments are complementary to the studies described here. A single BEC may contain as few as several hundred atoms, comparable to the PFNS10 or TPPF152 molecules, or up to 10^9 atoms all occupying one single-particle state. But the parameter range of highly diluted, weakly bound ultracold atoms at temperatures below 1 μK differs by many orders of magnitude from that of molecular and cluster physics, where hundreds of atoms are bound together in a small but dense piece of condensed matter at internal excitations well above room temperature. In contrast to cold atom experiments, in cluster interferometry the entire compound is delocalized and interferes as a single entity. This is implied by the fact that, unlike in a BEC, the de Broglie wavelength is given by the mass of the whole object.

Our experiments are also complementary to proposals for using mechanical oscillators to test the limits of the quantum superposition principle (Marshall *et al.*, 2003; O'Connell *et al.*, 2010; Romero-Isart, Pflanzer, Blaser *et al.*, 2011). Mechanical devices are orders of magnitude more massive than even the largest clusters conceivable in foreseeable matter-wave experiments. However, the high cantilever mass limits the maximal spatial separation between two superposed center-of-mass wave packets. It will remain many orders of magnitude smaller than the separation routinely achieved in molecule interferometry.

Bose-Einstein condensation, interferometry with nanoparticles, and quantum studies with nanomechanical oscillators are therefore truly complementary approaches to investigate the nature of macroscopic quantum physics.

ACKNOWLEDGMENTS

We are indebted to many students, postdocs, and collaborators in Vienna over many years. Special thanks go to Anton Zeilinger for initiating and stimulating the research program on macromolecule interferometry and for continuous encouragement along the way. We thank Marcel Mayor and Jens Tüxen, University of Basel, for the synthesis and characterization of many molecules described in this work. We acknowledge financial support through the Austrian FWF Wittgenstein Grant No. Z149-N16 and CoQuS No. C33N16, as well as the ESF EuroQuasar Project MIME No. I146-N16.

REFERENCES

Abfalterer, R., C. Keller, S. Bernet, M. K. Oberthaler, J. Schmiedmayer, and A. Zeilinger, 1997, Phys. Rev. A **56**, R4365.
Adler, S., 2007, J. Phys. A **40**, 2935.
Anderson, M. H., J. R. Ensher, M. R. Matthews, C. E. Wieman, and E. A. Cornell, 1995, Science **269**, 198.
Arndt, M., O. Nairz, J. Voss-Andreae, C. Keller, G. V. der Zouw, and A. Zeilinger, 1999, Nature (London) **401**, 680.
Bassi, A., D. Deckert, and L. Ferialdi, 2010, Europhys. Lett. **92**, 50 006.
Bassi, A., and G. Ghirardi, 2003, Phys. Rep. **379**, 257.
Batelaan, H., 2007, Rev. Mod. Phys. **79**, 929.
Berman, P., and V. Malinovsky, 2010, *Principles of Laser Spectroscopy and Quantum Optics* (Princeton University Press, Princeton, NJ).
Berman, P. R., 1997, *Atom Interferometry*, edited by P. R. Berman (Academic Press, New York).
Berninger, M., A. Stéfanov, S. Deachapunya, and M. Arndt, 2007, Phys. Rev. A **76**, 013607.
Berry, M., I. Marzoli, and W. Schleich, 2001, Phys. World **14**, No. 6, 39.
Bethlem, H. L., G. Berden, and G. Meijer, 1999, Phys. Rev. Lett. **83**, 1558.
Bialynicki-Birula, I., and J. Mycielski, 1976, Ann. Phys. (N.Y.) **100**, 62.
Bohr, N., 1949, in *Albert Einstein, Philosopher-Scientist*, edited by P. Schilpp (Tudor, New York).
Bordé, C., N. Courtier, F. D. Burck, A. Goncharov, and M. Gorlicki, 1994, Phys. Lett. A **188**, 187.
Born, M., and E. Wolf, 1993, *Principles of Optics* (Pergamon Press, Oxford).
Brezger, B., M. Arndt, and A. Zeilinger, 2003, J. Opt. B **5**, S82.
Brezger, B., L. Hackermüller, S. Uttenthaler, J. Petschinka, M. Arndt, and A. Zeilinger, 2002, Phys. Rev. Lett. **88**, 100404.
Brühl, R., R. Guardiola, A. Kalinin, O. Kornilov, J. Navarro, T. Savas, and J. P. Toennies, 2004, Phys. Rev. Lett. **92**, 185301.
Cahn, S. B., A. Kumarakrishnan, U. Shim, T. Sleator, P. R. Berman, and B. Dubetsky, 1997, Phys. Rev. Lett. **79**, 784.

Campbell, E. E. B., G. Ulmer, and I. V. Hertel, 1991, Phys. Rev. Lett. **67**, 1986.
Carnal, O., A. Faulstich, and J. Mlynek, 1991, Appl. Phys. B **53**, 88.
Case, W. B., M. Tomandl, S. Deachapunya, and M. Arndt, 2009, Opt. Express **17**, 20966.
Casimir, H. B. G., and D. Polder, 1948, Phys. Rev. **73**, 360.
Chang, D. E., C. A. Regal, S. B. Papp, D. J. Wilson, J. Ye, O. Painter, H. J. Kimble, and P. Zoller, 2010, Proc. Natl. Acad. Sci. U.S.A. **107**, 1005.
Chapman, M. S., C. R. Ekstrom, T. D. Hammond, R. A. Rubenstein, J. Schmiedmayer, S. Wehinger, and D. E. Pritchard, 1995, Phys. Rev. Lett. **74**, 4783.
Chapman, M. S., T. D. Hammond, A. Lenef, J. Schmiedmayer, R. A. Rubenstein, E. Smith, and D. E. Pritchard, 1995, Phys. Rev. Lett. **75**, 3783.
Clauser, J., 1997, in *Experimental Metaphysics*, edited by R. Cohen, M. Horne, and J. Stachel (Kluwer Academic, Dordrecht), p. 1.
Clauser, J. F., and S. Li, 1994, Phys. Rev. A **49**, R2213.
Clauser, J. F., and M. Reinsch, 1992, Appl. Phys. B **54**, 380.
Compagnon, I., R. Antoine, M. Broyer, P. Dugourd, J. Lermé, and D. Rayane, 2001, Phys. Rev. A **64**, 025201.
Compagnon, I., R. Antoine, D. Rayane, M. Broyer, and P. Dugourd, 2002, Phys. Rev. Lett. **89**, 253001.
Cronin, A. D., J. Schmiedmayer, and D. E. Pritchard, 2009, Rev. Mod. Phys. **81**, 1051.
Davis, K. B., M.-O. Mewes, M. R. Andrews, N. J. van Druten, D. S. Durfee, D. M. Kurn, and W. Ketterle, 1995, Phys. Rev. Lett. **75**, 3969.
De Heer, W. A., and V. V. Kresin, 2010, *Handbook of Nanophysics: Clusters and Fullerenes*, edited by K. D. Sattler, Handbook of Nanophysics (CRC Press, Boca Raton, FL), Chap. 10, p. 1.
Diosi, L., 1989, Phys. Rev. A **40**, 1165.
Dubetsky, B., and P. R. Berman, 1997a, in *Atom Interferometry*, edited by P. R. Berman (Academic Press, San Diego), p. 407.
Dubetsky, B., and P. R. Berman, 1997b, Phys. Rev. A **56**, R1091.
Eibenberger, S., S. Gerlich, M. Arndt, J. Tüxen, and M. Mayor, 2011, New J. Phys. **13**, 043033.
Ekstrom, C., J. Schmiedmayer, M. Chapman, T. Hammond, and D. Pritchard, 1995, Phys. Rev. A **51**, 3883.
Estermann, I., and O. Stern, 1930, Z. Phys. **61**, 95.
Fenn, J. B., M. Mann, C. K. Meng, S. F. Wong, and C. M. Whitehouse, 1989, Science **246**, 64.
Feynman, R., R. B. Leighton, and M. L. Sands, 1965, *The Feynman Lectures on Physics*, Vol. III, Quantum Mechanics (Addison-Wesley, Reading, MA).
Fray, S., C. A. Diez, T. W. Hänsch, and M. Weitz, 2004, Phys. Rev. Lett. **93**, 240404.
Fulton, R., A. I. Bishop, and P. F. Barker, 2004, Phys. Rev. Lett. **93**, 243004.
Geim, A., and K. Novoselov, 2007, Nature Mater. **6**, 183.
Gerlich, S., S. Eibenberger, M. Tomandl, S. Nimmrichter, K. Hornberger, P. J. Fagan, J. Tüxen, M. Mayor, and M. Arndt, 2011, Nature Commun. **2**, 263.
Gerlich, S., M. Gring, H. Ulbricht, K. Hornberger, J. Tüxen, M. Mayor, and M. Arndt, 2008, Angew. Chem., Int. Ed. Engl. **47**, 6195.
Gerlich, S., *et al.*, 2007, Nature Phys. **3**, 711.
Ghirardi, G. C., P. Pearle, and A. Rimini, 1990, Phys. Rev. A **42**, 78.
Ghirardi, G. C., A. Rimini, and T. Weber, 1986, Phys. Rev. D **34**, 470.
Gring, M., *et al.*, 2010, Phys. Rev. A **81**, 031604.
Grisenti, R. E., W. Schöllkopf, J. P. Toennies, G. C. Hegerfeldt, and T. Köhler, 1999, Phys. Rev. Lett. **83**, 1755.
Großardt, A., and D. Giulini, 2011, arXiv:1105.1921v1.
Gupta, M., and D. R. Herschbach, 1999, J. Phys. Chem. A **103**, 10670.
Gustavson, T. L., P. Bouyer, and M. A. Kasevich, 1997, Phys. Rev. Lett. **78**, 2046.
Haberland, H., M. Karrais, and M. Mall, 1991, Z. Phys. D **20**, 413.
Hackermüller, L., K. Hornberger, B. Brezger, A. Zeilinger, and M. Arndt, 2003, Appl. Phys. B **77**, 781.
Hackermüller, L., K. Hornberger, B. Brezger, A. Zeilinger, and M. Arndt, 2004, Nature (London) **427**, 711.
Hanley, L., and R. Zimmermann, 2009, Anal. Chem. **81**, 4174.
Hansen, K., and E. E. B. Campbell, 1998, Phys. Rev. E **58**, 5477.
Hasselbach, F., 2010, Rep. Prog. Phys. **73**, 016101.
Holmgren, W., M. Revelle, V. Lonij, and A. Cronin, 2010, Phys. Rev. A **81**, 053607.
Horak, P., G. Hechenblaikner, K. M. Gheri, H. Stecher, and H. Ritsch, 1997, Phys. Rev. Lett. **79**, 4974.
Hornberger, K., 2006, Phys. Rev. A **73**, 052102.
Hornberger, K., S. Gerlich, H. Ulbricht, L. Hackermüller, S. Nimmrichter, I. Goldt, O. Boltalina, and M. Arndt, 2009, New J. Phys. **11**, 043032.
Hornberger, K., L. Hackermüller, and M. Arndt, 2005, Phys. Rev. A **71**, 023601.
Hornberger, K., J. E. Sipe, and M. Arndt, 2004, Phys. Rev. A **70**, 053608.
Hornberger, K., S. Uttenthaler, B. Brezger, L. Hackermüller, M. Arndt, and A. Zeilinger, 2003, Phys. Rev. Lett. **90**, 160401.
Jacob, A., 2011, University of Duisburg-Essen (private communication).
Jönsson, C., 1961, Z. Phys. **161**, 454.
Joos, E., H. D. Zeh, C. Kiefer, D. Giulini, J. Kupsch, and I.-O. Stamatescu, 2003, *Decoherence and The Appearance of A Classical World in Quantum Theory* (Springer, Berlin), 2nd ed.
Juffmann, T., S. Truppe, P. Geyer, A. Mayor, S. Deachapunya, H. Ulbricht, and M. Arndt, 2009, Phys. Rev. Lett. **103**, 263601.
Kapitza, P. L., and P. A. M. Dirac, 1933, Proc. Cambridge Philos. Soc. **29**, 297.
Karolyhazy, F., 1966, Nuovo Cimento A **42**, 390.
Kasevich, M., D. S. Weiss, E. Riis, K. Moler, S. Kasapi, and S. Chu, 1991, Phys. Rev. Lett. **66**, 2297.
Keith, D. W., M. L. Schattenburg, H. I. Smith, and D. E. Pritchard, 1988, Phys. Rev. Lett. **61**, 1580.
Lau, E., 1948, Ann. Phys. (Leipzig) **437**, 417.
Leggett, A. J., 2002, J. Phys. Condens. Matter **14**, R415.
Lisdat, C., M. Frank, H. Knöckel, M.-L. Almazor, and E. Tiemann, 2000, Eur. Phys. J. D **12**, 235.
Marshall, W., C. Simon, R. Penrose, and D. Bouwmeester, 2003, Phys. Rev. Lett. **91**, 130401.
Martin, T. P., 1984, J. Chem. Phys. **81**, 4426.
McMorran, B. J., and A. D. Cronin, 2009, New J. Phys. **11**, 033021.
Miffre, A., M. Jacquey, M. Büchner, G. Trenec, and J. Vigue, 2006a, Phys. Rev. A **73**, 011603(R).
Miffre, A., M. Jacquey, M. Büchner, G. Trénec, and J. Vigué, 2006b, Appl. Phys. B **84**, 617.
Molhave, K., and M. Drewsen, 2000, Phys. Rev. A **62**, 011401.
Moshinski, M., 1952, Phys. Rev. **88**, 625.
Moskowitz, P. E., P. L. Gould, S. R. Atlas, and D. E. Pritchard, 1983, Phys. Rev. Lett. **51**, 370.
Nairz, O., M. Arndt, and A. Zeilinger, 2003, Am. J. Phys. **71**, 319.
Nairz, O., B. Brezger, M. Arndt, and A. Zeilinger, 2001, Phys. Rev. Lett. **87**, 160401.

PHYSICAL REVIEW A **83**, 043621 (2011)

Testing spontaneous localization theories with matter-wave interferometry

Stefan Nimmrichter,[1] Klaus Hornberger,[2,3] Philipp Haslinger,[1] and Markus Arndt[1]
[1]*University of Vienna, Vienna Center for Quantum Science and Technology (VCQ), Faculty of Physics, Boltzmanngasse 5, 1090 Vienna, Austria*
[2]*University of Duisburg-Essen, Faculty of Physics, Lotharstraße 1-21, 47048 Duisburg, Germany*
[3]*Max-Planck Institute for the Physics of Complex Systems, Nöthnitzer Straße 38, 01187 Dresden, Germany*
(Received 18 February 2011; published 27 April 2011)

We propose to test the theory of continuous spontaneous localization (CSL) in an all-optical time-domain Talbot-Lau interferometer for clusters with masses exceeding 10^6 amu. By assessing the relevant environmental decoherence mechanisms, as well as the growing size of the particles relative to the grating fringes, we argue that it will be feasible to test the quantum superposition principle in a mass range excluded by recent estimates of the CSL effect.

DOI: 10.1103/PhysRevA.83.043621 PACS number(s): 03.75.−b, 03.65.Ta, 03.65.Yz, 36.40.Vz

I. INTRODUCTION

It is a basic unresolved question of quantum mechanics whether the Schrödinger equation holds for truly macroscopic systems. Unitarity would then imply that even measurement devices or conscious observers could, in principle, be brought into a superposition of macroscopically distinct states. Most of the offered answers can be put into one of three categories. The affirmative statement, preferred in quantum cosmology, requires some interpretational exercise to explain why definite measurement outcomes are perceived in spite of all outcomes being simultaneously realized in a multitude of "Everett worlds." A quite different attitude, expressed most stringently in the operationalist formulation of quantum mechanics, attributes a fundamental role to the divide between "quantum system" and measurement device, such that it is meaningless to pose the question in the first place. The third option is to hypothesize that there is an objective modification of the unitary Schrödinger dynamics that gives rise to a macrorealist description of the physics on macroscopic scales [1].

Whatever one thinks about the need or plausibility of such unconventional theories of the quantum-to-classical transition, they have the clear advantage that they can be tested in principle. In this way they bring back to physics what is otherwise an issue of logical consistency and epistemology. Another motivation to consider the possibility that quantum physics is only an approximation to a deeper underlying theory may be drawn from the difficulties encountered when trying to reconcile it with the theory of gravity [2].

One of the best-studied models for the emergence of macrorealism is the theory of Ghirardi, Rimini, and Weber (GRW) [3], along with its refinement, the theory of continuous spontaneous localization (CSL) [4]. Its predictions are consistent with all quantum experiments so far, but they strongly deviate from quantum theory when applied to macroscopic objects [5]. According to the model, a delocalized quantum state of a material particle may experience a random "collapse," which localizes the wave function to a scale of about 100 nm. In the case of composite objects, the rate of these collapse events increases with mass, due to an inherent amplification mechanism. The values of the localization parameters are chosen such that they affect only systems considered to be in the macroscopic domain.

In this paper, we propose to test the CSL model by performing matter wave interference with clusters in the mass range between 10^6 and 10^8 amu. We assess the various relevant environmental decoherence processes expected to occur in an optimized time-domain Talbot-Lau interferometer with ultraviolet laser gratings, paying particular attention to the enhanced signal loss due to the finite cluster size. We conclude that it will become technologically feasible to test the quantum superposition principle at mass and time scales at which it is predicted to fail according to recent estimates by Adler and Bassi [6,7].

II. EFFECTS OF CONTINUOUS SPONTANEOUS LOCALIZATION

The observable consequences of the CSL model are accounted for in the framework of second quantization by adding the Lindblad term,

$$\frac{8\pi^{3/2} r_c^3 \lambda_0}{m_0^2} \int d\boldsymbol{x} \left[\mathsf{m}(\boldsymbol{x}) \varrho \, \mathsf{m}(\boldsymbol{x}) - \frac{1}{2} \{ \mathsf{m}^2(\boldsymbol{x}), \varrho \} \right], \qquad (1)$$

to the von Neumann equation for the many-particle density operator ϱ of a system of massive particles. Here, $\mathsf{m}(\boldsymbol{x})$ is the spatially blurred mass density operator, defined in terms of the number density operators $\mathsf{n}_k(\boldsymbol{x})$ of the constituent boson and fermion species and their respective masses m_k,

$$\mathsf{m}(\boldsymbol{x}) = \int d\boldsymbol{x}' \, g(\boldsymbol{x} - \boldsymbol{x}') \sum_k m_k \mathsf{n}_k(\boldsymbol{x}'). \qquad (2)$$

The function $g(\boldsymbol{x})$ is a normalized Gaussian whose width $r_c = 100$ nm is one of the parameters of the model. The second parameter is the term λ_0/m_0^2. One conventionally chooses the reference mass m_0 to be given by a nucleon, $m_0 = 1$ amu; as discussed in [6,7], reasonable lower bounds for the associated localization rate λ_0 are then in the range of 10^{-8} to 10^{-12} Hz. This is substantially larger than the value of 10^{-16} Hz originally suggested by GRW [3], since the CSL model implies a quadratic mass dependence of the effective

localization rate. It is a consequence of the second quantization formulation, which guarantees that the exchange symmetry of bosons and fermions remains unaffected by the collapse events.

In a molecule or a cluster, where the interparticle distances are much smaller than the localization scale r_c, the collapses affect only the quantum state ρ of the center of mass motion. One arrives at an effective master equation $\partial_t \rho = (i\hbar)^{-1}[\mathsf{H},\rho] + \mathcal{L}\rho$, with

$$\mathcal{L}\rho = \lambda\left[8\pi^{3/2} r_c^3 \int d\boldsymbol{x}'\, g(\mathsf{X}-\boldsymbol{x}')\rho\, g(\mathsf{X}-\boldsymbol{x}') - \rho\right]. \quad (3)$$

Here, X is the center-of-mass position operator, and $\lambda = \lambda_0(m/m_0)^2$, the effective localization rate depending quadratically on the total mass m [6,7].

We note that the master equation (3) is equivalent to a collisional decoherence master equation [8]. This implies that it induces a basis of localized, soliton-like pointer states for sufficiently large λ, which move without dispersion on the classical Newtonian trajectories [9].

III. TESTING SPONTANEOUS LOCALIZATION WITH NEAR-FIELD INTERFERENCE

We learn from Eq. (3) that continuous spontaneous localization can be tested as soon as a very massive particle is brought into a superposition state of different positions that exceed the distance of $r_c = 100$ nm for a sufficiently long time. We propose that a viable experiment can be based on the optical time-domain ionizing matter (OTIMA) interferometer described in [10].

In that experiment, a pulsed slow cloud of clusters is subjected to three pulsed standing light waves, generated for instance by an ultraviolet fluorine laser beam ($\lambda_L = 157$ nm), such that the particles in the antinodes are ionized and removed from the cloud. The number of remaining neutral clusters is then recorded as a function of the delay times between the grating pulses. This way, the first laser pulse generates spatial coherence in the cluster cloud by modulating its initial density. After a delay time T, the second pulse acts as a combined absorption and phase grating, where the nodes of the standing light field play the role of the "grating slits" with a period of $d = \lambda_L/2$, while the phases of the matter waves get shifted by the dispersive light-matter interaction. Talbot-Lau-type near-field interference finally produces a periodic cluster density pattern after a second time delay T, provided that T is close to an integer multiple of the Talbot time $T_T = md^2/h$—that is, $T = NT_T + \delta T$, with $\delta T/T \ll 1$. The recorded signal is predicted [10] to show high-contrast interference fringes as a function of δT, which are conveniently characterized by the sinusoidal visibility $\mathcal{V}$ defined as the ratio of amplitude and offset of a fitted sine curve.

If CSL exists, we predict a reduction of the interference visibility, which can be calculated by incorporating the CSL master equation (3) into the theoretical description of the interferometer, as in the case of environmental decoherence [11]. One arrives at the closed expression

$$\frac{\mathcal{V}_{CSL}}{\mathcal{V}} = \exp\left\{-2\lambda_0 T_0 N \frac{m^3}{m_0^3}\left[1 - \frac{\sqrt{\pi} r_c}{Nd}\,\mathrm{erf}\left(\frac{Nd}{2r_c}\right)\right]\right\}. \quad (4)$$

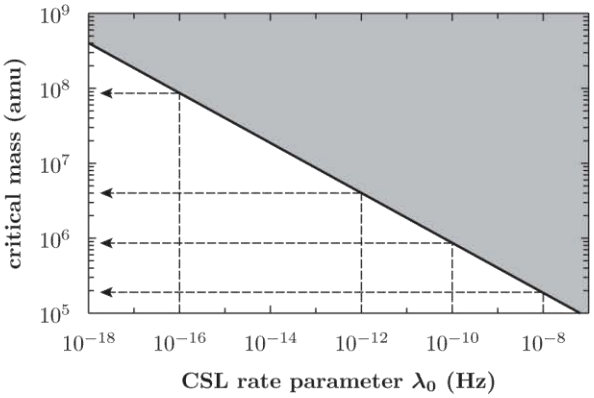

FIG. 1. Critical mass m_c for testing continuous spontaneous localization (CSL) as a function of the localization rate λ_0, assuming the geometry of the proposed experiment with $N = 2$. The shaded area indicates the parameter region where interference should be unobservable according to the CSL model. The dashed arrows mark the critical masses associated with reasonable estimates for the lower bound of λ_0 [6,7].

Here, we introduced the Talbot time per atomic mass unit $T_0 = m_0 d^2/h$. The cubic mass dependence in the exponent is the reason why an interferometric test of the CSL model becomes conceivable.

Figure 1 shows the critical cluster mass m_c where CSL predicts the reduction $\mathcal{V}_{CSL} = \mathcal{V}/2$ in the proposed OTIMA experiment. Observing substantial interference at m_c thus puts a strict upper bound on the localization rate λ_0 by ruling out values greater than those given by the solid line. Here, we take $N = 2$—that is, the second Talbot order. This ensures that the effective interference path separation $Nd = 157$ nm exceeds the localization scale r_c, such that the factor in square brackets takes an appreciable value.

Using Fig. 1, we can assess whether the literature values for the CSL rate can be tested in the proposed setup. The most recent calculations suggest that $\lambda_0 = 10^{-10\pm2}$ Hz [6,7], while the original GRW estimate was $\lambda_0 = 10^{-16}$ Hz [3]. These values require the cluster mass to reach $m_c = 10^{5.9\pm0.7}$ and 9×10^7 amu, respectively, as marked by the dashed arrows in Fig. 1. Remarkably, the lower value already touches the range that should be reached with present-day technology in the OTIMA interferometer [10]. However, for a distinctive test of CSL, one must venture beyond that, which requires one to cope in particular with two additional types of contrast limiting effects [12].

First, the total interference time $2NT_T$ grows linearly with the cluster mass. At 10^6 amu, it already amounts to about 60 ms at the second Talbot order, if a 157 nm laser is used. At 10^8 amu, the gravitational free fall must be compensated for and the cluster velocity must be controlled with high precision. This requires motional slowing, guiding [13], and trapping techniques [14,15] for large clusters, and possibly a microgravitational environment [16]. The increased interference time also aggravates the decohering influence of environmental interactions and external forces, as discussed in the following section.

Second, the size of the clusters grows with increasing mass. Apart from enhancing the interaction with the radiation field and with residual gas particles, this implies that the cluster size becomes comparable to the period $d = \lambda_L/2$ of the optical gratings. Starting with this last problem, we proceed to analyze under what conditions OTIMA interference will be possible with ultramassive clusters, so as to provide a testing ground for spontaneous localization.

IV. OTIMA INTERFERENCE IN THE LIMIT OF HIGH PARTICLE MASSES

In the molecular matter-wave interference experiments carried out so far, it was justified to treat the delocalized objects as polarizable point particles. Since this approximation breaks down beyond 10^6 amu, we formulate the interaction between the ionizing optical gratings and the finite-size spherical clusters using Mie theory [17]. As explained in [10], both coherent diffraction and photoabsorption are described by $n(x)$, the average number of photons absorbed by each cluster during a laser pulse,

$$n(x) = n_0 + n_1 \cos\left(\frac{2\pi x}{d}\right). \tag{5}$$

Here, x is the transverse center-of-mass position of the cluster, and n_0 is the position-averaged mean number of absorbed photons. Only the modulation n_1 gives rise to interference; the corresponding visibility [10]

$$\mathcal{V} = 2\frac{I_1^2(n_1)I_2(n_1)}{I_0^3(n_1)} \tag{6}$$

is independent of the Talbot order N, and involves modified Bessel functions of the first kind. The position average n_0, on the other hand, determines the total transmissivity $\mathcal{T}$ of the three gratings—that is, the fraction of remaining neutral clusters after three grating pulses,

$$\mathcal{T} = \exp(-3n_0)I_0^3(n_1). \tag{7}$$

For clusters that are small compared to the laser wave length, the point particle approximation yields $n_1 = n_0 = 2F_L\sigma_{abs}/h\nu_L$, proportional to the absorption cross section and to the energy flux F_L of the running-wave laser input [10]. For large clusters, the corresponding expressions can be obtained by computing the absorbed power of a dielectric sphere with radius R in a standing-wave field. A lengthy calculation yields

$$\begin{matrix} n_1 \\ 0 \end{matrix} = \frac{4F_L}{h\nu_L}\sum_{\ell=1}^{\infty}\frac{(2\ell+1)\pi}{k_L^2\rho}(\mp)^{\ell-1}\left(\sigma_\ell^{(E)} \pm \sigma_\ell^{(H)}\right), \tag{8}$$

with the electric and magnetic multipole components

$$\sigma_\ell^{(E)} = \frac{\mathrm{Im}\{\varepsilon j_\ell[\sqrt{\varepsilon}\rho j_{\ell-1} - \ell j_\ell]^*\}}{|\ell(\varepsilon-1)j_\ell h_\ell + \sqrt{\varepsilon}\rho[j_{\ell-1}h_\ell - \sqrt{\varepsilon}\, j_\ell h_{\ell-1}]|^2},$$
$$\sigma_\ell^{(H)} = \frac{\mathrm{Im}\{\sqrt{\varepsilon}\, j_\ell^* j_{\ell-1}\}}{\rho|j_\ell h_{\ell+1} - \sqrt{\varepsilon}\, j_{\ell+1}h_\ell|^2}. \tag{9}$$

The latter are determined by the scaled cluster radius $\rho = k_L R = 2\pi R/\lambda_L$ and by the relative permittivity ε of the material. We use a shorthand notation for the spherical Bessel function in the dielectric, $j_\ell \equiv j_\ell(\sqrt{\varepsilon}\rho)$, and for the vacuum solutions $h_\ell \equiv h_\ell^{(1)}(\rho)$, given by spherical Hankel functions of the first kind.

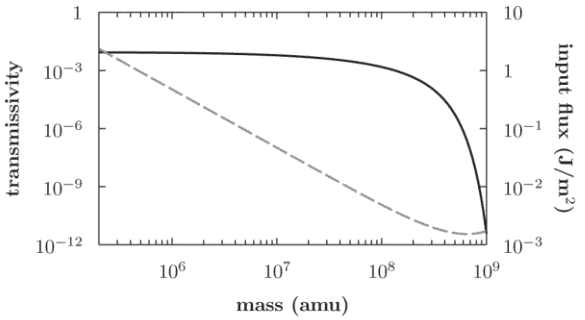

FIG. 2. Transmissivity [Eq. (7)] of the OTIMA interferometer vs the gold cluster mass. The dashed line (right scale) gives the laser flux, required to fix the visibility at $\mathcal{V} = 85\%$.

As the clusters grow in size, both absorption parameters n_0 and n_1 increase. This can be compensated for by turning down the grating laser flux F_L. However, if we want to maintain a fixed visibility [Eq. (6)] for growing clusters, the detection probability per particle $\mathcal{T}$ drops rapidly. This is because the ratio n_0/n_1 grows drastically once the cluster radius becomes comparable to the grating period, which is the main effect of the cluster size in the subwavelength regime.

Figure 2 shows the OTIMA transmissivity for gold clusters as a function of their mass. The relative permittivity at $\lambda_L = 157$ nm is approximated by the bulk value $\varepsilon = 0.9 + 3.2i$, as is the mass density. We keep the interference fringe visibility [Eq. (6)] at 85% by varying the laser flux (dashed line). When comparing the medium-sized Au_{1000} with a cluster 1000 times more massive, a laser pulse almost 1000 times weaker will suffice for the latter. The transmissivity, however, drops then from $\mathcal{T} = 1\%$ to 4×10^{-4} of the incident cluster flux. This shows that the signal loss becomes prohibitively large beyond 10^8 amu, where cluster size and wavelength become comparable even for the densest metals.

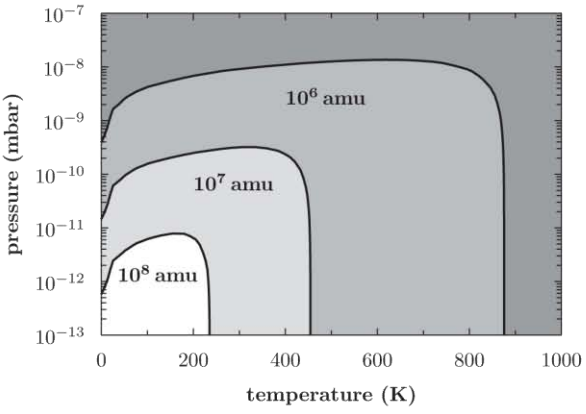

FIG. 3. The contour lines give the critical residual gas pressures and the critical ambient temperatures for observing interference of gold clusters with masses of 10^6, 10^7, and 10^8 amu.

However, even before this size-induced mass limit is reached, environmental decoherence will become important if the cluster particles are not properly isolated and cooled. We identify three relevant decoherence processes: (i) the elastic scattering of laser photons during the grating pulses, (ii) collisions with residual gas particles, and (iii) the emission, absorption, and scattering of thermal black-body photons. The first process was shown [10] to be negligible below 10^9 amu. The other two effects pose constraints on the background pressure and the temperature of the setup. Both effects are well understood [11,18,19]. Their dependence on the cluster mass differs from the CSL effect (4), and allows one in principle to separate the environmentally induced visibility reduction due to CSL by independently varying the temperature and the pressure of the interferometer chamber.

In Fig. 3, we plot the critical background pressure p_c and temperature T_c, where environmental decoherence reduces the interference visibility by a factor of 2. The contour lines correspond to the cluster masses $m/\text{amu} = 10^6, 10^7$, and 10^8, with the shaded area indicating where interference is largely suppressed by the environment. The area of high fringe visibility shrinks with growing cluster mass, since the optical absorption, the Rayleigh scattering cross section, and the collisional cross section all grow with size. Here we assume that the residual gas consists of N_2, and we use the electric properties of bulk gold to assess all decoherence processes. The cluster temperature is assumed to be in equilibrium with the environment, implying that in addition to the thermal emission of radiation, both the absorption and the elastic scattering of black-body photons contribute significantly to the thermal decoherence effect.

We infer from Fig. 3 that decoherence can be fairly easily controlled for 10^6-amu clusters at a pressure of 10^{-9} mbar and room temperature. An experiment with 10^8 amu, in contrast, will require cooling the setup and the clusters to below 200 K, in a chamber evacuated below 10^{-12} mbar. This is challenging but feasible, as demonstrated by cryogenic trap experiments at 10^{-17} mbar and 4.2 K [20].

V. CONCLUSIONS

For a long time, the implications of the theory of continuous spontaneous localization were thought to be practically unobservable. Our present assessment shows that this is not the case. Indeed, experiments aimed at demonstrating matter-wave interference with massive clusters in the range between 10^6 and 10^8 amu will provide an ideal testing ground for this unconventional theory of the quantum-to-classical transition, one of the leading contenders in resolving the fundamental question of macroscopic realism.

ACKNOWLEDGMENTS

We thank the Austrian Science Fund (FWF) for support within the projects Wittgenstein Z149-N16 and DK-W1210 CoQuS. We also acknowledge financial support within the MIME project of the ESF EuroQUASAR program, through FWF and the Deutsche Forschungsgemeinschaft (DFG).

[1] A. J. Leggett, J. Phys. Condens. Mat. **14**, R415 (2002).
[2] R. Penrose, *The Road to Reality* (Jonathan Cape, London, 2004).
[3] G. C. Ghirardi, A. Rimini, and T. Weber, Phys. Rev. D **34**, 470 (1986).
[4] P. Pearle, Phys. Rev. A **39**, 2277 (1989); G. C. Ghirardi, P. Pearle, and A. Rimini, *ibid.* **42**, 78 (1990).
[5] A. Bassi and G. Ghirardi, Phys. Rep. **379**, 257 (2003).
[6] S. Adler, J. Phys. A **40**, 2935 (2007); S. Adler and A. Bassi, Science **325**, 275 (2009).
[7] A. Bassi, D.-A. Deckert, and L. Ferialdi, Europhys. Lett. **92**, 50006 (2010).
[8] B. Vacchini, J. Phys. A **40**, 2463 (2007).
[9] M. Busse and K. Hornberger, J. Phys. A **43**, 015303 (2010).
[10] S. Nimmrichter, P. Haslinger, K. Hornberger, and M. Arndt, e-print arXiv:1102.3644v1 [quant-ph] (2011).
[11] K. Hornberger, J. E. Sipe, and M. Arndt, Phys. Rev. A **70**, 053608 (2004).
[12] In A. Bassi, E. Ippoliti, and S. L. Adler, Phys. Rev. Lett. **94**, 030401 (2005), it was suggested to test CSL in a superposition experiment with a mirror, which would have to be cooled to its vibrational ground state and be sufficiently isolated to prevent environmental decoherence. If 50% of the coherence could be maintained during one oscillation period, this would imply $\lambda_0 < 7 \times 10^{-9}$ Hz, which touches only the upper end of the recent estimates.
[13] M. Schiffer, M. Rauner, S. Kuppens, M. Zinner, K. Sengstock, and W. Ertmer, Appl. Phys. B. **67**, 705 (1998).
[14] A. E. Cohen, Phys. Rev. Lett. **94**, 118102 (2005).
[15] D. E. Chang, C. A. Regal, S. B. Papp, D. J. Wilson, J. Ye, O. Painter, H. J. Kimble, and P. Zoller, Proc. Natl. Acad. Sci. USA **107**, 1005 (2010).
[16] H. Selig, H. Dittus, and C. Lämmerzahl, Micrograv. Sci. Tech. **22**, 539 (2010).
[17] H. C. van de Hulst, *Light Scattering by Small Particles* (Dover, New York, 1981); J. D. Jackson, *Classical Electrodynamics*, 3rd ed. (Wiley, Hoboken, NJ, 1999).
[18] L. Hackermüller, K. Hornberger, B. Brezger, A. Zeilinger, and M. Arndt, Appl. Phys. B **77**, 781 (2003).
[19] L. Hackermüller, K. Hornberger, B. Brezger, A. Zeilinger, and M. Arndt, Nature (London) **427**, 711 (2004).
[20] G. Gabrielse, X. Fei, L. A. Orozco, R. L. Tjoelker, J. Haas, H. Kalinowsky, T. A. Trainor, and W. Kells, Phys. Rev. Lett. **65**, 1317 (1990).

New Journal of Physics
The open-access journal for physics

Concept of an ionizing time-domain matter-wave interferometer

Stefan Nimmrichter[1], **Philipp Haslinger**[1], **Klaus Hornberger**[2] **and Markus Arndt**[1,3]

[1] Vienna Center for Quantum Science and Technology (VCQ), University of Vienna, Faculty of Physics, Boltzmanngasse 5, 1090 Vienna, Austria
[2] Max-Planck Institute for the Physics of Complex Systems, Nöthnitzer Straße 38, 01187 Dresden, Germany
E-mail: markus.arndt@univie.ac.at

New Journal of Physics **13** (2011) 075002 (23pp)
Received 15 October 2010
Published 5 July 2011
Online at http://www.njp.org/
doi:10.1088/1367-2630/13/7/075002

Abstract. We discuss the concept of an all-optical and ionizing matter-wave interferometer in the time domain. The proposed setup aims at testing the wave nature of highly massive clusters and molecules, and it will enable new precision experiments with a broad class of atoms, using the same laser system. The propagating particles are illuminated by three pulses of a standing ultraviolet laser beam, which detaches an electron via efficient single-photon absorption. Optical gratings may have periods as small as 80 nm, leading to wide diffraction angles for cold atoms and to compact setups even for very massive clusters. Accounting for the coherent and the incoherent parts of the particle–light interaction, we show that the combined effect of phase and amplitude modulation of the matter waves gives rise to a Talbot–Lau-like interference effect with a characteristic dependence on the pulse delay time.

[3] Author to whom any correspondence should be addressed.

Contents

1. Introduction

1.1. Interferometry with molecules

In recent decades, matter-wave interferometry has developed into a highly active research field, ranging from the foundations of physics to quantum enhanced precision measurements. Beam splitters, mirrors, diffraction gratings, traps or wave guides are nowadays readily available for electrons [1], neutrons [2] and atoms [3], but they still represent a substantial challenge for large clusters or molecules.

Diffraction and interference experiments with molecules were started systematically only in the mid-1990s and led to the exploration of far-field diffraction effects at nanomechanical [4–6] and optical gratings [7], as well as at opaque discs [8]. Interferometers were operated using nanogratings in a Mach–Zehnder configuration [9], running laser waves in a Ramsey–Bordé arrangement [10, 11], mechanical gratings in a near-field Talbot–Lau design [12, 13] or, more recently, in a combination of mechanical and optical phase gratings [14, 15].

All these designs have their merits and drawbacks. While far-field experiments are conceptually appealing and allow one to spatially separate the diffraction orders, it was already pointed out by Clauser [16] that the use of a near-field configuration, such as the Talbot–Lau interferometer (TLI), offers several advantages, in particular much reduced collimation and coherence requirements and therefore increased signals.

1.2. Optical elements for matter-wave interferometry

Nanomechanical gratings, which serve to block a part of the particle beam, are the most natural diffraction elements for matter waves. Using modern lithographic techniques, it is nowadays possible to nanofabricate, e.g., silicon nitride structures with a precision that guarantees a predefined slit period to within a few angstroms, even over millimeter-sized areas [17]. Such masks are of great importance for many applications in atom [18, 19] and electron interferometry [20, 21] since they do not rely on any internal particle property.

However, for highly polarizable and slow particles, the presence of dispersion forces near the grating walls becomes increasingly important [6, 12, 22, 23]. These van der Waals or Casimir–Polder interactions introduce a phase shift with a strong position and velocity dependence [24, 25]. The force may even remove a substantial part of the molecules from the beam when they get too close to the surface.

In contrast to that, optical standing-wave gratings can be neither destroyed nor clogged by large particles. Narrow-band lasers allow one to define the grating period with high precision and the grating transmission function, defined by the particle–light interaction, can be controlled and modulated *in situ* and on a short time scale via the laser intensity [26, 27].

1.3. From phase gratings to absorptive gratings of light

The use of optical phase gratings is by now well established in atom interferometry (e.g. [27–31]), with electron beams [32] and for complex molecules [7, 14]. Interferometry with phase gratings requires a prior effort in preparing sufficient transverse coherence in the particle beam. This is naturally provided by an atomic Bose–Einstein condensate [33] or if the diffracting particles start already in a periodic arrangement predefined by a potential [34]. A spatially extended and incoherent molecular beam requires us, however, to use an absorptive grating prior to the diffracting phase mask to prepare some transverse coherence. An elegant way of realizing an absorptive optical grating for atoms is to pump them into a dark state, i.e. into an undetected internal state. This strategy works rather well for atoms [35, 36], but clusters and molecules usually do not offer the needed addressability of selected states.

In this paper, we focus on the implementation of absorptive gratings via single-photon ionization (SPI) in the anti-nodes of an ultraviolet (UV) standing light wave [37]. Modern (V)UV lasers readily provide the photon energy required to surpass the ionization threshold of many kinds of neutral atoms, clusters and molecules. The optical grating will imprint a nanostructured periodic amplitude profile onto the particle beam, very much like a material mask, and separate charged and neutral particles. We study, in particular, the sequence of three ionizing optical grating pulses in the time domain. The delay between the pulses serves as a control parameter, while the spatial positions of the gratings are fixed.

The high time resolution of modern lasers allows us to take advantage of all the benefits that are shared by other atom interferometers in the time domain [27, 30, 38]: the interference fringe

positions can be largely independent of the particle velocity and the interference pattern can be scanned with very high accuracy and without any moving mechanical parts. While the idea of ionization gratings is here worked out for massive clusters, the method is naturally extended to atoms as well.

2. Optical time-domain ionizing matter interferometer

In the following, we will consider particles that are much smaller than the laser wave length, and refer to them as 'clusters', even though the concept also applies to atoms or some molecules. The particle–light interaction is then governed by two parameters, the (real) optical dipole polarizability α and the absorption cross-section σ_{abs} at the laser frequency.

2.1. Interferometric setup

The layout and time sequence of an optical time-domain ionizing matter-wave (OTIMA) interferometer are depicted in figure 1. A pulsed cluster beam passes alongside a plane mirror which serves to retro-reflect the beam of a UV laser. The light source illuminates each cluster cloud in three short pulses, separated by the equal time delay T. We denote them by G_1, G_2 and G_3. The laser beam waist is chosen such that all clusters are covered equally by the standing light waves, thus ensuring that all particles with the same distance to the mirror experience the same light intensity. Depending on the velocity of the cluster beam, this can be realized by a single laser of high repetition rate or three pulses that follow the particle cloud along its direction of motion.

The particles are also subjected to a (weak) constant force perpendicular to the mirror plane, e.g. gravity or an electric field with $\nabla E^2 = \mathrm{const}$. The field will also serve to remove all ions from the beam. Since all relevant forces only depend on the cluster–mirror distance, we restrict our attention to this x-axis.

A grating pulse acts in several ways: firstly, the optical dipole potential imprints a sinusoidal phase modulation onto the center-of-mass state of the clusters. The period d is given by half the laser wavelength, $d = \lambda_{\mathrm{L}}/2$. The maximal phase shift ϕ_0 is proportional to the real part of the optical polarizability α and to the laser pulse energy. Secondly, even a single absorbed photon will ionize a given cluster. The probability of such ionization events is again an oscillating function of the transverse position x. The average number n_0 of absorbed photons in the antinodes is proportional to the absorption cross-section σ_{abs} and to the laser pulse energy. The spatially periodic ionization of the clusters, and their removal by the electric field, then results in an amplitude modulation of the particle beam, much like in a material grating. It is important that a cluster does indeed ionize with high probability after the absorption of a single photon. Photoabsorption results in a momentum kick of $\pm h/\lambda_{\mathrm{L}}$ with a random sign. This could blur the interference pattern if the particles were not ionized and removed. A third effect is the radiation pressure exerted on the clusters due to Rayleigh scattering. This is a potential source of decoherence since the scattered photons impart momentum kicks onto the clusters which are comparable to the 'grating momentum' $\Delta p_{\mathrm{G}} = h/d$ but randomly directed (see section 4.1). Behind the interferometer the remaining neutral clusters are detected mass-selectively. The interference pattern will manifest itself in a characteristic dependence of the count rate on the particle mass m, the pulse separation T, the external acceleration a and the laser pulse intensity.

IOP Institute of Physics DEUTSCHE PHYSIKALISCHE GESELLSCHAFT

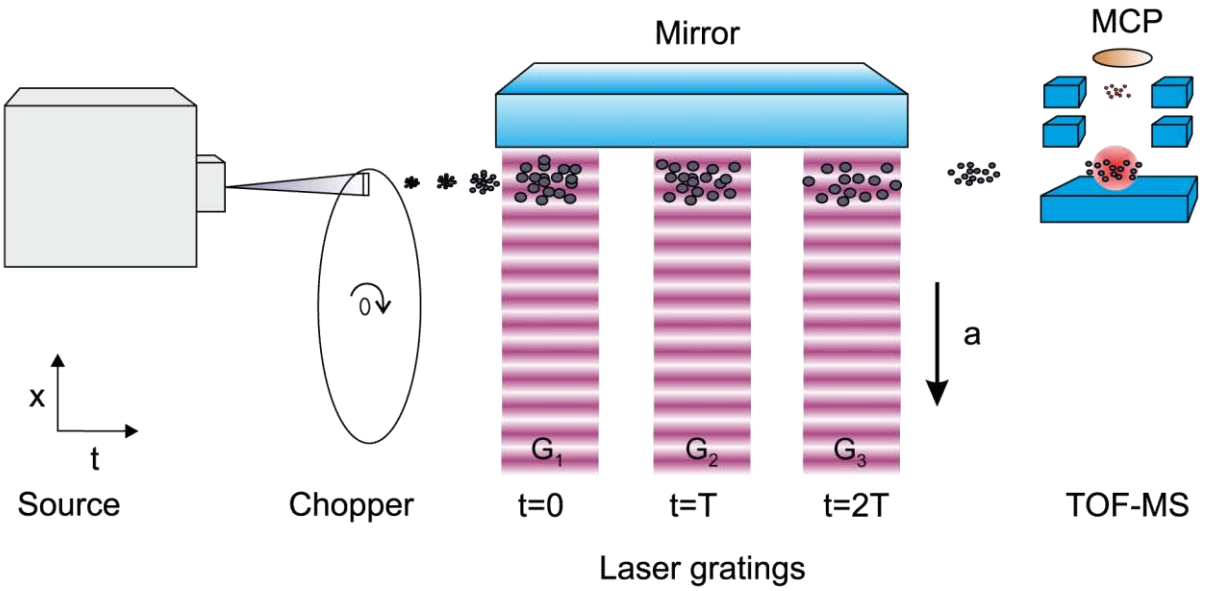

Figure 1. Experimental layout and pulse sequence for an OTIMA interferometer. A beam of nanoparticles is chopped into bunches, each of which is subsequently illuminated by the same three laser pulses (G_1, G_2 and G_3), separated by a variable but equal delay time T of the order of the Talbot time T_T. The retro-reflection of the laser light at a common plane mirror generates a phase-stable standing wave. The laser wave length is sufficiently short to ionize the particles with high probability at the antinodes after absorbtion of a single photon. The ions are removed by a homogeneous electric field. The remaining neutral particles fly into a time-of-flight mass spectrometer (TOF-MS), where they are photo-ionized, accelerated and detected by a multi-channel plate (MCP). This scheme allows one to post-select the clusters with a mass selectivity of better than 0.1% and to perform the experiment with a large number of different masses simultaneously. A quantum interference fringe pattern is observed in the count rate by varying the pulse separation T, provided the clusters are exposed to an additional constant acceleration a, e.g. due to gravitation or a constant electrical field gradient.

2.2. Near-field interference

Near-field TLIs are particularly well suited for exploring quantum wave mechanics with massive particles and short de Broglie wave lengths [12, 14, 16, 24, 25]. In our time-domain version, the laser pulses modify the x-component of the motional cluster state in the same way as the three gratings of a TLI 'in space'. The two concepts are related to each other by a change of the reference frame.

Compared to a mechanical Talbot–Lau setup, the optical analogue adds substantial control due to the precisely defined delay between the pulses and the possibility of tuning the pulse strengths individually. This allows one to overcome source imperfections, in particular the longitudinal velocity spread in the beam, and to optimize the fringe visibility. In contrast to the spatial near-field interferometer, which is characterized by the Talbot distance $L_T = d^2/\lambda$,

the characteristic scale in the time domain is given by the Talbot time [27]

$$T_{\mathrm{T}} = md^2/h. \tag{1}$$

This is the typical time for the self-imaging of a pulsed diffraction grating under coherent illumination.

In practice, the x-momentum distribution Δp_x of the particle cloud will be much broader than the 'grating momentum' h/d. The role of G_1 at $t = 0$ is therefore reduced to acting as a mask that prepares spatial coherence by only transmitting particles from many parallel but very narrow 'sources' in the nodes of the standing laser wave. Some transverse coherence thus emerges after time $t = T$, when the second grating pulse G_2 is applied. The amplitude and phase modulation at G_2 then leads to a resonant spatial modulation of the cluster density at time $t = 2T$ [27, 39]. The normalized particle density (section 3) then takes the form

$$w_{2T}(x) = \frac{1}{d}\sum_{\ell=-\infty}^{\infty} B_{-\ell}^{(1)}(0) B_{2\ell}^{(2)}\left(\ell\frac{T}{T_{\mathrm{T}}}\right)\exp\left(\frac{2\pi \mathrm{i}\ell(x - aT^2)}{d}\right). \tag{2}$$

This pattern is again periodic in x, with period d, but it is shifted in the presence of an acceleration a.

The Fourier components characterizing the fringe pattern (2) can be specified in terms of the Talbot–Lau coefficients of the kth grating [15],

$$B_m^{(k)}(\xi) = \mathrm{e}^{-n_0^{(k)}/2}\left[\frac{\zeta_{\mathrm{coh}} - \zeta_{\mathrm{ion}}}{\zeta_{\mathrm{coh}} + \zeta_{\mathrm{ion}}}\right]^{m/2} J_m\left(\mathrm{sgn}(\zeta_{\mathrm{coh}} + \zeta_{\mathrm{ion}})\sqrt{\zeta_{\mathrm{coh}}^2 - \zeta_{\mathrm{ion}}^2}\right), \tag{3}$$

involving the expressions

$$\zeta_{\mathrm{ion}} = n_0^{(k)}\cos(\pi\xi)/2, \tag{4}$$

$$\zeta_{\mathrm{coh}} = \phi_0^{(k)}\sin(\pi\xi). \tag{5}$$

Here J_{m} is the Bessel function of the first kind and $n_0^{(k)}$ and $\phi_0^{(k)}$ are the above-mentioned grating pulse parameters, specifying the maximal mean number of absorbed photons and the maximum phase shift, respectively. They are defined in section 3 by equations (11) and (17).

Note in equation (2) how the dependence on $\xi = \ell T/T_{\mathrm{T}}$ in the second grating coefficient modulates the parameters (4) and (5) of ionization and phase shift and thus relates the pulse timing T to the Talbot time T_{T}. It is in this functional dependence that the quantum scale T_{T} enters, leading to the rich fringe structures characteristic of near-field interference phenomena.

The components attributed to the first grating mask ($k = 1$) take the simpler form

$$B_{\mathrm{m}}^{(k)}(0) = \exp\left(-\frac{n_0^{(k)}}{2}\right) I_{\mathrm{m}}\left(-\frac{n_0^{(k)}}{2}\right), \tag{6}$$

where I_{m} is the modified Bessel function of the first kind. Note that this factor depends only on the photon absorption $n_0^{(k)}$, not on the phase shift. In the limit of small photon absorption $n_0^{(1)} \to 0$, we find that $B_{\mathrm{m}}^{(1)}(0) = \delta_{\mathrm{m},0}$. This implies that if the first optical grating does not ionize the clusters the final density distribution (2) will be as uniform as the initial particle cloud, even though there is a substantial additional phase shift. In the case of equal time delays T between the pulses, the first grating must therefore be ionizing, i.e absorptive, in order to generate a fringe pattern.

Near-field interference may arise behind pure phase gratings, under some circumstances: as discussed in section 3, coherent rephasing effects can be expected at times $T+\tau$ after the second pulse, with $|\tau| \ll T$. Such transient near-field diffraction phenomena were observed in several time-domain experiments [27, 40, 41] where the Bragg reflection of the third laser pulse was used to detect the reconstructed atomic density pattern. In contrast to that, our present proposal uses the symmetric Talbot–Lau recurrence with its high visibility and robustness, as required for slow cluster beams detected by a third absorptive mask.

2.3. Fringe visibility

The fringe pattern (2) is finally probed by the third laser field G_3 which ionizes and extracts the clusters in its antinodes and transmits the remaining neutrals to the detector. Their fraction is proportional to

$$S = \sum_{\ell=-\infty}^{\infty} \underbrace{B_{-\ell}^{(1)}(0)\, B_{2\ell}^{(2)}\left(\ell \frac{T}{T_{\mathrm{T}}}\right) B_{-\ell}^{(3)}(0)}_{\equiv S_\ell} \exp\left(\frac{2\pi \mathrm{i} \ell a T^2}{d}\right). \tag{7}$$

When recorded as a function of the transverse acceleration a, this periodic signal has a form similar to the density pattern (2). The Fourier coefficients now merely contain in addition the components $B_n^{(3)}(0)$ of the third grating pulse. A useful interference pattern can be recorded even if the force is constant as in the presence of gravity $a = g$: in this case one varies the pulse delay T on the scale $\Delta T \lesssim d/2gT$. If this is much smaller than the Talbot time T_{T}, the resulting pattern is practically periodic in T^2 since the Fourier coefficients then hardly change on that scale. This is naturally the case for massive clusters, while one requires a high multiple $M \gg 1$ of the Talbot time, $T = MT_{\mathrm{T}}$, for atoms and light molecules.

The fringe visibility of the periodic signal (7) is conventionally defined as

$$\mathcal{V} = \frac{S_{\max} - S_{\min}}{S_{\max} + S_{\min}}. \tag{8}$$

In practice, the pattern is often close to sinusoidal, allowing one to describe the experimental observation by fitting a d-periodic sine curve with offset S_0 and amplitude $2S_1$ to the measured data. It is then more appropriate to consider the 'sinusoidal visibility' $\mathcal{V}_{\sin}$, the visibility associated with the first Fourier component. For the expected signal (7), and after the insertion of (3) and (6), it is given by

$$\mathcal{V}_{\sin} = \frac{2|S_1|}{S_0} = 2\frac{I_1\left(n_0^{(1)}/2\right)}{I_0\left(n_0^{(1)}/2\right)} \cdot \frac{\left|(\zeta_{\mathrm{coh}} - \zeta_{\mathrm{ion}})\, J_2\left(\sqrt{\zeta_{\mathrm{coh}}^2 - \zeta_{\mathrm{ion}}^2}\right)\right|}{|\zeta_{\mathrm{coh}} + \zeta_{\mathrm{ion}}|\, I_0\left(n_0^{(2)}/2\right)} \cdot \frac{I_1\left(n_0^{(3)}/2\right)}{I_0\left(n_0^{(3)}/2\right)}. \tag{9}$$

Note that the sinusoidal visibility may assume values larger than one, while the conventional visibility (8) by definition cannot exceed 100%.

2.4. Quantum or classical patterns?

It is important to keep in mind that the observation of fringes in a two-grating or three-grating setup is, by itself, not yet conclusive proof of quantum interference, since moiré-type shadow patterns can also be created by particles moving on classical trajectories. The genuine quantum

origin of the patterns is revealed by their characteristic dependence on the quantum scale (1) and the detailed functional dependence of the fringe visibility on various parameters. It is encoded, formally, in the oscillating ξ dependence of the Talbot–Lau coefficients (3) for the second grating pulse, while the actions of G_1 and G_3 are the same in the quantum and the classical formulation. Calculating the deflection of a classical trajectory under the influence of a standing light-wave one obtains classical analogues of the Talbot–Lau coefficients [15]. Their form is identical to the quantum coefficients (3), except for the definitions (4) and (5) of the parameters $\zeta_{\rm ion}$ and $\zeta_{\rm coh}$. They are now simply given by $\zeta_{\rm ion} = n_0^{(k)}/2$ and $\zeta_{\rm coh} = \phi_0^{(k)}\pi\xi$; in particular, they do not oscillate with ξ.

In agreement with intuitive expectations, the classical and the quantum description converge in the limit of large masses, $m \to \infty$, or for short pulse separations, $T \to 0$, where the argument of the Talbot–Lau coefficients (3) tends to zero. They do differ markedly for finite masses and times. Genuine quantum interference becomes clearly distinguishable from any classical dynamics when the pulse delay time T exceeds at least the Talbot time, $T \gtrsim T_{\rm T}$.

2.5. *Expected visibilities for high-mass clusters*

We now discuss how the expected interference visibility (9) depends on the laser pulse parameters and on the optical cluster properties for high-mass metal clusters. The photon absorption parameters $n_0^{(k)}$ grow linearly with the laser intensities; they determine the 'survival factors' $B_0^{(k)}(0)$ for each grating pulse, i.e. the spatially averaged probabilities of a particle not to be ionized during the kth pulse. The optimal laser power is therefore a compromise: large photon numbers may increase the interference visibility, but they also decrease the number of clusters that arrive at the detector, $S_0 = B_0^{(1)}(0)\,B_0^{(2)}(0)\,B_0^{(3)}(0)$.

While the first and the third grating pulse are fully characterized by the absorption parameters $n_0^{(1)}$ and $n_0^{(3)}$, the second pulse shapes the interfering matter wave in amplitude and phase with parameters $n_0^{(2)}$ and $\phi_0^{(2)}$. To account for the specific optical properties of the interfering particle independently of the laser intensity, it is therefore convenient to use the dimensionless ratio

$$\beta = \frac{n_0^{(2)}}{2\phi_0^{(2)}} = \frac{\lambda_{\rm L}\sigma_{\rm abs}}{8\pi^2\alpha}, \tag{10}$$

with $\lambda_{\rm L}$ being the laser wave length. We assume this to be 157 nm, as will be justified below.

In order to visualize the expected interference patterns, we keep the first and third grating intensities fixed at $n_0^{(1)} = n_0^{(3)} = 8$ and choose the cluster parameter $\beta = 1.0$ to be characteristic of large gold clusters, essentially independent of the particle size. Figure 2(a) depicts the sinusoidal visibility as a function of the delay time T in units of the Talbot time $T_{\rm T}$ for $n_0^{(2)} = 8$. Figure 2(b), on the other hand, shows the fringe contrast at $T = T_{\rm T}$ when the intensity of G_2 is varied between $n_0^{(2)} = 0$ and $n_0^{(2)} = 10$. Both the quantum prediction (solid and dash-dotted curves) and the classical prediction (dashed curves) are included, and the circles in panels (a) and (b) identify the point of equal time and power in both graphs. We observe pronounced visibility peaks recurring at multiples of the Talbot time, a feature clearly absent in the classical calculation. In the following we therefore consider only the quantum case. Note also that the sinusoidal visibility is not always a sufficient approximation to the full fringe contrast (8). As seen in figure 2, it can overestimate the proper fringe amplitude in high-contrast regions (solid

IOP Institute of Physics DEUTSCHE PHYSIKALISCHE GESELLSCHAFT

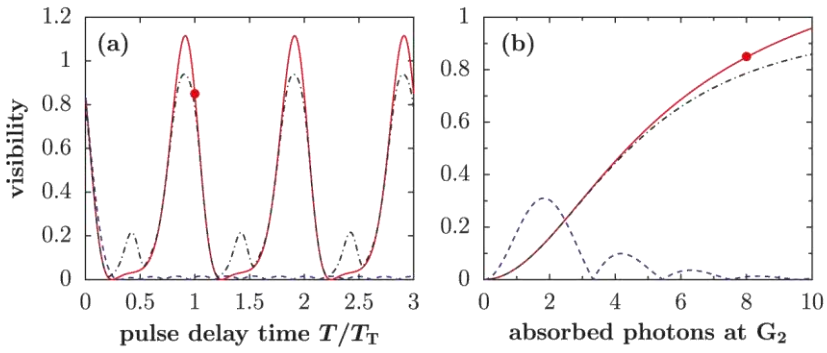

Figure 2. (a) Simulation of the 'sinusoidal' quantum interference visibility $\mathcal{V}_{\sin}$ (solid line), the conventional quantum contrast $\mathcal{V}$ (dash-dotted line) and the classical expectation for the fringe contrast (dashed line) as a function of T/T_T for $n_0^{(2)} = 8$. (b) The same contrast curves as a function of $n_0^{(2)}$ for fixed $T = T_T$. The simulation assumes the material characteristics of gold clusters, $\beta = 1.0$.

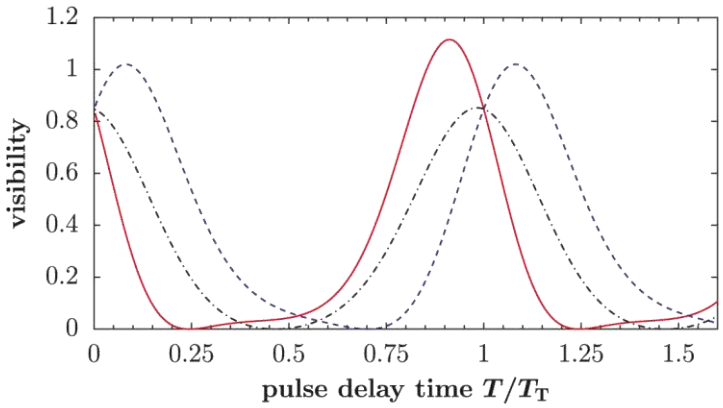

Figure 3. Predicted quantum interference contrast as a function of the pulse delay time T/T_T for different cluster materials, i.e. for different values of the parameter β. The solid line corresponds to gold ($\beta = 1.0$), the dashed line to cesium ($\beta = -1.3$) and the dashed-dotted line to silver ($\beta = 9.2$). The β-values are obtained from equation (17), using dielectric functions of the bulk materials [42]. The power of the second pulse is set to $n_0^{(2)} = 8$.

line), but it can also vanish where the total contrast is still finite (dash-dotted line). Depending on the experimental data analysis, higher-order Fourier coefficients may need to be accounted for in such cases.

Figure 3 illustrates the influence of the material parameter β on the sinusoidal visibility as a function of the pulse separation for three different materials, cesium, gold and silver clusters. Their β-values are representative of most ionizable cluster materials. The peaks of the visibility curves resize and move away from integer multiples of the Talbot time, depending on the magnitude and sign of β. The general shape, however, is mainly determined by the number of absorbed photons $n_0^{(2)}$ and stays roughly the same for all $|\beta| \gtrsim 1$. The negative value $\beta = -1.3$ for cesium implies that it is a low field seeker at the wavelength $\lambda_L = 157$ nm.

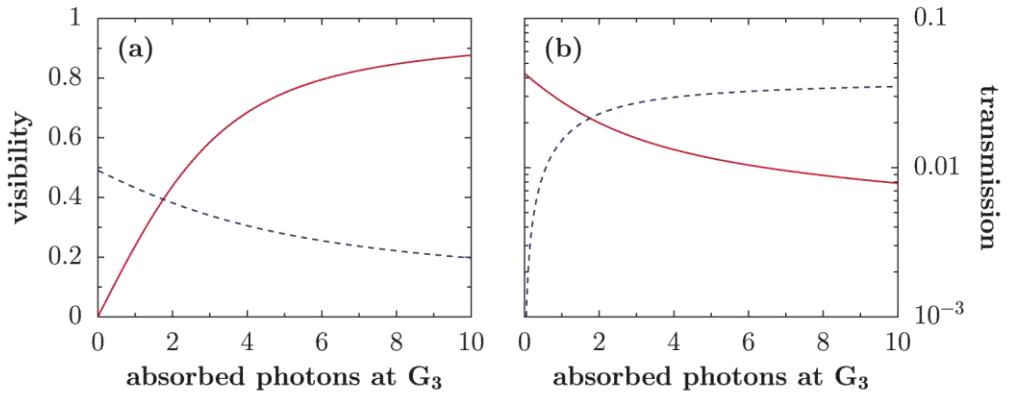

Figure 4. (a) Computed quantum interference contrast and (b) transmissivity when the third grating laser power is varied. The power is expressed in terms of the number of absorbed photons. For the solid line in both plots the final signal is given by the transmitted neutral particles. The dashed line represents the case of an 'inverted' grating G_3. Here, the ions are counted directly. The increasing laser power then broadens the effective slit width of the third grating pulse.

Finally, to see the effects of large laser powers, we plot in figure 4(a) the quantum contrast and in figure 4(b) the transmissivity as a function of light intensity in G_3 while keeping the other parameters at the values of the marked points of figure 2. This case corresponds to the solid lines in figure 4. While the visibility grows with increasing laser power, the transmissivity decreases; the same holds for an intensity variation of G_1. In this regard, it is noteworthy that the experiment can also be set up such that the count rate increases with increasing laser power in the third pulse, by counting the charged clusters directly. Even though this 'inverse grating' configuration optimizes the detected cluster flux, it again reduces the fringe contrast, as shown by the dashed lines in figure 4, since now any increase in laser intensity will broaden the 'effective slit width' in G_3.

3. Theoretical description

In this section, we recapitulate the description of complex gratings that are both ionizing and phase shifting. They are combined with the three-grating interferometer which we then model in phase space [24], [43–46] to reconstruct the final particle distribution and the detected interference signal. Finally, we also incorporate elastic laser light scattering.

3.1. Complex light gratings

Given a normalized transverse mode profile $f(y, z)$, with $\int \mathrm{d}y\mathrm{d}z\, f(y, z) = 1$, of the laser beam, the three-dimensional (3D) intensity distribution of the standing light wave is described by

$$I(x, y, z, t) = 4P_{\mathrm{L}}(t)\, f(y, z) \cos^2\left(\frac{2\pi x}{\lambda_{\mathrm{L}}}\right), \tag{11}$$

where the total absorption is governed by the pulse energy $E_{\mathrm{L}} = \int \mathrm{d}t\, P_{\mathrm{L}}(t)$. There is no need to average over the spatial laser beam profile since we assume the clusters to be centered in the

laser beam. In the case of a Gaussian laser beam, the profile function is described by

$$f(y,z) = \frac{2}{\pi w_y w_z} \exp\left(-\frac{2y^2}{w_y^2} - \frac{2z^2}{w_z^2}\right). \tag{12}$$

The cloud extension is of even less importance for pulsed lasers prepared with a flat-top spatial intensity profile.

If the particles are effectively at rest during the nanosecond pulse duration, we can assign a complex *grating transmission function* $t^{(k)}(x)$ to each laser pulse $k = 1, 2, 3$, which transforms a particle's wave function $\psi(x) \to t^{(k)}(x)\psi(x)$, according to a scattering model [46]. The modulus square $|t^{(k)}(x)|^2 \leqslant 1$ then gives the probability for a particle to be transmitted by the grating. The mean number of absorption processes per cluster and pulse reads

$$n^{(k)}(x) = \frac{4\sigma_{\rm abs} E_{\rm L}^{(k)} \lambda_{\rm L}}{hc} f(0,0) \cos^2\left(\frac{\pi x}{d}\right) \equiv n_0^{(k)} \cos^2\left(\frac{\pi x}{d}\right), \tag{13}$$

with the ionization cross-section $\sigma_{\rm abs}$. The pulse energy $E_{\rm L}^{(k)}$ can be varied from pulse to pulse. Given the dielectric function $\varepsilon = \varepsilon_1 + {\rm i}\varepsilon_2$ of the cluster material the absorption cross-section of a spherical sub-wavelength cluster reads [47]

$$\sigma_{\rm abs} = 4\pi R^3 \frac{2\pi}{\lambda_{\rm L}} {\rm Im}\left(\frac{\varepsilon - 1}{\varepsilon + 2}\right) = \frac{18\pi m}{\varrho \lambda_{\rm L}} \frac{\varepsilon_2}{(\varepsilon_1 + 2)^2 + \varepsilon_2^2}, \tag{14}$$

where R is the cluster radius and $\varrho = 3m/4\pi R^3$ its mass density.

The probability for not absorbing any photon during the light pulse is $|t^{(k)}(x)|^2 = \exp(-n^{(k)}(x))$. This can be expanded in a Fourier series

$$|t^{(k)}(x)|^2 = \sum_{n=-\infty}^{\infty} B_n^{(k)}(0) \exp\left(\frac{2\pi {\rm i} n x}{d}\right), \tag{15}$$

where the Fourier coefficients are given by equation (6).

In addition, the transmission function $t^{(k)}(x)$ also carries a phase due to the dipole energy [24, 46, 48]. It is mediated by the real part of the particle's dipole polarizability $\alpha_{\rm SI}(\lambda_{\rm L})$ at the laser wavelength, which we use in volume units, $\alpha = \alpha_{\rm SI}(\lambda_{\rm L})/4\pi\varepsilon_0$. For sub-wavelength clusters it is given by

$$\alpha = R^3 \, {\rm Re}\left(\frac{\varepsilon - 1}{\varepsilon + 2}\right) = \frac{3m}{4\pi\varrho} \frac{\varepsilon_1^2 + \varepsilon_2^2 + \varepsilon_1 - 2}{(\varepsilon_1 + 2)^2 + \varepsilon_2^2}. \tag{16}$$

We obtain the phase shift $\phi^{(k)}(x) = \phi_0^{(k)} \cos^2(\pi x/d)$, with $\phi_0^{(k)} = n_0^{(k)}/2\beta$ and

$$\beta = \frac{\lambda_{\rm L}\sigma_{\rm abs}}{8\pi^2\alpha} = \frac{3\varepsilon_2}{\varepsilon_1^2 + \varepsilon_2^2 + \varepsilon_1 - 2}. \tag{17}$$

This leads to the total grating transmission function

$$t^{(k)}(x) = \exp\left(-\frac{n^{(k)}(x)}{2} + {\rm i}\phi^{(k)}(x)\right) = \exp\left[\left(-\frac{n_0^{(k)}}{2} + {\rm i}\phi_0^{(k)}\right) \cos^2\left(\frac{\pi x}{d}\right)\right]. \tag{18}$$

Its Fourier coefficients are

$$b_n^{(k)} = \exp\left(-\frac{n_0^{(k)}}{4} + {\rm i}\frac{\phi_0^{(k)}}{2}\right) I_n\left(-\frac{n_0^{(k)}}{4} + {\rm i}\frac{\phi_0^{(k)}}{2}\right). \tag{19}$$

In contrast to the Kapitza–Dirac TLI [14, 15] where photoabsorption led to a contrast-reducing momentum recoil instead of the removal of molecules from the beam, both the phase-imprint and the SPI in G_2 are independently capable of causing matter-wave interference in the present OTIMA interferometer.

3.2. Phase-space model

Starting from an initially bunched ensemble of particles at $t = 0$, we are now going to derive an expression for its final state at $t = T_1 + T_2$ using a 1D phase-space description of its time evolution [15, 24, 46]. The motional density matrix ρ can be rewritten as the Wigner function

$$w(x, p) = \frac{1}{2\pi\hbar} \int \mathrm{d}s \, \exp(\mathrm{i}ps/\hbar) \left\langle x - \frac{1}{2}s \middle| \rho \middle| x + \frac{1}{2}s \right\rangle, \tag{20}$$

which is a real function of the phase-space coordinates x and p. We assume the initial Wigner function to be spatially constant on the scale of the grating period d, since the incident cluster cloud with spatial extension Δx is uniformly distributed over many periods of the standing wave, $\Delta x \gg d$. The momentum dependence is given by the 1D marginal distribution

$$D(p) = \int \mathrm{d}p_y \mathrm{d}p_z \, \mu(p, p_y, p_z), \tag{21}$$

where $\mu(\boldsymbol{p})$ represents the 3D momentum distribution of the particle cloud. The Fourier transform

$$\widetilde{D}(s) = \int \mathrm{d}p \, D(p) \exp\left(-\mathrm{i}ps/\hbar\right), \tag{22}$$

which is normalized to $\widetilde{D}(0) = \int \mathrm{d}p \, D(p) = 1$, characterizes the transverse coherence of the ensemble. We assume the initial ensemble to be incoherent on the scale of the grating period d, i.e. the function $\widetilde{D}(s)$ is sharply peaked around $s = 0$ and nonzero only for arguments $|s| \ll d$. This is equivalent to saying that the momentum distribution $D(p)$ is broad and approximately constant on the scale of the grating momentum, i.e. $\Delta p \gg \hbar/d$. This is the reason why a single grating does not suffice to observe quantum interference starting from such an initial state.

Once subjected to the first grating transformation, the initial state $w_0(x, p) = D(p)/\Delta x$ undergoes a convolution in phase space $w_0(x, p) \to \int \mathrm{d}p_0 \, T^{(1)}(x, p - p_0) w_0(x, p_0)$. The grating kernel $T^{(k)}(x, p)$ relates to the transmission function $t^{(k)}(x)$ of the kth grating via

$$T^{(k)}(x, p) = \frac{1}{2\pi\hbar} \int \mathrm{d}s \, \exp\left(\frac{\mathrm{i}}{\hbar} ps\right) t^{(k)}\left(x - \frac{s}{2}\right) \left[t^{(k)}\left(x + \frac{s}{2}\right)\right]^*. \tag{23}$$

After G_1 the state propagates freely during the time T_1. This corresponds to a shearing in phase space, $x \to x - pT_1/m$. The same convolution and propagation transformation then applies to the subsequent diffraction due to G_2 and the following evolution during T_2. In order to obtain the final position distribution we integrate the Wigner function $w_{T_1+T_2}(x, p)$ over the momentum to obtain the spatial probability density

$$w_{T_1+T_2}(x) = \frac{1}{\Delta x} \int \mathrm{d}p \, \mathrm{d}p_1 \, \mathrm{d}p_0 \, T^{(2)}\left(x - \frac{pT_2}{m}, p - p_1\right) T^{(1)}\left(x - \frac{pT_2 + p_1T_1}{m}, p_1 - p_0\right) D(p_0). \tag{24}$$

Due to the periodicity of the grating kernels (23), $w_{T_1+T_2}(x)$ is a d-periodic oscillatory function in x. It can be stated in terms of the Talbot–Lau coefficients of the kth grating

$$B_n^{(k)}(\xi) = \sum_{j=-\infty}^{\infty} b_j^{(k)} \left(b_{j-n}^{(k)}\right)^* \exp[\mathrm{i}\pi\xi\,(n-2j)]\,, \tag{25}$$

which involves the Fourier coefficients from equation (19). We allow for different laser powers, i.e. different parameters $n_0^{(k)}$, $\phi_0^{(k)}$, and following the procedure described in [15] we arrive first at an expression for the Talbot–Lau coefficients $B_n^{(k)}(\xi)$ (equation (3)) and then at the spatial probability density

$$w_{T_1+T_2}(x) = \frac{1}{\Delta x} \sum_{n,\ell=-\infty}^{\infty} \exp\left(\frac{2\pi\mathrm{i}\ell x}{d}\right) \widetilde{D}\left(\frac{d(nT_1+\ell T_2)}{T_\mathrm{T}}\right) B_n^{(1)}\left(\frac{nT_1+\ell T_2}{T_\mathrm{T}}\right) B_{\ell-n}^{(2)}\left(\frac{\ell T_2}{T_\mathrm{T}}\right). \tag{26}$$

3.3. Resonance approximation

A clear quantum interference pattern can be observed in the density distribution (26) when the pulses are at least separated of the order of the Talbot time. In this case the sharply peaked function $\widetilde{D}$ reduces the range of summation indices (n, ℓ) that contribute significantly to $w_{T_1+T_2}(x)$. Only those (n, ℓ) count which fulfill $|nT_1 + \ell T_2| \ll T_\mathrm{T}$. For $T_1, T_2 \simeq T_\mathrm{T}$ this generally implies a unique integer n for each ℓ [25]. Here, we restrict ourselves to the case when the delay T_2 after the second grating pulse is close to an integer multiple of the first pulse separation $T_1 = T$, $T_2 = NT + \tau$, with $|\tau| \ll T$. The double summation is then simplified by the resonance approximation

$$\widetilde{D}\left(\frac{d(nT_1+\ell T_2)}{T_\mathrm{T}}\right) \approx \delta_{n,-N\ell}\,\widetilde{D}\left(\frac{\ell d\tau}{T_\mathrm{T}}\right). \tag{27}$$

We then arrive at

$$w_{(N+1)T}(x) = \frac{1}{\Delta x} \sum_{\ell=-\infty}^{\infty} \widetilde{D}\left(\frac{\ell d\tau}{T_\mathrm{T}}\right) B_{-N\ell}^{(1)}\left(\frac{\ell\tau}{T_\mathrm{T}}\right) B_{(N+1)\ell}^{(2)}\left(\frac{\ell(NT+\tau)}{T_\mathrm{T}}\right) \exp\left(\frac{2\pi\mathrm{i}\ell x}{d}\right) \tag{28}$$

for the position distribution immediately before the third laser pulse. In the resonant case, $\tau = 0$, we find the ideal Talbot–Lau interference pattern as described by (2) for $N = 1$. As noted previously, the Talbot–Lau coefficients of the first grating $B_n^{(1)}(0)$ then reduce to the Fourier components (6), and the first pulse serves as a classical mask without any phase modulation. This also shows that for an interference pattern to be formed, the first grating must not be a pure phase grating.

This is, however, no longer true for $\tau \neq 0$, where a transient near-field interference effect emerges because of the phase modulation at both the first and the second grating. This phenomenon was observed in Talbot–Lau interferometry of thermal atoms using pure phase gratings [27, 34]. The maximum time span for such a transient interference signal is limited by the width of the initial momentum distribution, $|\tau| \lesssim md/\Delta p$. Given a typical velocity spread of $\Delta v = \Delta p/m = 1\,\mathrm{m\,s^{-1}}$, transient interference effects would occur for time shifts τ of mostly a few hundred nanoseconds with optical phase gratings. Absorptive gratings, on the other hand, offer a resonant Talbot–Lau interference effect with high contrast, as shown in section 2.5 and discussed below.

3.4. Fringe shifts and the role of the third grating

In our previous derivation of (28), we assumed the particles to propagate freely between the grating pulses. Now, we admit a constant force $F = ma$ along x acting during the entire pulse sequence. The propagation in the force field then causes an accelerated shearing of the Wigner function

$$w_t(x, p) = w_0\left(x - \frac{pt}{m} + \frac{a}{2}t^2, p - mat\right). \tag{29}$$

Our earlier calculation can be performed again for all pulses, and reveals a shift $x \to x + \delta x$ of the density pattern (28) at time $(N+1)T$, given by

$$\delta x = -\frac{a}{2}N(N+1)T^2. \tag{30}$$

Since all three grating laser beams are retro-reflected by the same fixed mirror, we may now exploit the fringe shift, equation (30), to scan the interference pattern by tuning the time separation. This will shift the fringe coordinate x_S and modify the Fourier components of the detection signal after the third pulse,

$$S(x_S) = \int \mathrm{d}x\, w_{(N+1)T}(x + x_S)\left|t^{(3)}(x)\right|^2 = \int \mathrm{d}x\, w_{(N+1)T}(x)\left|t^{(3)}(x - x_S)\right|^2. \tag{31}$$

In practice, the Earth's gravitational acceleration $a = g$ provides a highly homogeneous and constant force that can be easily used to shift the fringe pattern if the x-direction is chosen to have a vertical component. Alternatively, one may also use electrostatic fields.

When the signal is recorded as a function of T it will no longer be strictly periodic. In practice, however, the time variation $d/N(N+1)gT$ required to shift the pattern by about one grating period d can be made small compared to the Talbot time T_T by increasing either the pulse separation time T or the mass of the particles. The sinusoidal visibility then remains a good measure. After inserting (28) into (31), we obtain the final signal

$$S(x_S) = \sum_{\ell=-\infty}^{\infty} \widetilde{D}\left(\frac{\ell d\tau}{T_T}\right) B^{(1)}_{-N\ell}\left(\frac{\ell\tau}{T_T}\right) B^{(2)}_{(N+1)\ell}\left(\frac{\ell(NT+\tau)}{T_T}\right) B^{(3)}_{-\ell}(0)\exp\left(\frac{2\pi \mathrm{i}\ell x_S}{d}\right). \tag{32}$$

Its fringe contrast is

$$\mathcal{V}_{\sin} = 2\left|\frac{B^{(1)}_{-N}(\tau/T_T)\, B^{(2)}_{(N+1)}((NT+\tau)/T_T)\, B^{(3)}_{-1}(0)}{B^{(1)}_0(0) B^{(2)}_0(0) B^{(3)}_0(0)}\,\widetilde{D}\left(\frac{d\tau}{T_T}\right)\right|. \tag{33}$$

This shows that it is favorable to keep the pulse delays T_1 and T_2 equal, i.e. to set $N = 1$: any larger N increases the index of the Talbot–Lau coefficients (3) and thus reduces the maximum fringe contrast. In addition, the simulations of section 2.5 show that a high visibility is realized with ionizing gratings in the resonant case $\tau = 0$. Equation (33) suggests that this deteriorates rapidly with increasing $|\tau|$ because of the sharply peaked Fourier transform $\widetilde{D}(s)$ of the momentum distribution. We therefore consider the resonant case $\tau = 0$ with equal pulse timing, $N = 1$, in the following. The signal expression (32) and the visibility (33) then reduce to equations (7) and (9), respectively.

In an alternative 'inverse configuration' of G_3, where the ions are counted instead of the neutral clusters, we have to replace $|t^{(3)}(x)|^2$ by $1 - |t^{(3)}(x)|^2$. The grating coefficients in (32) then change from equation (6) into $B^{(3)}_n(0) = \delta_{n,0} - \exp(-n^{(3)}_0/2) I_n(-n^{(3)}_0/2)$.

4. Challenges and limitations

4.1. Rayleigh scattering in the grating

To date the influence of the optical gratings has been treated as a coherent transformation that modulates the cluster wave function through the complex transmission function (18). However, in addition to the absorption of photons and their virtual scattering within the laser wave the diffracted nanoparticles may also give rise to Rayleigh scattering, where the photon is re-emitted elastically. This process causes momentum diffusion [9, 49] and thus deteriorates the interference pattern.

For short laser pulse durations we can treat the Rayleigh scattering independently of the coherent grating transformations. We model it by a Lindblad-type master equation for the density matrix [50–52]

$$\partial_t \rho = \gamma_{\mathrm{R}} \left[\int_{|\boldsymbol{u}|=1} \mathrm{d}\boldsymbol{u}\, N(\boldsymbol{u}) \cos\left(k_{\mathrm{L}}\mathsf{x}\right) \mathrm{e}^{-\mathrm{i}k_{\mathrm{L}}u_x\mathsf{x}} \rho\, \mathrm{e}^{\mathrm{i}k_{\mathrm{L}}u_x\mathsf{x}} \cos\left(k_{\mathrm{L}}\mathsf{x}\right) - \frac{1}{2}\left\{\rho, \cos^2(k_{\mathrm{L}}\mathsf{x})\right\} \right]. \tag{34}$$

The position operator is denoted by x. The equation describes the elastic scattering of a single photon from the diffracting laser field into a random direction $\boldsymbol{u}$. The corresponding momentum recoil is represented by the operators for the standing-wave mode $\cos k_{\mathrm{L}}\mathsf{x}$ and the plane wave modes $\exp\left(\mathrm{i}k_{\mathrm{L}}u_x\mathsf{x}\right)$. The number of recoils is determined by the total scattering rate γ_{R} at the antinodes of the light field, and $N(\boldsymbol{u})$ gives the distribution of scattering directions, as described by the dipole pattern $N(\boldsymbol{u}) = 3\sin^2\vartheta/8\pi$. Here ϑ is the angle between $\boldsymbol{u}$ and the polarization vector of the laser field.

We can solve the master equation (34) in the position representation. The density matrix then transforms according to $\langle x|\rho|x'\rangle \to \eta(x,x')\langle x|\rho|x'\rangle$, with the decoherence function

$$\eta(x,x') = \exp\left[\frac{n_{\mathrm{R}}}{2}\left(2\int_{|\boldsymbol{u}|=1} \mathrm{d}\boldsymbol{u}\, N(\boldsymbol{u}) \mathrm{e}^{\mathrm{i}k_{\mathrm{L}}u_x(x'-x)} \cos k_{\mathrm{L}}x \cos k_{\mathrm{L}}x' - \cos^2 k_{\mathrm{L}}x - \cos^2 k_{\mathrm{L}}x'\right)\right]. \tag{35}$$

It is trace-preserving, $\eta(x,x) = 1$, and it only acts on the spatial coherences. The mean number of scattered photons at the antinodes of the kth grating is related to the number of absorbed photons via the ratio of the associated cross sections, $n_{\mathrm{R}}^{(k)} = n_0^{(k)}\sigma_{\mathrm{R}}/\sigma_{\mathrm{abs}}$. In phase-space representation, decoherence due to elastic scattering (35) is then represented by the integral kernel

$$\begin{aligned} T_{\mathrm{R}}^{(k)}(x,p) &= \frac{1}{2\pi\hbar}\int \mathrm{d}s\, \exp\left[\frac{\mathrm{i}}{\hbar}ps + n_{\mathrm{R}}^{(k)}\eta\left(x-\frac{s}{2}, x+\frac{s}{2}\right)\right] \\ &= \sum_{n=-\infty}^{\infty} \exp\left(\frac{2\pi\mathrm{i}nx}{d}\right)\int \mathrm{d}s\, \exp\left(\frac{\mathrm{i}}{\hbar}ps\right) R_n^{(k)}\left(\frac{s}{d}\right), \end{aligned} \tag{36}$$

which has to be applied at each grating pulse k in addition to the coherent grating kernel (23). Again, the periodicity of the kernel in x allows us to expand it as a Fourier series, where the closed expression for the Fourier coefficients

$$R_n^{(k)}(\xi) = \exp\left\{\frac{3n_{\mathrm{R}}^{(k)}}{4}\left[\cos\pi\xi\left(j_0(\pi\xi) - \frac{j_1(\pi\xi)}{\pi\xi}\right) - \frac{2}{3}\right]\right\} I_n\left[\frac{3n_{\mathrm{R}}^{(k)}}{4}\left(j_0(\pi\xi) - \frac{j_1(\pi\xi)}{\pi\xi} - \frac{2}{3}\cos\pi\xi\right)\right] \tag{37}$$

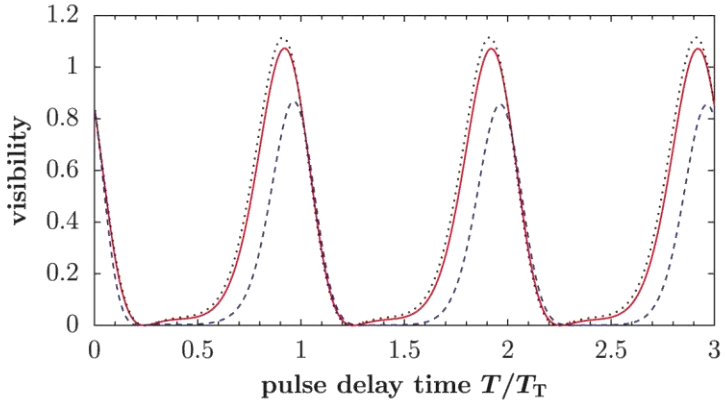

Figure 5. Calculated fringe visibility including Rayleigh scattering of laser photons as a function of T/T_T for a fixed $n_0^{(2)}$ and gold clusters of different masses. The solid and the dashed lines correspond to $m = 10^8$ amu and $m = 10^9$ amu, respectively. The dotted line reproduces the quantum contrast curve of figure 2(a) without Rayleigh scattering, which is a good approximation for cluster masses $\lesssim 10^8$ amu.

follows from a lengthy calculation involving combined integrals over trigonometric expressions and Bessel functions. The symbol j denotes the spherical Bessel function of the first kind. Combining the coherent kernel (23) and the scattering kernel (36) results in the modified Talbot–Lau coefficients

$$\hat{B}_n^{(k)}(\xi) = \sum_{j=-\infty}^{\infty} R_{n-j}^{(k)}(\xi) B_j^{(k)}(\xi) \tag{38}$$

for each grating. Since $\hat{B}_n^{(k)}(0) = B_n^{(k)}(0)$ the Rayleigh scattering acts as a purely decohering agent and does not influence the periodic masking by the gratings. This means, in particular, that only the treatment of the second grating needs to be modified.

With growing cluster size the role of elastic light scattering becomes increasingly important. Since the scattered photons have the same short wavelength as the grating light, they can decohere the previously delocalized matter waves. We may disregard this effect only as long as the number of scattering events $n_R^{(2)}$ is small compared to the number of absorption processes $n_0^{(2)}$. Their ratio is given by their total cross sections

$$\frac{n_R^{(2)}}{n_0^{(2)}} = \frac{\sigma_R}{\sigma_{abs}} = \frac{2}{9}\frac{(\varepsilon_1 - 1)^2 + \varepsilon_2^2}{\varepsilon_2}(k_L R)^3 = \frac{4\pi^2}{3}\frac{(\varepsilon_1 - 1)^2 + \varepsilon_2^2}{\varepsilon_2}\frac{m}{\rho \lambda_L^3} \tag{39}$$

and it is proportional to the mass, assuming that the dielectric function $\varepsilon = \varepsilon_1 + i\varepsilon_2$ and the density ϱ are constant. The influence of Rayleigh scattering on the interference contrast is shown in figure 5, where the expected sinusoidal fringe visibility is plotted as a function of the pulse delay around the Talbot time, both for gold clusters of $m = 10^8$ amu (solid line) and for $m = 10^9$ amu (dashed line). The power of the UV laser gratings is adjusted such that the absorption parameters are kept constant at $n_0^{(1)} = n_0^{(2)} = n_0^{(3)} = 8$ (as in section 2.5). While the solid line still resembles the predicted visibility without Rayleigh scattering (dotted line), the overall contrast of the dashed curve is somewhat suppressed due to the increased

scattering cross-section of $\sigma_R = 0.9\sigma_{abs}$ at $m = 10^9$ amu. This corresponds to a gold cluster of 55 nm diameter, a size where the point particle approximation ceases to be valid. It also exceeds by two to three orders of magnitude the mass limit where the experiments have to be modified in order to compensate for the influence of gravity (see section 4.3).

4.2. Collisional decoherence and thermal emission

Another concern in interferometry with massive particles is their uncontrolled interaction with the environmental degrees of freedom. The most prominent causes of decoherence are collisions with residual gas particles and the emission or scattering of thermal radiation [53, 54]. We find that the unperturbed interference of a 10^6 amu gold cluster after a delocalization time of $2T_T \simeq 30$ ms requires that the background gas pressure is kept at $p \lesssim 10^{-9}$ mbar and the internal cluster temperature at $T \lesssim 1000$ K. Both values can be readily achieved in an experiment. For this estimate, we chose N_2 as the background gas and use the London dispersion formula to compute its interaction strength with the gold clusters, assuming the ionization potential of N_2 to be 15.6 eV and its static polarizability $\alpha_{N_2} = 4\pi\varepsilon_0 \times 1.74\,\text{Å}^3$. The dielectric function of gold at thermal photon wavelengths is here assumed to follow Drude's model with a work function of $W = 5.4$ eV, a plasmon frequency of $\omega_P = 1.3 \times 10^{16}$ Hz and a resonance width of $\Gamma_P = 1.1 \times 10^{14}$ Hz. The static polarizability of gold is taken to be that of an ideal metal cluster.

4.3. Fringe averaging on the Earth

As seen in section 3.4, gravity can cause a fringe shift if the direction of the force is parallel to the diffraction grating vector. For usual interferometers this phase shift is dispersive, i.e. larger for clusters of lower velocity and longer falling time. Even a small width of the cluster velocity distribution can then cause a rapid fringe averaging in the plane of G_3. This problem can be eliminated in an OTIMA interferometer where all clusters are exposed to the gravitational field for exactly the same amount of time. All phase shifts are therefore equal and one can still expect high contrast interference, independent of the grating orientation in space.

What remains is the issue of the classical falling distance. At 10^6 amu a cluster needs a passage time of about 30 ms, assuming F_2 laser gratings with a period of 78.5 nm. During this time it will fall by about 4.6 mm. At $m = 10^7$ amu and a time of 300 ms the free fall distance reaches already half a meter. This illustrates that the force of gravity will have to be compensated for at some point by electrical or magnetic fields or to be eliminated in a microgravity environment.

In contrast to gravity, the Coriolis force $F_C = 2m\vec{v} \times \vec{\Omega}$ depends on the cluster velocity in both modulus and direction. It cannot be compensated for by clever timing. However, OTIMA still offers an advantage over a fixed-length interferometer because it allows us to align the mirror orientation normal to $\vec{\Omega}$. The resulting Coriolis force is then intrinsically orthogonal to the grating vector $\vec{d}$, such that the acceleration does not contribute to the fringe shift.

With growing masses and Talbot times the interferometer becomes more sensitive to vibrations. For low-frequency vibrations, the total fringe shift depends on the position change Δd of each individual grating according to $\Delta d = \Delta d^{(1)} - 2\Delta d^{(2)} + \Delta d^{(3)}$. The single mirror design of the proposed OTIMA interferometer (figure 1) ensures that many conceivable contributions drop out, such as quasi-static mirror shifts and mirror tilts. All dynamical mechanical effects have to be suppressed on the level of about 5–10 nm, which can be done using established spring suspension systems.

5. Experimental considerations

Having described the general idea, we now discuss the compatibility of existing beam sources, diffraction elements and detectors with our suggested scheme and we start with the availability of SPI gratings [37] for various materials.

5.1. Grating requirements

For our present proposal, we consider only particles for which efficient SPI has already been observed [55–57], for example, metal clusters. The cluster ionization energy usually exceeds the work function of the bulk by less than 1–2 eV. It decreases with the particle radius like $E_{\rm ion} \simeq W + 0.42e^2/4\pi\varepsilon_0 R$ and approaches the bulk value at 20–100 atoms per cluster [55]. Dozens of materials are therefore suitable candidates for SPI diffraction and detection, provided that the photon energy is higher than 5 eV, i.e. $\lambda \leqslant 250$ nm.

Although SPI yields are not quantitatively known for all materials, the process has been shown to be dominant in several systems, also in competition with fragmentation and photoemission. This applies to semiconductor nanoparticles [58] as well as to metal clusters [59]. In our simulations (figures 2–4) we have assumed a yield of $\eta_{\rm SPI} \simeq 1$.

In the following, we distinguish between interferometry with particles of mass below 20 000 amu and from 10^4 to 10^6 amu, since they may require different implementations of the same idea.

We envisage a de Broglie wavelength of $\lambda_{\rm dB} \simeq 5 \times 10^{-13}$ m, to fit the entire interferometer on the same two-inch mirror. This is compatible with a velocity of 40 m s^{-1} for clusters with $m \leqslant 20\,000$ amu. This layout is driven by the desire to have a short and ultrastable base for all laser gratings, which is important for high signals and with regard to a high common-mode rejection for phase fluctuations related to vibrations and rotations of the mirror mount.

For this setting, a F_2 excimer laser is well adapted. It emits a few hundreds of vacuum UV (VUV) light pulses per second with an energy of >1 mJ and a duration of <5 ns. Retroreflection of the laser light generates a diffraction grating with a period of $d = 78.5$ nm. The F_2 laser wavelength is fixed at $\lambda = 157.630\,94(10)$ nm with a line width of <1 pm [60]. The gain profile of fluorine allows, in principle, a five times weaker line at $\lambda = 157.524\,33(10)$ nm, as well. The *longitudinal* coherence length of >1 cm guarantees sufficient grating periodicity up to a distance of 2 mm from the retro-reflecting mirror. This covers the entire width of the cluster beam and about 10^5 grating periods.

The *transverse coherence* of excimer lasers is limited and often determined by diffraction of the light beam at the laser outcoupler window. Following the van Cittert–Zernike theorem [61] and also recent measurements, the transverse coherence is estimated to be 80 μm in a meter behind the laser window [62]. The homogeneity of the standing light wave is dominated by the quality of the mirror surface. A flatness of better than $d/10$ is available for VUV wavelengths. Given this, even the limited transverse coherence is still sufficient for the formation of a homogeneous diffraction grating, provided that the laser beam divergence is limited to about 1 mrad.

All this suggests that an F_2 laser is the ideal basis for building a compact and rugged OTIMA interferometer which allows one to address a large range of materials. This flexibility is achieved, however, at the price of working with VUV laser light, which requires purged beam lines and specialized optics.

The short laser pulse width is an advantage for precision measurements but also entails some further consequences related to the fact that the standing light wave needs some time to form and that it also experiences an overall temporal amplitude modulation. The finite speed of light is the reason why the clusters will interact with a running wave during a fraction of the laser pulse duration. For a cluster beam confined to within 1 mm from the mirror surface, this running wave is limited to 0.5% of the total pulse energy. Also the low reflectivity of even the best mirrors which are available for 157 nm ($R \geqslant 98\%$) causes the cluster beam to be exposed to a running light wave of 2% of the total pulse energy. This slightly affects the final count rate but not the visibility, since only the neutral particles reach the detector.

Amplitude variations of the laser light field, realistically of the order of 3–5%, modulate the population of different diffraction orders but they cannot destroy the interference pattern, since the fringe positions are solely determined by the laser wavelength. Also the pointing instability of the grating lasers is negligible if one can ensure that all detected particles have interacted with all three gratings. A critical point is the accurate timing, i.e. a low jitter, of the laser gratings. With existing technologies a timing accuracy of 1 ns can be achieved, which is sufficient for the purpose.

Although the Talbot time $T_T = d^2 m/h$ is intrinsically independent of the particle's velocity, clusters of different speeds will travel different distances between the gratings of the same interferometer. Therefore, the cluster beam must be sliced into packets (figure 1) such that all particles of a batch always interact with the same spatially extended laser pulse, independent of their velocity. The combination of a chopped source with a pulsed TOF-MS detector will, in practice, select a velocity band of $\Delta v/v \simeq 2\%$ in the proposed experiments up to 10^4 amu. A selection of de Broglie wavelengths is then achieved in combination with the detecting mass spectrometer. In principle, an interferogram may then be recorded even without scanning the velocity, time or grating position, provided the source emits a sufficiently dense set of cluster masses.

In the range of 10^6 amu the particle cloud will already expand quite significantly during a total interferometer time of 30–60 ms, even if we assume a cluster velocity of $1\,\mathrm{m\,s^{-1}}$, which is a challenge in itself. We thus require a laser with a spectral coherence of $\Delta\nu \leqslant 0.1\,\mathrm{cm^{-1}}$, as for instance provided by a grating-stabilized ArF laser at 193 nm, the fifth harmonic of a seeded Nd : YAG laser at 213 nm, a frequency-doubled dye laser or an optical parametric oscillator in the wavelength range between 210 and 250 nm. Since the absorption cross-sections of metal clusters grow linearly with the mass for a given atomic species, their higher values will then compensate for the intensity loss when the UV laser beam must be expanded to cover the growing cluster cloud. Finally, in the high-mass range the temporal envelope of the laser beams grows in relevance. The expanded cloud will now see a running wave for up to several per cent of the total pulse width. This time may be reduced by making a standing light wave from counterpropagating laser beams.

5.2. Source properties

On the source side, different options are at hand for different mass ranges: interestingly, even an *effusive beam source* may match the requirements of an OTIMA interferometer. The most probable velocity for $m = 10^6$ amu at $T = 500\,\mathrm{K}$ is $v_{mp} \simeq 3\,\mathrm{m\,s^{-1}}$ and recent experiments have shown that there is still hope for the thermal volatilization of highly massive but chemically tailored organic molecules [63].

However, for the purpose of the present proposal, we restrict ourselves to a *cluster condensation source*, which first volatilizes the atoms and then recondenses them in a cold noble gas stream. The initial atomization may be done thermally, for some materials such as alkali atoms [55] and fullerenes [64], or using a magnetron sputter technique for a large range of metal clusters with higher melting points [65]. A gas aggregation source ejects a broad distribution of clusters, ranging from a few up to several ten thousands of atoms per cluster with a brilliance of up to 10 mg srad s^{-1}.

Our own preliminary studies show that under conditions comparable to OTIMA, we can count about 100 cluster ions on the TOF-MS MCP in a time window of 200 μs. To achieve adequate visibility, each laser grating has to reduce the cluster beam by a factor of three. After the interferometer we thus retain 4% of the initial beam, i.e. 600 ions per second with virtually no background during the measurement period, which is sufficient for the purpose of interferometry.

In the setup of figure 1 the cluster velocity is determined by the flow of the cold carrier gas, which is usually a mixture of helium and argon. The most probable cluster velocity in a nitrogen-cooled setup amounts to about $v_{mp} = 300\,m\,s^{-1}$. This can be lowered by a cryogenic cooling stage, using a neon buffer gas at 30 K [66] to achieve a cluster velocity in the range of less than 100 m s^{-1} if we include the relative velocity slip of massive clusters in light noble gases [67]. From this distribution one may still select the low-velocity tail to get to particles in the range of 40–50 m s^{-1}. Moreover, experiments aimed at surface cleaning also showed that laser acoustic desorption is capable of generating nanoparticle beams with speeds in the range of 10–50 m s^{-1} [68].

Many complementary methods are still conceivable. Of particular interest are those techniques that focus on the improvement of cooling for freely suspended mesoscopic particles [69–72]. Although most published proposals are still best adapted to small source volumes and a few particles, a rapidly growing community is currently investigating methods for preparing mesoscopic isolated particles, which may eventually also be coupled to our proposed interferometer scheme. All this suggests that there are ample possibilities for further progress to masses up to 10^6 amu.

6. Conclusions and outlook

The proposed OTIMA interferometer is universal in the sense that a single experimental setup will enable experiments with a large class of nanoparticles, ranging from single atoms to metal clusters, semiconductor nanocrystals, and possibly even some biomolecular complexes, as long as ionization or neutralization is the dominant response to the absorption of a single photon. This covers a mass range from 6–7 amu for lithium isotopes to 10^6 amu for cold giant clusters.

The setup is promising for testing the foundations of wave mechanics, and its intrinsic features, such as high common mode rejection, non-dispersiveness and good control over the grating pulse times, are well adapted to interference-assisted cluster metrology. The OTIMA concept could thus enable new insights into cluster physics, including collisional and absolute photoabsorption cross sections, electric and magnetic properties, etc.

Our calculations show that a high interference contrast may be expected for a wide range of masses under otherwise very similar conditions. This could become relevant in explorations of the equivalence principle as well as in experiments that probe currently speculative fundamental limitations of the Schrödinger equation [73–78].

In contrast to many other experiments where source purity is a value in itself, the OTIMA interferometer can profit from the broad distribution of particles ejected by a magnetron clusters source [65]. Performing experiments with different cluster types under otherwise identical conditions provides a high degree of 'common mode noise rejection' and a good way of identifying systematic phase shifts under variations of mass, baryon composition, geometrical structure and other cluster properties.

Acknowledgments

We thank the Austrian Science Fund (FWF) for support through the projects Wittgenstein Z149-N16 and DK-W1210 CoQuS. We also acknowledge financial support from the MIME project of the ESF EuroQUASAR program, from FWF and from Deutsche Forschungsgemeinschaft.

References

[1] Hasselbach F 2010 *Rep. Prog. Phys.* **73** 016101
[2] Rauch H and Werner A 2000 *Neutron Interferometry: Lessons in Experimental Quantum Mechanics* (Oxford: Oxford University Press)
[3] Cronin A D, Schmiedmayer J and Pritchard D E 2009 *Rev. Mod. Phys.* **81** 1051
[4] Schöllkopf W and Toennies J P 1994 *Science* **266** 1345
[5] Arndt M, Nairz O, Voss-Andreae J, Keller C, der Zouw G V and Zeilinger A 1999 *Nature* **401** 680
[6] Brühl R, Fouquet P, Grisenti R E, Toennies J P, Hegerfeldt G C, Köhler T, Stoll M and Walter C 2002 *Europhys. Lett.* **59** 357
[7] Nairz O, Brezger B, Arndt M and Zeilinger A 2001 *Phys. Rev. Lett.* **87** 160401
[8] Reisinger T, Patel A, Reingruber H, Fladischer K, Ernst W, Bracco G, Smith H and Holst B 2009 *Phys. Rev.* A **79** 53823
[9] Chapman M S, Hammond T D, Lenef A, Schmiedmayer J, Rubenstein R A, Smith E and Pritchard D E 1995 *Phys. Rev. Lett.* **75** 3783
[10] Bordé C, Courtier N, Burck F D, Goncharov A and Gorlicki M 1994 *Phys. Lett.* A **188** 187
[11] Lisdat C, Frank M, Knöckel H, Almazor M L and Tiemann E 2000 *Eur. Phys. J.* D **12** 235
[12] Brezger B, Hackermüller L, Uttenthaler S, Petschinka J, Arndt M and Zeilinger A 2002 *Phys. Rev. Lett.* **88** 100404
[13] Hackermüller L, Uttenthaler S, Hornberger K, Reiger E, Brezger B, Zeilinger A and Arndt M 2003 *Phys. Rev. Lett.* **91** 90408
[14] Gerlich S *et al* 2007 *Nat. Phys.* **3** 711
[15] Hornberger K, Gerlich S, Ulbricht H, Hackermüller L, Nimmrichter S, Goldt I, Boltalina O and Arndt M 2009 *New J. Phys.* **11** 043032
[16] Clauser J 1997 De Broglie-wave interference of small rocks and live viruses *Experimental Metaphysics* ed R Cohen, M Horne and J Stachel (Dordrecht: Kluwer) pp 1–11
[17] Savas T A, Shah S N, Schattenburg M L, Carter J M and Smith H I 1995 *J. Vac. Sci. Technol.* B **13** 2732
[18] Keith D W, Schattenburg M L, Smith H I and Pritchard D E 1988 *Phys. Rev. Lett.* **61** 1580
[19] Carnal O and Mlynek J 1991 *Phys. Rev. Lett.* **66** 2689
[20] Gronniger G, Barwick B, Batelaan H, Savas T, Pritchard D and Cronin A 2005 *Appl. Phys. Lett.* **87** 124104
[21] Cronin A D and McMorran B 2006 *Phys. Rev.* A **74** 061602
[22] Grisenti R E, Schöllkopf W, Toennies J P, Hegerfeldt G C and Köhler T 1999 *Phys. Rev. Lett.* **83** 1755
[23] Perreault J D and Cronin A D 2006 *Phys. Rev.* A **73** 033610
[24] Hornberger K, Sipe J E and Arndt M 2004 *Phys. Rev.* A **70** 53608
[25] Nimmrichter S and Hornberger K 2008 *Phys. Rev.* A **78** 023612

[26] Steane A, Szriftgiser P, Desbiolles P and Dalibard J 1995 *Phys. Rev. Lett.* **74** 4972
[27] Cahn S B, Kumarakrishnan A, Shim U, Sleator T, Berman P R and Dubetsky B 1997 *Phys. Rev. Lett.* **79** 784
[28] Martin P J, Oldaker B G, Miklich A H and Pritchard D E 1988 *Phys. Rev. Lett.* **60** 515
[29] Pfau T, Spälter S, Kurtsiefer C, Ekstrom C and Mlynek J 1994 *Phys. Rev. Lett.* **73** 1223
[30] Szriftgiser P, Guéry-Odelin D, Arndt M and Dalibard J 1996 *Phys. Rev. Lett.* **77** 4
[31] Keller C, Oberthaler M K, Abfalterer R, Bernet S, Schmiedmayer J and Zeilinger A 1997 *Phys. Rev. Lett.* **79** 3327
[32] Freimund D L, Aflatooni K and Batelaan H 2001 *Nature* **413** 142
[33] Deng L, Hagley E W, Wen J, Trippenbach M, Band Y, Julienne P S, Simsarian J E, Helmerson K, Rolston S L and Phillips W D 1999 *Nature* **398** 218
[34] Turlapov A, Tonyushkin A and Sleator T 2005 *Phys. Rev.* A **71** 43612
[35] Abfalterer R, Keller C, Bernet S, Oberthaler M K, Schmiedmayer J and Zeilinger A 1997 *Phys. Rev.* A **56** R4365
[36] Cohen L J L, Dubetsky B and Berman P R 2000 *Phys. Rev.* A **61** 033610
[37] Reiger E, Hackermüller L, Berninger M and Arndt M 2006 *Opt. Commun.* **264** 326
[38] Kasevich M and Chu S 1991 *Phys. Rev. Lett.* **67** 181
[39] Dubetsky B and Berman P 1999 *Phys. Rev.* A **59** 2269
[40] Wu S, Su E J and Prentiss M 2005 *Eur. Phys. J.* D **35** 111
[41] Tonyushkin A and Sleator T 2006 *Phys. Rev.* A **74** 053615
[42] Palik E and Ghosh G 1998 *Handbook of Optical Constants of Solids: Five-Volume Set* (New York: Academic)
[43] Wigner E 1932 *Phys. Rev.* **40** 749
[44] Ozorio de Almeida A M 1998 *Phys. Rep.* **295** 265
[45] Schleich W P 2001 *Quantum Optics in Phase Space* (Weinheim: Wiley)
[46] Nimmrichter S, Hornberger K, Ulbricht H and Arndt M 2008 *Phys. Rev.* A **78** 063607
[47] Kreibig U and Vollmer M 1995 *Optical Properties of Metal Clusters* (Berlin: Springer)
[48] Brezger B, Arndt M and Zeilinger A 2003 *J. Opt. B: Quantum Semiclass. Opt.* **5** S82
[49] Kokorowski D A, Cronin A D, Roberts T D and Pritchard D E 2001 *Phys. Rev. Lett.* **86** 2191
[50] Kazantsev A, Surdutovich G and Yakovlev V 1990 *Mechanical Action of Light on Atoms* (Singapore: World Scientific)
[51] Dyrting S and Milburn G J 1994 *Phys. Rev.* A **49** 4180
[52] Domokos P, Horak P and Ritsch H 2001 *J. Phys. B: At. Mol. Opt. Phys.* **34** 187
[53] Hornberger K, Uttenthaler S, Brezger B, Hackermüller L, Arndt M and Zeilinger A 2003 *Phys. Rev. Lett.* **90** 160401
[54] Hackermüller L, Hornberger K, Brezger B, Zeilinger A and Arndt M 2004 *Nature* **427** 711–4
[55] de Heer W A 1993 *Rev. Mod. Phys.* **65** 611
[56] Wahl M and Wucher A 1994 *Nucl. Instrum. Methods Phys. Res.* B **94** 36
[57] Koch D, Wahl M and Wucher A 2007 *Z. Phys.* D **32** 137
[58] Schäfer R and Becker J 1997 *Z. Phys.* D **40** 490
[59] Wucher A and Wahl M 1996 *Nucl. Instrum. Methods Phys. Res.* B **115** 581
[60] Sansonetti C J, Reader J and Vogler K 2001 *Appl. Opt.* **40** 1974
[61] Born M and Wolf E 1993 *Principles of Optics* (Oxford: Pergamon)
[62] Dyer P, Walton C and Zakaria R 2009 *Appl. Phys.* A **95** 319
[63] Gerlich S, Eibenberger S, Tomandl M, Nimmrichter S, Hornberger K, Tüxen J, Mayor M and Arndt M 2011 *Nat. Commun.* **2** 263
[64] Martin T P and Kakizaki A 1984 *J. Chem. Phys.* **80** 3956
[65] Haberland H and Karrais M M 1991 *Z. Phys.* D **20** 413
[66] Patterson D, Rasmussen J and Doyle J M 2009 *New J. Phys.* **11** 055018
[67] Rosemeyer M, Schäfer R and August Becker J 2001 *Chem. Phys. Lett.* **339** 323
[68] Geldhauser T, Ziese F, Merkt F, Erbe A, Boneberg J and Leiderer P 2007 *Appl. Phys.* A **89** 109

IOP PUBLISHING NANOTECHNOLOGY
Nanotechnology **20** (2009) 455501 (6pp) doi:10.1088/0957-4484/20/45/455501

A superconducting NbN detector for neutral nanoparticles

Markus Marksteiner[1], Alexander Divochiy[2], Michele Sclafani[1], Philipp Haslinger[1], Hendrik Ulbricht[1,3], Alexander Korneev[2], Alexander Semenov[2], Gregory Gol'tsman[2] and Markus Arndt[1]

[1] Faculty of Physics, University of Vienna, Boltzmanngasse 5, A-1090 Vienna, Austria
[2] Department of Physics, Moscow State Pedagogical University, M Pirogovskaya Street 1, Moscow 119992, Russia
[3] School of Physics and Astronomy, University of Southampton, Highfield, Southampton SO17 1BJ, UK

E-mail: markus.arndt@univie.ac.at

Received 6 July 2009, in final form 11 September 2009
Published 13 October 2009
Online at stacks.iop.org/Nano/20/455501

Abstract
We present a proof-of-principle study of superconducting single photon detectors (SSPD) for the detection of individual neutral molecules/nanoparticles at low energies. The new detector is applied to characterize a laser desorption source for biomolecules and allows retrieval of the arrival time distribution of a pulsed molecular beam containing the amino acid tryptophan, the polypeptide gramicidin as well as insulin, myoglobin and hemoglobin. We discuss the experimental evidence that the detector is actually sensitive to isolated neutral particles.

(Some figures in this article are in colour only in the electronic version)

1. Introduction

The detection of isolated neutral molecules and nanoparticles in the gas phase is both a necessity and a challenge for many experiments that range from physical chemistry to environmental monitoring [1] to the foundations of physics. Our own work was originally motivated by matter wave interferometry with massive molecules [2–4] and applications in molecule metrology [5, 6]. The extension of such experiments to higher masses also requires improved methods for detecting neutral nanoparticles. While ionization techniques are routinely used for particles up to about 2000 Da, post-ionization of organic molecules beyond that mass has remained a significant challenge [7, 8]. Recent experiments observed photoionization of tryptophan–metal complexes and nucleotide clusters up to 6000 Da [9, 10]. But for the majority of high-mass biomolecules this method seems to be precluded.

Hyperthermal surface ionization [12] was shown to allow the detection of some neutral molecules, with insulin currently setting the mass record [13].

Modern nanofabrication technologies also allow the building of nanoscale oscillators which change their resonance frequency when their mass is augmented by even a single molecule. Such cantilever based detectors [14, 15] have a lower rather than an upper mass limit. They currently reach a sensitivity of below 200 Da [16]. The first proof-of-principle mass spectrometer applications showed the capability to detect single proteins [17].

Whenever mass cannot be measured directly, bolometer detectors [18–20] may convert molecular energy first into sensor temperature and then into an electrical signal. However, the translational energy of a single amino acid, such as tryptophan, does not exceed 0.3 eV, even at a molecular velocity of 500 m s^{-1}. This is why the first bolometers [21] still operated with a minimum detection threshold of about 10^7 molecules s^{-1}. Superconductors were suggested as promising sensors [22, 19, 23] since their conductivity changes strongly with temperature in the vicinity of the phase transition edge.

The implementation of superconducting tunneling junctions (STJ) made it possible to detect charged individual molecules [24–26]. This is interesting for mass spectrometry, because the STJ response depends on the particle's energy [27]. This allows us in principle to combine the mass discrimination of a time-of-flight spectrometer with a detector whose efficiency remains constant over a wide mass range. Tunneling junction detectors, however, require cooling well below 4 K and up to now they have only been used for recording either

ensembles of slow neutral particles or for detecting individual but energetic charged particles.

In this paper we present our first experimental evidence that a combination of both is feasible, i.e. a detector for single neutral molecules of low kinetic and low internal energy. Our nanowire detector was originally fabricated as a superconducting single photon detector. Its sensitivity to single photons was demonstrated across the entire spectrum from UV to mid-IR, with quantum efficiencies up to 30% [28–32]. Before we started the experiments, it was far from obvious that such a device would also be sensitive to slow nanoparticles. In the following we discuss the acquired evidence that this detector is capable of recording the incidence of isolated neutral biomolecules.

2. Experimental setup

The experimental setup consists of a pulsed molecular beam, a free flight trajectory in high vacuum and the superconducting nanowire detector in a differentially pumped helium cryostat, about 76 cm behind the source.

2.1. Superconducting detectors

Two different types of detector were tested: superconducting single photon counting devices (SSPDs) and superconducting bolometers (SBs).

The SSPDs were fabricated by depositing a NbN film of 3.5–4 nm thickness on a sapphire substrate. We tested chips with an open area of either 10×10 μm^2 or 20×20 μm^2. The 100–120 nm wide superconducting wire meanders on the surface with a filling factor of 60%. The critical temperature of NbN is $T_c = 10$–11 K and the critical current density amounts to $j_c = 3.5 \times 10^6$ A cm^{-2}.

The SSPD fabrication process was described in detail elsewhere [33]. In brief, NbN superconducting films were deposited on R-cut sapphire substrates by DC reactive magnetron sputtering in an Ar and N_2 mixture. The film was patterned by direct electron beam lithography and reactive ion etching. Gold contacts were added using photolithography and wet etching. In figure 1(a) we show electron microscopy images of the sensitive element. We operate the device in a liquid helium bath cryostat at 4.2 K and apply a DC bias current slightly smaller than the critical current. The signal is capacitively coupled from the chip to the oscilloscope.

The detection mechanism may be understood as follows: when a molecule hits the film surface, it creates high-energy acoustic phonons. These phonons are rapidly absorbed by the electron subsystem of the film due to their short inelastic mean free path. Excess quasiparticles are then created which, in turn, dispose of their energy by the emission of second generation phonons. This triggers an avalanche multiplication cascade. The process is similar to what happens during photon detection. The distinctive difference lies in the first step: the photon detection cascade starts from a single high-energy quasiparticle created by the photon. The dynamics of the subsequent stages is determined only by the absorbed energy.

When the energy of the quasiparticles decreases to a value around 10 K, the electron–electron interaction becomes more

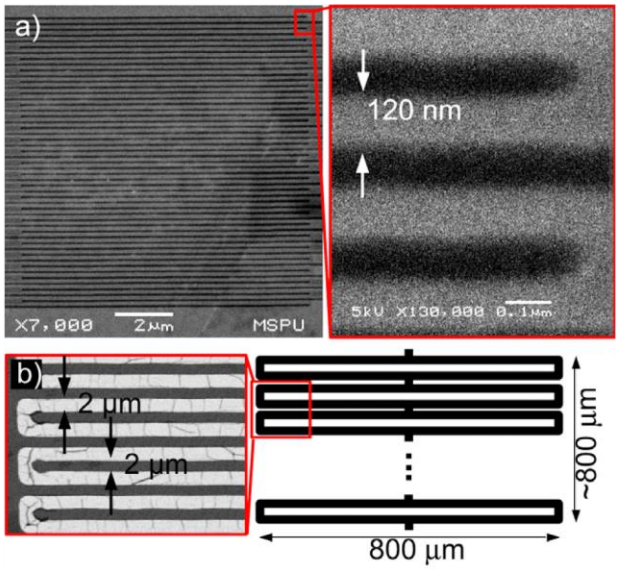

Figure 1. (a) Electron microscopy image of the 10 μm $\times$ 10 μm sensitive SSPD element. The NbN film is shown in gray. (b) Sketch (right) and SEM image (left) of the superconducting NbN bolometer. The bolometer strips and gaps are about 2 μm wide.

efficient for the multiplication of the quasiparticles than the electron–phonon interaction. Due to this fact, the main part of the energy that is initially deposited in the film remains in the quasiparticle subsystem. At the end of the cascade, a hot spot of excess quasiparticles is formed and the supercurrent is forced to flow around the new normal-conducting area. If the hot spot is sufficiently large the current density in the 'sidewalks' increases beyond the critical current density. This results in a short breakdown of superconductivity across the entire width of the nanostripe and in a voltage pulse that can be easily detected [28–31]. For photons, a typical pulse response lasts over 10 ns.

The second detector type that we tested was a classical superconducting bolometer. These chips were made from the same NbN film, again using photolithography and wet etching. Figure 1(b) presents a sketch of its sensitive element and an SEM image. The bolometer chip is working at the critical temperature T_c. The additional energy delivered to the surface by the impacting molecules may heat the superconductor above T_c and cause a voltage peak. The incident energy has to be sufficiently high to induce the required temperature change. Because of the large width of the stripes this condition can often not be met by a single molecule alone and the sensors respond only to many simultaneously impacting particles. With this second detector type we were not able to detect any molecular signal in our experiments. This type of superconducting wide-area bolometer is therefore not discussed further in the following where we rather focus on our explorations of nanostructured SSPD chips.

2.2. Molecular beam source

The details of our laser desorption source have already been described elsewhere [9, 10]: organic molecules were laser

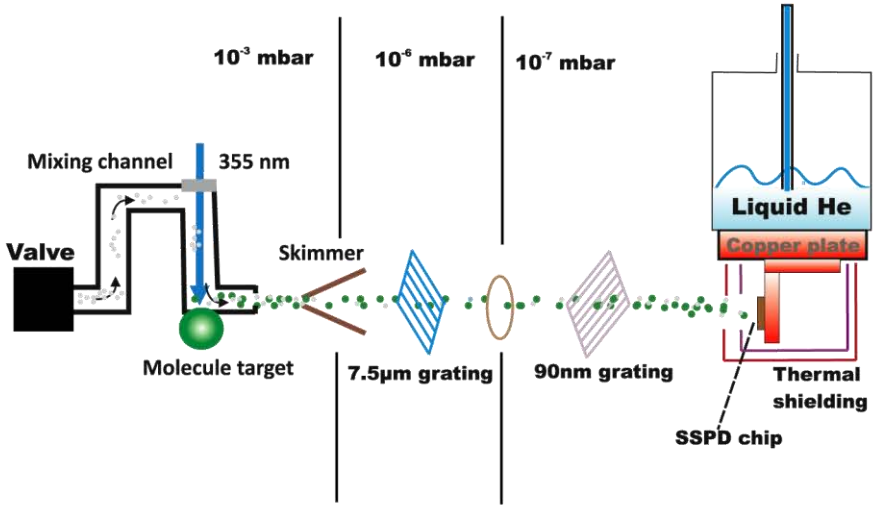

Figure 2. A pulsed laser desorbs biomolecules, which are then entrained by a supersonically expanding noble gas jet. After two-fold mechanical filtering the molecular beam hits the superconducting NbN detector. The impact of the molecules releases a voltage pulse which is stored by an oscilloscope and a timer card.

desorbed by a Nd:YAG laser beam (355 nm, 5 ns, 6–10 mJ), which was focused to a spot on a pressed powder sample (figure 2). The desorbed molecules are cooled and entrained by a jet of helium gas that fills the mixing channel before it exits through a 1 mm opening into a vacuum of 10^{-3} mbar. About 2 cm behind the mixing channel the beam passes a skimmer of 1 mm diameter, which separates the source from a differential pumping stage. In this second chamber the molecular beam is filtered by a copper mesh with 7.5 μm openings. This microstructure is used to reject grains of powder that might be ejected during the ablation process.

The stream of single molecules as well as possibly a background of microscopic particles leaves the second pumping stage through a 1 cm diameter opening into the detection chamber where the SSPD chip is attached to a helium bath cryostat. The overall distance from the desorption spot to the superconducting chip is 76 cm. For some experiments we added a second mechanical filter: a SiN_x line grating with a period of 266 nm and openings as small as 90 nm was attached to the entrance window of the cryostat. This addition further limited the transmitted particle size and also helped to extend the lifetime of the SSPD chips, which was otherwise strongly affected by the accumulation of molecular material. Even with the additional filter in place, the active time of an individual chip was limited to about 20 000 desorption shots, after which time a layer of molecules had covered the surface and made it insensitive. It is known [11] that SSPD chips can even be used to resolve the energy of incident photons. Similar energy dependent measurements with molecules were, however, still impeded in our present proof-of-principle study by the time-varying surface coverage.

3. Results

In order to explore its detection capabilities the SSPD chip was placed into the laser desorbed biomolecular beam. The

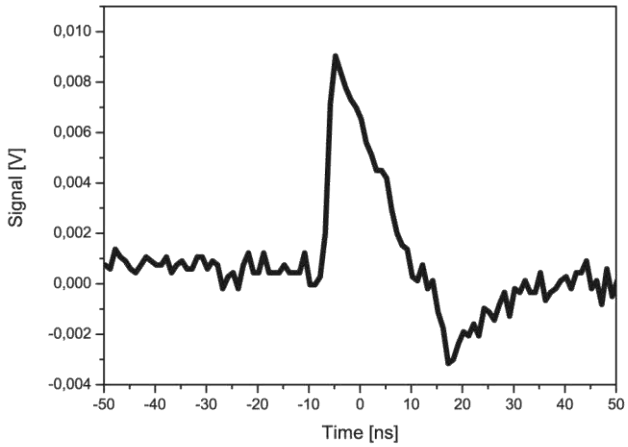

Figure 3. A typical individual peak, that is attributed to the impact of neutral molecules on the chip. The 20 μm × 20 μm SSPD chip was biased with a current of 19.5 μA. The signal was amplified by 20 dB.

first experiments were performed with a mixture of several molecules containing 0.2 g myoglobin (17 kDa), 0.3 g β-carotene (537 Da), 0.3 g insulin (5.8 kDa), 0.25 g bovine serum albumin (BSA,66 kDa) and 0.5 g cellulose of unspecified chain length to mechanically bind the other components.

In this first test we used a 20 × 20 μm^2 SSPD chip and in figure 3 we show a typical individual detection event from the desorbed molecule mixture. The peak is about 10 ns wide (FWHM) and indicates a high temporal detector resolution also for neutral nanoparticles.

We performed several tests to corroborate the evidence for the SSPD's sensitivity to isolated molecules and to exclude other possible reasons for the observed signals such as for instance the co-propagating seed gas or co-desorbed cellulose.

The influence of the rapidly expanding seed gas can be tested by switching off the desorbing laser beam. We searched

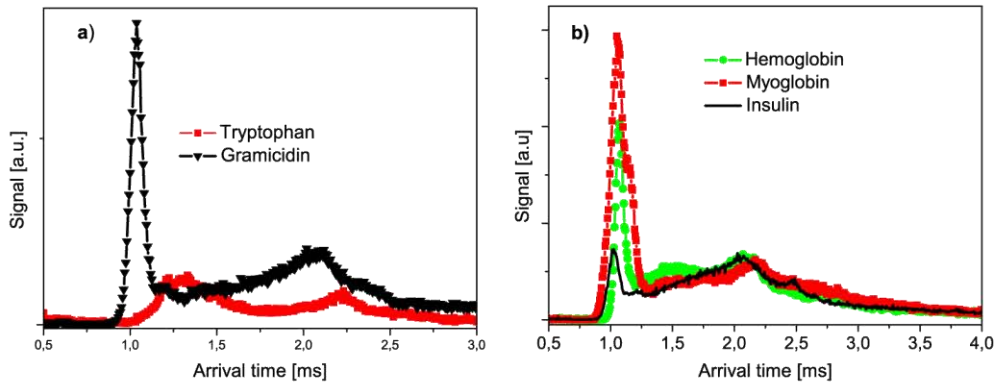

Figure 4. (a) Arrival time distribution of tryptophan and gramicidin. (b) Arrival time distribution of myoglobin, insulin and hemoglobin. All molecules were detected using the 20 μm × 20 μm SSPD chip.

for signs of the expanding helium carrier gas pulse alone, and the complete absence of any signal in this setting indicates that the SSPD chip is not capable of detecting individual helium atoms. The same is also true for all of the heavier noble gases such as neon, argon, krypton or xenon. None of them showed any detectable signal under our experimental conditions.

One might speculate that the higher kinetic energy of the more massive biomolecules could be outweighed by the larger number of lighter noble gas atoms. This argument would be supported by the fact that seed gas atoms must be much more abundant than the laser implanted biomolecules—otherwise supersonic expansion would never occur. However, since no signal was detected for the pure noble gas beams alone, a collective effect by the dense gas jet can be excluded. Since the biomolecular beam is more dilute than the carrier gas, a collective effect of organic particles is even less likely.

This finding is at variance with that for classic bolometers where the incidence of many particles is actually required to trigger a signal [21]. It has, however, to be noted that these detectors were not nanostructured and they were exploiting a different mechanism. Our result thus gives the first evidence that the SSPD chip is indeed not sensitive to the intense particle flux of atoms but rather to the local energy density of single complex nanoparticles.

As mentioned before, the molecules were always admixed with cellulose to achieve mechanical stabilization of the sample. In order to separate matrix signals from analyte signals we also performed a separate desorption experiment with pure cellulose powder alone. The complete absence of any measurable signal indicates again that the ablated matrix particles do not contribute any background in the SSPD counter. In order to enable a more quantitative evaluation we switched to a pulse counting mode and recorded time-of-flight curves for various experimental settings. The molecular velocity may differ from that of a free supersonic expansion, since the molecules can be delayed inside the gas mixing channel before they exit. This delay may lead to an underestimation of the actual velocity. The velocities and kinetic energies below are therefore reasonable lower limits.

In all the following experiments the samples contained only biomolecules from one species mixed 1:1 with cellulose. In figure 4(a) we show the arrival time distribution for tryptophan (204 Da) and gramicidin (1.9 kDa) samples, respectively. Figure 4(b) depicts the distributions for insulin, myoglobin and porcine hemoglobin (66 kDa) samples. All curves in figure 4 were recorded using the same 20 μm×20 μm SSPD chip, the same discriminator level, a bias current of 20±1 μA and two particle filters in the beam line, i.e. a 7.5 μm mesh as well as the 90 nm SiN filter. The opening time of the valve was set to 700 μs for all recorded curves in figure 4, except for that of tryptophan as discussed below. The arrival time distributions in figure 4 show a double structure which is a result of the particular valve setting in these experiments.

The agreement of the detected arrival times with the expected flight times may already be interpreted as a good indication for the detection of neutral particles. It is, however, desirable to corroborate this statement by complementary measurements which must rely on alternative detectors. As they are not readily available in the mass range beyond 2000 Da, where ionization detectors start to fail [7, 8] and nanomechanical detectors are not yet commercially available, it is also still unknown whether high-mass molecules (e.g. hemoglobin) can survive the desorption process as intact particles or whether the observed signals are rather caused by smaller neutral fragments generated in the source.

This is why our first checks were focused on characterizing the molecular beam source for tryptophan and gramicidin, where it is known [34, 35] that VUV laser ionization is soft and capable of detecting isolated molecules as well as larger clusters [9, 10]. A F_2 laser (157 nm, 5 ns, up to 3 mJ) is here combined with time-of-flight mass spectrometry (TOF-MS) to reveal the arrival time and mass distribution of all molecules emerging from the source.

Figure 5 shows a representative arrival time distribution for tryptophan, measured using TOF-MS and the same source settings as in the SSPD experiments. The flight distance between source and detector was shortened to 0.5 m. This also reduces the molecular flight times.

The arrival time distribution, recorded in photoionization TOF-MS at the mass of the single monomer (figure 4), has the same structure as the signals recorded by the SSPD (figure 5). Small differences in the arrival times can be assigned to

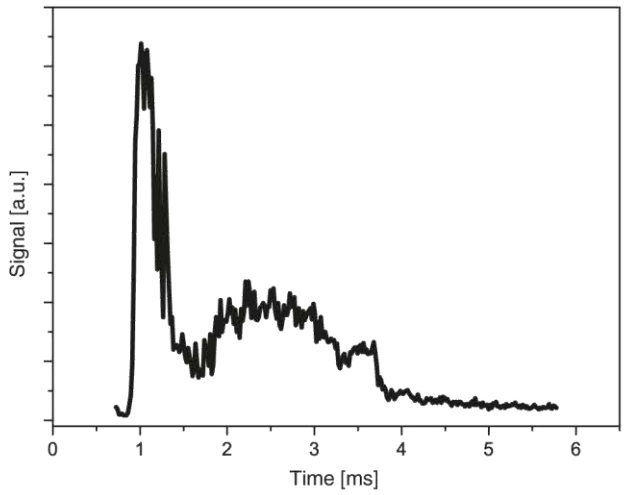

Figure 5. Arrival time distribution of tryptophan recorded via laser post-ionization and time-of-flight (TOF) mass spectrometry. The shape of the TOF distribution reproduces the distribution recorded by the superconducting chip (see figure 4).

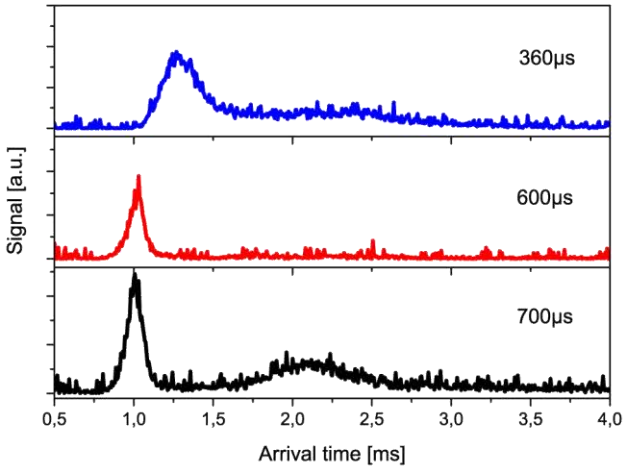

Figure 6. Arrival time distribution of gramicidin for different valve opening times, using a 10 μm × 10 μm SSPD chip. A reduction of the valve opening time leads to shifted arrival time distributions (slower molecules).

an accidental reduction of the valve opening time which influences both the pressure inside the mixing channel and the velocity of the expanding molecules. This is supported by figure 6, which depicts the arrival time distribution for gramicidin for three different valve opening times recorded by the SSPD chip. For short pulse times (figure 6, top) the arrival time distribution resembles the one recorded for tryptophan in figure 4(a), where the molecule arrival time was delayed. Interestingly, valve times around 600 μs do not show the double structure, as can be seen in figure 6 (center). We chose a slightly higher opening time of 700 μs (figure 6, bottom) for our experiments. This causes a double peak in the arrival time but also adds to the signal.

From these tests we gather the general insight that the arrival time distributions are rather identical for both the SSPD and the ionization detector. They are both consistent with the arrival of individual molecules. The absence of any signal related to the individual carrier gas atoms hints at an energy threshold in the SSPD which can only be overcome by sufficiently massive and energetic molecules. In our experiments the least energetic molecules detected by the SSPD were tryptophan particles in the velocity band of 300–500 m s^{-1}, i.e. with a kinetic energy of 100–300 meV if we assume we are seeing isolated molecules.

Compared with that value, all rare gas beams still have too little kinetic energy to be detected. Helium at 800 m s^{-1} reaches only 10 meV and xenon at 250 m s^{-1} would only attain 40 meV—still well below the value for tryptophan, which carries internal energy in addition.

4. Conclusion

The present experiments are just the promising start of an interesting journey into single neutral molecule detection using SSPDs. Our experiments give good first evidence that SSPDs can be used to register the incidence of neutral single nanoparticles.

As of today there is no efficient easily implemented way of detecting neutral large proteins to cross-check our results with individual, isolated insulin, hemoglobin or myoglobin. But we see a good consistency between the SSPD results and photoionization mass spectrometry in the flight times for tryptophan and gramicidin.

One might furthermore ask whether a high *internal* excitation may also add sufficient energy to the chip, which will be tested in future experiments by systematically varying the internal temperature of the molecules.

The possibility of detecting more massive neutral and labile molecules is promising for many applications in physical chemistry and also for matter wave interferometry. Even if the SSPD method cannot (yet) discriminate between different masses, de Broglie interferometry itself has been shown to be capable of discriminating different molecular properties [5] and experiments with clean and mass selected sources would only require a good sensitivity to the existence, not to the mass, of the particle.

The technology certainly requires further development and exploration but it may allow us to close a ‘detector loophole’ for particles which are too complex to be efficiently photoionized and yet too small to be well detected by other means.

Acknowledgments

This work was supported by the Austrian Science Funds FWF within the Wittgenstein program Z149 as well as by the Italian Fondazione Angelo Della Riccia. We thank Sanofi-Aventis Inc. for the donation of pure insulin powder. This work was also supported by the Russian Agency of Science and Innovation (contract 02.513.11.3446) and the Russian Foundation for Basic Research (grant 09-02-12364).

References

[1] Noble C A and Prather K A 2000 Real-time single particle mass spectrometry: a historical review of a quarter century of the chemical analysis of aerosol *Mass Spectrom. Rev.* **19** 248–74

[2] Schöllkopf W and Toennies J P 1996 The nondestructive detection of the helium dimer and trimer *J. Chem. Phys.* **104** 1155–8

[3] Arndt M, Nairz O, Voss-Andreae J, Keller C, Van der Zouw G and Zeilinger A 1999 Wave–particle duality of C60 molecules *Nature* **401** 680–2

[4] Hackermüller L, Uttenthaler S, Hornberger K, Reiger E, Brezgerand B, Zeilinger A and Arndt M 2003 Wave nature of biomolecules and fluorofullerenes *Phys. Rev. Lett.* **91** 90408

[5] Gerlich S, Gring M, Ulbricht H, Hornberger K, Tüxen J, Mayor M and Arndt M 2008 Matter-wave metrology as a complementary tool for mass spectrometry *Angew. Chem. Int. Edn Engl.* **47** 6195–8

[6] Ulbricht H, Berninger M, Deachapunya S, Stefanov A and Arndt M 2008 Gas phase sorting of fullerenes, polypeptides and carbon nanotubes *Nanotechnology* **19** 045502

[7] Schlag E W and Grotemeyer J 1992 Do large molecules ionize? *Chem. Phys. Lett.* **190** 521–7

[8] Becker C H and Wu K J 1995 On the photoionization of large molecules *J. Am. Soc. Mass Spectrom.* **6** 883–8

[9] Marksteiner M, Haslinger P, Sclafani M, Ulbricht H and Arndt M 2008 Gas-phase formation of large neutral alkaline-earth metal tryptophan complexes *J. Am. Soc. Mass Spectrom.* **19** 1021–6

[10] Marksteiner M, Haslinger P, Sclafani M, Ulbricht H and Arndt M 2009 UV and VUV ionization of organic molecules, clusters and complexes *J. Phys. Chem.* A **113** 9952–7

[11] Reiger E *et al* 2007 Spectroscopy with nanostructured superconducting single photon detectors *IEEE J. Sel. Top. Quantum Electron.* **13** 934–43

[12] Amirav A 1991 Electron impact and hyperthermal surface ionization mass spectrometry in supersonic molecular beams *Org. Mass Spectrom.* **26** 1–17

[13] Weickhardt C, Draack L and Amirav A 2003 Laser desorption combined with hyperthermal surface ionization time-of-flight mass spectrometry *Anal. Chem.* **75** 5602

[14] Ilic B, Craighead H G, Krylov S, Senaratne W, Ober C and Neuzil P 2004 Attogram detection using nanoelectromechanical oscillators *J. Appl. Phys.* **95** 3694–703

[15] Li M, Tang H X and Roukes M L 2007 Ultra-sensitive nems-based cantilevers for sensing, scanned probe and very high-frequency applications *Nat. Nanotechnol.* **2** 114–20

[16] Jensen K, Kim K and Zettl A 2008 An atomic-resolution nanomechanical mass sensor *Nat. Nanotechnol.* **3** 533–7

[17] Naik A K, Hanay M S, Hiebert W K, Feng X L and Roukes M L 2009 Towards single-molecule nanomechanical mass spectrometry *Nat. Nanotechnol.* **4** 445–50

[18] Low F J 1961 Low-temperature germanium bolometer *J. Opt. Soc. Am.* **51** 1300–4

[19] Kraus H 1996 Superconductive bolometers and calorimeters *Supercond. Sci. Technol.* **9** 827–42

[20] Enss C and McCammon D 2008 Physical principles of low temperature detectors: ultimate performance limits and current detector capabilities *J. Low Temp. Phys.* **151** 524

[21] Cavallini M, Meneghetti L, Scoles G and Yealland M 1971 Molecular beam scattering apparatus with low temperature bolometer detector *Rev. Sci. Instrum.* **42** 1759

[22] Andrews D H, Milton R M and Desorbo W 1946 A fast superconducting bolometer *J. Opt. Soc. Am.* **36** 518–24

[23] Booth N E and Goldie D J 1996 Superconducting particle detectors *Supercond. Sci. Technol.* **9** 493–516

[24] Frank M, Mean C-A, Labov S E, Benner W-H, Horn D, Jaklevic J M and Barfknecht A-T 1996 High-efficiency detection of 66 000 Da protein molecules using a cryogenic detector in a matrix-assisted laser desorption/ionization time-of-flight mass spectrometer *Rapid Commun. Mass Spectrom.* **10** 1946–50

[25] Twerenbold D, Vuilleumier J-L, Gerber D, Tadsen A, van den Brandt B and Gillevet P M 1996 Detection of single macromolecules using a cryogenic particle detector coupled to a biopolymer mass spectrometer *Appl. Phys. Lett.* **68** 3503–5

[26] Esposito E, Cristiano R, Pagano S, Perez de Lara D and Twerenbold D 2002 Fast Josephson cryodetector for time of flight mass spectrometry *Physica* C **372–376** 423–6

[27] Twerenbold D, Gerber D, Gritti D, Gonin Y, Netuschill A, Rossel F, Schenker D and Vuilleumier J-L 2001 Single molecule detector for mass spectrometry with mass independent detection efficiency *Proteomics* **1** 66–9

[28] Goltsman G N, Okunev O, Chulkova G, Lipatov A, Semenov A, Smirnov K, Voronov B, Dzardanov A, Williams C and Sobolewski R 2001 Picosecond superconducting single-photon optical detector *Appl. Phys. Lett.* **79** 705–7

[29] Semenov A D, Goltsman G N and Korneev A A 2001 Quantum detection by current carrying superconducting film *Physica* C **351** 349–56

[30] Verevkin A, Zhang J, Sobolewski R, Lipatov A, Okunev O, Chulkova G, Korneev A, Smirnov K, Goltsman G N and Semenov A 2002 Detection efficiency of large-active-area NbN single-photon superconducting detectors in the ultraviolet to near-infrared range *Appl. Phys. Lett.* **80** 4687–9

[31] Korneev A *et al* 2005 Quantum efficiency and noise equivalent power of nanostructured, NbN, single-photon detectors in the wavelength range from visible to infrared *IEEE Trans. Appl. Supercond.* **15** 571–4

[32] Goltsman G *et al* 2007 Middle-infrared to visible-light ultrafast superconducting single-photon detector *IEEE Trans. Appl. Supercond.* **17** 246–51

[33] Gol'tsman G, Smirnov K, Kouminov P, Voronov B, Kaurova N, Drakinsky V, Zhang J, Verevkin A and Sobolewski R 2003 Fabrication of nanostructured superconducting single-photon detectors *IEEE Trans. Appl. Supercond.* **13** 192–5

[34] Köster C and Grotemeyer J 1992 Single-photon and multi-photon ionization of infrared laser-desorbed biomolecules *Org. Mass Spectrom.* **27** 463–71

[35] Arps Jh, Chen Ch, McCann Mp and Datskou I 1989 Ionization of organic-molecules using coherent vacuum ultraviolet-light *Appl. Spectrosc.* **43** 1211–4

10 Acknowledgements

Time has passed really fast! That's a good sign! The time I have spent at University was always exciting and I always looked forward for the next day in the lab. That´s mainly thanks to you, my co-worker and friends at university. I have enjoyed exploring nature with you a lot. All the silly jokes and Friday afternoon ideas spiced my life and I wouldn´t have liked to miss them.

Markus, your calm and optimistic character pushed me forward. Thank you for all your support, assistance and time for guiding me into the scientific world.

Great Thanks to all my coworkers and friends for spending time with me in and outside from the lab: Markus Marksteiner, Michele Sclafani, Stefan Nimmrichter, Philipp Schmidt, Philipp Geyer, Nadine Dörre and Jonas Rodewald.

I would also like to thank Sandra Eibenberger, Peter Asenbaum, Stefan Gerlich, Christian Knobloch, Stefan Kuhn, Mathias Tomandl and especially Thomas Juffmann for all the discussions, not only about physics. Besides, all my years wouldn´t have been that easy without our administrative crew with its high level humour.

Thanks to Enar de Dios Rodriguez and Nadine Dörre for proof-reading this thesis.

Last but not least I want to thank my family as well as Enar for their love, support and inspiration.

11 Curriculum Vitae

PERSONAL INFORMATION:

Name:	Philipp
Surname:	Haslinger
Date of Birth:	1.12.1982
Parents:	Hedwig and Friedrich Haslinger
Address:	Gebr. Pichlergasse 16
	2143 Großkrut
	Austria
tel.:	+4325567471
e-mail:	philipp.haslinger@univie.ac.at

Education (University):

10/2002 – 06/2008	Physics (Uni Wien) diploma thesis: „Pulsed molecular beam sources for matter wave interferometery“) under the supervision of Markus Arndt at the University of Vienna
10/2008 – today	Physics PhD (Uni Wien) under the supervision of Markus Arndt at the University of Vienna
10/2002 – today	Mathematics (Uni Wien)

Research exchange:

09/2006 - 02/2007 ERASMUS at university Jagiellonski at Krakau, Poland

I have worked in the group of Prof. Wojciech Gawlik on magneto optical traping and cooling of Rubidium atoms.

05/2011-09/2011 University of California, Berkeley, USA

Supported by a „Scientific exchange grant“ of the university of Vienna as well as by a scholarship of the University of California Berkeley I have worked in the group of Prof. Holger Müller on a Cs Interferometer with large momentum transfer and large pulse separation time.

Teaching experience:

- Tutor of „ Analysis für Physiker“ at the department of mathematics
- Responsible for practical work for students in quantum optics (winter and summer term 2008/09 and 2009/10)
- Responsible for Proseminar in „Experimentelle Physik 3“(winter term 2010/11)

12 Bibliography

[1] De Broglie L. *Recherches sur la théorie des quanta* (Migration-université en cours d'affectation), (1924).

[2] Davisson C and Germer L. The scattering of electrons by a single crystal of nickel *Nature* **119** 558–60, (1927).

[3] Einstein A, Podolsky B and Rosen N. Can quantum-mechanical description of physical reality be considered complete? *Physical review* **47** 777 – 780, (1935).

[4] Schrödinger E. Die gegenwärtige Situation in der Quantenmechanik *Naturwissenschaften* **6** 823–8, (1935).

[5] Lan S-Y, Kuan P-C, Estey B, Haslinger P and Müller H. Influence of the Coriolis Force in Atom Interferometry *Physical Review Letters* **108** 090402, (2012).

[6] Haslinger P, Dörre N, Geyer P, Rodewald J, Nimmrichter S and Arndt M. A universal matter-wave interferometer with optical ionization gratings in the time domain *Nature Physics* **9** 144–8, (2013).

[7] Nimmrichter S, Haslinger P, Hornberger K and Arndt M. Concept of an ionizing time-domain matter-wave interferometer *New Journal of Physics* **13** 075002, (2011).

[8] Cahn S, Kumarakrishnan A, Shim U, Sleator T, Berman P and Dubetsky B. Time-Domain de Broglie Wave Interferometry *Physical Review Letters* **79** 784–7, (1997).

[9] Lan S-Y, Kuan P-C, Estey B, English D, Brown J M, Hohensee M and Müller H. A clock directly linking time to a particle's mass *Science* **339** 554–7, (2013).

[10] Reiger E, Hackermüller L, Berninger M and Arndt M. Exploration of gold nanoparticle beams for matter wave interferometry *Optics Communications* **264** 326–32, (2006).

[11] Young T. *A course of lectures on natural philosophy and the mechanical arts, Volume 1* (Johnson), (1807).

[12] Juffmann T, Milic A, Müllneritsch M, Asenbaum P, Tsukernik A, Tüxen J, Mayor M, Cheshnovsky O and Arndt M. Real-time single-molecule imaging of quantum interference. *Nature nanotechnology* **7** 297–300, (2012).

[13] Arndt M, Nairz O, Vos-Andreae J, Keller C, Van der Zouw G and Zeilinger A. Wave-particle duality of C(60) molecules. *Nature* **401** 680–2, (1999).

[14] Akoury D, Kreidi K, Jahnke T, Weber T, Staudte A, Schöffler M, Neumann N, Titze J, Schmidt L P H, Czasch A, Jagutzki O, Costa Fraga R a, Grisenti R E, Díez Muiño R, Cherepkov N a, Semenov S K, Ranitovic P, Cocke C L, Osipov T, Adaniya H, Thompson J C, Prior M H, Belkacem A, Landers a L, Schmidt-Böcking H and Dörner R. The simplest double slit: interference and entanglement in double photoionization of H2 *Science* **318** 949–52, (2007).

[15] Schumm T, Hofferberth S, Andersson L M, Wildermuth S, Groth S, Bar-Joseph I, Schmiedmayer J and Krüger P. Matter-wave interferometry in a double well on an atom chip *Nature Physics* **1** 57–62, (2005).

[16] Schmid P, Stöhr F, Arndt M, Tüxen J and Mayor M. Single-Photon Ionization of Organic Molecules Beyond 10 kDa. *Journal of the American Society for Mass Spectrometry* **24** 602–8, (2013).

[17] Tüxen J, Eibenberger S, Gerlich S, Arndt M and Mayor M. Highly Fluorous Porphyrins as Model Compounds for Molecule Interferometry *European Journal of Organic Chemistry* **2011** 4823–33, (2011).

[18] Born M and Wolf E. *Principles of Optics* (Pergamon Press, Oxford), (1993).

[19] Clauser J and Li S. Talbot-vonLau atom interferometry with cold slow potassium *Physical Review A* **49** 2213–7, (1994).

[20] Brezger B, Hackermüller L, Uttenthaler S, Petschinka J, Arndt M and Zeilinger A. Matter-Wave Interferometer for Large Molecules *Physical Review Letters* **88** 100404, (2002).

[21] Hornberger K, Gerlich S, Haslinger P, Nimmrichter S and Arndt M. Colloquium: Quantum interference of clusters and molecules *Reviews of Modern Physics* **84** 157–73, (2012).

[22] Gerlich S, Hackermüller L, Hornberger K, Stibor A, Ulbricht H, Gring M, Goldfarb F, Savas T, Müri M, Mayor M and Arndt M. A Kapitza–Dirac–Talbot–Lau interferometer for highly polarizable molecules *Nature Physics* **3** 711–5, (2007).

[23] Talbot H F. LXXVI. Facts relating to optical science. No. IV *Philosophical Magazine Series 3* **9** 401–7, (1836).

[24] Lau E. Beugungserscheinungen an Doppelrastern *Annalen der Physik* **437** 417–23, (1948).

[25] P. Haslinger, S. Nimmrichter, N. Dörre, P. Geyer and M A. Towards the limits of cluster interferometry. *2nd Vienna Symposium on the Foundations of Modern Physics*, (2009).

[26] Chapman M and Ekstrom C. Near-field imaging of atom diffraction gratings: The atomic Talbot effect *Physical Review A* **51** 14–7, (1995).

[27] Hagley E W, Deng L and Kozuma M. A Well-Collimated Quasi-Continuous Atom Laser *Science* **283** 1706–9, (1999).

[28] Andrews M R, Townsend C G, Miesner H-J and Ketterle W. Observation of Interference Between Two Bose Condensates *Science* **275** 637–41, (1997).

[29] Chu S, Hollberg L, Bjorkholm J, Cable A and Ashkin A. Three-dimensional viscous confinement and cooling of atoms by resonance radiation pressure *Physical Review Letters* **55** 48–51, (1985).

[30] Hänsel W, Hommelhoff P, Hänsch T W and Reichel J. Bose-Einstein condensation on a microelectronic chip. *Nature* **413** 498–501, (2001).

[31] Sleator T, Pfau T, Balykin V and Mlynek J. Imaging and focusing of an atomic beam with a large period standing light wave *Applied Physics B* **54** 375–9, (1992).

[32] McLachlan A D. Van der Waals forces between an atom and a surface *Molecular Physics* **7** 381–8, (1964).

[33] Juffmann T, Nimmrichter S, Arndt M, Gleiter H and Hornberger K. New Prospects for de Broglie Interferometry *Foundations of Physics* **42** 98–110, (2012).

[34] Dzyaloshinskii I, Lifshitz E and Pitaevskii L. GENERAL THEORY OF VAN DER WAALS'FORCES *Soviet Physics Uspekhi* **73** 153 –176, (1961).

[35] Nairz O, Arndt M and Zeilinger A. Quantum interference experiments with large molecules *American Journal of Physics* **71** 319–25, (2003).

[36] Grisenti R, Schöllkopf W, Toennies J, Hegerfeldt G and Köhler T. Determination of Atom-Surface van der Waals Potentials from Transmission-Grating Diffraction Intensities *Physical Review Letters* **83** 1755–8, (1999).

[37] Schedin F, Geim A K, Morozov S V., Hill E W, Blake P, Katsnelson M I and Novoselov K S. Detection of individual gas molecules adsorbed on graphene *Nature Materials* **6** 652–5, (2007).

[38] Longhi S. Gap solitons in metamaterials *Waves in Random and Complex Media* **15** 119–26, (2005).

[39] Hornberger K, Gerlich S, Ulbricht H, Hackermüller L, Nimmrichter S, V Goldt I, Boltalina O and Arndt M. Theory and experimental verification of Kapitza–Dirac–Talbot–Lau interferometry *New Journal of Physics* **11** 043032, (2009).

[40] Gerlich S, Eibenberger S, Tomandl M, Nimmrichter S, Hornberger K, Fagan P J, Tüxen J, Mayor M and Arndt M. Quantum interference of large organic molecules. *Nature communications* **2** 263, (2011).

[41] Samaroo D, Vinodu M, Chen X and Drain C M. meso-Tetra(pentafluorophenyl)porphyrin as an Efficient Platform for Combinatorial Synthesis and the Selection of New Photodynamic Therapeutics using a Cancer Cell Line *Journal of Combinatorial Chemistry* **9** 998–1011, (2007).

[42] Eibenberger S, Gerlich S, Arndt M, Mayor M and Tüxen J. Molecular libraries for testing the quantum superposition principle beyond 10 kDa *Submitted*, (2013).

[43] Deng L, Hagley E and Denschlag J. Temporal, matter-wave-dispersion Talbot effect *Physical Review Letters* **83** 5407–11, (1999).

[44] Kasevich M and Chu S. Atomic interferometry using stimulated Raman transitions *Physical Review Letters* **67** 181–4, (1991).

[45] Lawall J and Prentiss M. Demonstration of a novel atomic beam splitter *Physical review letters* **72** 993–7, (1994).

[46] Szriftgiser P, Guéry-Odelin D, Arndt M and Dalibard J. Atomic Wave Diffraction and Interference Using Temporal Slits. *Physical review letters* **77** 4–7, (1996).

[47] Abfalterer R, Keller C, Bernet S, Oberthaler M, Schmiedmayer J and Zeilinger A. Nanometer definition of atomic beams with masks of light *Physical Review A* **56** 4365–8, (1997).

[48] Johnson K, Chu A, Berggren K and Prentiss M. Demonstration of a blazed grating beam splitter for two-level atoms *Optics communications* **126** 326–38, (1996).

[49] Rasel E and Oberthaler M. Atom wave interferometry with diffraction gratings of light *Physical review letters* **75** 2633–7, (1995).

[50] Cronin A D and Pritchard D E. Optics and interferometry with atoms and molecules *Reviews of Modern Physics* **81** 1051–129, (2009).

[51] Hulst H C and Van De Hulst H C. *Light scattering: by small particles* (Courier Dover Publications), (1981).

[52] Grimm R, Weidemüller M and Ovchinnikov Y. Optical dipole traps for neutral atoms *Advances In Atomic, Molecular, and Optical Physics* **42** 95–170, (2000).

[53] Meschede D. *Gerthsen Physik* (SPRINGER VERLAG), (2002).

[54] Aharonov Y and Bohm D. Significance of electromagnetic potentials in the quantum theory *Physical Review* **115** 485–91, (1959).

[55] Hohensee M a., Estey B, Hamilton P, Zeilinger A and Müller H. Force-Free Gravitational Redshift: Proposed Gravitational Aharonov-Bohm Experiment *Physical Review Letters* **108** 230404, (2012).

[56] Caprez A, Barwick B and Batelaan H. Macroscopic Test of the Aharonov-Bohm Effect *Physical Review Letters* **99** 210401, (2007).

[57] Nimmrichter S and Hornberger K. Theory of near-field matter-wave interference beyond the eikonal approximation *Physical Review A* **78** 023612, (2008).

[58] Dörre N. *Design and development of an optical matter wave interferometer*, (2010).

[59] Rodewald J. *Setup of an optical time-domain matter wave interferometer for heavy particles*, (2011).

[60] Scoles G, Bassi D, Buck U and Laine D. *Atomic and Molecular Beam Methods, Vol. I.* vol 28 (Oxford University Press), (1988).

[61] Luria K, Christen W and Even U. Generation and propagation of intense supersonic beams. *The journal of physical chemistry. A* **115** 7362–7, (2011).

[62] Even U, Jortner J, Noy D, Lavie N and Cossart-Magos C. Cooling of large molecules below 1 K and He clusters formation *The Journal of Chemical Physics* **112** 8068, (2000).

[63] Haberland H, Karrais M and Mall M. A new type of cluster and cluster ion source *Zeitschrift für Physik D Atoms, Molecules and Clusters* **20** 413–5, (1991).

[64] Marksteiner M, Haslinger P, Ulbricht H, Sclafani M, Oberhofer H, Dellago C and Arndt M. Gas-phase formation of large neutral alkaline-earth metal tryptophan complexes. *Journal of the American Society for Mass Spectrometry* **19** 1021–6, (2008).

[65] Brizzolara R A and Cooper C B. Measurements of energy distributions and yields of neutral Cu2 and Cu3 species sputtered from Cu by low energy Ar+ ions **43** 136–45, (1989).

[66] Schöllkopf W and Toennies J P. Nondestructive mass selection of small van der Waals clusters. *Science* **266** 1345–8, (1994).

[67] Morse M D. 2. Super Sonic Beam Sources *Atomic, Molecular, and Optical Physics: Atoms and Molecules* **29** 21 – 47, (1996).

[68] Anderson J B. Molecular beams from nozzle sources *In: Molecular beams and low density gasdynamics. (A75-28372 12-72) New York, Marcel Dekker, Inc., 1974, p. 1-91.*

[69] Marksteiner M, Haslinger P, Sclafani M, Ulbricht H and Arndt M. UV and VUV ionization of organic molecules, clusters, and complexes. *Journal of Physical Chemistry A* **113** 9952–7, (2009).

[70] Juffmann T. *Surface based detection schemes for molecular matter wave interferometry*, (2012).

[71] Sansonetti C J, Reader J and Vogler K. Precision measurement of wavelengths emitted by a molecular fluorine laser at 157 nm. *Applied optics* **40** 1974–8, (2001).

[72] Yoshino K, Parkinson W H, Ito K and Matsui T. Absolute Absorption Cross Section Measurements of Schumann-Runge Continuum of O2 at 90 K and 295 K *Journal of Molecular Spectroscopy* **229** 238–43, (2005).

[73] Kunz R R, Liberman V and Downs D K. Experimentation and modeling of organic photocontamination on lithographic optics *Journal of Vacuum Science & Technology B: Microelectronics and Nanometer Structures* **18** 1306–13, (2000).

[74] Bates A K, Rothschild M, Bloomstein T M, Fedynyshyn T H, Kunz R R, Liberman V and Switkes M. Review of technology for 157-nm lithography *IBM Journal of Research and Development* **45** 605–14, (2001).

[75] Chiow S, Herrmann S, Chu S and Müller H. Noise-Immune Conjugate Large-Area Atom Interferometers *Physical Review Letters* **103** 050402, (2009).

[76] Rodewald J. *Vibration detection on an all-optical Talbot-Lau molecular interferometer.*, (2010).

[77] Marchese F T and Jaffé H H. The calculation of ground and excited state molecular polarizabilities: A simple perturbation treatment *Theoretica Chimica Acta* **45** 241–7, (1977).

[78] Malloci G, Mulas G and Joblin C. Electronic absorption spectra of PAHs up to vacuum UV Towards a detailed model of interstellar PAH photophysics *Astronomy and Astrophysics* **426** 105–17, (2004).

[79] Gilmore I S and Seah M P. Ion detection efficiency in SIMS : dependencies on energy , mass and composition for microchannel plates used in mass spectrometry *International Journal of Mass Spectrometry* **202** 217–29, (2000).

[80] Hornberger K, Uttenthaler S, Brezger B, Hackermüller L, Arndt M and Zeilinger A. Collisional Decoherence Observed in Matter Wave Interferometry *Physical Review Letters* **90** 160401, (2003).

[81] Hornberger K, Hackermüller L and Arndt M. Influence of molecular temperature on the coherence of fullerenes in a near-field interferometer *Physical Review A* **71** 023601, (2005).

[82] Cronin A D and Pritchard D E. Optics and interferometry with atoms and molecules *Reviews of Modern Physics* **81** 1051–129, (2009).

[83] Arndt M. personal communication, (2013).

[84] Gring M, Gerlich S, Eibenberger S, Nimmrichter S, Berrada T, Arndt M, Ulbricht H, Hornberger K, Müri M, Mayor M, Böckmann M and Doltsinis N L. Influence of conformational molecular dynamics on matter wave interferometry *Physical Review A* **81** 031604, (2010).

[85] Berninger M, Stefanov A, Deachapunya S and Arndt M. Polarizability measurements of a molecule via a near-field matter-wave interferometer *Physical Review A* **76** 013607, (2007).

[86] Bonin K D and Kresin V V. *Electric - Dipole Polarizabilities of Atoms, Molecules and Clusters* (World Scientific Publishing Company), (1997).

[87] De Heer W. The physics of simple metal clusters: Experimental aspects and simple models, Rev *Reviews of Modern Physics* **65** 611–76, (1993).

[88] Amini J and Gould H. High Precision Measurement of the Static Dipole Polarizability of Cesium *Physical Review Letters* **91** 153001, (2003).

[89] Eibenberger S, Gerlich S, Arndt M, Tüxen J and Mayor M. Electric moments in molecule interferometry *New Journal of Physics* **13** 043033, (2011).

[90] Ballard a., Bonin K and Louderback J. Absolute measurement of the optical polarizability of C60 *The Journal of Chemical Physics* **113** 5732, (2000).

[91] Gerlich S, Gring M, Ulbricht H, Hornberger K, Tüxen J, Mayor M and Arndt M. Matter-wave metrology as a complementary tool for mass spectrometry. *Angewandte Chemie* **47** 6195–8, (2008).

[92] Hackermüller L, Hornberger K, Gerlich S, Gring M, Ulbricht H and Arndt M. Optical polarizabilities of large molecules measured in near-field interferometry *Applied Physics B* **89** 469–73, (2007).

[93] Gerlach W and Stern O. Das magnetische Moment des Silberatoms *Zeitschrift für Physik* **9** 353–5, (1922).

[94] Billas I, Chatelain A and De Heer W. Magnetism of Fe, Co and Ni clusters in molecular beams *Journal of Magnetism and Magnetic Materials* **168** 64–84, (1997).

[95] Mairhofer L. *Deflectometry in a Kapitza-Dirac-Talbot-Lau interferometer for matter waves*, (2013).

[96] Kreibig U and Vollmer M. *Optical properties of metal clusters* (Springer Series in Materials Science), (1995).

[97] Berkowitz J. *Atomic and Molecular Photoabsorption: Absolute Total Cross Sections* (Elsevier), (2002).

[98] Bennett Jr W R. Hole burning effects in a He-Ne optical maser *Physical Review* **126** 580–93, (1962).

[99] Taylor S, Spain E M and Morse M D. Spectroscopy and electronic structure of jet-cooled NiPd and PdPt *The Journal of Chemical Physics* **92** 2710–20, (1990).

[100] Morse M D, Hansen G P, Langridge-Smith P R R, Zheng L-S, Geusic M E, Michalopoulos D L and Smalley R E. Spectroscopic studies of the jet-cooled nickel dimer *The Journal of Chemical Physics* **80** 5400–5, (1984).

[101] Cheng P Y, Willey K F and Duncan M A. Vibronic spectroscopy of Ag2-Ar *Chemical Physics Letters* **163** 469–74, (1989).

[102] Morse M D, Hopkins J B, Langridge-Smith P R R and Smalley R E. Spectroscopic studies of the jet-cooled copper trimer *The Journal of Chemical Physics* **79** 5316–28, (1983).

[103] Rohlfing E and Valentini J J. Laser-excited fluorescence spectroscopy of the jet-cooled copper trimer *Chemical Physics Letters* **126** 113–8, (1986).

[104] Woodward J, Cobb S and Gole J. Gas-phase laser-induced excitation spectrum of nickel trimer *The Journal of Physical Chemistry* **92** 1404–6, (1988).

[105] Page R H and Gudeman C S. Rotationally resolved dicopper (Cu2) laser-induced fluorescence spectra *The Journal of Chemical Physics* **94** 39–51, (1991).

[106] Menezes W J C and Knickelbein M B. Photodissociation spectroscopy of NbnArm complexes *The Journal of Chemical Physics* **98** 1856–66, (1993).

[107] Knickelbein M B. The absorption spectra of small nickel clusters via photodissociation: NinArm→Nin+mAr *The Journal of Chemical Physics* **99** 2377–82, (1993).

[108] Heikal A, Bañares L, Semmes D H and Zewail A H. Real-time dynamics of vibrational predissociation in anthracene-Arn (n = 1, 2, 3) *Chemical Physics* **157** 231–50, (1991).

[109] Yang S and Knickelbein M B. Photoionization studies of transition metal clusters: Ionization potentials for Fen and Con *The Journal of Chemical Physics* **93** 1533–9, (1990).

[110] Saunders W, Fayet P and Wöste L. Photodestruction of positively and negatively charged aluminum-cluster ions *Physical Review A* **39** 4400–5, (1989).

[111] Knickelbein M B and Menezes W J C. Metal cluster-rare gas van der Waals complexes: NbnArm and FenKrm *Chemical Physics Letters* **184** 433–8, (1991).

[112] Fielicke A, Kirilyuk A, Ratsch C, Behler J, Scheffler M, Von Helden G and Meijer G. Structure Determination of Isolated Metal Clusters via Far-Infrared Spectroscopy *Physical Review Letters* **93** 023401, (2004).

[113] Nimmrichter S, Hornberger K, Ulbricht H and Arndt M. Absolute absorption spectroscopy based on molecule interferometry *Physical Review A* **78** 063607, (2008).

[114] Simard B, Dénommée S, Rayner D M, Van Heijnsbergen D, Meijer G and Von Helden G. IR multiphoton depletion spectroscopy of metal cluster–ligand complexes *Chemical Physics Letters* **357** 195–203, (2002).

[115] Pfau T, Spälter S, Kurtsiefer C, Ekstrom C and Mlynek J. Loss of spatial coherence by a single spontaneous emission. *Physical review letters* **73** 1223–6, (1994).

[116] Chapman M, Hammond T, Lenef A, Schmiedmayer J and Rubenstein, Richard A and Smith, Edward and Pritchard D E. Photon scattering from atoms in an atom interferometer: coherence lost and regained *Physical Review Letters* **75** 3783–7, (1995).

[117] Kokorowski D, Cronin A, Roberts T and Pritchard D. From Single- to Multiple-Photon Decoherence in an Atom Interferometer *Physical Review Letters* **86** 2191–5, (2001).

[118] Hackermüller L, Hornberger K, Brezger B, Zeilinger A and Arndt M. Decoherence of matter waves by thermal emission of radiation. *Nature* **427** 711–4, (2004).

[119] Haberland H. Melting of Clusters *Proceedings of the Summer School on Clusters and Nanoparticles*, (2000).

[120] Hornberger K, Hackermüller L and Arndt M. Influence of molecular temperature on the coherence of fullerenes in a near-field interferometer *Physical Review A* **71** 023601, (2005).

[121] Gradshteyn and Ryzhik. Table of Integrals, Series and Products, (2007).

[122] Schinke R. *Photodissociation Dynamics: Spectroscopy and Fragmentation of Small Polyatomic Molecules* (Cambridge University Press), (2008).

[123] Keller B A, Felder P and Huber J R. Molecular beam photodissociation study of methyl nitrite in the near-ultraviolet region *Journal of Physical Chemistry* **91** 1114–20, (1987).

[124] Minemoto S, Terasaki A, Imoto H and Kondow T. Electronic structure of vanadium tetramer ion studied by optical absorption spectroscopy *Journal of Chemical Physics* **109** 9737, (1998).

[125] Gruene P, Rayner D M, Redlich B, Van der Meer A F G, Lyon J T, Meijer G and Fielicke A. Structures of neutral Au7, Au19, and Au20 clusters in the gas phase. *Science* **321** 674–6, (2008).

[126] Wood K V and W.Taylor J. A photoionization mass spectrometric study of autoionization in ethylene and trans-2-butene *International Journal of Mass Spectrometry and Ion Physics* **30** 307–18, (1979).

[127] Yencha A J and El-Sayed M A. Lowest Ionization Potentials of Some Nitrogen Heterocyclics *Journal of Chemical Physics* **48** 3469–75, (1968).

[128] Lewis B R and Carver J H. Temperature dependence of the carbon dioxide photoabsorption cross section between 1200 and 1970 Å *Journal of Quantitative Spectroscopy and Radiative Transfer* **30** 297–309, (1983).

[129] Kuo C T, Chen Y M, Wang S Y, Li S C and Nee J B. The Photoabsorption Spectrum of CO2 at 104-170 nm *Chinese Journal of Physics* **42** 65–73, (2004).

[130] Wu C Y R, Chen F Z and Judge D L. Temperature-dependent photoabsorption cross sections in the VUV-UV region : Ethylene *Journal of Geophysical Research* **109** E07S15, (2004).

[131] Walker I C and Palmer M H. The electronic states of the azines. IV. Pyrazine, studied by VUV absorption, near-threshold electron energy-loss spectroscopy and ab initio multi-reference configuration interaction calculations *Chemical Physics* **153** 169–87, (1991).

[132] Dimopoulos S, Graham P W, Hogan J M, Kasevich M a. and Rajendran S. Gravitational wave detection with atom interferometry *Physics Letters B* **678** 37–40, (2009).

[133] Snadden M, McGuirk J, Bouyer P, Haritos K and Kasevich M. Measurement of the Earth's Gravity Gradient with an Atom Interferometer-Based Gravity Gradiometer *Physical Review Letters* **81** 971–4, (1998).

[134] Fixler J B, Foster G T, McGuirk J M and Kasevich M A. Atom interferometer measurement of the newtonian constant of gravity. *Science* **315** 74–7, (2007).

[135] Coriolis G G. *Mémoire sur les équations du mouvement relatif des systèmes de corps* (Bachelier), (1835).

[136] Müller H, Chiow S, Long Q, Herrmann S and Chu S. Atom Interferometry with up to 24-Photon-Momentum-Transfer Beam Splitters *Physical Review Letters* **100** 180405, (2008).

[137] Müller H, Chiow S and Chu S. Atom-wave diffraction between the Raman-Nath and the Bragg regime: Effective Rabi frequency, losses, and phase shifts *Physical Review A* **77** 023609, (2008).

[138] Chiow S, Kovachy T, Chien H-C and Kasevich M. 102hbar k Large Area Atom Interferometers *Physical Review Letters* **107** 130403, (2011).

[139] Douglas D J, Frank A J and Mao D. Linear ion traps in mass spectrometry. *Mass spectrometry reviews* **24** 1–29, (2005).

[140] Schwartz J, Senko M and Syka J. A two-dimensional quadrupole ion trap mass spectrometer *Journal of the American Society for Mass Spectrometry* **13** 659–69, (2002).

[141] Wester R. Radiofrequency multipole traps: tools for spectroscopy and dynamics of cold molecular ions *Journal of Physics B: Atomic, Molecular and Optical Physics* **42** 154001, (2009).

[142] Asvany O and Schlemmer S. Numerical simulations of kinetic ion temperature in a cryogenic linear multipole trap *International Journal of Mass Spectrometry* **279** 147–55, (2009).

[143] Nimmrichter S, Hornberger K, Haslinger P and Arndt M. Testing spontaneous localization theories with matter-wave interferometry *Physical Review A* **83** 043621, (2011).

[144] Sassin N a, Everhart S C, Dangi B B, Ervin K M and Cline J I. Fluorescence and photodissociation of rhodamine 575 cations in a quadrupole ion trap. *Journal of the American Society for Mass Spectrometry* **20** 96–104, (2009).

[145] Dashtiev M, Azov V, Frankevich V, Scharfenberg L and Zenobi R. Clear evidence of fluorescence resonance energy transfer in gas-phase ions. *Journal of the American Society for Mass Spectrometry* **16** 1481–7, (2005).

[146] Marksteiner M, Divochiy A, Sclafani M, Haslinger P, Ulbricht H, Korneev A, Semenov A, Gol'tsman G and Arndt M. A superconducting NbN detector for neutral nanoparticles. *Nanotechnology* **20** 455501, (2009).

[147] Dörre N, Haslinger P, Geyer P, Rodewald J, Nimmrichter S and Arndt M. In preparation, (2013).

[148] Ghirardi G, Rimini A and Weber T. Unified dynamics for microscopic and macroscopic systems. *Physical review D* **34** 470–91, (1986).

[149] Pearle P. Combining stochastic dynamical state-vector reduction with spontaneous localization *Physical Review A* **39** 2277–89, (1989).

[150] Ghirardi G, Pearle P and Rimini A. Markov processes in Hilbert space and continuous spontaneous localization of systems of identical particles *Physical Review A* **42** 78–89, (1990).

[151] Adler S L and Bassi A. Physics. Is quantum theory exact? *Science* **325** 275–6, (2009).

[152] Thielemann T, Schmidt S and Gerling J P. Lignite and hard coal: Energy suppliers for world needs until the year 2100—An outlook *International Journal of Coal Geology* **72** 1–14, (2007).